Interplay of Ordering Behavior and Optical Properties in Organic Semiconductor Blends

Dissertation

der Mathematisch-Naturwissenschaftlichen Fakultät

der Eberhard Karls Universität Tübingen

zur Erlangung des Grades eines

Doktors der Naturwissenschaften

(Dr. rer. nat.)

vorgelegt von

Katharina Broch

aus Neu-Ulm

Tübingen

2013

Tag der mündlichen Qualifikation:	22.07.2013
Dekan:	Prof. Dr. Wolfgang Rosenstiel
1. Berichterstatter:	Prof. Dr. Frank Schreiber
2. Berichterstatterin:	Prof. Dr. Monika Fleischer
3. Berichterstatter:	Prof. Dr. Henning Sirringhaus

Contents

1 Introduction **1**

2 Fundamentals **5**
2.1 Optics . . . 5
2.1.1 Absorption of light: the dielectric tensor . . . 5
2.1.2 Reflection and transmission: the Fresnel-coefficients . . . 7
2.2 Organic semiconductors . . . 8
2.2.1 π-electron system . . . 8
2.2.2 Intermolecular interactions . . . 9
2.2.3 Excitations in organic molecules . . . 11
2.2.3.1 Born-Oppenheimer approximation . . . 11
2.2.3.2 Franck-Condon principle and vibronic progression . . . 11
2.2.3.3 Molecular crystal spectra . . . 12
2.3 Thin film growth . . . 14
2.4 Mixtures of organic semiconductors . . . 15
2.4.1 Theoretical description . . . 15
2.4.1.1 Mixtures of non-interacting spheres . . . 15
2.4.1.2 Mixtures of interacting spheres . . . 16
2.4.2 Optical properties of mixed films . . . 17
2.4.2.1 Effective medium approximation . . . 17
2.4.2.2 Charge transfer . . . 18
2.5 Materials . . . 19
2.5.1 Pentacene (PEN) . . . 19
2.5.2 Perfluoropentacene (PFP) . . . 20
2.5.3 Diindenoperylene (DIP) . . . 21

3 Experimental methods **23**
3.1 Sample preparation . . . 23
3.1.1 Organic molecular beam deposition (OMBD) . . . 23
3.1.2 Substrates . . . 23

3.1.3 UHV-chamber . . . 23
3.1.4 Film growth . . . 25
3.1.4.1 Growth procedure . . . 25
3.1.4.2 Experimental parameters and scale factor determination . 25
3.1.4.3 Determination of the mixing ratio . . . 27
3.2 Differential reflectance spectroscopy (DRS) . . . 27
3.2.1 Fundamentals . . . 27
3.2.2 Setup . . . 29
3.3 Spectroscopic ellipsometry (SE) . . . 30
3.3.1 Fundamentals . . . 30
3.3.2 Setup . . . 32
3.4 X-ray reflectivity (XRR) and grazing incidence X-ray diffraction (GIXD) . 33
3.5 Atomic force microscopy (AFM) . . . 35
3.6 Further experiments . . . 35
3.6.1 Near-edge X-ray absorption fine structure spectroscopy (NEXAFS) 35
3.6.2 Polarization dependent transmission spectroscopy (PDTS) . . . 37
3.6.3 Real-time GIXD measurements . . . 39

4 Results and discussion I: Post growth measurements 41
4.1 Structure, morphology and mixing behavior . . . 41
4.1.1 Blends of PFP and PEN . . . 41
4.1.2 Blends of PFP and DIP . . . 43
4.1.3 Blends of PEN and DIP . . . 48
4.1.4 Rationalization of the observed mixing and ordering behavior . . . 50
4.2 Absorption spectra of PFP:PEN blends . . . 54
4.2.1 $\epsilon_{2,xy}(E)$ . . . 54
4.2.2 Non-linear mixing effects . . . 58
4.2.3 Surface roughness and chemical inhomogeneities . . . 58
4.2.4 $\epsilon_{2,z}(E)$ . . . 60
4.2.5 Varying the substrate temperature . . . 61
4.2.5.1 NEXAFS experiments . . . 61
4.2.5.2 $\epsilon_{2,xy}(E)$ and $\epsilon_{2,z}(E)$ . . . 64
4.2.6 Summary . . . 66
4.3 Absorption spectra of PFP:DIP blends . . . 66
4.3.1 Absorbance at different angles of incidence . . . 67
4.3.2 $\epsilon_{2,xy}(E)$ . . . 69
4.3.3 Non-linear mixing effects . . . 71
4.3.4 $\epsilon_{2,z}(E)$ . . . 74
4.3.5 Comparison of transmission spectroscopy and VASE . . . 75
4.3.6 Varying the substrate temperature . . . 75
4.3.7 Summary . . . 76
4.4 Absorption spectra of PEN:DIP blends . . . 76
4.4.1 Absorbance at different angles of incidence . . . 77

4.4.2 $\epsilon_{2,xy}(E)$ . . . 78
4.4.3 Non-linear mixing effects . . . 83
4.4.4 $\epsilon_{2,z}(E)$ . . . 83
4.4.5 Comparison of transmission spectroscopy and VASE . . . 85
4.4.6 Varying the substrate temperature . . . 85
4.4.7 Summary . . . 85
4.5 Comparison . . . 86

5 Results and discussion II: Real-time investigations 89
5.1 Real-time grazing incidence X-ray diffraction experiments . . . 90
5.1.1 Blends of PFP and DIP . . . 90
5.1.2 Blends of PEN and DIP . . . 92
5.2 Real-time investigations of $\epsilon_{2,xy}(E)$: Blends of PFP and PEN . . . 94
5.3 Real-time investigations of $\epsilon_{2,xy}(E)$: Blends of PFP and DIP . . . 100
5.4 Real-time investigations of $\epsilon_{2,xy}(E)$: Blends of PEN and DIP . . . 105
5.5 Comparison . . . 109

6 Summary 111

7 Outlook 115

8 Appendix 117
8.1 AFM images of bare substrates . . . 117
8.2 DRS: Comparison of experimental data and fit results . . . 118

List of abbreviations 123

Bibliography 125

Chapter 1

Introduction

More than 100 years after their first description [1–3] organic semiconductors (OSCs) have found applications in devices like cell phone displays or light emitting diodes [3–18]. In addition, current research focuses on the improvement of the efficiency of organic solar cells [9, 19–25], which have some advantages compared with inorganic silicon based solar cells, such as low production costs and the possibility to use flexible substrates [13, 26–28]. With the increasing number of OSC devices, also the number of geometries employed is increasing. This refers not only to device geometries but also to the photo-active layer formed by the OSC itself. Here, apart from films containing only one compound, more complex structures like layered heterostructures or intermixed structures (blends) are used [19, 29–48].

One important advantage of organic semiconductors is the possibility to synthesize molecules with different chemical composition, steric properties and accordingly, different optical and electronic properties [17, 49–62]. This leads to a variety of possible combinations in blends and corresponding film structures. The observed mixing and ordering behavior ranges from phase separation to intermixing on a molecular level and all possible scenarios between these two extremes [29, 36, 63, 64].

Tightly connected to the film structure are the opto-electronic properties [65, 66], which are not only crucial for device optimization but also important for fundamental research as they shed light on intermolecular interaction mechanisms in the systems. Furthermore, interfaces in the film influence the optical properties. Even in pure films the differences in the molecular environment at the interface between film and substrate or film and surrounding environment can alter the optical properties compared with the spectrum of the molecule in a bulk material or in solution [7, 8, 59, 67]. This influence is even more pronounced in heterostructures and blended systems, where many different types of interfaces are present, such as the interface between the different compounds, between the bulk and the substrate or between the bulk and the surrounding environment. In addition, differences in the film structure compared with the pure films, such as changes in the unit cell parameters, the arrangement of the molecules within the unit cell and the long-range order, may influence the optical properties of mixed systems. Finally, also intermolecular interactions, including partial or full transfer of charges from one molecule to another [68–

73], significantly affect the optical properties, in particular in donor-acceptor systems. This results in various scenarios for the optical properties of blends ranging from spectra strongly influenced by intermolecular interactions between the different compounds to spectra resembling a superposition of the pure compound properties [74–80]. In addition, the structural and optical properties of a film may change with time and increasing film thickness [65, 67, 81–90], due to transitions between structural phases [91–96] or changing molecule-substrate and molecule-molecule interactions [97–100].

It is crucial for device optimization as well as a challenge for fundamental research to understand the mechanisms of structure formation in blends and how this influences the optical and electronic properties of these complex systems [40, 60, 73, 101–107].

Compared with the huge variety of possible mixed systems, there are only few systematic studies addressing the impact of pure compound properties on film structure or optical properties of blends [29, 63, 108] and there are even less investigations focussing on real-time experiments [29, 109]. In this work, a systematic, comparative study of the influences of steric properties and the strength of intermolecular interactions on the structural and optical properties of blends is presented by investigating all possible combinations of binary mixtures of the three prototypical organic semiconductors pentacene (PEN), perfluoropentacene (PFP) and diindenoperylene (DIP). PEN is one of the most thoroughly investigated organic semiconductors with high charge-carrier mobilities and high crystalline order [59, 67, 77, 110–122]. Its perfluorinated counterpart PFP is reported to have promising properties [58–61, 123–131], in particular in devices combined with PEN [123, 124, 127, 132]. Films of the third compound, DIP, exhibit high crystalline order [133] and high charge-carrier mobilities [94, 109, 134–148]. Furthermore, for solar cells containing DIP and C_{60} a high fill factor of 75% is reported [143] which makes DIP an interesting compound for applications.

Studying blends of these three compounds in different combinations (Fig. 1.1) allows to investigate the influence of steric properties and the strength of intermolecular interactions on the mixing and ordering behavior as well as on the associated optical properties. Here, intermolecular interactions include mostly van-der-Waals interactions and electrostatic interactions involving possibly higher multipole moments, but no chemical interactions in the sense of chemical bonds. PFP and PEN are expected to interact strongly and are because of their almost identical steric properties perfectly suited to study intermolecular interactions in blends. Replacing PEN by DIP reduces the steric compatibility of the two compounds in the mixed system, as DIP is slightly larger and wider than PFP. The strength of intermolecular interactions in PFP:DIP blends, though, is expected to be comparably strong to that in PFP:PEN blends. Therefore, the comparison of PFP:PEN and PFP:DIP blends allows to investigate the influence of steric incompatibility on the properties of mixtures of strongly interacting compounds. Finally, blends of PEN and DIP complete the triangle. These two compounds do not interact strongly and are sterically slightly different, although, not as different as, for example DIP and C_{60}. Investigating the mixing and ordering behavior and the optical properties of PEN:DIP blends gives insight into structure formation in systems of weakly

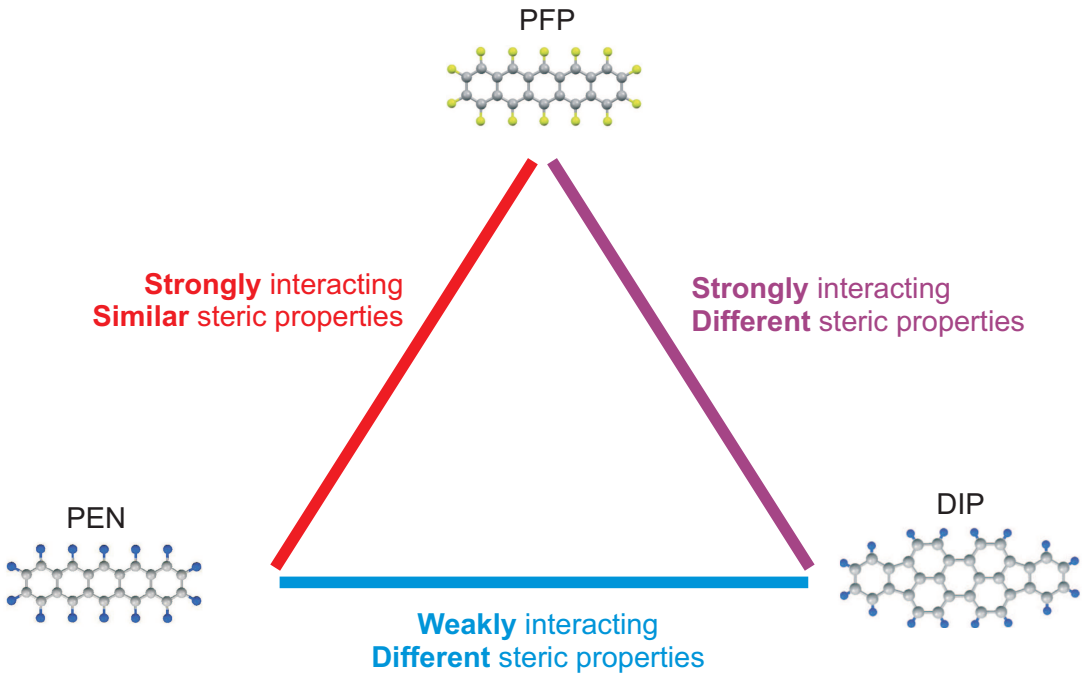

Figure 1.1: The triangle of steric compatibility and intermolecular interactions formed by PFP, PEN and DIP.

interacting compounds with differing steric properties.

This thesis is organized as follows. In Chap. 2 some fundamental principles will shortly be introduced, including mean-field models for a theoretical description of blends. In this chapter the issue of a definition of "strong" or "weak" intermolecular interactions will also be addressed via an interaction parameter (Sec. 2.4.1.2). The experimental methods used will be described in Chap. 3, focussing on two methods of optical spectroscopy. The results are separated in two parts, the structural and optical properties of the blends measured post growth (Chap. 4) and in real-time during growth (Chap. 5). In Sec. 4.1 the mixing and ordering behavior of the blends will be introduced, relating to published results, including an extension of the mean-field models introduced in Chap. 2. The absorption spectra measured post growth will be discussed in detail in Secs. 4.2, 4.3 and 4.4, for each of the three mixed systems, concentrating on the influence of mixing ratio and preparation temperature on the shape of the spectra. The results of this first section will be related to the differences in the mixing and ordering behavior. Chap. 5 covers the second part of the results, focussing on real-time experiments. The dependence of the evolution of the shape of the absorption spectra on the mixing ratio and the preparation temperature will be presented for the three blended systems separately in Secs. 5.2, 5.3 and 5.4. The thesis concludes with a summary of the results (Chap. 6) and an outlook on further possible experiments (Chap. 7).

Chapter 2

Fundamentals

2.1 Optics

In the following the behavior of electromagnetic waves in a medium and at the interface between two media is discussed briefly. For details the reader is referred to textbooks, e.g. Refs. [149–153].

2.1.1 Absorption of light: the dielectric tensor

An external electromagnetic wave described by $\vec{E}$ induces oscillating dipoles in a material, described by the displacement field $\vec{D} = \tilde{\epsilon}\vec{E}$, with $\tilde{\epsilon} = \tilde{\epsilon}\epsilon_0$ [150]. Here, $\tilde{\epsilon}$ is the *dielectric constant* of the material and ϵ_0 is the permittivity of vacuum. In general, $\tilde{\epsilon}$ is a tensor, as the response of the medium to an external electric field can be anisotropic. Each element of $\tilde{\epsilon}$ is a complex function[1] and depends on the energy (wavelength) of the incoming electromagnetic wave [150]. The wavelength dependent, complex elements of $\tilde{\epsilon}$ will in the following be referred to as the *dielectric function*. If possible, the diagonalization of $\tilde{\epsilon}$ yields the principal values ("Hauptwerte"), which can be used to describe the optical axes in case of anisotropic materials [149, 150, 152, 153]. Three different cases of anisotropy can be distinguished [149, 153] (Fig. 2.1):

1. Biaxial anisotropy: All principal values of $\tilde{\epsilon}$ are different.
2. Uniaxial anisotropy: Two principal values are identical, one is differing.
3. Isotropy: All three principal values are identical, ϵ is a scalar.

The real ($\epsilon_{1,ii}$) and imaginary ($\epsilon_{2,ii}$) part of each principal value of $\tilde{\epsilon}$ are related to the dispersion and extinction of the electromagnetic wave in the medium, respectively. They are connected by the Kramers-Kronig relation:

$$\varepsilon_1(\omega) - 1 = \frac{2}{P}\int_0^\infty \frac{\omega'\varepsilon_2(\omega')}{\omega'^2 - \omega^2} d\omega' \tag{2.1}$$

[1] Due to a phase shift between the exciting electromagnetic wave and the wave emitted by the oscillating dipoles, see Ref. [150].

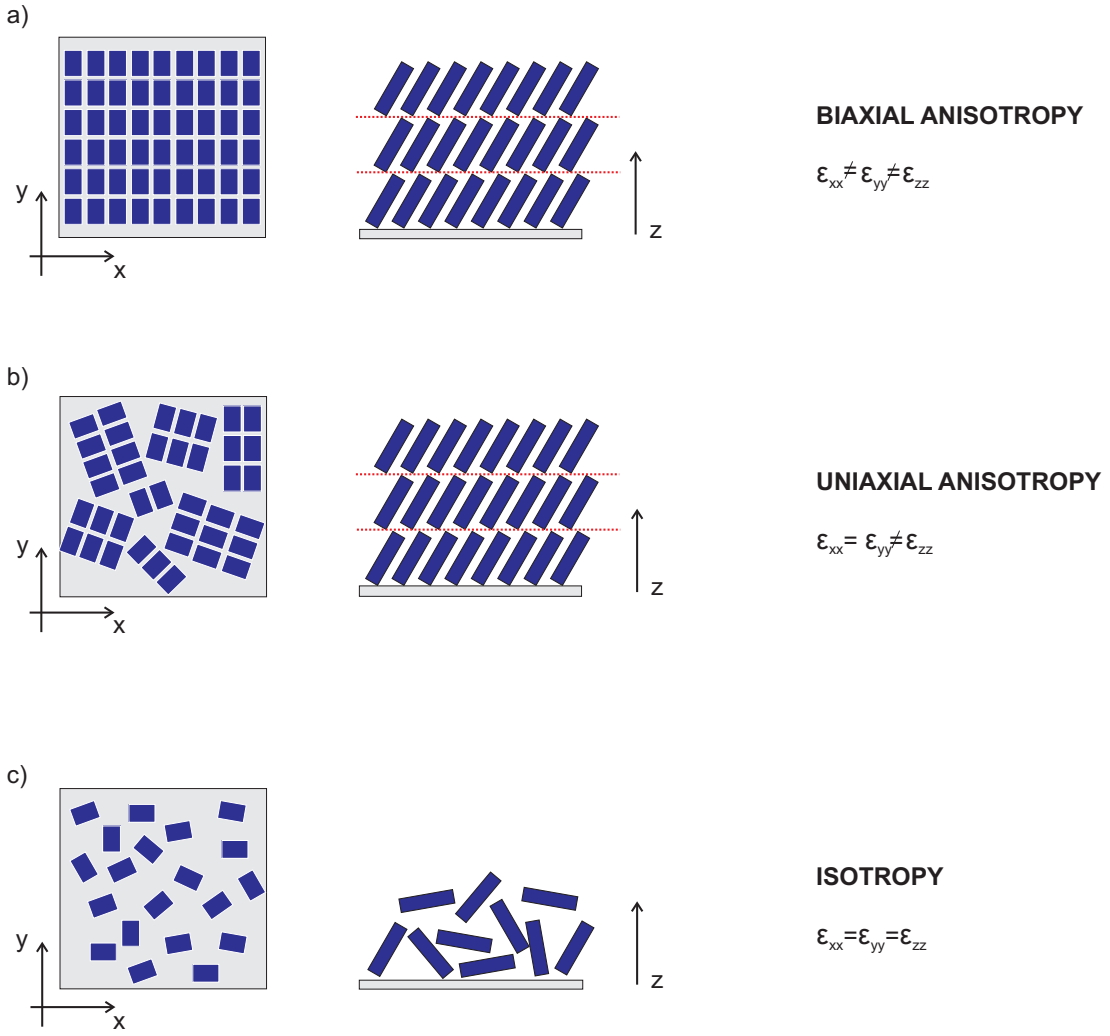

Figure 2.1: Sketches of thin films exhibiting a) biaxial anisotropy, b) uniaxial anisotropy, c) isotropy. The rectangles schematically depict molecules.

with ω being the frequency and P the Cauchy principal value, which allows to calculate ϵ_1 if ϵ_2 is known in an infinite energy range $E = \hbar\omega$. For practical reasons this condition is difficult to fulfill. However, it is sufficient to know ϵ_2 in a finite energy range, if it becomes small enough at the boundaries.

For completeness it is noted that also the complex refractive index $\tilde{n} = n + ik$ can be used to describe the electromagnetic properties of a medium. Here, n is the real refractive index and k is the extinction coefficient. $\tilde{\epsilon}$ and $\tilde{n}$ are connected by $\tilde{n} = \sqrt{\tilde{\epsilon}}$ and can therefore, be directly derived from one another by

$$\epsilon_1 = n^2 - k^2, \qquad \epsilon_2 = 2nk \tag{2.2}$$

In many spectroscopic experiments the probed quantity is the transmittance T, which is the fraction of the transmitted intensity I and the incoming intensity I_0 when light of a wavelength λ_0 has travelled the distance Δz in a medium with extinction coefficient k:

$$T = e^{-\alpha \Delta z} \tag{2.3}$$

Here, α is the *absorption coefficient* which is related to k and $\tilde{\epsilon}$, respectively, by [152]

$$\alpha = \frac{4\pi k}{\lambda_0} = \frac{4\pi}{\lambda_0} \frac{\sqrt{-\epsilon_1 + |\tilde{\epsilon}|}}{\sqrt{2}} \tag{2.4}$$

α is related to the *absorbance* A of the material by

$$A = -\frac{1}{0.0434} \alpha \Delta z = -log(T) \tag{2.5}$$

2.1.2 Reflection and transmission: the Fresnel-coefficients

The Fresnel-coefficients relate the reflection and transmission properties of a material with its dielectric function. They are defined in the following:

$$r_{p,s} = \frac{E^r_{p,s}}{E^{in}_{p,s}}, \qquad t_{p,s} = \frac{E^{trans}_{p,s}}{E^{in}_{p,s}} \tag{2.6}$$

Here, $r_{p,s}$ and $t_{p,s}$ are the Fresnel-coefficients for reflection r and transmission t and $E^r_{p,s}$ ($E^{trans}_{p,s}$) corresponds to the reflected (transmitted) electric field, while $E^{in}_{p,s}$ denotes the incoming electric field. s and p describe the polarization state of the light, with s (p) corresponding to light polarized perpendicular (parallel) to the plane of incidence.

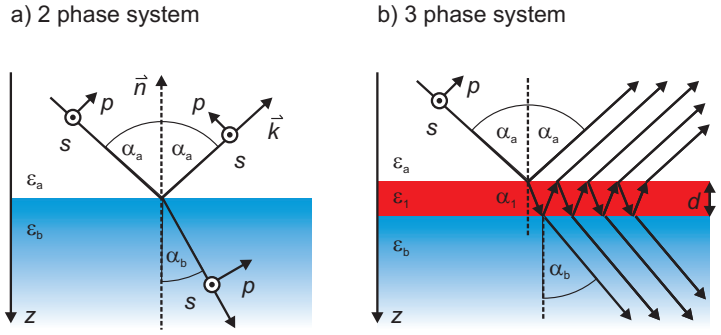

Figure 2.2: a) Two-phase system. b) Three-phase system. Picture taken from Ref. [154].

In the case of reflection at an interface of a two-phase system consisting of material A and B (Fig. 2.2a), $r_{p,s}$ depends on the angle of incidence relative to the substrate normal and the complex refractive indices $\tilde{n}_a$ and $\tilde{n}_b$ of the two materials:

$$r^{ab}_p = \frac{\tilde{n}_b cos\Phi_a - \tilde{n}_a cos\Phi_b}{\tilde{n}_b cos\Phi_a + \tilde{n}_a cos\Phi_b} \qquad r^{ab}_s = \frac{\tilde{n}_a cos\Phi_a - \tilde{n}_b cos\Phi_b}{\tilde{n}_a cos\Phi_a + \tilde{n}_b cos\Phi_b} \tag{2.7}$$

Using these formulae the reflection of an arbitrarily polarized electromagnetic wave $\vec{E} = a_s\vec{E}_s + b_p\vec{E}_p$ at the interface of a two-phase system can be described. The fraction of reflected intensity $I^r_{p,s}$ and incoming intensity $I^{in}_{p,s}$ is called reflectivity $R_{p,s}$ of the interface ($R_{p,s} = |r_{p,s}|^2$) for p- and s-polarized light [150].

For a three-phase system (Fig. 2.2b) multiple reflections between the interfaces have to be taken into account, resulting in the *Pseudo-Fresnel-coefficients* (homogeneous phases with sharp boundaries are assumed) [149, 154, 155]:

$$R_{p/s} = \frac{\sum_i (E^r_{i,\mathrm{p/s}})}{E^{in}_{\mathrm{p/s}}} = \frac{r_{\mathrm{b1,p/s}} + r_{\mathrm{1a,p/s}} e^{i2\beta}}{1 + r_{\mathrm{b1,p/s}} r_{\mathrm{1a,p/s}} e^{i2\beta}} \tag{2.8}$$

with the phase thickness $\beta = 2\pi \frac{d}{\lambda}\sqrt{\epsilon_1}\cos\alpha_1$ and $r_{\mathrm{b1,p/s}}$ ($r_{\mathrm{1a,p/s}}$) the Fresnel-coefficient for the reflection at the interface between material B and 1 (1 and A).

For more complex systems the Fresnel-coefficients are calculated via matrix methods, see e.g. Refs. [149, 154, 155].

2.2 Organic semiconductors

In general, one distinguishes two classes of organic semiconductors (OSCs): polymers and small molecules. While polymers consist of several subunits and therefore, have a typical length of several 100 nm, small molecules are usually only a few nm long. This work concentrates on small molecules and in the following their properties will be discussed briefly. For details the reader is referred to Refs. [7, 8, 156, 157].

2.2.1 π-electron system

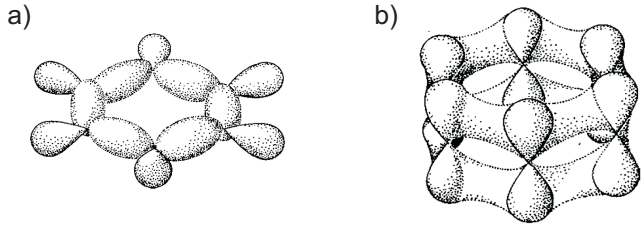

Figure 2.3: Benzene ring with a schematic sketch of the a) σ-orbital, b) π-orbital. Picture taken from Ref. [8].

OSCs are polycyclic aromatics and consist of carbon in combination with hydrogen, fluorine or other elements. The carbon atoms form a ring, in which the bond between neighboring carbon atoms is formed by sp^2-hybridisation [158]. In this case the s- and

two p-orbitals of the two carbon atoms build three coplanar and energetically degenerated molecular σ-orbitals (see Fig. 2.3a). The third atomic p_z-orbital remains unaffected and is oriented perpendicular to the ring plane, contributing to the molecular π-orbital (Fig. 2.3b) [8]. The bonds between neighbouring carbon atoms in the ring are alternating single and double bonds. This results in the formation of a resonance structure and consequently in a delocalization of the electrons in the π-orbital over the ring. Electrons in the π-orbitals have the lowest excitation energies. Therefore, optical spectroscopy in the visible spectral range probes usually transitions of these electrons [8].

2.2.2 Intermolecular interactions

In the following, a short overview over interactions between molecules in thin films or crystals is given, which influence the ordering behavior of the molecules in a solid. Details can be found in Refs. [8, 159, 160].

In a solid, organic molecules are bound together mostly by electrostatic interactions and van-der-Waals bonds, which result from the attractive interactions between fluctuating dipoles in non-polar molecules [8]. The potential which a molecule experiences in the solid, can in many cases be described by a Lennard-Jones potential plus possibly further terms. It is a combination of the attractive and additional repulsive forces such as Coulomb forces and Pauli-repulsion. The latter prevents a collapse of the crystal lattice [8].

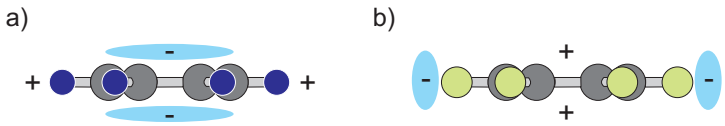

Figure 2.4: Sketch of the quadrupole moment of a) benzene and b) hexafluorobenzene. Pictures modified from Ref. [161].

Many (but not all) OSCs are non-polar molecules, which means, their first non-zero multipole moment is the quadrupole moment resulting from the charge-distribution over the molecule [160]. In Fig. 2.4a and b the charge distribution for a benzene and a hexafluorobenzene molecule is shown. If these molecules form a pure solid (i.e. a solid containing only benzene or only hexafluorobenzene) one may image two possible configurations:

1. The face-to-edge configuration (Fig. 2.5a), which maximizes the electrostatic attraction between the negative net charge distribution perpendicular to the ring plane and the positive net charge distribution at the egdes of the ring [160].

2. The parallel displaced face-to-face arrangement (Fig. 2.5b), which is a compromise between a high surface overlap (and accordingly, strong van-der-Waals attraction) and the minimization of the electrostatic repulsion due to the quadrupole moments [159, 160].

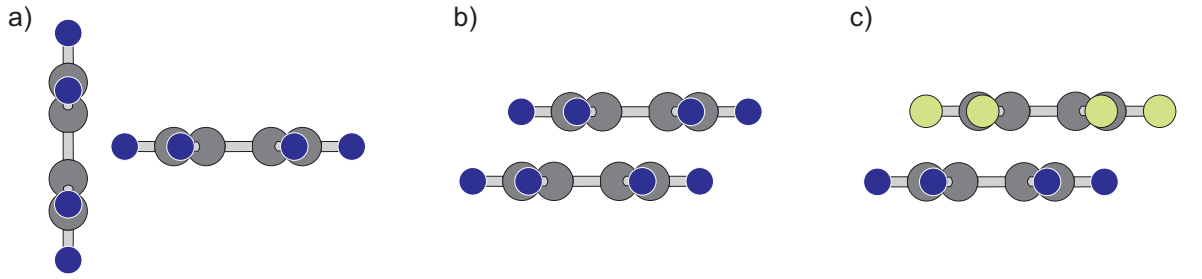

Figure 2.5: a) Face-to-edge configuration and b) face-to-face configuration of two benzene molecules. c) Face-to-face configuration of a benzene-perfluorobenzene dimer. Pictures modified from Ref. [161].

Since the delocalized π-electron system contributes dominantly to the charge distribution, these interactions are also referred to as π-π interactions [159].

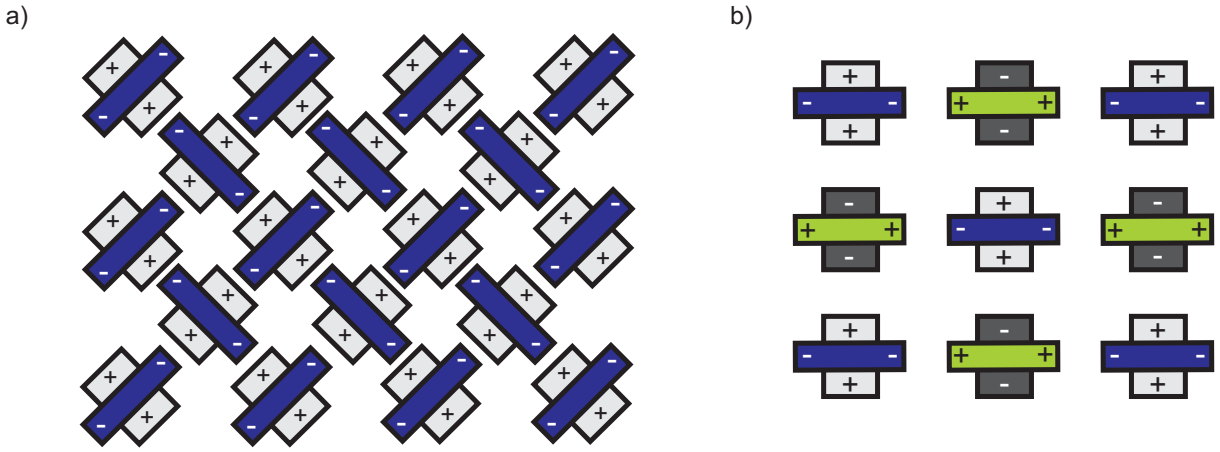

Figure 2.6: a) Sketch of the herringbone structure in a solid of benzene. b) Sketch of the A-B stacking in a solid of benzene-hexafluorobenzene. Pictures modified from Ref. [160].

The combination of the two configurations mentioned above results in a characteristic assembly of the molecules in the solid, which is called herringbone-structure (see Fig. 2.6a) [160]. Besides the influence of attractive van-der-Waals forces and the attractive and repulsive electrostatic interactions, which determine the packing motif, the interplanar distances are also affected by short-range repulsive interactions (e.g. Pauli-repulsion) [159].

If the solid contains more than one compound, additional interactions may influence the molecular packing. One of the most important interactions is the interaction between arenes and perfluoroarenes, such as e.g. benzene and hexafluorobenzene [159, 160]. Due to the strong electronegativity of the fluorine the negative net charge is distributed at the

edges of the ring and the sign of the quadrupole moment of the perfluorinated compound is reversed compared with the quadrupole moment of the hydrogenated compound (see Fig. 2.4b) [159]. The resulting electrostatic interaction between the perfluorinated and the hydrogenated compound leads to a preferred face-to-face stacking with alternating layers of the two compounds (Fig. 2.5c and Fig. 2.6b) [159, 160].

In addition to the arene-perfluoroarene interaction, the molecular stacking in mixed solids is influenced by further interactions, such as charge transfer, but also by the sterical compatibility of the two compounds involved. These effects will be discussed in Secs. 2.4 and 4.1.4.

2.2.3 Excitations in organic molecules

2.2.3.1 Born-Oppenheimer approximation

This thesis discusses absorption spectra of organic molecular films. They originate from the excitation of electronic transitions in the molecules. Compared with atoms, additional excitations contribute to the spectra of molecules, such as vibrational and rotational excitations [8,156]. In the *Born-Oppenheimer approximation*, which is a very common starting point of a quantum-mechanical description of radiative and non-radiative processes in organic molecules [156] the wavefunction of a free molecule of a state involving electronic, vibrational and rotational energy can be written as the product of the wavefunctions of the electronic, the vibrational and the rotational state. Accordingly, the energy of a free molecule can be written as a sum of the three different contributions [156]:

$$E = E_{el} + E_{vib} + E_{rot} \tag{2.9}$$

Rotational transitions ΔE_{rot} can be observed in the far infrared and in the microwave region, as the energy difference between rotational sublevels of excited electronic states are in the order of 0.01 eV [8,156]. In the near infrared transitions involving rotational (ΔE_{rot}) and vibrational sublevels (ΔE_{vib} in the order of 0.1 eV) occur. Relevant for this work are transitions involving electronic (ΔE_{el} in the order of 1-5 eV) and vibrational excitations (the so-called *vibronic transitions*), which can be observed in the visible, ultraviolet or near-infrared [8, 156]. The energetically lowest lying electronic transitions are transitions between π-orbitals, since π-electrons are more weakly bound than the electrons in σ-orbitals. The electronic transition, which is usually probed by absorption spectroscopy, is the transition between the highest occupied molecular orbital (HOMO) and the lowest unoccupied molecular orbital (LUMO).

2.2.3.2 Franck-Condon principle and vibronic progression

The *Franck-Condon principle* states that atoms do not follow instantly an electronic excitation of a molecule due to their heavy mass. Therefore, the most probable vibronic transition is that which does not include a change in the nuclear configuration of the molecule [156]. However, for most systems the nuclear configuration in the first excited

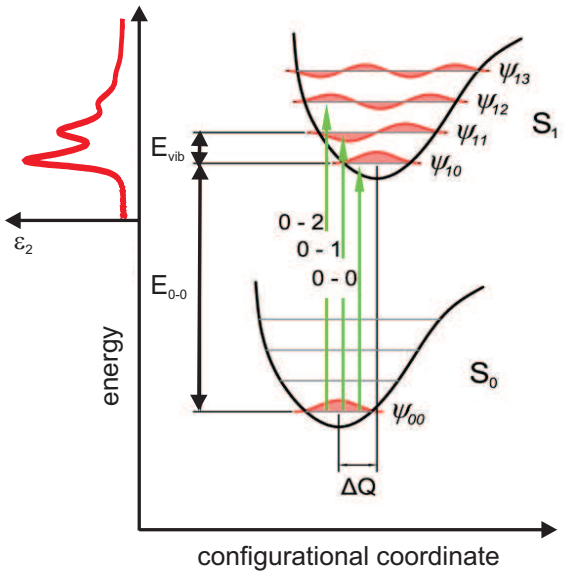

Figure 2.7: Scheme of the origin of a *vibronic progression*. The figure shows the internuclear potential of the ground and the first excited state with their vibronic sub-levels as a function of the configurational coordinate Q. The deformation of the molecule under excitation leads to a shift ΔQ of the minima of ground and first excited state. This results in the excitation of higher vibronic sub-levels during an optical transition, described by the arrows and a characteristic line shape (left). Picture taken from Ref. [154].

electronic state will be different from that of the ground state [156, 162]. This leads to a shift of the nuclear potential minima by ΔQ, see Fig. 2.7, and to the excitation of higher vibronic levels during an absorption process. The transitions to the different vibronic levels of the first excited state result in a characteristic line shape, see left hand side of Fig. 2.7, the so-called *vibronic progression* [163].

2.2.3.3 Molecular crystal spectra

When going from a free molecule to a molecular crystal the shape of the spectra does not necessarily change completely. This is due to a low intermolecular interaction in the molecular crystal by van-der-Waals forces, thus, a molecular crystal can in a good approximation be described as an oriented gas [8]. Although the transitions of the monomer can still be found in the crystal spectra, there are differences observable, which will be discussed in the following. For details the reader is referred to Refs. [7, 8].

1. **Excitons:** There is an important difference between the excitations in atomic crystals and molecular crystals, which influences properties like charge carrier mobility to a great extent. In molecular crystals photo excitation does not produce free charge carriers as observed in atomic crystals, but neutral, bound electron-hole pairs, so-called excitons, see Fig. 2.8 [7].

   (a) Mott-Wannier exciton: A neutral electron-hole pair, bound by Coulomb-interactions, where the distance between the electron and the hole is much larger than the lattice constant a of the molecular crystal.

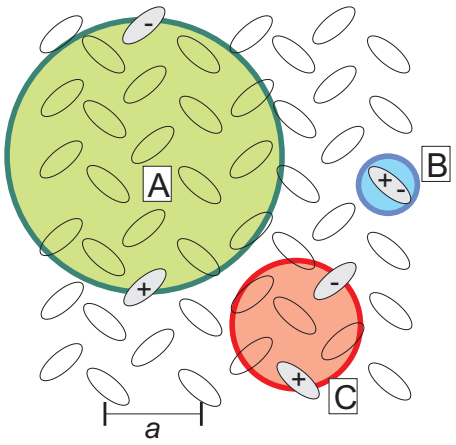

Figure 2.8: Different types of excitons. a) Mott-Wannier exciton. Binding radius much larger than lattice constant a. b) Frenkel exciton. Binding radius much smaller than lattice constant a. c) Charge transfer exciton. Binding radius in the order of the lattice constant a. Picture modified from Ref. [7].

(b) Frenkel exciton: An excited state of a molecular aggregate, in which the exciton is located on one molecule, i.e. with an exciton radius much smaller than the lattice constant a of the molecular crystal. It moves from lattice site to lattice site mostly by dipole interactions.

(c) Charge transfer exciton: A neutral, polar electron hole pair of which the distance between electron and hole is in the order of the lattice constant a, see also Sec. 2.4.2.2.

2. **Davydov-splitting:** If there are two (or more) translationally inequivalent molecules per unit cell in a molecular crystal the energy levels may split up into two (or more) components (Fig. 2.9). The corresponding transitions in the crystal spectrum differ in their energy position and also in their polarization properties [7]. This splitting was explained by Davydov [165] as a result of resonant interaction between the two translationally inequivalent excited molecules [8, 165]. For a dimer the allowed transitions are characterized by the transition dipole moment $M_{(\pm)}=\frac{1}{\sqrt{2}}(M_1 \pm M_2)$, with M_1 and M_2 the transition dipole moments of the contributing molecules [8]. If the dipole moments are parallel, either $M_{(+)}$ or $M_{(-)}$ will be zero, depending whether the molecules are beside one another or in a line [8]. The corresponding transition will be dipole forbidden and not visible in the spectrum. Though, if the molecules are translationally inequivalent, the transitions corresponding to $M_{(+)}$ and $M_{(-)}$ will both be allowed, resulting in a splitting of the transition into the two Davydov components [7, 8, 165].

3. **Solvent shift:** When comparing the absorption spectrum of a free molecule with that of the same molecule in solution, the energy positions of the peaks of the latter are usually red shifted [8, 154, 156]. This effect is referred to as the *solvent shift* [166, 167] and explained by differences in the polarizability of the surrounding medium for a free molecule and a molecule in solution. Under excitation the molecule forms a dipole, which polarizes the surrounding medium, causing a reaction field [156]. This

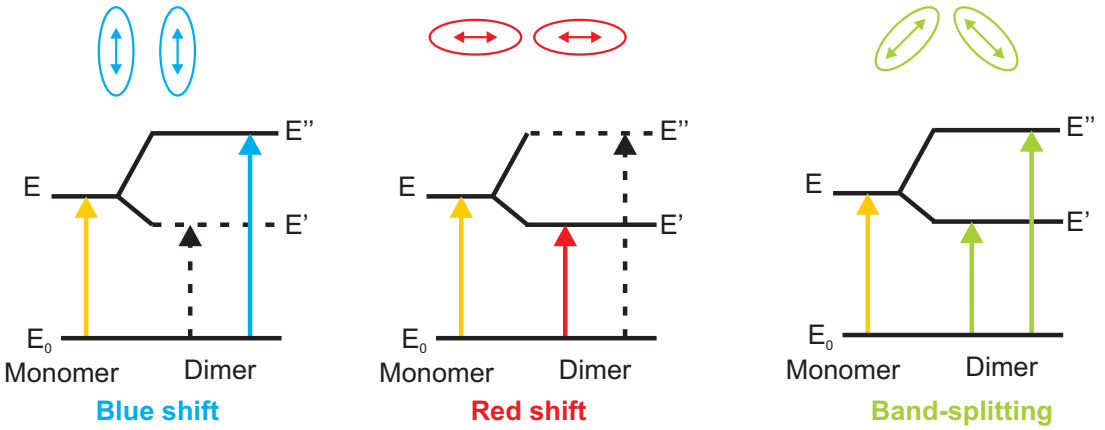

Figure 2.9: Schematic drawing of the shifts in energy position or the splitting of levels in a dimer depending on the orientation of the transition dipole moments. Picture modified from Refs. [7, 164].

reaction field will reduce the ground-state energy level of the molecule $S_{0,\text{solution}}$ relative to the corresponding level S_0 of the free molecule. If the relaxation time of the excited vibronic state is faster than the relaxation time of the surrounding (which will be the case, as it is stated by the Franck-Condon principle) the molecule will not relax in the state S_0, but in $S_{0,\text{solution}}$ and the corresponding transition will be red shifted [156]. A similar effect can be observed when spectra of a molecule in solution and in a thin film (or molecular crystal) are compared.

2.3 Thin film growth

In the following, the process of film growth will be discussed briefly. Details can be found in Refs. [168, 169]. When molecules, which are evaporated from heated sources reach a substrate surface, there are several effects which can take place. The molecules can *adsorb* and stick to one specific site or *diffuse* along the surface to reach the energetically most favorable position [169]. Especially at elevated substrate temperatures, the molecules can also *re-desorb* and leave the surface. However, for the systems and substrate temperatures discussed here, re-desorbtion can be neglected.

The diffusion behavior strongly influences the growth of the film and its structure, as well as the morphology of the film surface. Generally, there are two processes, the *inter-* and *intra*-layer diffusion. While *intralayer diffusion* describes the movement of molecules within one layer, *interlayer diffusion* describes the movement of molecules between different layers [169].

In general, the growth of a thin film of molecules can be described by three growth modes (Fig. 2.10) [168]:

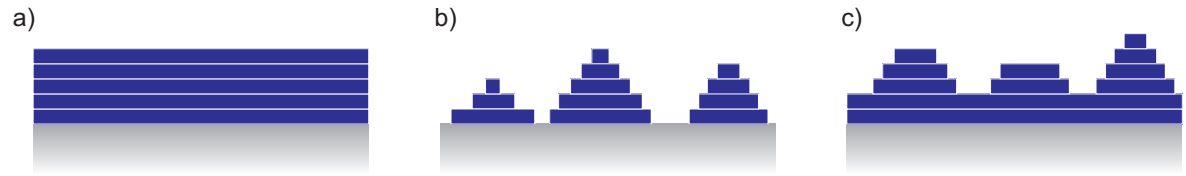

Figure 2.10: Growth modes. a) Frank-van der Merwe or layer-by-layer growth. b) Vollmer-Weber or island growth. c) Stranski-Krastanov growth. Pictures modified from Ref. [154].

- Frank-van der Merwe or layer-by-layer growth (Fig. 2.10a): If the favorable interaction between the substrate and the molecules is stronger than the interaction between the molecules, the film grows in a layer-by-layer fashion, maximizing the contact area between molecules and substrate.

- Vollmer-Weber or island growth (Fig. 2.10b): If the interaction between the molecules is more favorable than the interaction between the molecules and the substrate, the molecules tend to grow in islands, minimizing the contact area between molecules and substrate.

- Stranski-Krastanov growth (Fig. 2.10c): This growth mode is usually observed for organic semiconducting thin films on weakly interacting substrates such as e.g. natively oxidized silicon or glass. It is a mixture of layer-by-layer and island growth. Usually the first few layers of molecules will grow in a layer-by-layer mode and with increasing film thickness the film will get rougher.

2.4 Mixtures of organic semiconductors

The focus of the present work lies on the optical properties of binary mixtures (blends) of OSCs, which may depend on the mixing and ordering behavior of the two compounds. Therefore, in the following some concepts of a theoretical description of the mixing and ordering behavior of OSCs in mixed films will be introduced. Details can be found in Refs. [29, 36, 170–172].

2.4.1 Theoretical description

2.4.1.1 Mixtures of non-interacting spheres

When mixing two kinds of ideal, non-interacting spherical particles A and B, different mixing scenarios are possible, see Fig. 2.11. The probability for each scenario is given by a binomial distribution, where the probability $p(n, m)$ to find n spheres of kind A and m

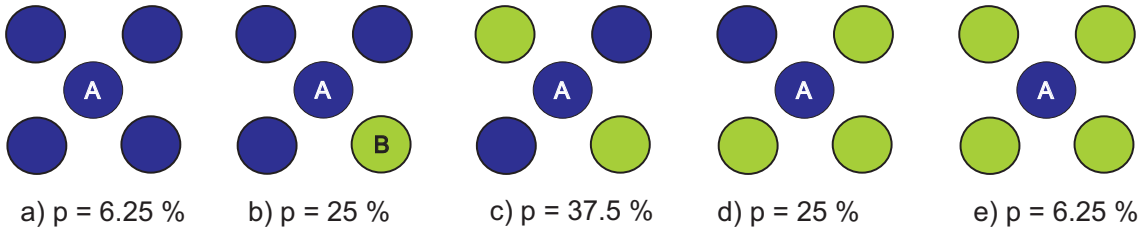

Figure 2.11: Schematic drawings of possible mixing scenarios for mixtures of ideal, non-interacting spheres on a lattice. The most probable configuration is that in which a sphere of kind A is surrounded by an equal amount of spheres A and B.

spheres of kind B at four different lattice sites around a sphere A is:

$$p(n,m) = \begin{pmatrix} 4 \\ n \end{pmatrix} \cdot \left(\frac{1}{2}\right)^n \cdot \left(\frac{1}{2}\right)^m \tag{2.10}$$

Figure 2.11 c) shows the most probable configuration resulting from Eq. 2.10, i.e. perfect intermixing of the two kinds of spheres.

2.4.1.2 Mixtures of interacting spheres

The behavior discussed before may change when interparticle interactions are taken into account. Already in 1929 J. H. Hildebrandt studied solutions of solids, concentrating on *regular solutions*, which are defined as solutions of particles with random distribution and orientations and without chemical interactions [170]. Based on his considerations Kitaigorodski published a theoretical description of mixtures of spherical particles A and B in the framework of a mean-field model, i.e. taking only nearest-neighbour interactions into account [171, 172]. According to this model, which can also be applied to crystalline systems [172], the free energy of mixing ΔF_{mix} can be written as:

$$\Delta F_{mix} = k_B T[(x_A \ln x_A + x_B \ln x_B) + \chi x_A x_B]. \tag{2.11}$$

Here, x_A and x_B are the respective relative concentrations of the two kinds of particles. The ln terms are due to entropy and the influence of the interparticle interactions is described by the interaction parameter χ:

$$\chi = \frac{Z}{k_B T}(W_{AA} + W_{BB} - 2W_{AB}), \tag{2.12}$$

where Z is the coordination number and W_{AB} and W_{AA} (W_{BB}) are the interaction energies between dissimilar compounds A and B or between like compounds A (B), respectively. Depending on the balance of χ, resulting from the interaction energies W_{ij} (with i,j=A,B), and the entropy contribution, three different mixing scenarios are possible, see Fig. 2.12:

a) $\chi < 0.5$: The interparticle interaction energies W_{AB} for particles of different compounds are dominating over the interaction energies W_{AA} (W_{BB}) for particles of the

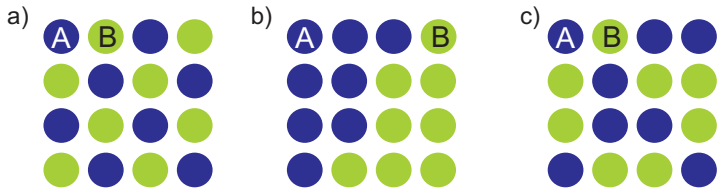

Figure 2.12: Mixing scenarios of interacting spherical particles on a lattice depending on the interaction parameter χ. a) $\chi < 0.5$: Intermixing with preference for A-B pairing and long-range order. b) $\chi > 2$: Phase separation. c) $\chi \approx 0$: Statistical mixing.

same compound. Consequently, there is a preference for a particle of compound A to have a neighbour particle of B. The two compounds intermix very well and can form a new intermixed crystal phase with distinctive long-range order.

b) $\chi > 2$: The interparticle interaction energies W_{AB} for dissimilar compounds are much smaller than the interaction energies W_{AA} (W_{BB}) for the same compound. Therefore, it is highly unfavorable for a particle A to have neighbour particles B, which results in phase separation of the two compounds.

c) $\chi \approx 0$: The interparticle interaction energies W_{AB} are comparable with W_{AA} (W_{BB}) resulting in no strong preference for mixing or phase separation. The mixing behavior will be determined by the entropy terms, which favor statistical mixing.

It is noted that in this work the term "strongly interacting" ("weakly interacting") will refer to systems with χ <0.5 ($\chi \approx 0$).

2.4.2 Optical properties of mixed films

2.4.2.1 Effective medium approximation

Mixing two OSCs not only influences the structural properties of the resulting film, but can also lead to changes in the absorption or photoluminescence spectra [30, 38, 74, 75, 78, 173–180]. Based on effective medium approximation (EMA) theories [181], there are different approaches for a theoretical prediction of the optical properties of a mixed system containing a fraction f_A of molecules A and a fraction f_B of molecules B without taking intermolecular interactions into account:

a) Linear superposition (see Fig. 2.13a): For ideal smooth and homogeneous interfaces the effective $\tilde{\epsilon}_{mix}$ of the mixed system can in this simplest case be described by a linear superposition of $\tilde{\epsilon}$ of the pure compounds:

$$\tilde{\epsilon}_{mix} = f_A \tilde{\epsilon}_A + f_B \tilde{\epsilon}_B \tag{2.13}$$

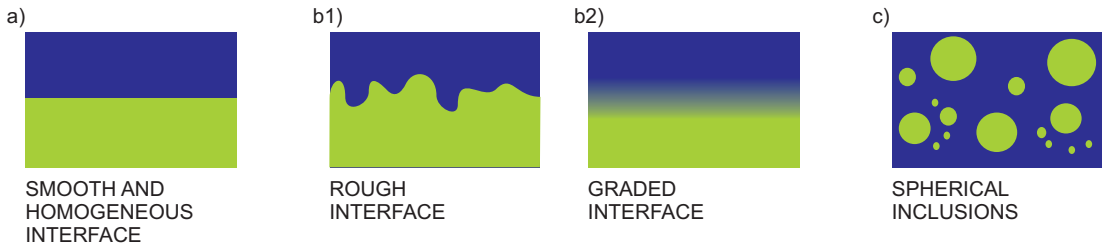

Figure 2.13: Effective medium approximations for mixed systems. a) Linear superposition assuming perfectly smooth and homogeneous interfaces. b1) Bruggeman-model describing interface roughness, b2) Bruggeman-model for a graded interface. c) Maxwell-Garnett model in the case of spherical inclusions in a matrix.

b) Bruggeman model [182] (see Fig. 2.13b1 and b2): If the interface between material A and B is rough or graded, $\tilde{\epsilon}_{mix}$ can be calculated by solving

$$f_A \frac{\tilde{\epsilon}_A - \tilde{\epsilon}_{mix}}{\tilde{\epsilon}_A + 2\tilde{\epsilon}_{mix}} + f_B \frac{\tilde{\epsilon}_B - \tilde{\epsilon}_{mix}}{\tilde{\epsilon}_B + 2\tilde{\epsilon}_{mix}} = 0 \tag{2.14}$$

c) Maxwell-Garnett model [183] (see Fig. 2.13c): The optical properties of a mixed system consisting of inclusions of A in a matrix of B have been described theoretically in terms of the Maxwell-Garnett model, where the effective $\tilde{\epsilon}_{mix}$ of the system is given by the solution of

$$\frac{\tilde{\epsilon}_{mix} - \tilde{\epsilon}_A}{\tilde{\epsilon}_{mix} + 2\tilde{\epsilon}_A} = f_B \frac{\tilde{\epsilon}_B - \tilde{\epsilon}_A}{\tilde{\epsilon}_B + 2\tilde{\epsilon}_A} \tag{2.15}$$

2.4.2.2 Charge transfer

The optical properties of many mixed films cannot be described by the EMA-models mentioned above. This can be due to differences in the structural order, the molecular arrangement (e.g. the tilt angle) or the intermolecular environment in the blend compared with the pure films. However, in some cases the differences in the optical properties of the pure and the mixed film cannot exclusively be explained by the former effects and intermolecular interactions between the different compounds have to be taken into account. These interactions may include the entire or partial transfer of charge from one molecule (the donor) to another (the acceptor) [7, 69]. The corresponding optical transition involves the excitation of a charge transfer exciton (see Sec. 2.2.3.3). Its energy often lies below the HOMO-LUMO transition [7] and can also be observed in pure thin films, although with very weak oscillator strengths [7, 67]. While in pure films donor and acceptor are from the same molecular species, in mixed systems donor and acceptor are constituted by the different compounds. Ref. [7] distinguishes two classes of mixed systems, which can be described as donor-acceptor systems:

a) The *charge transfer complexes* are neutral in their ground state and bound by weak van-der-Waals forces. Crystalline charge transfer complexes are formed by a regular sequence of donor and acceptor molecules [7].

b) The ground state of *radical ion salts* consists of positively and negatively charged ions and donor and acceptor in separated stacks [7].

2.5 Materials

The focus of this work is on binary mixtures of three OSCs in different combinations. In the following these compounds will be described and the properties of the pure films will be discussed briefly.

2.5.1 Pentacene (PEN)

Pentacene ($C_{22}H_{14}$, PEN) is one of the most intensively studied OSCs due to its high charge carrier mobility [184], high structural order [121] and excellent commercial availability. The optical [59,113,185] as well as the structural [91,92,112,117,121,186–189] and charge transport properties [190–193] of pentacene in thin films and single crystals have been subject of thorough studies. The chemical structure of PEN is shown in Fig. 2.14a.

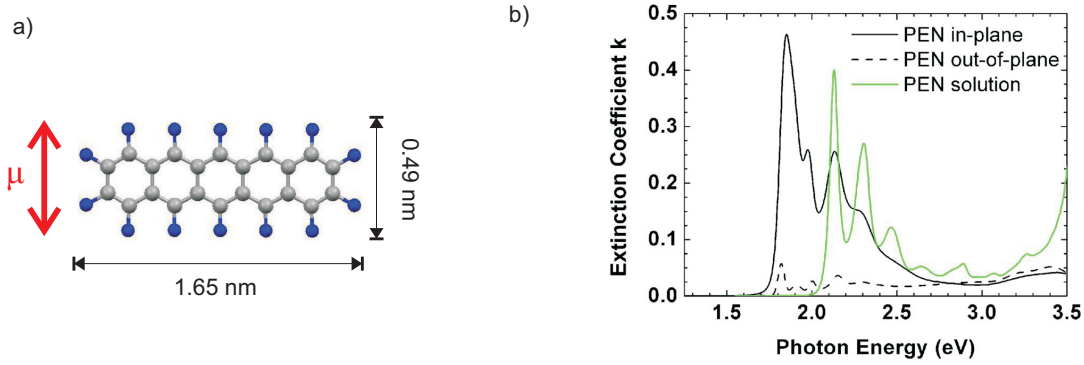

Figure 2.14: a) Schematical depiction of a PEN-molecule. The red arrow indicates the orientation of the transition dipole moment μ for the HOMO-LUMO transition. b) Absorption spectra of PEN in solution and in a thin film phase. Pictures modified from Ref. [59]. Dimensions of PEN measured using the Cambrigde Structural Database.

PEN is a blue dye, which crystallizes on natively oxidized silicon in a herringbone structure in different polymorphs depending on the film thickness and substrate temperature [92]. Relevant for this work is the thin film phase, which was reported to grow for thin films ($d_{Film} < 50$ nm) at room temperature [92] on silicon with a $d(001)$-lattice

a [nm]	b [nm]	c [nm]	α [°]	β [°]	γ [°]	V [nm^3]
0.593	0.756	1.565	98.6	93.3	89.8	0.693

Table 2.1: Lattice parameters of the PEN thin film phase. The unit cell is triclinic [187].

spacing of 1.57 nm [187], corresponding to PEN molecules standing almost upright on the sample surface. The unit cell parameters of the triclinic thin film phase are compiled in Table 2.1.

On amorphous substrates, such as e.g. natively oxidized silicon, PEN thin films are polycrystalline. Their optical properties are uniaxial anisotropic and can be described by two dielectric functions $\tilde{\epsilon}_{xy}$ and $\tilde{\epsilon}_z$ (Fig. 2.1b), or by two extinction coefficients k_{xy} and k_z. Fig. 2.14b shows the extinction coefficient k_{xy} and k_z in comparison with the solution spectra [59]. The first two peaks in $k_{xy}(E)$ can be assigned to the HOMO-LUMO transition, which is split into two Davydov-components [118,185] at $E = 1.85$ eV and $E = 1.97$ eV. The peaks at higher photon energies are assigned to a vibronic progression [59].

The transition dipole moment of the HOMO-LUMO transition of PEN is oriented along the short molecular axis [59, 113]. In the case of standing molecules this results in a very weak $k_z(E)$, see Fig. 2.14b, which will not be discussed in detail.

2.5.2 Perfluoropentacene (PFP)

Perfluorination is a suitable tool to change the charge transport properties of OSCs and to improve the stability against oxidation [57, 194–197]. Replacing all hydrogen atoms of PEN by fluorine atoms leads to perfluorinated PEN (PFP, $C_{22}F_{14}$, Fig. 2.15a), which has a lower charge carrier mobility compared with PEN, but can also be used in devices [58, 123, 124]. PFP was first synthesized less than 10 years ago [123]. Therefore, it has not been studied in such detail as PEN yet. Nevertheless the structural [58, 60, 85, 127, 129] and optical properties [127, 128] have been published.

For PFP thin film growth on natively oxidized silicon one structural phase with a herringbone arrangement of the molecules and a d(100) lattice spacing of 1.58 nm and a monoclinic unit cell was reported [60]. For the unit cell parameters see Table 2.2.

Thin films of PFP grow polycrystalline on amorphous substrates, resulting in uniaxial anisotropy of the optical properties. In Fig. 2.15b the absorption spectrum of PFP in solution and in the thin films is shown [127]. The first peak at 1.78 eV in $k_{xy}(E)$ corresponds to the HOMO-LUMO transition with a shoulder at 1.94 eV, which is assigned either to a Davydov-splitting of the HOMO-LUMO transition or to a vibronic progression [128]. The peaks at higher photon energies correspond to a vibronic progression [59]. Similar to PEN, the transition dipole moment of the HOMO-LUMO transition of PFP is oriented along the short axis of the molecule [59], resulting in a weak $k_z(E)$ with the two most pronounced features at 2.75 eV and 2.92 eV.

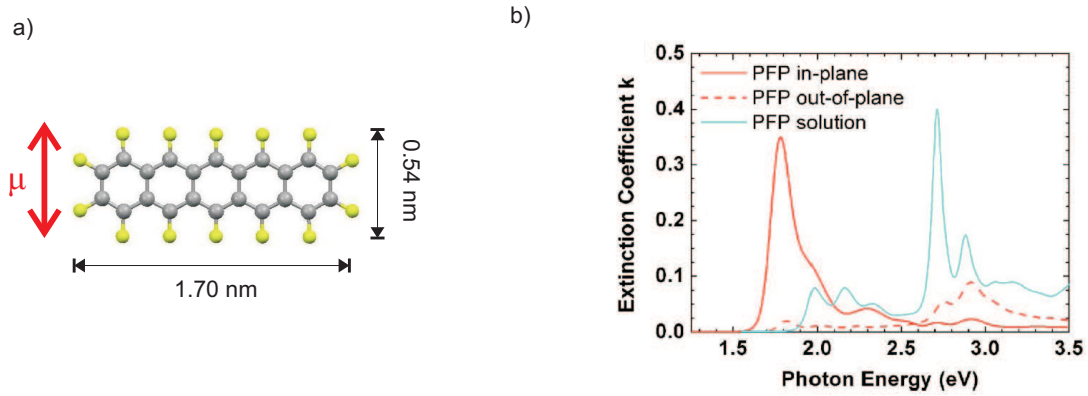

Figure 2.15: a) Schematical depiction of a PFP-molecule. The red arrow indicates the orientation of the transition dipole moment μ for the HOMO-LUMO transition. b) Absorption spectra of PFP in solution and in a thin film phase. Pictures modified from Ref. [59]. Dimensions of PFP measured using the Cambrigde Structural Database.

a [nm]	b [nm]	c [nm]	β [°]	V [nm^3]
1.576	0.451	1.148	90.4	0.816

Table 2.2: Lattice parameters of the PFP thin film phase. The unit cell is monoclinic [60].

2.5.3 Diindenoperylene (DIP)

Diindenoperylene ($C_{32}H_{16}$, DIP) is a red dye with promising properties for applications, such as high crystallinity and charge carrier mobility [133, 143].

DIP crystallizes in a herringbone arrangement of the molecules. For single crystals two different structural phases have been reported, the high temperature phase (HT) with a monoclinic unit cell and the low temperature phase (LT) with a triclinic unit cell [136, 137]. On natively oxidized silicon, DIP grows polycrystalline in the thin film phase (Table 2.3) with unit cell parameters which differ only slightly from the DIP HT phase [87, 137]. Two different molecular orientations can be found, the σ- and the λ-orientation, which exhibit differing orientations of the molecular long axis relative to the substrate surface [87, 147]. The lattice spacing perpendicular to the substrate surface is $d_\perp = 1.66$ nm for the σ-orientation corresponding to molecules almost standing upright. While PFP and PEN grow for most preparation conditions almost upright standing on the substrate surface, for DIP films grown at a substrate temperature of 300 K there may be a significant amount of lying molecules [87]. At substrate temperatures of 223 K, another polymorph was reported, which has different unit cell parameters [87].

Similar to PFP and PEN, DIP exhibits on amorphous substrates uniaxial anisotropic

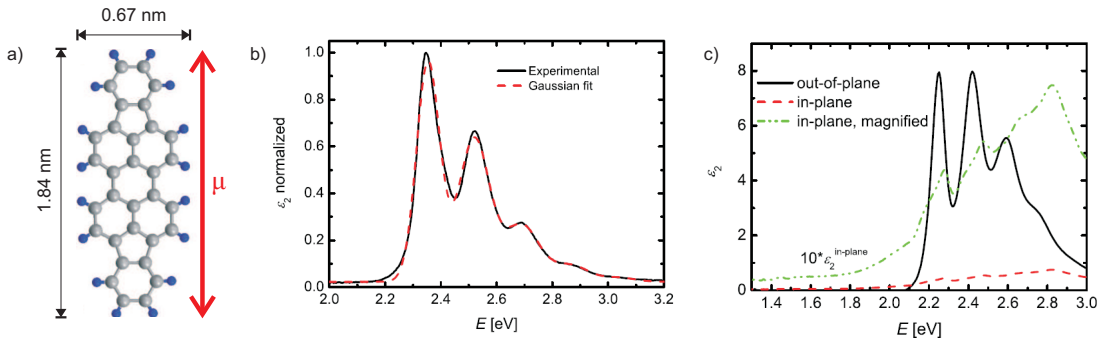

Figure 2.16: a) Schematical depiction of a DIP-molecule. The red arrow indicates the orientation of the transition dipole moment μ for the HOMO-LUMO transition. Absorption spectra of DIP: b) in solution, c) in a thin film phase. Pictures modified from Ref. [139]. Dimensions of DIP measured using the Cambrigde Structural Database.

a [nm]	b [nm]	c [nm]	α [°]	β [°]	γ [°]	V [nm^3]
0.709	0.867	1.69	90.0	92.2	90.0	1.02

Table 2.3: Lattice parameters of the DIP thin film phase with a monoclinic unit cell. After Refs. [87, 137].

optical properties. The orientation of the transition dipole moment of the HOMO-LUMO transition of DIP is along the long molecular axis [139]. Therefore, $\epsilon_{2,z}(E)$ is much stronger than $\epsilon_{2,xy}(E)$, see Fig. 2.16. The peak at 2.25 eV corresponds to the HOMO-LUMO transition with a following vibronic progression in both, $\epsilon_{2,xy}(E)$ and $\epsilon_{2,z}(E)$ [139]. Interestingly, it was found that the peak at 2.8 eV in $\epsilon_{2,xy}(E)$ does not belong to the vibronic progression, as its intensity is changing with film thickness relative to the other peaks [67]. This so-called *fourth mode* was assigned to contributions from Frenkel- and charge transfer excitons of higher transition [67].

Chapter 3

Experimental methods

3.1 Sample preparation

3.1.1 Organic molecular beam deposition (OMBD)

The samples, which are studied in this work have been prepared using organic molecular beam deposition (OMBD) [198, 199] in ultra-high vacuum (UHV). For OMBD the compounds are evaporated from heated Knudsen-cells and adsorb as thin organic film on the substrate surface. The preparation under UHV-conditions minimizes the amount of impurities in the film and prevents oxidation during growth. In the following the different steps of film growth will be addressed.

3.1.2 Substrates

Three different substrates have been used: i) Silicon wafers covered with a native oxide layer (NtveSi, $d_{oxide} \sim 2$ nm) bought from Si-Mat (doped with boron, resistance: 17-23 Ωcm), ii) thermally oxidized silicon wafers (ThermSi, $d_{oxide} \sim 147$ nm), for details see Ref. [154] and iii) quartz glass (Schott GmbH, $d = 0.5$ mm, transparent for $\lambda = 200\text{ nm} - 1100\text{ nm}$).

All substrates were cleaned prior to film growth in an ultrasonic bath using acetone, isopropanol and deionized water for 3 min each. After the cleaning process the substrates were heated for 5 min to remove the water and glued on a tantalum sample holder using conducting silver paste. Before inserting in the vacuum chamber the sample holder with the substrates was heated again for 3 min to dry the silver paste and remove the solvents.

3.1.3 UHV-chamber

Fig. 3.1 shows a sketch of the vacuum system used for film preparation. It consists of two main parts: the load lock, which can be vented to insert the samples and the main chamber in which the films are grown. The load lock is pumped by a turbo molecular pump (TMP), which can also be connected to the main chamber during transfer and film

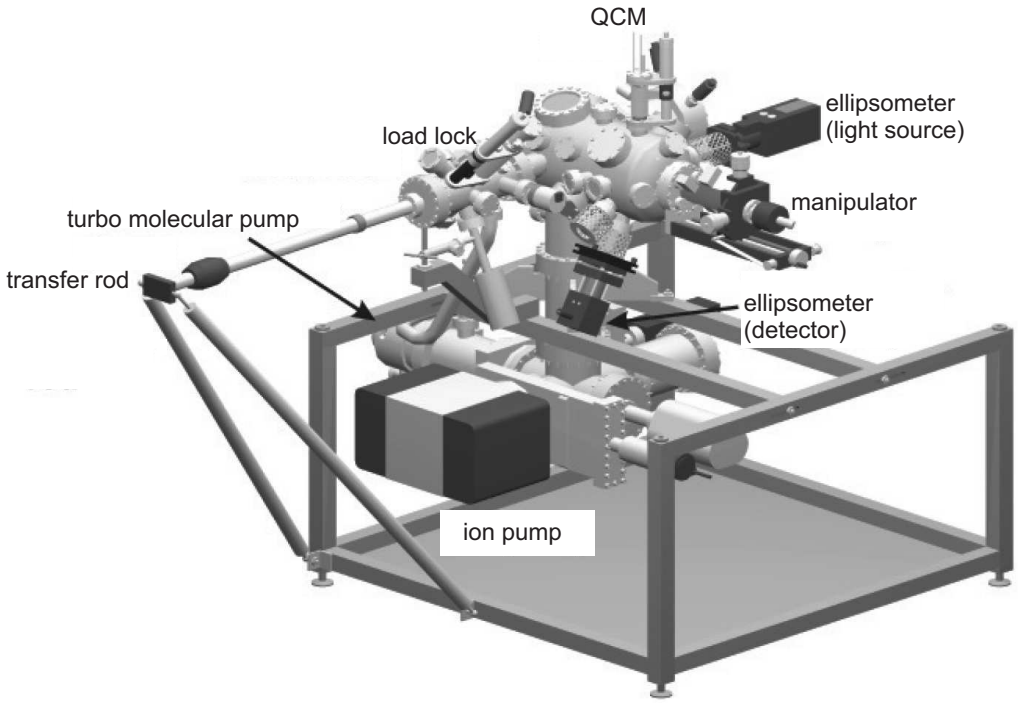

Figure 3.1: Vacuum system. The samples are inserted in the load lock and heated over night under HV-conditions ($p < 10^{-6}$ mbar). After heating the samples are transferred using the transfer rod into the main chamber ($p \approx 2 \times 10^{-10}$ mbar), where the films are grown. The film thickness can be monitored during the film growth with the QCM. Using the manipulator the sample position can be adjusted in the main chamber. The vacuum is preserved by a turbo molecular pump (TMP) and an ion pump. Picture taken from Ref. [200].

growth to preserve the UHV. The main chamber is pumped by an ion getter pump and a titan sublimation pump.

Prior to film growth the cleaned substrates were inserted in the load lock ($p < 10^{-6}$ mbar) and heated there over night for at least 8 hours at $T > 400$ K to remove water and impurities. Afterwards the substrates were transferred into the main chamber ($p \approx 2 \times 10^{-10}$ mbar) using the transfer rod and heated there for 5 min over $T = 600$ K for final cleaning. In the main chamber, the substrates were put on a manipulator, which can be moved in three directions and rotated additionally, allowing an exact adjustment of the sample position for film growth and *in situ* optical spectroscopy. Two setups can be used for *in situ* optical spectroscopy during film growth in the main chamber, namely differential reflectance spectroscopy (DRS, see Sec. 3.2) and spectroscopic ellipsometry (SE, see Sec. 3.3). During film growth the substrates can be heated or cooled and two

thermocouples connected with the manipulator can be used to measure the substrate temperature T_{sub}. A quartz crystal microbalance (QCM) allows to monitor the evaporation rate and film thickness during growth.

3.1.4 Film growth

3.1.4.1 Growth procedure

For film growth the materials are evaporated from Knudsen-cells connected to the UHV-chamber. The materials are contained in a ceramic crucible which is wrapped by a tungsten wire, through which it can be resistively heated. Under heating the molecules sublimate, enter the chamber as molecular beam and adsorb on the substrate. The crucible is covered by a tantalum foil with a small hole, defining the angular distribution of the evaporating compounds. The cell itself is closed by a moveable tantalum sheet ("shutter"). By opening or closing this shutter the beginning and the end of the film growth can be defined. After growth the samples are transferred to the load lock and removed for *ex situ* measurements.

The samples studied in this work were prepared by coevaporation to obtain intermixed films. For this purpose, two cells containing the two different compounds were heated simultaneously to the evaporation temperature of the respective compound and the two shutters were opened at the same time. The final film thickness for each of the samples was between 19 nm and 28 nm.

3.1.4.2 Experimental parameters and scale factor determination

There are several parameters, which influence the film growth, such as the choice of the substrate, the substrate temperature and the evaporation rate, which defines for mixed systems also the relative volume fraction of the compounds.

The films studied in this work are prepared at three different substrate temperatures T_{sub} (180 K, 300 K and 340 K). During film growth T_{sub} was measured with a thermocouple, but not controlled with a Eurotherm temperature controller, as this induces artefacts in the DRS spectra. However, the drift of T_{sub} during growth was monitored and was found to be less than 2 K in 120 min. Therefore, the substrate temperature can be considered as constant during film growth. All films have been prepared at a constant evaporation rate around 1.9 Å/min. The rate can be adjusted by the temperature of the crucible, which is measured using a thermocouple and controlled by a Eurotherm temperature controller.

The evaporation rate is monitored with a QCM, which is an oscillating quartz crystal whose oscillation frequency is damped when molecules are adsorbing. Monitoring the frequency damping as a function of time allows to obtain the amount of adsorbing molecules per time interval. However, this value will depend on the position of the cell relative to the QCM, the angular distribution of the molecular beam and the density of the molecular layer adsorbing. Additionally, as the position of the sample relative to the cells is different from the position of the QCM, the amount of molecules adsorbing on

Cell	PFP	PEN	DIP
Scale factor	0.23	0.09	0.51

Table 3.1: Scale factors for the three molecules studied in this work for a density set arbitrarily to 0.1 g/cm^3.

System	Mixing ratio	Corrected rates [Å/min]	Overall growth rate [Å/min]
PFP:PEN	4:1	1.6:0.4	2.0
PFP:PEN	2:1	1.4:0.7	2.1
PFP:PEN	1:1	0.9:0.9	1.8
PFP:PEN	1:2	1.4:0.7	2.1
PFP:PEN	1:4	0.4:1.6	2.0
PFP:DIP	4:1	1.28:0.6	1.88
PFP:DIP	2:1	1.12:0.7	1.82
PFP:DIP	1:1	0.8:1	1.8
PFP:DIP	1:2	0.5:1.2	1.7
PFP:DIP	1:4	0.3:1.6	1.9
PEN:DIP	4:1	1.6:0.6	2.2
PEN:DIP	2:1	1.2:0.9	2.1
PEN:DIP	1:1	0.8:1.2	2.0
PEN:DIP	1:2	0.5:1.5	2.0
PEN:DIP	1:4	0.3:1.8	2.1

Table 3.2: Mixing ratios, rates corrected for the volume of the respective unit cell and overall growth rates for the different mixed systems studied in this work.

the sample surface differs from that adsorbing on the QCM. The transformation of the rate measured by the QCM in the rate of molecules which are actually adsorbing on the sample surface is performed by multiplying the readout of the QCM with the scale factor α. α is determined for each cell separately by growing a film, measuring its thickness (d_{XRR}) with X-ray reflectivity (XRR, see Sec. 3.4) and comparing it to the corresponding readout of the QCM (d_{QCM}). The factor, with which the readout of the QCM has to be multiplied to obtain the actual thickness of the film (and accordingly the actual rate of molecules adsorbing on the sample surface) is $\alpha = \frac{d_{XRR}}{d_{QCM}}$. For the determination of α a density of the film of 0.1 g/cm^3 (which is only a tenth of the ususal density of organic materials) was arbitrarily chosen to increase the accuracy of the QCM-readout. However, as stated before, the scale factor corrects -amongst other effects- for differences in the density of the material adsorbing on the QCM and the substrate. Therefore, the chosen density of 0.1 g/cm^3 has no influence on the measurements. The different scale factors for the molecules investigated are compiled in Table 3.1.

Mixing ratio / T_{sub} [K]	4:1	2:1	1:1	1:2	1:4
180 K	-	-	x	-	-
300 K	x	x	x	x	x
330 K	-	-	x	-	-

Table 3.3: Mixing ratios (PFP:PEN, PFP:DIP and PEN:DIP) and preparation temperatures for the different samples (marked with x) studied in this work.

3.1.4.3 Determination of the mixing ratio

For mixed systems the relative volume fraction of the two compounds, which is determined by the evaporation rate of the respective cells, is crucial for many properties. In order to study the effect of changing mixing ratio on the absorption spectra of the mixed films five different mixing ratios (4:1, 2:1, 1:1, 1:2, 1:4) of the respective compounds were chosen and the corresponding rates were determined prior to film growth.

In this work *particle* mixtures were studied, which means an equimolar mixture (mixing ratio (A:B) = 1:1) contains the same amount of *molecules* of compound A and compound B. Therefore, the rates have to be corrected for the difference in the volume of the unit cells of the respective compounds. This results - e.g. in the case of PEN:DIP - in a PEN-rate of 0.8 Å/min and a DIP-rate of 1.2 Å/min to obtain an equimolar mixture. In contrast to that, the PEN- and DIP-rates to obtain a *volume* mixture would be the same, e.g. 1 Å/min each. This would result in a mixed film (with an overall thickness of e.g. $d = 20$ nm) containing 10 nm PEN and 10 nm DIP, but - due to the different volume of the unit cells - more PEN than DIP molecules. In Table 3.2 the different mixing ratios with the corresponding rates are compiled and Table 3.3 shows the different preparation conditions and mixing ratios for all of the samples studied in this work.

3.2 Differential reflectance spectroscopy (DRS)

3.2.1 Fundamentals

The optical properties of the mixed films were studied *in situ* using differential reflectance spectroscopy (DRS). This technique is especially suited to study thin films during growth, as it is very sensitive to small signals, fast and non-invasive.

The measured quantity is the change in reflectivity of a bare substrate when a film of e.g. organic molecules, is adsorbing. The DRS signal is defined as

$$DRS = \frac{R(d) - R_0}{R_0} \tag{3.1}$$

with $R(d)$ the reflectivity of the substrate covered with a film with thickness d and $R(d)$ the reflectivity of the bare substrate [81, 201].

One advantage of DRS is the data analysis, which, in particular for thin films ($d_{film}/\lambda \ll 1$) and transparent substrates, is very reliable, as in this case the DRS signal is directly proportional to ϵ_2 [202]

$$DRS = \frac{8\pi d}{\lambda(1 - n_{\text{sub}}^2)}\epsilon_2 \tag{3.2}$$

For intransparent substrates $\epsilon_2(E)$ has to be determined by a fit of the DRS data based on the matrix method in order to take reflections from the different interfaces in the system into account [149,154,155]. In the literature there are two different fitting approaches [67, 203]. Both have in common that they vary $\epsilon_2(E)$ to model the measured reflectivity for all film thicknesses separately, but the fit parameters themselves are different.

The first approach models $\epsilon_2(E)$ with a number of Gaussian oscillators [67, 154, 201], obtained by a Kramers-Kronig consistent fit of $\epsilon_2(E)$ measured with spectroscopic ellipsometry (SE), see Sec. 3.3 [67]. The fit parameters are amplitude, width and energy position of the oscillators. Additionally, Cauchy parameters are used to correct for errors in the Kramers-Kronig transformation due to the experimentally limited energy range. This approach has the advantage that thickness dependent changes in energy positions or intensity of specific peaks can directly be investigated. A disadvantage of this approach is its dependence on the initial parameters determined by SE. Although wide boundaries can be chosen for the fitting parameters, the fit results are influenced by the number of Gaussian oscillators, which is defined by the initial parameters. Furthermore, Gaussian oscillators cannot be Kramers-Kronig transformed. In order to obtain ϵ_1, ϵ_2 has to be calculated from the Gaussian oscillators, and a Kramers-Kronig (KK) transformation has to be performed.

In a second approach the data are fitted numerically without using Gaussian oscillators [203–205] assuring that ϵ_1 and ϵ_2 are directly KK consistent. However, this method requires the measurement of the dielectric function in a spectral range where ϵ_2 becomes small enough at the boundaries to apply the KK transformation. This condition will not always be fulfilled. In addition, the approach has the drawback that any shifts in energy position or intensity of peaks can only be plotted as a function of film thickness after fitting the respective spectrum with Gaussian oscillators to obtain the energy positions of the peaks.

Both approaches have been tested on one set of DRS data. The results obtained with the first approach were found to be in best agreement with the results of SE measurements. The results obtained with the second approach are consistent regarding the relative intensities of the peaks in ϵ_2, but exhibited slight differences regarding the absolute intensities. Since in this work results obtained using SE and DRS will be presented, the DRS data were analyzed using the first approach for a better comparability of the results.

Independent of the fitting procedure, DRS has the great advantage that it is performed at normal incidence. In the case of uniaxial anisotropic samples, such as the samples which were studied in this work, only ϵ_{xy} will be probed and has therefore to be taken into account in the analysis. This simplifies the data analysis and enhances the reliability.

3.2.2 Setup

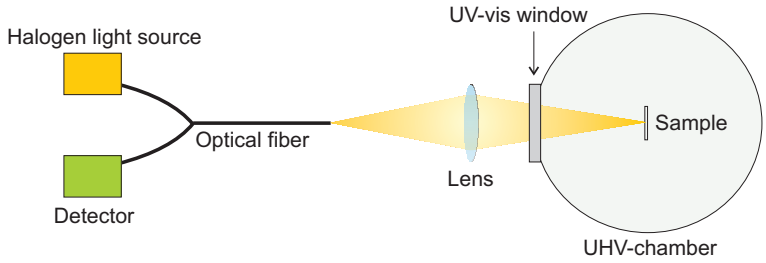

Figure 3.2: DRS setup for *in situ* measurements at normal incidence ($g = 14$ cm, $b = 19$ cm). The light of a halogen lamp is focused by a lens on the sample surface and the reflected light is detected with a CCD-detector. Due to the bifurcated fiber which guides the incident light to the chamber and the reflected light to the CCD-detector, the measurement takes place at normal incidence.

Fig. 3.2 shows the setup of a DRS measurement [154]. The light of a white light source (DH-2000 deuterium-tungsten halogen lamp, Micropack) is guided by a bifurcated optical fiber (Ocean Optics) close to the chamber. The fiber exit is placed at a distance of ~ 14 cm to an achromatic lens (focal length $f = 8$ cm). This lens is mounted ~ 1 cm in front of a quartz glass window on the chamber and focuses the light on the sample surface inside the chamber. The distance between lens and sample is $b \approx 19$ cm, the spot diameter on the sample is approx. 1 mm.

The light is reflected from the sample surface and detected by the second arm of the bifurcated fiber at almost the same spot where the light is emitted. Therefore, a measurement at normal incidence is assured. The reflected light is detected by a CCD-detector (USB2000+, Ocean Optics) in the energy range of $E = 1.4 - 3$ eV with a resolution of $\Delta\lambda < 0.004$ eV, where spectra can be measured within 3 ms. The spectra are displayed and saved using the program *Spectra Suite* by Ocean Optics.

For all DRS measurements glass was used as substrate and the substrate backside was roughend to avoid back-reflections. Directly before film growth the reflectivity of the bare substrate was measured. In order to increase the signal to noise ratio, the intensity of the signal was maximized by adjusting the sample position (especially the tilt angle) and the distance between fiber exit and lens. Furthermore, the number of spectra to average was chosen as high as possible. This resulted in a usual integration time (t_{int}) of 40 msec, corresponding to 3000 spectra to average and one averaged spectrum each 120 sec. As the growth rate was at maximum 2.2 Å/min, 4 spectra could be measured per 1.6 nm ($\approx$ 1 monolayer (ML)) and the time resolution was high enough to follow the film growth in real-time. Based on the raw data the DRS signal was calculated according to Eq. 3.1.

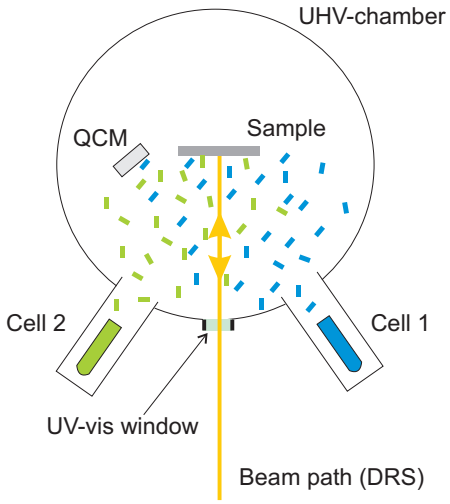

Figure 3.3: Sketch of the UHV-chamber with two evaporation cells for coevaporation and the light path of a DRS measurement.

3.3 Spectroscopic ellipsometry (SE)

3.3.1 Fundamentals

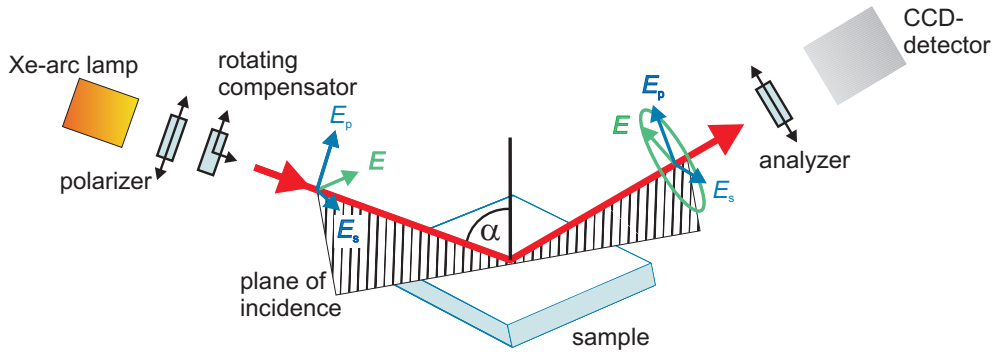

Figure 3.4: Setup of the Woollam M-2000 ellipsometer: The light of a Xenon-arc lamp is polarized by a polarizer and a rotating compensator and is reflected from the sample surface. The change of the polarization state is detected as time dependent intensity signal by an analyzer and a CCD-camera. Picture taken from Ref. [154].

While DRS probes $\epsilon_{2,xy}(E)$, spectroscopic ellipsometry (SE) is a technique to determine $\epsilon_{xy}(E)$ and $\epsilon_z(E)$ in the case of samples exhibiting uniaxial anisotropy [181, 206]. This technique is based on the fact that the Fresnel-coefficients for reflection from a sample are different for p- and s-polarized light (where s (p) corresponds to a polarization perpendicular (parallel) to the plane of incidence). Therefore, the polarization state of polarized light will be changed under reflection[1] from the sample surface. The measured

[1]SE can also be measured in transmission [206]. However, this will not be discussed as all measurements

quantities are the two ellipsometric angles Ψ and Δ, which are related to this change.

In the following a short motivation of the measured quantities and their relation to the optical properties of the material investigated is given, following the SE manual by Woolam [181].

In a SE measurement the polarization state of light emitted from a white light source is periodically changed from linear to elliptical to circular and back, which results in a time dependent intensity signal measured by a detector [181]:

$$V(t) = \text{offset} + a\cos(2\omega t) + b\sin(2\omega t) \tag{3.3}$$

The normalized Fourier components α and β of this signal are connected to Ψ and Δ by [181]:

$$\alpha = \frac{a}{\text{offset}} = \frac{\tan^2\Psi - \tan^2 P}{\tan^2\Psi + \tan^2 P} \qquad \beta = \frac{b}{\text{offset}} = \frac{2\tan\Psi\cos\Delta\tan P}{\tan^2\Psi + \tan^2 P} \tag{3.4}$$

Here, P is the polarizator azimuth with respect to the plane of incidence, which corresponds to P=0°. Ψ and Δ are connected to the Fresnel-coefficents for p- and s-polarized light of the sample by the following relation [181]:

$$\rho = \frac{r_p}{r_s} = \tan\Psi\exp(i\Delta) \tag{3.5}$$

As the Fresnel-coefficients are connected to ϵ of the material, it is possible to derive ϵ from a SE-measurement of an ideal two phase system, if the thickness d of the sample investigated is known[2].

Usual samples, including the films studied here, although, are no ideal two phase system, as they are composed of the substrate and the thin film. In this case, the Fresnel-coefficients have to be replaced by the pseudo-Fresnel-coefficients and fit procedures have to be applied to obtain ϵ from a SE measurement. All SE data discussed in this work have been analyzed using the program *WVase32* by Woollam. This program provides two possible fitting procedures both based on the Levenberg-Marquardt algorithm [181]:

a) *Point-by-point fit:* For each wavelength and angle of incidence separately, Ψ and Δ are fitted such that they best describe the data. This fit procedure has to be applied, if the optical constants of the material investigated are unknown, as a point-by-point fit is independent of the initial parameters. However, the resulting ϵ_1 and ϵ_2 are not necessarily Kramers-Kronig consistent.

b) *Normal fit:* The data are fitted for *all* wavelengths at the same time but separately for each angle of incidence. This fit procedure is applied to obtain Kramers-Kronig consistent optical constants by modeling the optical constants obtained with a point-by-point fit by e.g. Gaussian oscillators. The results of a normal fit will depend on the initial parameters.

in this work were performed in reflection.

[2]Vice versa, the thickness d can be determined, if the optical properties of the sample are known.

3.3.2 Setup

Fig. 3.4 shows the setup of the Woollam M-2000 ellipsometer with rotating compensator, which was used in this work. The light of a Xenon-arc lamp (spectral range $1.23-5$ eV) is polarized linearly by a fixed polarizer and passes a rotating compensator (RC), which is a birefringent crystal. Depending on the angle between the polarizer and the fast axis of the RC, the light either stays linearly polarized or becomes circularly or elliptically polarized. It hits the sample and is reflected. The reflected light passes a fixed analyzer and is detected by a four-quadrant diode, which is connected with a CCD-detector by an optical fiber. Due to the RC and the fixed analyzer the CCD-detector measures a time-dependent intensity signal. The Fourier components of this signal are connected to the ellipsometric angles Ψ and Δ (see Eq. 3.4), which are connected to ϵ via the Fresnel-coefficents (see Sec. 2.1.2).

After each start the ellipsometer has to be calibrated to define the angles of polarizer and analyzer relative to the plane of incidence. The calibration is performed using a smooth and isotropic sample, such as NtveSi, to avoid depolarization effects [181, 207]. After the calibration there are two possible measurement setups. Firstly, the *in situ* measurements, for which the light source and the detector are mounted on two strain reduced quartz glass windows at the UHV-chamber and secondly, *ex situ* measurements for which the light source and the detector are mounted on a goniometer. For uniaxial anisotropic samples *in situ* SE has some drawbacks as the measurement is performed under a fixed angle of incidence of $\sim 60°$ and on one substrate. Therefore, ϵ_{xy} and ϵ_z are measured simultaneously and cannot be analyzed independently. Due to this reason in this work SE was solely used for *ex situ* measurements which will be discussed in more detail in the following.

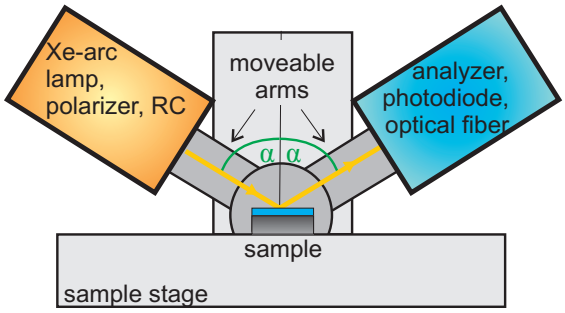

Figure 3.5: Setup of an *ex situ* ellipsometry experiment. α can be varied from 40° to 90°.

Fig. 3.5 shows the setup of an *ex situ* VASE measurement. The light source with the polarizer and the rotating compensator and the fixed analyzer together with the four-quadrant-diode are mounted on two arms of a goniometer. SE data can be acquired in an angular range of 40° to 90° relative to the surface normal. Usually the angle of incidence (AOI) is varied in steps of 5° from 40° to 80° with 300 revolutions per measurement of the RC. Measurements at an AOI higher than 80° have not been performed due to the limited size of the sample.

The data are analyzed applying a *multi-sample analysis* [208, 209]. This solves the problem that there are only two quantities measured in a SE experiment (Ψ, Δ), but four unknown variables ($\epsilon_{1,xy}$, $\epsilon_{2,xy}$, $\epsilon_{1,z}$ and $\epsilon_{2,z}$) in case of uniaxial anisotropy. In order to determine ϵ_{xy} and ϵ_z the films are grown simultaneously on two substrates (NtveSi and ThermSi). Due to the simultaneous preparation, the film thickness and the optical properties are assumed to be identical on the two different substrates. Post growth both samples are measured, resulting in four measured quantities (Ψ_{NtveSi}, Δ_{NtveSi}, Ψ_{ThermSi} and $\Delta_{\mathrm{ThermSi}}$) and four unknown variables ($\epsilon_{1,xy}$, $\epsilon_{2,xy}$, $\epsilon_{1,z}$ and $\epsilon_{2,z}$), which allows to determine ϵ_{xy} and ϵ_z separately. For details the reader is referred to Refs. [154, 208, 209].

3.4 X-ray reflectivity (XRR) and grazing incidence X-ray diffraction (GIXD)

X-ray reflectivity (XRR) and grazing incidence X-ray diffraction (GIXD) measurements of the samples have been performed in order to relate changes in the optical properties with structural changes in the film. In the following a short description of the experimental geometry and provided information is given. For details the reader is referred to Refs. [161, 210, 211].

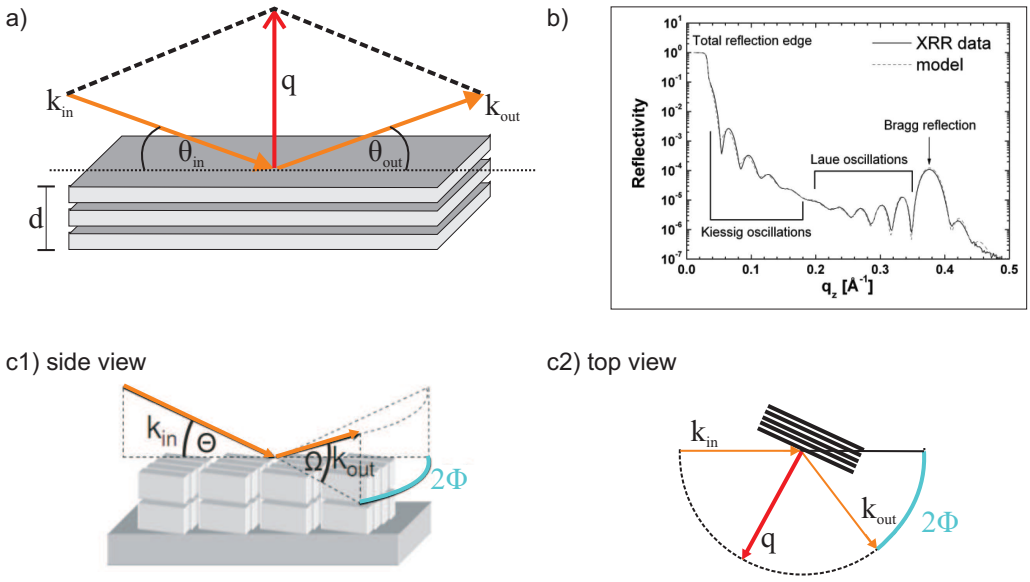

Figure 3.6: a) Setup of a XRR experiment with angle of incidence Θ_{in} and b) a typical XRR scan. c) Setup of a GIXD experiment with angle of incidence Θ_{in} and detector angle Φ. Pictures modified from Ref. [161].

In a specular X-ray reflectivity measurement the scattering plane is perpendicular to

the sample surface and the intensity of the scattered beam is detected under the exit angle (detector angle) Θ_{out} being the same as the incidence angle Θ_{in}, which corresponds to a scattering angle $2\Theta_{in}$ (Fig. 3.6a). Fig. 3.6b shows a typical XRR scan. There are several pieces of information, which can be derived from this scan:

a) **Kiessig-fringes** arise from the interference of waves reflected at the two interfaces vacuum (air)-film and film-substrate. From the period and the damping of these Kiessig-oscillations the film thickness d and the surface roughness σ can be determined.

b) **Laue-oscillations** stem from coherent interference of waves scattered on a finite number of lattice planes parallel to the sample surface. The period of the Laue-oscillations is indirectly proportional to the average thickness of the coherently scattering crystallites in the film.

c) The **Bragg-peak** results from the constructive interference of waves reflected at lattice planes parallel to the sample surface. The *out-of-plane* lattice spacing $d_\perp$ (the distance between the scattering lattice planes perpendicular to the sample surface), is related to the position of the Bragg-peak Θ_{Bragg} via the Bragg law $n\lambda = 2d_\perp sin(\Theta_{\text{Bragg}})$, where λ is the wavelength of the X-rays.

By measuring not under specular conditions ($\Theta_{in} = \Theta_{out}$), but with an offset between incidence and detector angle (i.e. $\Theta_{in} = 2\Theta \pm \text{offset}$) information about diffuse scattering due to surface roughness and structural imperfections in the film can be obtained. In addition, by performing rocking scans (changing Θ_{in} while keeping the angle between source and detector constant), the mosaicity of the film, which is the average tilt angle between different crystallites in the substrate plane, can be measured.

Finally, grazing incidence X-ray diffraction (GIXD), see Fig. 3.6c allows to probe the size of coherently scattering crystallites and the lattice spacing parallel to the substrate surface (*in-plane*). These measurements are performed with fixed angles Θ_{in} and 2Θ and the detector is moved parallel to the substrate surface by the angle Φ, probing scattering by lattice planes oriented perpendicular to the substrate surface.

The measurements discussed in this work have been performed at three different sources. Most of the XRR-scans have been performed inhouse with a GE Seifert X-ray reflectometer with Cu K_α-radiation (λ = 1.541 Å) under air. The real-time XRR scans as well as the GIXD scans have been performed either at the European Synchrotron Radiation Facility (ESRF, Grenoble, France) at the beamline ID10B with λ = 0.9398 Å (PEN:DIP-mixtures) or at the beamline MS-Surf-Diffr at the Swiss Light Source (SLS, Villigen, Switzerland) with λ = 0.9537 Å (PFP:DIP-mixtures) using a portable UHV-chamber. For details of the portable UHV-chamber see Sec. 3.6.3 and Refs. [161, 212, 213].

The data analysis was performed using the programs Parratt32 [214, 215] and GenX [216]. A detailed description of the different fitting parameters and the fitting procedure using GenX can be found in Refs. [216, 217].

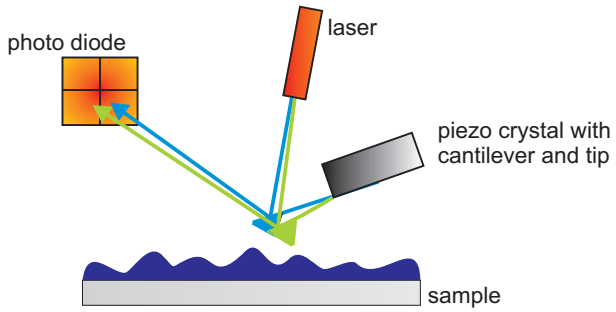

Figure 3.7: Setup of an AFM experiment. A cantilever with a sharp tip is mounted on top of a piezocrystal. The movement of the tip is measured by the deflection of a laser, which is detected by a photo diode.

3.5 Atomic force microscopy (AFM)

After the optical and structural characterization of the samples, their morphology was investigated by atomic force microscopy (AFM) using a JPK NanoWizard II AFM in *tapping mode*[3]. Here, the key points are briefly summarized, for details of AFM the reader is referred to textbooks, e.g. Ref. [218].

Fig. 3.7 shows the setup of an AFM measurement. A sharp tip which is mounted at the end of a cantilever is excited to vibrations by a piezo crystal. For the measurement the tip is moved at constant vibration frequency and height relative to the sample surface over the scanning area (in this work 5×5 μm^2). If the system of tip and cantilever is far away from the sample surface its vibration corresponds to a free vibration. However, as the tip comes closer to the surface the vibration of the tip is damped due to the interaction between tip and surface. This damping is influenced by the distance between sample and tip, which changes with changing sample morphology, e.g. if there are islands on the surface. The laser measures the deflection of the tip for every spot on the sample surface and, doing so, the morphology of the sample can be probed.

3.6 Further experiments

For each of the three systems studied in this work, one property or behavior was especially interesting and investigated using additional techniques, which will be briefly explained in the following. For details the reader is referred to the literature, e.g. Refs. [219–223].

3.6.1 Near-edge X-ray absorption fine structure spectroscopy (NEXAFS)

The tilt angle of the molecules in the PFP:PEN mixed films was determined by near-edge X-ray absorption fine structure spectroscopy (NEXAFS) [219–221]. The energy of a polarized, monochromatic X-ray beam is changed continuously around the absorption

[3] AFM measurements can also be performed in *contact mode*. However, since all measurements shown here have been performed in *tapping mode* only this mode will be discussed in the following

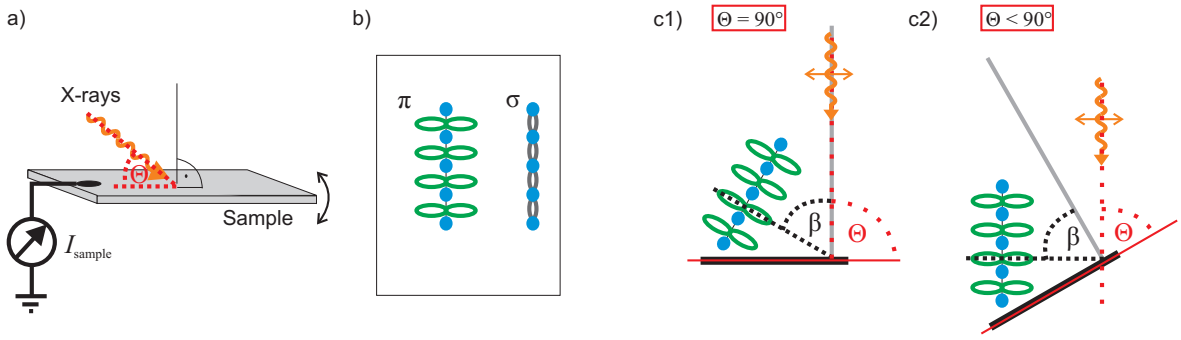

Figure 3.8: a) Setup of a NEXAFS experiment. b) Orientation of the molecular orbital relative to the molecular plane for π- and σ-orbitals. c) Scheme of the origin of an angular dependent intensity of the NEXAFS spectrum for different angles of incidence (AOI) Θ.

edge of a core-level of one element in the sample. By photoabsorption of the X-rays core electrons are excited into unoccupied molecular orbitals. The created core hole is filled with an electron by emission of radiation or of an Auger-electron [221]. Depending on the setup, different parameters are used to measure the amount (intensity) of photo-electrons.

a) Measurement of the photo-electrons using an electron analyzer.

b) Measurement of fluorescence due to the refilling of the core level by radiative decay of electrons of higher levels.

c) Measurement of the sample current I_{sample} due to the refilling of the core-level with electrons from a reservoir (grounded sample).

NEXAFS at the carbon K-edge usually probes transitions from the 1s core-level into unoccupied π*-orbitals[4] [221]. Measuring NEXAFS at different angles of incidence using X-rays, which are polarized parallel to the plane of incidence, allows to determine the molecular tilt angle, as it is shown in Fig. 3.8c, since the electrons are most efficiently excited if the $\vec{E}$-field of the X-ray beam is parallel to the orientation of the π*-orbital. From the angular dependence of the intensity of the NEXAFS spectrum one can calculate the tilt angle using the following formula [220, 225]:

$$I = C[P(\cos^2(\Theta)\cos^2(\beta) + \frac{1}{2}\sin^2(\Theta)\sin^2(\beta)) + \frac{1-P}{2}\sin^2(\beta)] \tag{3.6}$$

Here, C is a constant offset, P is the polarization degree of the X-ray beam, Θ is the angle of incidence of the X-ray beam relative to the substrate surface and β is the tilt angle of the corresponding π*-orbital relative to the surface normal corresponding to a tilt angle of the molecular plane relative to the surface normal of $\alpha = 90° - \beta$.

[4] This can be different for NEXAFS at the fluorine K-edge [224].

The experiments have been performed at the Optics Beamline of the BESSY II in Berlin (polarization degree P=0.97), in ultra-high vacuum using the SurICat-endstation. The sample current was probed to measure the amount of created photo-electrons (see Fig. 3.8a). Two different absorption edges have been chosen: the K-edge of carbon at $E = 286$ eV and the K-edge of fluorine at $E = 695$ eV. NEXAFS data have been measured by varying the photon energy from $E = 270$ eV to $E = 350$ eV around the carbon K-edge and from $E = 670$ eV to $E = 760$ eV around the fluorine K-edge at four different angles of incidence relative to the substrate surface (90°, 70°, 50°, 30°). Simultaneously to the measurements the current of the storage ring was monitored. A gold single crystal was measured as reference. The NEXAFS data have been normalized with the following procedure [212]:

a) The sample current was divided by the ring current to correct for fluctuations in the beam intensity. The same was done for the gold reference spectrum.

b) The corrected NEXAFS spectra of the sample were divided by the corrected spectra of the gold reference.

c) From the resulting spectra an offset was substracted so that the intensity before the ionisation edge is zero.

d) Finally, all spectra were normalized to the intensity resulting from the excitation of 1s-electrons into σ*-orbitals, 40 eV (30 eV) away from the K-edge of carbon (fluorine).

3.6.2 Polarization dependent transmission spectroscopy (PDTS)

The investigation of the absorption spectra of the PEN:DIP and PFP:DIP mixed films was completed by polarization dependent transmission spectroscopy (PDTS) experiments [222, 223, 226, 227]. Since the transmission of the sample is directly measured, the data do not have to be fitted or further processed (except for a baseline correction and a correction for the substrate transmission) and therefore, this technique is well suited to control the results obtained with DRS and SE regarding their reliability. Additionally, it provides the possibility to investigate the orientation of the transition dipole moments by the influence of the polarization state of incident light on the optical response of the material, which is valuable information for peak assignment.

The measurements are performed on transparent substrates and the transmission T of the material is investigated, which is connected to the absorbance A by $A = -log\ T$. All measurements discussed in this work have been performed with a Lambda 900 Spectrometer (Perkin Elmer) in the group of Prof. A. Sassella (Universitá degli studi materiali Milano Bicocca). Fig. 3.9 shows the optical path in such a spectrometer [228]. The light of a halogen lamp is monochromatized by two monochromators and split into a beam passing the sample and a reference beam passing an empty sample holder. This reference

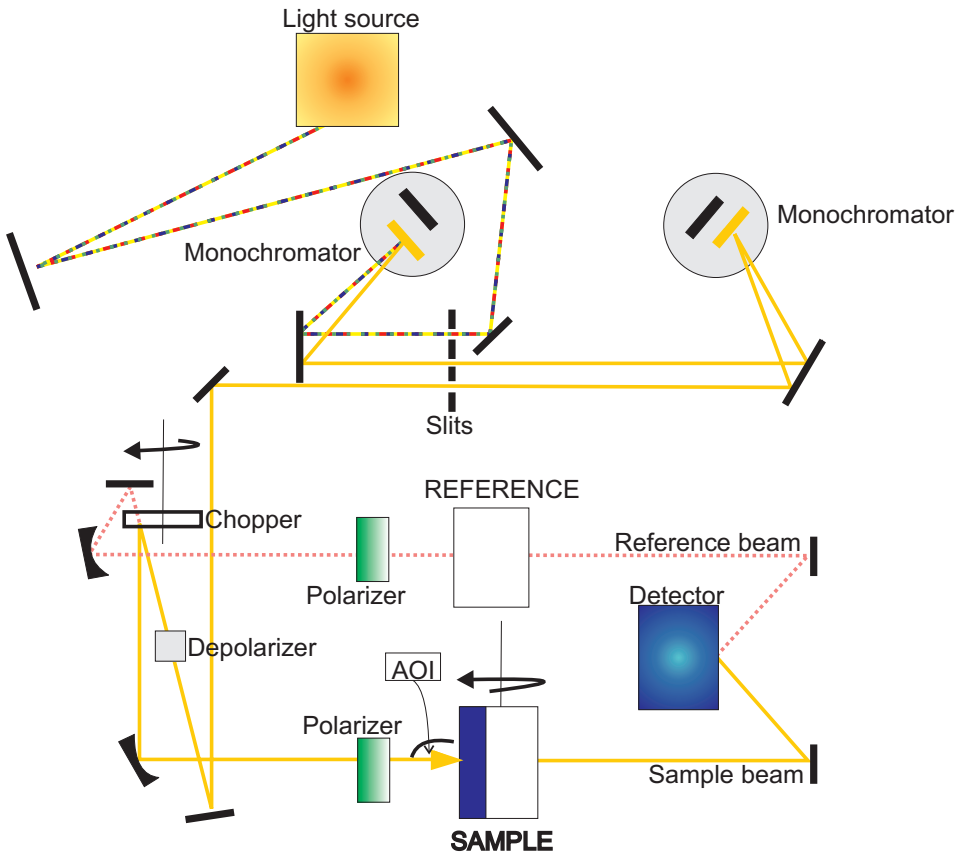

Figure 3.9: Optical components of the Perkin Elmer Lambda 900 spectrometer. Picture modified from Ref. [228].

beam enhances the signal to noise ratio of the measured spectra. The splitting of the beam is performed by a chopper, which is a rotating wheel consisting of four segments, which are a window, a mirror and two black segments. Depending on the segment which is hit by the beam, the optical path differs. If the beam passes the window, it is reflected from a mirror and follows the dotted optical path to work as the reference beam. If the beam is reflected from the mirror segment on the chopper wheel, it follows the optical path indicated by the solid line probing the transmission of the sample. The two black segments serve for distinguishing between the reference and sample beam and allow to correct for the electrical dark of the detector. After the splitting, the two beams pass two Glan-Taylor polarizers which allow to change the polarization state of the light. The sample is mounted on a rotatable sample holder with a micrometer scale for reproducible sample positioning. By rotating the sample holder the angle of incidence (AOI) can be varied. Independent of the optical path, both (reference and sample) beams are finally detected by a photo diode detector.

Before the measurement the spectrometer is calibrated and the detector is checked for

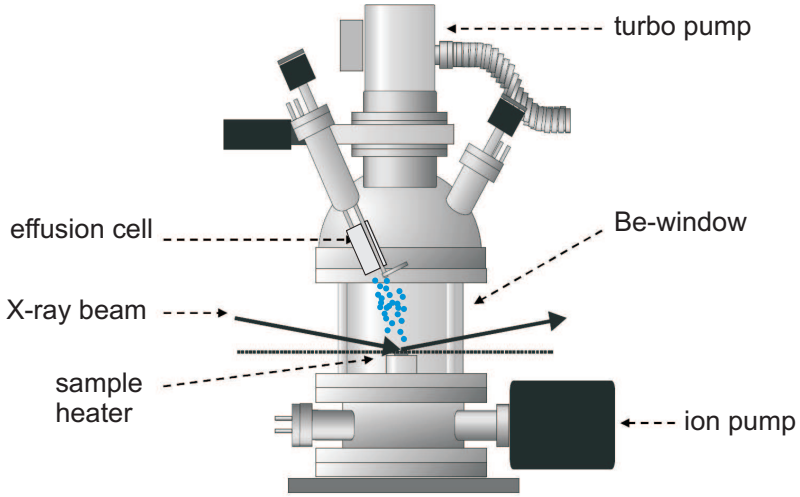

Figure 3.10: Scheme of the portable UHV-chamber used for the real-time measurements. Picture modified from Ref. [212].

accuracy by measuring the doublet peak of halogen at $\lambda = 656.1$ nm and $\lambda = 656.3$ nm. After calibration the baselines were obtained by measuring the sample and the reference beam passing empty sample holders. The measurements were obtained at three different angles of incidence (AOI) relative to the substrate normal of 0°, 30° and 60° and with two polarizer settings which differed by 90°. Additionally, at each AOI and for each polarizer setting, transmission spectra of a bare substrate were obtained for corrections.

3.6.3 Real-time GIXD measurements

For a better understanding of time dependent changes in the optical spectra during growth of PFP:DIP-mixtures, *in situ* real-time GIXD experiments [161, 212, 213] were performed at the beamline MS-SurfDiffr ($\lambda = 0.9537$ Å) at the SLS, Villigen, Switzerland. For this purpose the films were prepared in a portable UHV-chamber. Fig. 3.10 shows the setup of such a chamber. The vacuum ($p \approx 1 \times 10^{-9}$ mbar) is maintained by a TMP and the film thickness and growth rate was monitored by a QCM. The chamber was equipped with two cells, containing PFP and DIP, respectively. The films were grown on a NtveSi substrate with T_{sub} kept constant at 300 K. The chamber is equipped with a Beryllium window which is transparent for X-rays and allows to follow the film growth in real-time with GIXD. GIXD scans were performed in a $q_{||}$-range from 1.6 Å^{-1} to 2.0 Å^{-1}. Each scan took 4 min and the growth rate was chosen to be 1 Å/min to yield a high time-resolution of 4 scans per ML. Doing so, GIXD scans at different film thicknesses were obtained. The observed peaks were fitted with Lorentzians using the programm Fityk [229] and the size of coherently scattering islands was determined from the peak FWHM using the

Scherrer-formula [211], with $K_s \approx 1$:

$$ls = \frac{2\pi K_s}{\text{FWHM}} \tag{3.7}$$

Chapter 4

Results and discussion I

4.1 Structure, morphology and mixing behavior

In this work binary blends of the three organic semiconductors PEN, PFP, and DIP have been investigated in all possible combinations. This allows a comparative study of the influence of the film structure (mixing and ordering behavior) and the strength of intermolecular interactions on the optical properties. Before the results of optical spectroscopy experiments are discussed, the mixing and ordering behavior of the three systems will be introduced, as reported in Refs. [36, 60, 127, 161, 176, 217, 230, 231].

4.1.1 Blends of PFP and PEN

The mixing and ordering behavior of PFP:PEN blends with different mixing ratios prepared at different substrate temperatures was studied in Refs. [60,127,161,230,232]. Here, only a short summary of the results will be given.

Mixtures of PFP and PEN are expected to exhibit strong intermolecular interactions due to the presence of fluorine in PFP and hydrogen in PEN and the corresponding quadrupole moments of opposite sign (see Sec. 2.2.2). In addition, the two molecules have almost identical steric properties, which further facilitates mixing on a molecular level.

In Fig. 4.1a GIXD data of PFP:PEN blends with different mixing ratios are shown [127]. As the films are polycrystalline, several in-plane Bragg-reflections can be observed. The Bragg-peaks, which are labeled with A - D, are at q_{xy} positions which do not coincide with Bragg-peaks of pure PFP or PEN [127]. Furthermore, in the equimolar mixture only these new peaks are observed, whereas in non-equimolar mixtures Bragg-peaks attributed to the phase of the excess compound *and* the new peaks A - D are found (Fig. 4.1a). This indicates mixing on a molecular level of PFP and PEN in the equimolar blend with the formation of a new crystal structure and phase separation between the intermixed crystal phase and the pure phase of the excess compound in non-equimolar mixtures [127].

Figure 4.1b shows the XRR data of different PFP:PEN blends. From the pronounced Kiessig-fringes it can be concluded that the mixed films are smoother than pure PFP or

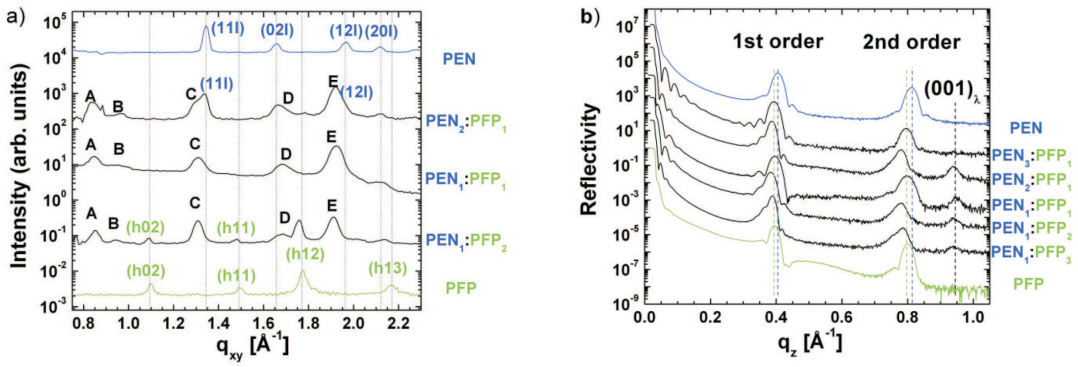

Figure 4.1: a) GIXD data and b) XRR data of PFP:PEN blends with different mixing ratios. Pictures taken from Ref. [127].

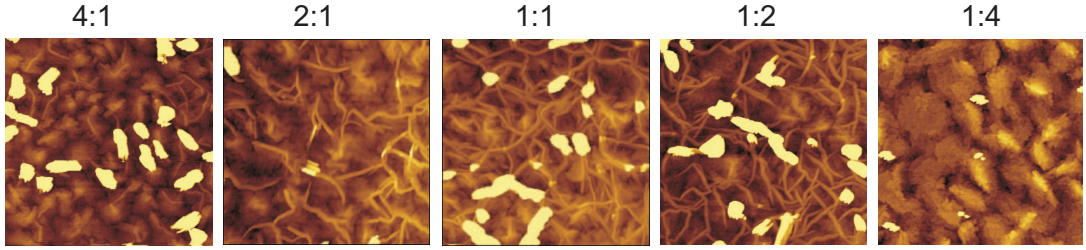

Figure 4.2: AFM images (area: 5 μm $\times$ 5 μm) of PFP:PEN blends with different mixing ratios. Note the changing amount of fiber-like structures with the mixing ratio.

pure PEN films and the PFP:PEN 1:4 blend shows the lowest roughness. This is also observed for PFP:DIP [231, 233] and for PEN:DIP [36], see respective sections.

Apart from the first order and the second order Bragg-peaks an additional Bragg-peak is observed in the XRR scans, which was attributed to domains consisting of molecules lying nearly parallel to the substrate surface (λ-orientation [127]), whereas the Bragg-peaks at lower q_z are assigned to domains consisting of molecules essentially standing upright on the substrate surface (σ-orientation [127]). The intensity of the $(001)_\lambda$-reflection depends on the mixing ratio, indicating that the nucleation of domains with λ-orientation is hindered in the presence of a PEN excess [127].

The morphology of the PFP:PEN blends was investigated using AFM (Fig. 4.2). Note the changing amount of fiber-like structures visible in the AFM images of the PFP:PEN 4:1, 2:1, 1:1 and 1:2 mixtures. These structures were attributed to the λ-orientation [127]. In agreement with the change in intensity of the $(001)_\lambda$-reflection in the XRR data, the surface coverage of the fibers is highest for the 2:1, 1:1 and 1:2 blends.

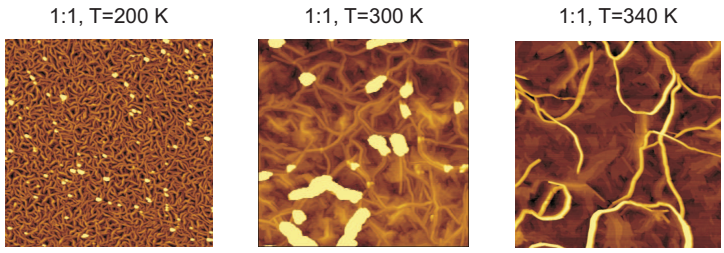

Figure 4.3: AFM images (area: 5 μm $\times$ 5 μm) of equimolar PFP:PEN blends prepared at different substrate temperatures T. Note the changing amount of fiber-like structures with T.

Apart from the dependence of the nucleation of domains in λ-orientation on the mixing ratio, it is also strongly influenced by the substrate temperature. For low substrate temperatures the nucleation of domains in λ-orientation is facilitated [127] and accordingly, the surface coverage of the fibers in the AFM images (Fig. 4.3) is highest for the equimolar blends prepared at substrate temperatures of $T = 200$ K. For blends prepared at a substrate temperature of $T = 180$ K (not shown) the fibers cover the whole area invesigated and the single fibers cannot longer be resolved by AFM.

In summary, blends of PFP and PEN exhibit mixing on a molecular level with the formation of a new mixed crystal structure and two orientations (σ- and λ-orientation), which differ in the tilt angle of the molecules relative to the substrate surface [127]. For non-equimolar mixing ratios a phase separation between the equimolar intermixed crystal phase and the pure film phase of the excess compound is observed [127].

4.1.2 Blends of PFP and DIP

The mixing and ordering behavior of PFP:DIP blends was investigated in Refs. [161, 176, 231]. In order to complete this study, XRR data of non-equimolar PFP:DIP blends and the corresponding AFM images were measured in the present work. The following section is based on Refs. [176, 233]. Similar to PFP and PEN, PFP and DIP are expected to exhibit strong intermolecular interactions due to their chemical composition, which favors intermixing on a molecular level. However, DIP is significantly larger than PFP and hence, the steric compatibility of the two compounds is lower compared with PFP and PEN.

Figure 4.4a shows the GIXD data of PFP:DIP blends with different mixing ratios [176]. Similar to PFP:PEN blends also for the equimolar PFP:DIP blend in-plane Bragg-reflections were observed at q_{xy} positions which do not coincide with the q_{xy} positions of reflections from the pure compounds. Hence, it was concluded that also PFP:DIP blends form an intermixed crystal phase with new unit cell parameters and mixing on a molecular level [176]. For non-equimolar mixing ratios a phase separation between the

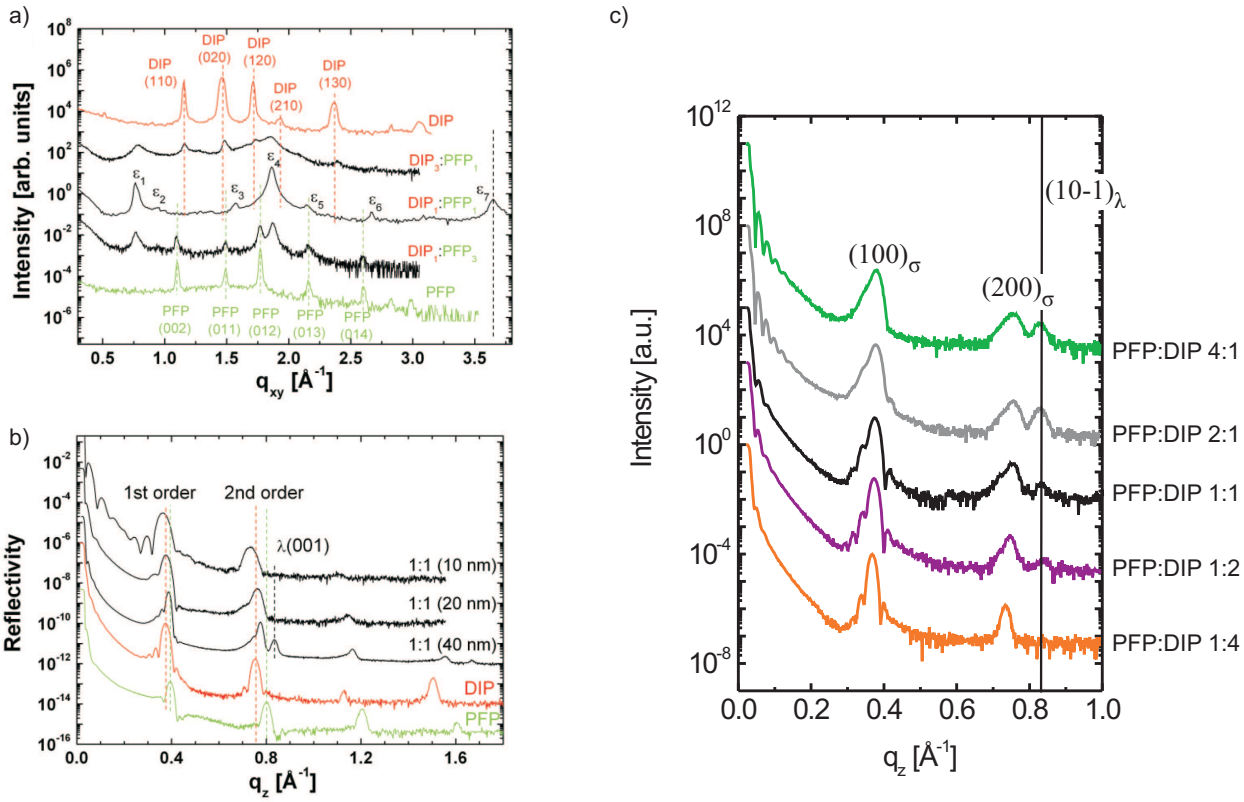

Figure 4.4: a) GIXD data and c) XRR data of PFP:DIP blends with different mixing ratios. The data are vertically offset for clarity. The straight line marks the Bragg-peak which was assigned to a phase of lying-down molecules [176]. Peak indexing is done according to Ref. [176]. b) XRR data of equimolar PFP:DIP blends of different film thicknesses. Pictures a) and b) taken from Ref. [176], c) taken from Ref. [233].

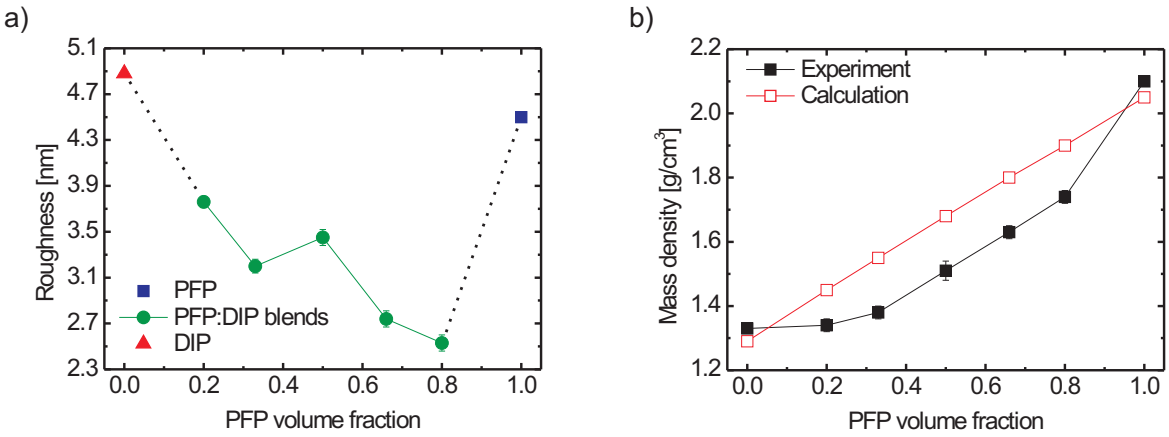

Figure 4.5: a) Roughness σ and b) mass density ρ_{exp}(black squares) resulting from the fit of the XRR data of PFP:DIP blends with different mixing ratios (Fig. 4.4 and Table 4.1). In a) σ of a pure PFP and a pure DIP film is also shown for comparison. In b) the red hollow squares denote the mass density ρ_{calc} calculated based on the unit cell volumes of PFP [60], DIP [87] and the equimolar PFP:DIP blend [176]. The error bars are in the range of the symbol size.

mixed crystal phase and the phase of the pure compound was observed [176].

In the XRR data (Fig. 4.4b and c) Bragg-peaks from two orientations can be observed. The peaks are indexed according to Ref. [176]. The data show that in the equimolar mixed films two types of domains can be distinguished by the molecular orientation: In the first type, the molecules are standing almost upright relative to the substrate (σ-orientation [176]). The second type consists of domains with nearly flat lying molecules and large mosaicity (λ-orientation [176]). Similar to the equimolar mixture, also in the XRR data of all non-equimolar mixtures the (100)- and (200)-reflection of the σ-orientation can be observed. Compared with the equimolar mixture the Bragg-peak positions are slightly shifted in the mixed films with non-equimolar mixing ratios. Since these blends exhibit a phase coexistence between a mixed and a pure film phase of the excess compound [176] the measured Bragg-peaks are composed of two Bragg-reflections, one stemming from the mixed film phase and the other one arising from the respective pure film phase, which can lead to a peak shift [127]. Using the GenX-software [216] the XRR data were fitted based on the Parratt formalism [214] for q_z near the total reflection egde ($q_z^{max} = 0.16$ Å^{-1}). In order to determine the film thickness, the roughness σ and the mass density ρ a model with three layers (*bulk Si-substrate* - SiO_2*-layer* ($d \approx 1.8$ *nm*) - *organic film*) was used. The fit results are compiled in Table 4.1.

Interestingly, the mixed films are smoother than the pure ones (see Fig. 4.5a). A similar

Mixing ratio	σ [nm]	ρ_{exp} [g/cm^3]	ρ_{calc} [g/cm^3]
Pure PFP	4.50	2.10	2.05
PFP:DIP 4:1	2.53	1.74	1.90
PFP:DIP 2:1	2.74	1.63	1.80
PFP:DIP 1:1	3.43	1.51	1.68
PFP:DIP 1:2	3.20	1.38	1.55
PFP:DIP 1:4	3.76	1.34	1.45
Pure DIP	4.88	1.33	1.29

Table 4.1: Roughness σ and mass density ρ_{exp} for the different samples (pure PFP, pure DIP, five PFP:DIP blends) determined by fits of the XRR data. For comparison the calculated mass density ρ_{calc} based on the molecular weight and the unit cell volumes of PFP [60], DIP [87] and the equimolar PFP:DIP blend [176] is also noted.

phenomenon was already observed for mixtures of PFP:PEN [127] and PEN:DIP [36]. With increasing relative volume fraction of DIP the roughness increases, as well as the coherently scattering volume of the film. In contrast, the mass density ρ_{exp}, determined from the fit of the XRR data, is decreasing with increasing volume fraction of DIP. This trend is in agreement with the calculated mass densities ρ_{calc} for the various mixtures based on the molecular weight and the unit cell volumes of PFP [60], DIP [87] and the equimolar PFP:DIP blend [176] (Table 4.1 and Fig. 4.5b).

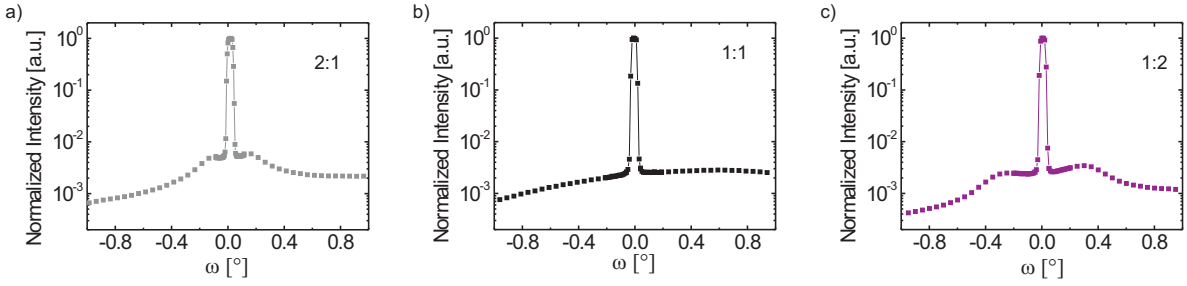

Figure 4.6: Rocking scans at the $\sigma(100)$ reflection for three different mixing ratios of PFP:DIP, with a sharp peak (FWHM $(0.05 \pm 0.01)^\circ$) and a diffuse scattering signal. Mixing ratios PFP:DIP: a) 2:1, b) 1:1 and c) 1:2.

The Bragg-peak at q_z=0.836 Å^{-1} was assigned to the (10-1)-reflection of the λ-orientation of the mixed crystal phase, which would correspond to nearly flat lying molecules [176]. Interestingly, the intensity of this peak changes significantly with the

Mixing ratio	D [nm]	Island size [nm]
PFP:DIP 2:1	480	440
PFP:DIP 1:2	350	280

Table 4.2: Characteristic length scale D resulting from the distance of the side maxima in diffuse X-ray scattering and island size in PFP:DIP mixtures determined by AFM.

mixing ratio, indicating that the nucleation of domains consisting of molecules in the λ-orientation is facilitated in mixtures containing more PFP. A similar behavior was found in blends of PFP:PEN [127]. The post growth studies were completed by rocking scans on samples with three different mixing ratios PFP:DIP 2:1, 1:1, 1:2. Independent of the mixing ratio the rocking scans show a sharp peak with a FWHM of $(0.05 \pm 0.01)^\circ$, which is related to the mosaicity of the film, and a diffuse scattering signal. Interestingly, for the non-equimolar mixing ratios two side maxima can be observed (Fig. 4.6a and c). The maxima result from surface modulations of a characteristic length scale D, which can be calculated as [234, 235]:

$$D = \frac{2\pi}{\frac{4\pi}{\lambda}\ sin(\frac{2\Theta}{2})\ sin(\omega)} \tag{4.1}$$

with $\lambda = 0.9537$Å. It is noted that due to the broad side maxima it is difficult to determine the exact ω-positions, leading to a large error bar for the calculated D-values. However, Eq. (4.1) yields $D \approx 350$ nm for the PFP:DIP 1:2 mixture ($\omega \approx \pm\ 0.30\ ^\circ$) and $D \approx 480$ nm for the PFP:DIP 2:1 ($\omega \approx \pm\ 0.18\ ^\circ$). Based on the comparison of these results with the film morphology measured using AFM (Fig. 4.7) the distance of the side maxima can be attributed to the island size, see Table 4.2.

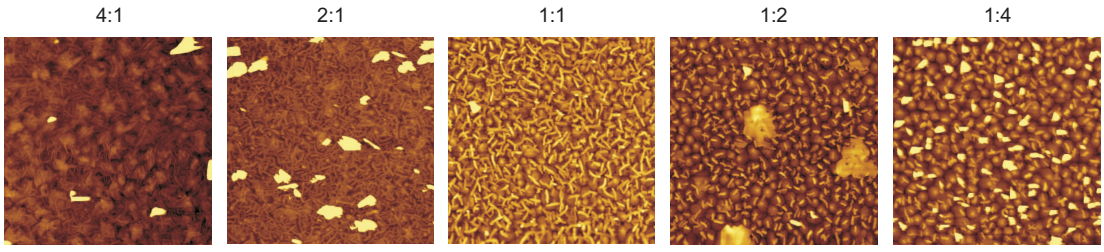

Figure 4.7: AFM images (area: 5 μm $\times$ 5 μm) of PFP:DIP blends with different mixing ratios. The origin of the amorphous structures visible in the AFM picture of the PFP:DIP 1:2 blend is unclear.

For the equimolar mixture no side maxima are observed, which may be due to a smaller island size compared with the non-equimolar mixtures. The side maxima can be expected

at higher ω compared with the PFP:DIP 2:1 mixture and are probably too low in intensity to be observed.

Summarizing this section, blends of PFP and DIP exhibit similar to PFP:PEN blends mixing on a molecular level with the formation of a new crystal structure. For non-equimolar blends phase separation between the equimolar intermixed crystal phase and the pure phase of the excess compound is observed [176].

4.1.3 Blends of PEN and DIP

Finally, the mixing and ordering behavior of PEN:DIP blends will be discussed. These results have been published in Ref. [36].

PEN and DIP exhibit high chemical similarity, since both are composed of carbon and hydrogen. Therefore, no strong intermolecular interactions are expected. Additionally, similar to PFP and DIP, the steric compatibility of PEN and DIP is low.

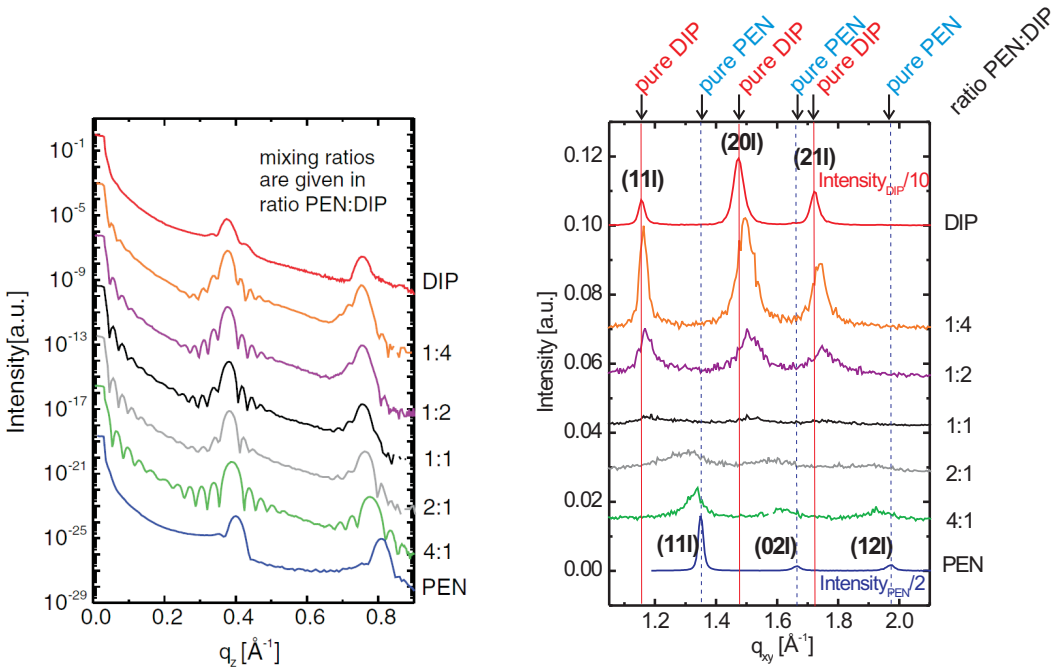

Figure 4.8: XRR data (left) and GIXD scans (right) for PEN:DIP blends with different mixing ratios. Pictures taken from Ref. [36].

The results of XRR and GIXD experiments on PEN:DIP blends are shown in Fig. 4.8. The most surprising finding is the almost complete disappearance of in-plane Bragg-reflections for the equimolar PEN:DIP blend indicating a vanishing long range order in-plane [36]. From the fact that there are no Bragg-reflections observable in the GIXD scans of the equimolar PEN:DIP blend which can be assigned to PEN or DIP, it can be concluded that there is no phase separation between PEN and DIP but mixing on a

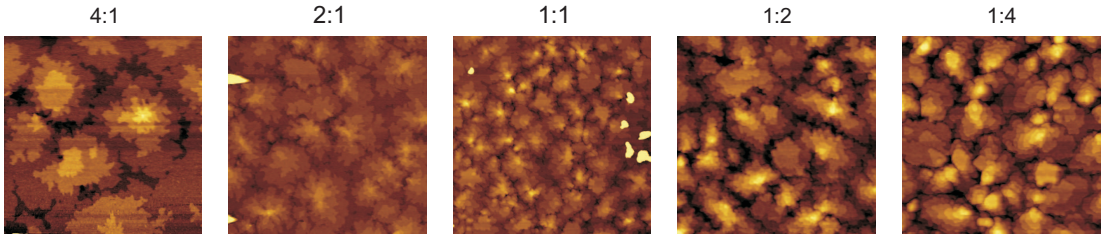

Figure 4.9: AFM images (area: 5 μm $\times$ 5 μm) of PEN:DIP blends with different mixing ratios. Data measured in collaboration with A. Aufderheide [217].

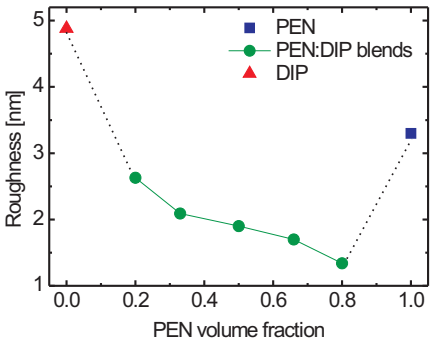

Figure 4.10: Roughness σ as a function of PEN volume fraction, determined from the fit of the XRR data for pure PEN, pure DIP and the PEN:DIP blends. Data measured and analyzed by A. Aufderheide [217]. The error bars are in the range of the symbol size.

molecular level [36].

For the non-equimolar PEN:DIP blends in-plane Bragg-peaks at q_{xy} positions slightly shifted from those of the respective excess compound are observed, which are significantly broadened for most of the mixing ratios. This indicates that in non-equimolar blends minority molecules randomly occupy sites in a lattice formed by the excess compound. The resulting defects in the lattice lead to the observed broadening of the peaks.

The XRR data show a good structural order perpendicular to the substrate surface which can be seen from the Bragg-reflections observable with pronounced Kiessig- and von Laue-fringes. In particular, the sample with a PEN:DIP mixing ratio of 4:1 exhibits a very low surface roughness and is coherently scattering over almost the whole film thickness [36]. Similar to blends of PFP:PEN and PFP:DIP the mixed films are smoother than the pure films (Fig. 4.10).

Combining the results of GIXD and XRR experiments, the mixing and ordering behavior of PEN:DIP blends can be described. While the two compounds mix on a molecular level the ordering behavior differs for the equimolar and the non-equimolar blends. For the equimolar mixture an ordering behavior similar to the smectic C phase of liquid crystals is found which is characterized by vanishing in-plane order and good structural order

perpendicular to the substrate surface [236]. For non-equimolar blends there is a statistical replacement of lattice sites by minority molecules in a lattice formed by the excess compound [36].

4.1.4 Rationalization of the observed mixing and ordering behavior

The mixing and ordering behavior observed for the three different mixed systems can be rationalized by extending the mean-field model introduced in Sec. 2.4.1.2, taking the strength of intermolecular interactions and the degree of steric compatibility of the molecules into account [36].

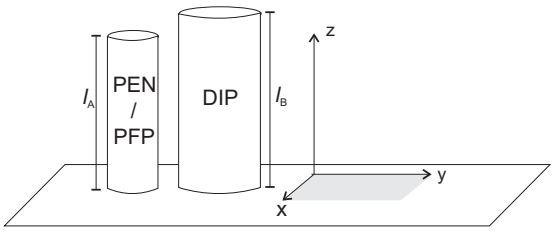

Figure 4.11: Definition of the directions used in the following discussion of anisotropic interactions.

The regular solution model discussed in Sec. 2.4.1.2 provides a first approach to rationalize the results for mixtures of OSCs [29]. However, most OSCs can only in a first approximation be described as spheres and, therefore, the validity of this model is limited. The model does not take into account anisotropies in the interparticle interactions as they may occur in systems with lower symmetry. For such systems additional issues arise and one has to distinguish *mixing* and *ordering* behavior. In the following *mixing behavior* will refer to the question, whether one specific particle is favorably surrounded by similar or dissimilar particles or whether the different particles are distributed statistically. *Ordering behavior* will refer to the question whether the particles in the mixture exhibit short-range or long-range order or whether neither of the two is observed.

The molecules discussed in this work can in a good approximation be described as cylinders with different diameter and height and are known to stand almost upright on the substrate for many preparation conditions. Due to the rotation symmetry of upright standing cylinders only two main directions relative to the substrate surface have to be considered to take anisotropies in the intermolecular interactions into account, namely the plane parallel to the sample surface (described by the xy-plane, in the following referred to as the *in-plane* or *xy-component*) and the direction perpendicular to the substrate surface (the *out-of-plane* or *z-component*). Fig. 4.11 shows a sketch of the substrate

surface plane with the cylinders representing the different compounds discussed and the two main directions for the anisotropic interactions.

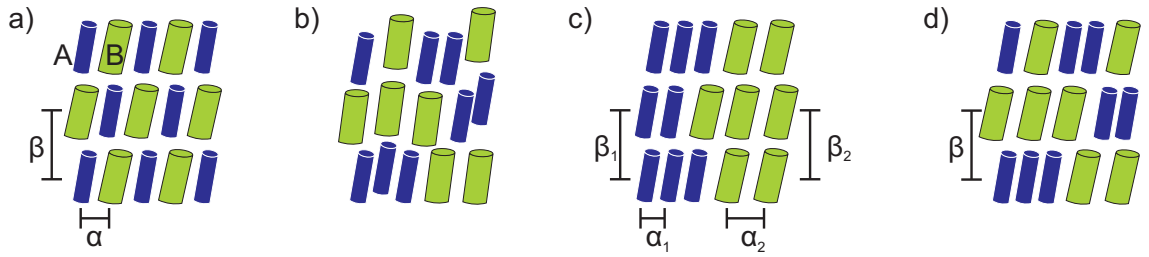

Figure 4.12: Mixing scenarios of binary mixtures of two different kinds of cylinders: a) Intermixing with a formation of a new crystal structure. b) Intermixing without long-range order in-plane and out-of-plane. c) Phase separation. d) Intermixing without long-range order in-plane, but with well defined order out-of-plane.

The following extension of the mean-field model for interacting particles was developed together with A. Aufderheide, Dr. J. Novák and Dr. R. Banerjee, inspired by Refs. [171, 172] and published in Ref. [36]. There, mixtures of two cylinders A and B, differing in height and diameter, are considered. Since the symmetry of the cylinders is lower compared with spheres, the interparticle interactions are anisotropic, i.e. different for the direction parallel and perpendicular to the substrate surface. In the extended model this is taken into account by introducing an anisotropic interaction parameter χ, which splits into two components χ_{xy} and χ_z. Additionally, mixing two cylinders of different height and diameter will induce strain and lattice deformations in the mixed system, which is included in the model via a strain energy term E^s. E^s depends on the elastic constant tensor $\hat{C}$, the tilt angles θ_A and θ_B of the cylinders and their length ratio $\beta_\alpha = l_{A\alpha}/l_{B\alpha}$ in the directions $\alpha = [xy, z]$, with $\beta_\alpha \approx 1$ and $\beta_\alpha \gtrless 1$ indicating high and low steric compatibility, respectively. Similar to χ, E^s splits into two components E^s_{xy} and E^s_z.

The free energy ΔF describing the mixing *and* ordering behavior of a mixed system of interacting cylinders can then be written as:

$$\begin{aligned}\Delta F =& \frac{1}{2} k_{\mathrm{B}} T \{ x_{\mathrm{A}} \ln x_{\mathrm{A}} + x^\star_{\mathrm{A}} \ln x^\star_{\mathrm{A}} + x_{\mathrm{B}} \ln x_{\mathrm{B}} + x^\star_{\mathrm{B}} \ln x^\star_{\mathrm{B}} \\ &+ \frac{1}{2} [\chi_{\mathrm{xy}} (x_{\mathrm{A}} x_{\mathrm{B}} + x^\star_{\mathrm{A}} x^\star_{\mathrm{B}}) + \chi_{\mathrm{z}} (x_{\mathrm{A}} x^\star_{\mathrm{B}} + x^\star_{\mathrm{A}} x_{\mathrm{B}})] \} \\ &+ E^{\mathrm{s}}_{xy}(\hat{C}, \beta_{xy}, \theta_A, \theta_B) + E^{\mathrm{s}}_z(\hat{C}, \beta_z, \theta_A, \theta_B), \end{aligned} \tag{4.2}$$

where x_μ and $x^\star_\mu$ stand for molar concentrations in alternate layers along the out-of-plane direction. The interplay between three contributions to ΔF determines the behavior of the system under mixing. These are *i) the contribution of entropy*, which favors statistical mixing, *ii) contributions of intermolecular interactions*, which, depending on the interaction parameter χ [171,172] (see Eq. 2.12) will either facilitate intermixing or phase separation, and *iii) the contribution of strain* (E_s), induced by the different steric prop-

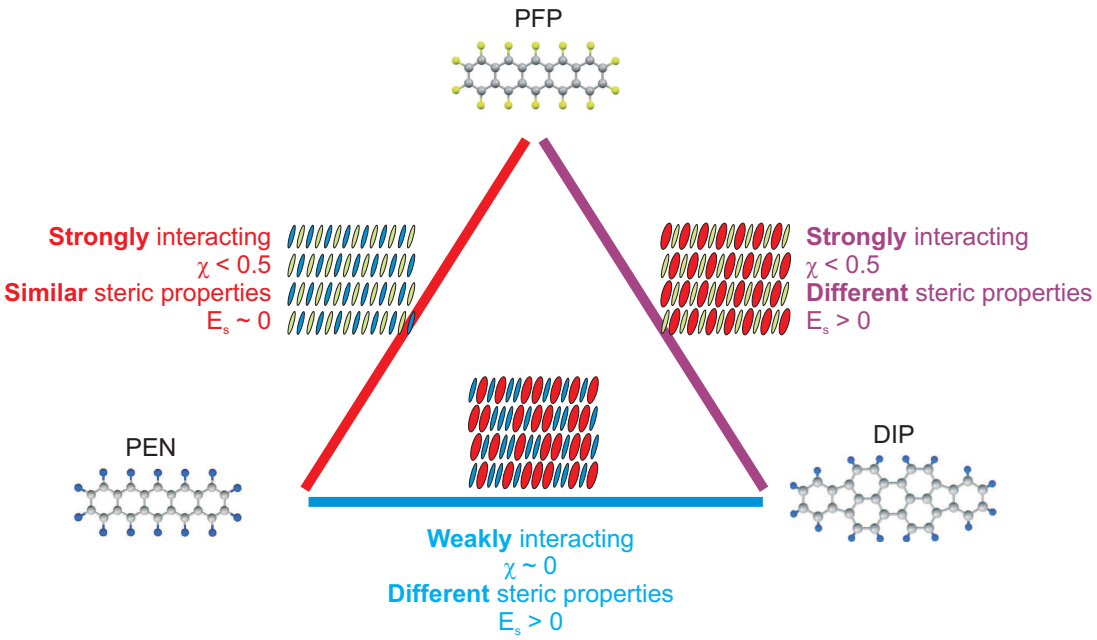

Figure 4.13: The triangle on structure and interactions, built from PFP, PEN and DIP.

erties, which is minimized either by the formation of a new crystal structure or by phase separation.

This model allows to rationalize the observed mixing and ordering behavior for the three different mixed systems. PFP:PEN blends are a strongly interacting system with high steric compatibility of the two compounds. Therefore, pairing of PFP and PEN is energetically favorable ($\chi < 0.5$) and not hindered by strain which might be induced by steric incompatibility ($E_s \approx 0$ due to the almost identical steric properties). The contribution of the strong intermolecular interactions dominates over the other two terms leading to a new intermixed crystal structure observed.

For PFP:DIP blends the intermolecular interaction is comparably strong and pairing of PFP and DIP is favored ($\chi < 0.5$). However, the steric incompatibility of the two compounds is significantly higher ($E_s \neq 0$). The ordering behavior is determined by the interplay between the steric incompatibility (and the resulting strain energy, favoring phase separation or the formation of a new crystal structure) and the intermolecular interactions (which favor pairing). Obviously, the intermolecular interaction dominates over the strain term and an intermixed crystal structure is still energetically favorable.

Finally, for the weakly interacting system PEN:DIP there is no preference for pairing of PEN and DIP ($\chi \approx 0$) and the ordering behavior is determined by the interplay between entropy and steric incompatibility ($E_s \neq 0$). While the entropy contribution leads to statistical mixing, the strain energy due to steric incompatiblity prevents in case of the equimolar mixture long-range order in-plane, obviously not being high enough to induce

phase separation. Perpendicular to the substrate surface the strain energy is reduced by the formation of ordered layers [36].

The differences in steric compatibility and strength of intermolecular interactions in the three systems will not only influence the film structure but also the optical properties, which highly depend on the structural order. This effect was the main topic of the present work and will in the following be investigated in detail, concentrating on ϵ_2, which describes the optical absorption of the systems.

Related to the structural properties, all mixtures studied here exhibit uniaxial anisotropic optical properties (see Fig. 2.1), which can be described by two dielectric functions $\epsilon_i = \epsilon_{i,1} + i\epsilon_{i,2}$, $(i = xy, z)$, where ϵ_{xy} describes the optical properties in the substrate plane and ϵ_z the optical properties perpendicular to the substrate plane.

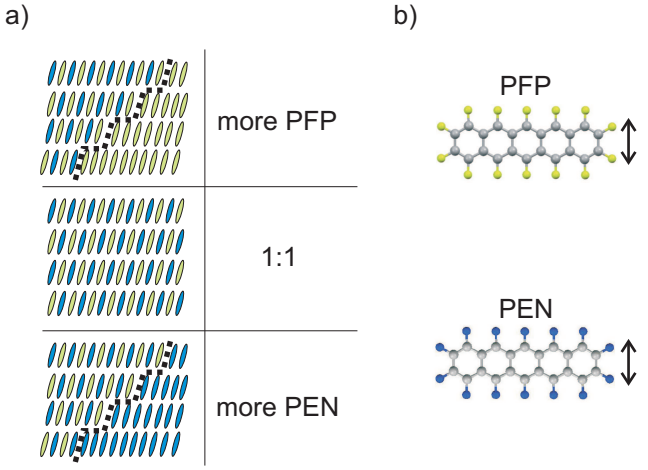

Figure 4.14: a) Schematic mixing scenarios for PFP:PEN depending on the mixing ratio. b) Sketches of the molecules. The arrows indicate the orientation of the transition dipole moments μ of the respective HOMO-LUMO transitions.

4.2 Absorption spectra of PFP:PEN blends

Blends of PFP and PEN are a model system for donor-acceptor complexes due to their high steric compatibility, their strong intermolecular interactions and the resulting mixing and ordering behavior, as described in the previous section. Hence, mixtures of PFP and PEN are perfectly suited to study the influence of intermolecular interactions on the optical properties of blends. The results discussed in this section have been published in Refs. [74, 237].

4.2.1 $\epsilon_{2,xy}(E)$

Figure 4.15 shows $\epsilon_{2,xy}(E)$ for the different mixing ratios of PFP and PEN, obtained with variable angle SE (VASE) applying a multi-sample analysis [139, 238]. Clear evidence for strong intermolecular coupling between PFP and PEN is the observation of a peak at $E_c = 1.6$ eV which does not arise from pure PEN or pure PFP. This new peak is present in all mixtures except the one with mixing ratio PFP:PEN 4:1. A related peak can also be observed in photoluminescence measurements [75].

A possible origin of this peak is a charge transfer (CT) in the excited state between PFP and PEN. The theoretical transition energy for the CT was calculated to be 1.73 eV, which has to be corrected for Coulomb interaction between the electron and the hole forming the CT state across the PEN-PFP interface [75]. Taking these corrections into account the experimentally determined energy position of 1.6 eV is in nice agreement with the calculations and the new peak can be assigned to CT between PFP and PEN (Fig. 4.16).

In the following further details of the spectra of the mixed films will be discussed. For clarity this will be done separately for blends with mixing ratios close to the equimolar mixture (2:1 and 1:2, see Fig. 4.15a) and the other two ratios (4:1 and 1:4, see Fig. 4.15b).

From Fig. 4.15a it can be seen clearly that the mixed film spectra are not a linear

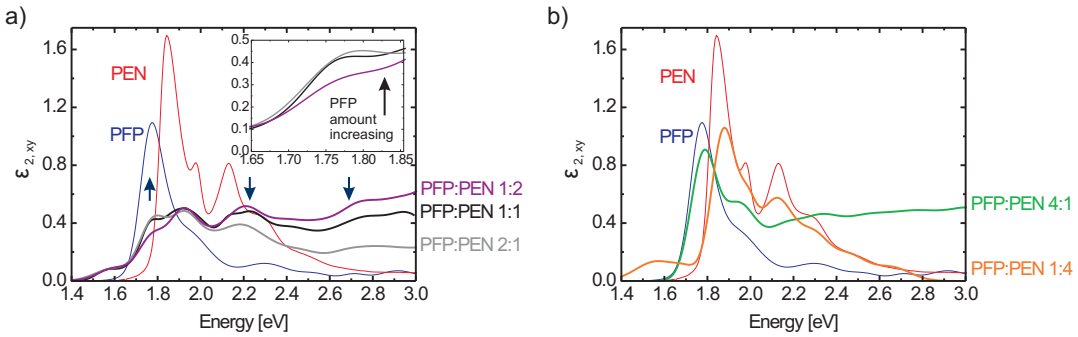

Figure 4.15: $\epsilon_{2,xy}(E)$ of PFP:PEN blends with different mixing ratios: a) 1:1, 2:1 and 1:2 (thick solid lines). The arrows are indicating the changes in distinct spectral regions with increasing amount of PFP. The inset shows a close-up of the spectral region 1.65 eV to 1.85 eV to point out the changes within this region. b) 4:1, 1:4 (thick solid lines). For comparison the pure film spectra of PFP and PEN (thin solid lines) of Ref. [59] are also shown. The error of the absolute intensities is below 10%. Taken from Ref. [74].

Mixing ratio	E_c [eV]	E_1 [eV]	E_2 [eV]	E_3 [eV]	E_4 [eV]
Pure PFP	-	1.75	1.94	2.28	2.48
PFP:PEN 4:1	-	1.78 ±0.01	1.94 ±0.01	2.15 ±0.03	2.31 ±0.09
PFP:PEN 2:1	1.60 ±0.01	1.77 ±0.01	1.91 ±0.01	2.16 ±0.01	2.46 ±0.05
PFP:PEN 1:1	1.60 ±0.01	1.77 ±0.01	1.92 ±0.01	(*) 2.20 ±0.03	2.41 ±0.09
PFP:PEN 1:2	1.58 ±0.01	1.77 ±0.01	1.92 ±0.01	2.20 ±0.04	2.46 ±0.06
PFP:PEN 1:4	1.60 ±0.02	1.88 ±0.01	1.98 ±0.01	2.12 ±0.01	2.31 ±0.07
Pure PEN	-	1.85	1.97	2.11	2.28

Table 4.3: Energy positions of the most pronounced peaks in the mixed films studied. The peak positions for PFP and PEN are obtained from Ref. [59]. E_c denotes the energy position of the first peak observable in the spectra of the mixed films that can be assigned to charge transfer. E_1 describes the energy position of the HOMO-LUMO transition of the pure component film spectra and the energy position of the first strong peak in the mixed film spectra, respectively. (*) For the 1:1-mixture one can discern two maxima at 2.18 and 2.24 eV; in the table the mean is quoted for comparison and consistency. Table taken from Ref. [74].

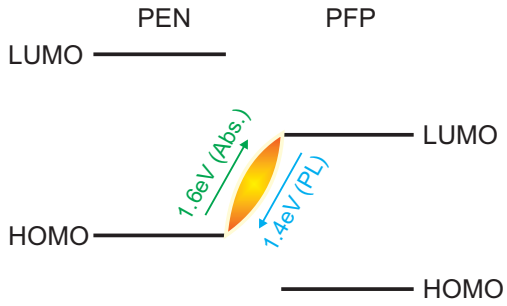

Figure 4.16: Possible scheme of the CT transition in absorption (Abs.) and photoluminescence (PL) between PEN and PFP. Energy position of the CT peak in PL and picture modified from [75].

combination of the single film spectra, which suggests strong intermolecular coupling [30, 180]. The peaks observed are relatively broad compared with the pure film spectra and exhibit no clearly discernible vibronic progression. The shapes of the absorption spectra resemble each other, but there are changes observable with increasing amount of PFP, see arrows in Fig. 4.15a. The feature at 1.77 eV becomes more pronounced going from a mixing ratio for PFP:PEN of 1:2 to 1:1 and 2:1 (inset in Fig. 4.15a). As its energy position almost matches the HOMO-LUMO transition of pure PFP, it can be assigned to this compound. On the other hand the feature at 2.2 eV decreases with increasing amount of PFP. Following the same argument and considering that PEN absorbs in this spectral region more strongly than PFP, this absorption band can tentatively be assigned to arise from PEN. The shape of $\epsilon_{2,xy}(E)$ changes strongly when the mixing ratio is close to the single component films (PFP:PEN 4:1 or 1:4, see Fig. 4.15b). In the energy range from 1.7 to 2.1 eV the shape of the spectra of the respective more abundant molecule is clearly dominating, so that the PFP:PEN 4:1 mixture gives a spectral shape essentially resembling pure PFP films and the 1:4-mixture the one of pure PEN. Nevertheless, even here the spectral shape is changed due to inhomogeneities in the film, resulting in a broadening of the peaks which can be deduced from the comparison of the mixed film spectra with the respective single film spectra in Fig. 4.15b. Interesting features are the first two pronounced peaks in the spectrum of pure PFP that are assigned either to a vibronic progression [59,128] or two Davydov-components of the HOMO-LUMO transition of PFP [128]. The peak at 1.94 eV is more intense in the mixed film spectrum with PFP as abundant molecule compared with the pure film spectrum, indicating differences in the molecular arrangement or in the intermolecular interactions. Except for the CT peak at 1.6 eV which is clearly not related to PFP or PEN, the first peak in $\epsilon_{2,xy}(E)$ of the mixed films is significantly blue shifted compared with pure PFP or PEN, see Table 4.4. This is probably related to the change in the polarizability of the intermolecular environment due to the formation of the new crystal structure and the presence of a second compound compared with the pure films.

PFP:PEN	4:1	2:1	1:1	1:2	1:4
ΔE [meV]	30	20	20	20	30

Table 4.4: Shift ΔE of the first peak (except the CT peak) in $\epsilon_{2,xy}(E)$ of the blends relative to the HOMO-LUMO transition of pure PFP (for mixing ratios PFP:PEN 4:1, 2:1, 1:1, 1:2) and the HOMO-LUMO transition of pure PEN (for the mixing ratio PFP:PEN 1:4).

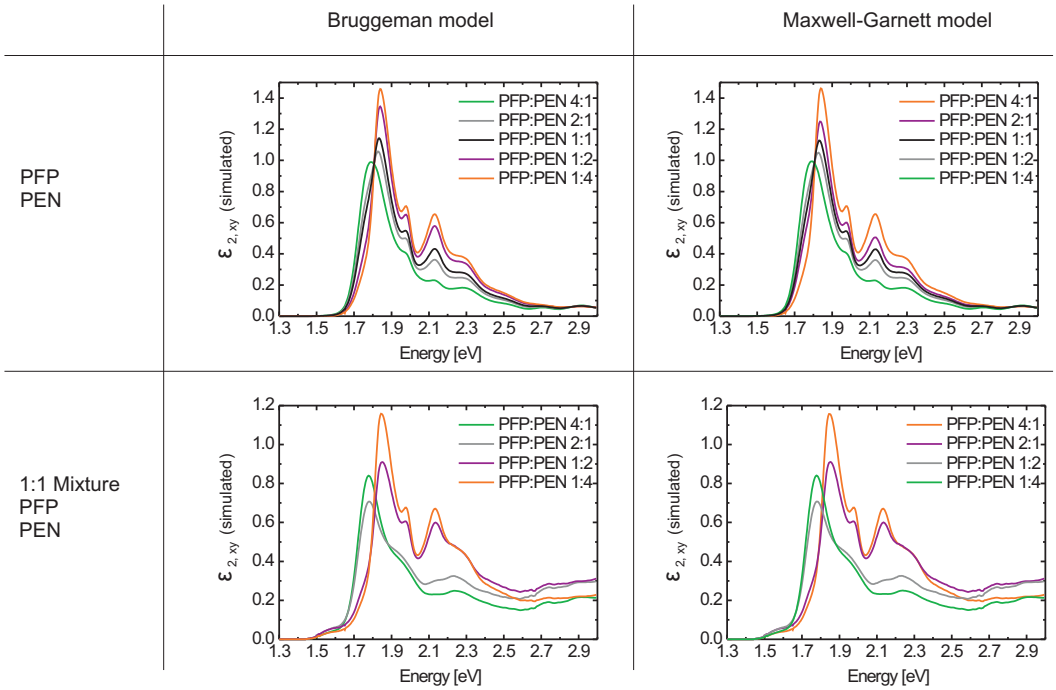

Figure 4.17: Calculated $\epsilon_{2,xy}^{eff}(E)$ for different mixing ratios of PFP:PEN using two different EMA models (see Sec. 2.4.2.1). Left column: Bruggeman model. Right column: Maxwell-Garnett model. Upper row: Based on $\epsilon_{2,xy}(E)$ of the pure compounds [59]. Lower row: Based on $\epsilon_{2,xy}(E)$ of the pure compounds and the equimolar mixture. For a detailed explanation see text.

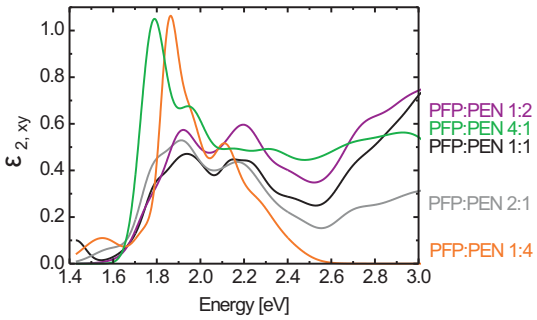

Figure 4.18: $\epsilon_{2,xy}(E)$ of the films with different mixing ratios measured using DRS. The comparison with the VASE data (Fig. 4.15) shows only small differences, which are probably due to photo-oxidation. Picture taken from Ref. [74].

4.2.2 Non-linear mixing effects

For two intermixing materials there are different possibilities to describe the effective dielectric function of the mixture without including intermolecular coupling effects. In the following two models for non-linear mixing (Maxwell-Garnett model [181,183] and the Bruggeman model [181,182], see Sec. 2.4.2.1) are tested, describing the effective dielectric function of the mixture with an effective medium approximation. Figure 4.17 (upper row) shows $\epsilon_{2,xy}^{eff}(E)$ calculated for different PFP:PEN mixtures based on $\epsilon_{2,xy}(E)$ of the pure compounds. It can be seen clearly that the models do not describe the experimental data. Hence, it can be concluded that besides the new peak at $E_c = 1.6$ eV, further relevant features result from intermolecular coupling.

For non-equimolar mixing ratios it is known from X-ray diffraction investigations [127] that there is phase separation between the intermixed phase (with mixing ratio PFP:PEN 1:1) and the pure phase of the excess compound. Therefore, it was tested, whether $\epsilon_{2,xy}(E)$ of blends with non-equimolar mixing ratios can be described by a combination of $\epsilon_{2,xy}(E)$ of the PFP:PEN 1:1 mixture and $\epsilon_{2,xy}(E)$ of the respective excess compound (see Fig. 4.17, lower row). While the CT peak is now also observed for the calculated $\epsilon_{2,xy}^{eff}(E)$ the shape of the spectra differs still significantly from the experimental data, in particular for mixing ratios PFP:PEN 2:1 and 1:2. This leads to the conclusion that more elaborated models have to be used in order to theoretically describe the optical properties of PFP:PEN blends due to the strong intermolecular interactions in these systems.

4.2.3 Surface roughness and chemical inhomogeneities

Besides intermolecular interactions the roughness of the film surface may influence the spectral shape. In order to investigate the possible influence of scattering from rough surfaces on $\epsilon_{2,xy}(E)$ of the mixed films in particular for spectral regions above 2.4 eV, spectra obtained using DRS and VASE were compared. As VASE measures the change in the polarization state of polarized light reflected from the sample, it is affected differently by rough surfaces or inhomogeneities in the film than DRS, which is sensitive to

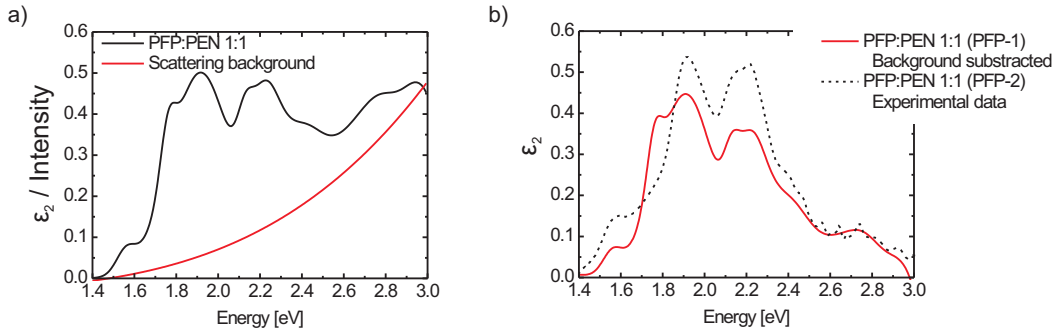

Figure 4.19: a) $\epsilon_{2,xy}(E)$ of an equimolar PFP:PEN mixture as shown in Fig. 4.15 (black line) and a $1/w^4$ background (red line). b) $\epsilon_{2,xy}(E)$ after substraction of the $1/w^4$ background (solid red line) and experimentally determined $\epsilon_{2,xy}(E)$ of an equimolar PFP:PEN mixture containing PFP-2 (black dotted line).

the absolute intensity. VASE is influenced by depolarization effects, whereas scattering decreases the reflected intensity measured with the DRS setup and, therefore, may cause artificial absorption features without pronounced structure in the spectra.

Figure 4.18 shows the spectra of the different mixing ratios of PFP and PEN measured using DRS. Due to the normal incidence geometry of the DRS setup only $\epsilon_{2,xy}(E)$ is probed. The data obtained using DRS are in good agreement with the results of VASE, although minor differences can be observed. These differences could partly be caused by photo-oxidation [239], but may also be due to practical limitations such as the spectral range of the light source used in the DRS experiment. Comparing both optical techniques, similar positions of the peaks, comparable line shapes, and an analogous behavior with changing relative amount of PEN and PFP are observed. Independent of the measurement technique, peaks above 2.4 eV were observed, leading to the conclusion that these features cannot solely be due to scattering effects.

After the publication of Ref. [74], containing the data discussed in this section, PFP from a different batch (PFP-2) was used for all further measurements. Surprisingly, this influenced the shape of the spectra for spectral regions above 2.4 eV. Figure 4.19a shows $\epsilon_{2,xy}(E)$ of an equimolar PFP:PEN blend, which contained PFP of the first batch (PFP-1). In order to test influences of scattering, a $1/w^4$ background (also shown in Fig. 4.19a) was substracted from these data. The result of the substraction is shown in Fig. 4.19b (red solid line) in comparison with $\epsilon_{2,xy}(E)$ of an equimolar PFP:PEN mixture containing PFP-2 (dotted line). Besides the small peak at 1.77 eV in the PFP-1:PEN blend which is probably due to a small PFP excess, the shape of the spectra is in good agreement regarding the energy position of the peaks and their relative intensities. In both spectra shown in Fig. 4.19b a peak around 2.7 eV can clearly be observed supporting the previous conclusion that not all of the peaks observed in the PFP-1:PEN mixtures above 2.4 eV

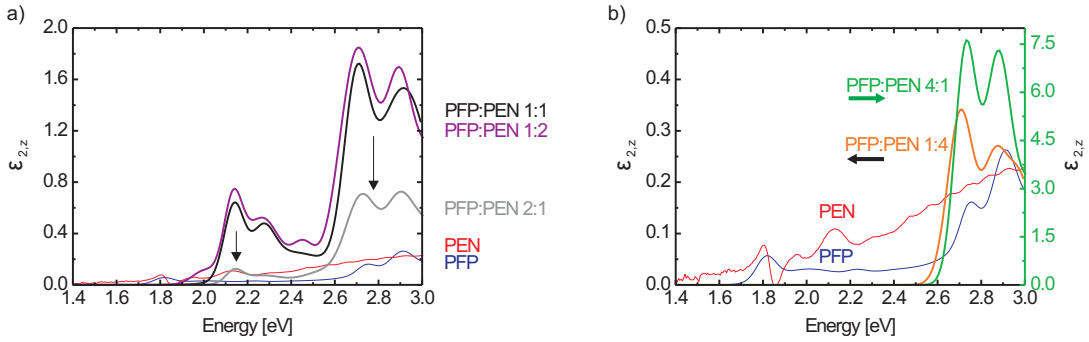

Figure 4.20: $\epsilon_{2,z}(E)$ of the films for different mixing ratios: a) PFP:PEN 1:1, 2:1 and 1:2 (thick solid lines). The arrows indicate changes with increasing amount of PFP. b) PFP:PEN 1:4 (thick solid line, left y-axis) and 4:1 (thick solid line, right y-axis). Note that the absolute amplitudes of the peaks depend on uncertainties in the film thickness d used in the analysis, while d was determined using X-ray reflectivity. The uncertainty of the absolute intensity of $\epsilon_{2,z}(E)$ is at maximum $\sim 50\%$. The relative error in intensity is below 10%. For comparison the pure film spectra of PFP and PEN (thin solid lines, left y-axis) similar to Ref. [59] are also shown. Picture taken from Ref. [74].

are due to scattering. However, chemical inhomogeneities obviously influence the overall shape of the spectra significantly, leading to the conclusion that in strongly interacting systems such as PFP:PEN, impurities are crucial for the optoelectronic properties, which is an effect already well-known for anorganic systems (see e.g. Ref. [240]). It is noted that none of the previous or following conclusions is influenced by these considerations as the CT peak and all other peaks discussed are also observed in the mixed films containing PFP-2 with only slightly differing relative intensities.

4.2.4 $\epsilon_{2,z}(E)$

So far only $\epsilon_{2,xy}(E)$ was discussed. Performing a multi-sample analysis [139] also $\epsilon_{2,z}(E)$ was determined. The results are shown in Fig. 4.20 and reveal pronounced influence of the intermolecular interactions on the spectra. The features at 2.7 and 2.9 eV observable for all mixing ratios can be related to PFP, since pure PFP exhibits an absorption feature in this energy range with comparable shape but less intense, as Fig. 4.20a and b show. As $\epsilon_{2,z}(E)$ is much more affected by errors in the film thickness than $\epsilon_{2,xy}(E)$, the development of the absolute intensities could be due to increased disorder in the film and will not be discussed in detail. Apart from the peaks at 2.7 and 2.9 eV there are the features in the energy range from 2.14 to 2.44 eV, which can only be observed for the mixing ratios 1:1, 2:1 and 1:2 (see Fig. 4.20a), but which are missing for the 4:1 and 1:4 mixtures (Fig. 4.20b).

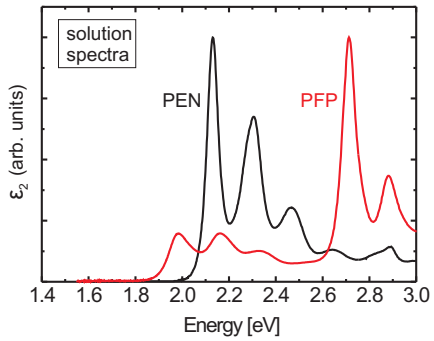

Figure 4.21: $\epsilon_2(E)$ of PFP and PEN measured in solution. Data from Ref. [59].

Since the intensity and the shape of these peaks depend more strongly on the relative amount of PEN and PFP than any of the features in $\epsilon_{2,xy}(E)$, it can be speculated that these peaks are caused by intermolecuar interactions between PEN and PFP.

Comparing $\epsilon_{2,z}(E)$ with solution spectra of the single compounds (see Fig. 4.21 and Ref. [59]), remarkable similarities can be observed. As the solution spectra include all components of the dielectric tensor, the observed similiarities could give a hint for structural changes and a possible reorientation of molecules in the mixed films [60, 127].

4.2.5 Varying the substrate temperature

4.2.5.1 NEXAFS experiments

As described in Sec. 4.1.1, in blends of PFP and PEN domains with molecules in two different orientations can be found, the σ-orientation with nearly upright standing molecules and the λ-orientation with nearly flat lying molecules [127]. Although no quantative value of the molecular tilt angle could be given, it was found that the nucleation of the λ-orientation is facilitated if the sample is prepared at low substrate temperatures T_{sub}, resulting in a changing fraction of molecules in the two orientations depending on T_{sub}.

In order to determine the tilt angle *quantitatively* NEXAFS experiments were performed on equimolar PFP:PEN blends prepared at three different substrate temperatures (T = 180 K, T = 300 K and T = 330 K) at the Optics beamline (BESSY II, Berlin, Germany) using the SurICat endstation. NEXAFS was measured around the K-egdes of carbon (E = 286 eV) and fluorine (E = 695 eV). Four different angles of incidence Θ relative to the substrate surface were choosen (90°, 70°, 50° and 30°). The following section is based on Ref. [178].

Figure 4.22 shows NEXAFS data of mixed films of PFP and PEN prepared at three different substrate temperatures T_{sub} measured at the K-edges of carbon (left column) and fluorine (right column) with four different angles of incidence Θ. Based on the results of NEXAFS measurements of pure PEN [241] and pure PFP [131] the peaks observed

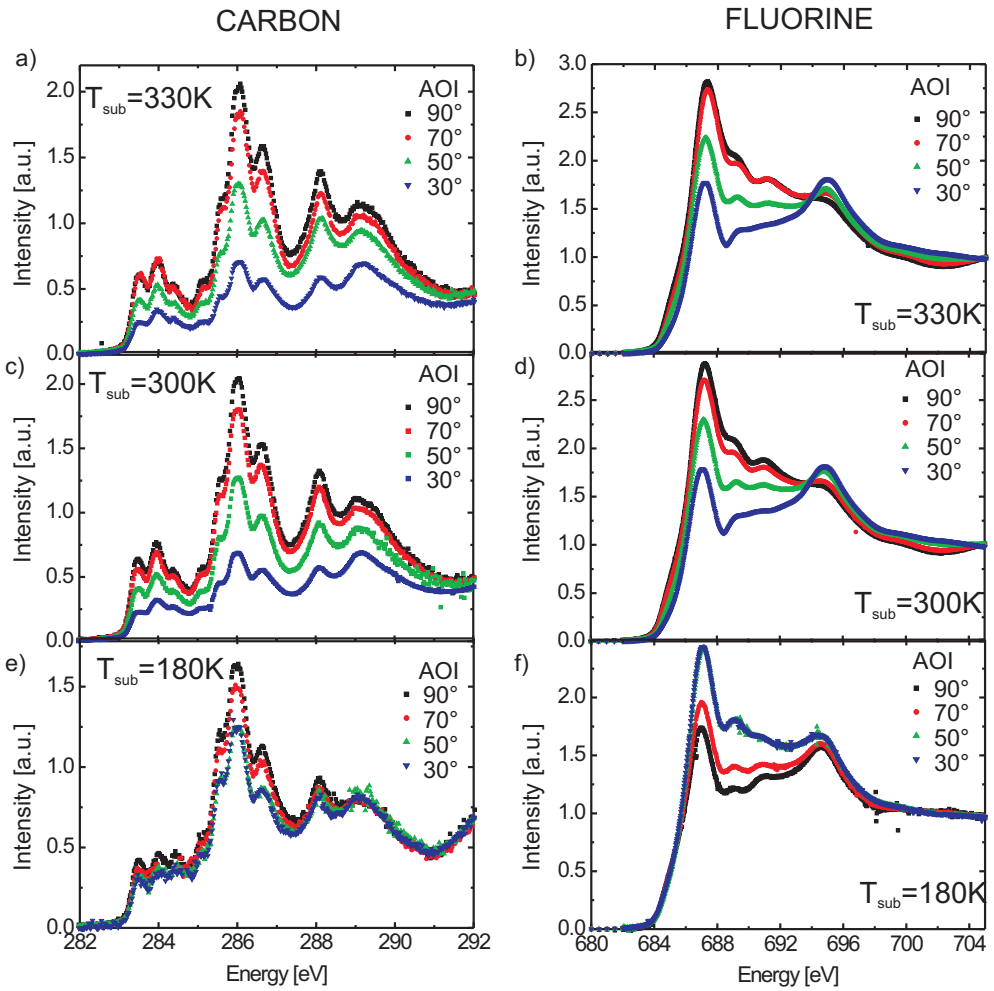

Figure 4.22: a)-f) NEXAFS data of PFP:PEN mixtures prepared at different substrate temperatures T_{sub} (a, b: T_{sub} = 330 K. c, d: T_{sub} = 300 K. e, f: T_{sub} = 180 K.). Left column: NEXAFS at the carbon K-edge. Right column: NEXAFS at the fluorine K-edge.

Peak position [eV]	Transition	Compound
283.5	1s $\rightarrow \pi^*$	PEN
284	1s $\rightarrow \pi^*$	PEN
284.4	1s $\rightarrow \pi^*$	PEN
285.6	1s $\rightarrow \pi^*$	PFP/PEN
286	1s $\rightarrow \pi^*$	PFP
286.7	1s $\rightarrow \pi^*$	PFP
288	1s $\rightarrow \pi^*$	PFP

Table 4.5: Peaks observed in the NEXAFS data at the carbon K-edge and their assignment to the two compounds based on Refs. [131, 241].

Substrate temperature	α_{PEN}	α_{PFP}
330 K	14°	12°
300 K	14°	13°
180 K	25°	25°

Table 4.6: Average molecular tilt angle α resulting from the fit of the intensities of the peak at 283.5 eV, which is assigned to PEN and the peak at 286 eV, which is assigned to PFP. The estimated error bar is 3°.

in the NEXAFS data at the carbon K-edge can be assigned to the pure compounds, see Table 4.5. Note that there are peaks in the NEXAFS data of pure PEN at photon energies above 286 eV which are assigned to transitions from the 1s into unoccupied σ^*-orbitals which overlap with peaks assigned to transitions from 1s to π^*-orbitals of PFP. However, the dependence on the AOI of the former peaks assigned to PEN is much weaker than for the latter peaks assigned to PFP [241]. This allows to determine the tilt angle of the PFP molecules based on the dependence of the peaks at 286 eV and higher photon energies without substracting the NEXAFS signal of PEN and may only slightly increase the error bar of the tilt angle determination. For the fluorine K-edge the peak assignment is more difficult, as in this case π^*- and σ^*-orbitals contribute to the signal [224].

Compared with the peak positions in pure films of PEN or PFP in the NEXAFS data of the blends only very small shifts of 0.4 eV in the energy position of the peaks are observed, indicating that the transitions from the core levels are not affected by mixing the two compounds. In order to determine the average molecular tilt angle relative to the surface normal separately for PEN and PFP, the intensity of the peaks at 283.5 eV and 286 eV was plotted as a function of the angle of incidence of the X-ray beam (Fig. 4.23) and fitted based on Eq. 4.3 (Refs. [220, 225]).

$$I = C[0.96(\cos^2(\Theta)\cos^2(\alpha) + \frac{1}{2}\sin^2(\Theta)\sin^2(\alpha)) + 0.02\sin^2(\alpha)] \tag{4.3}$$

The fit results are compiled in Table 4.6 and yield for both compounds similar values

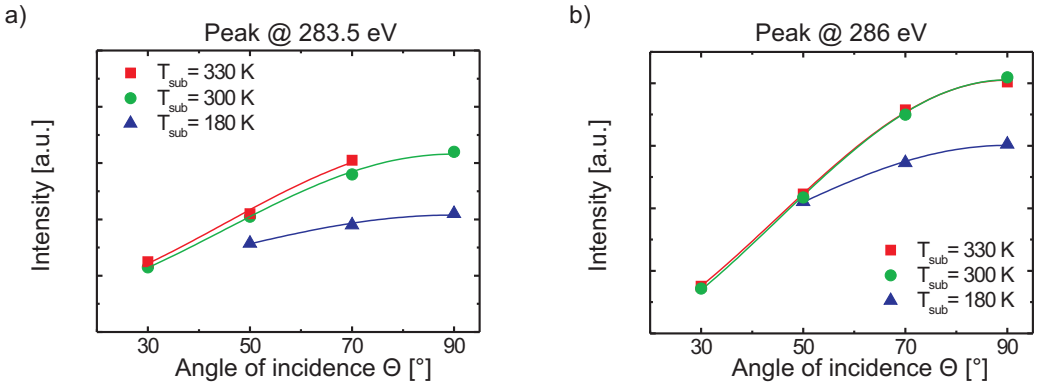

Figure 4.23: Intensities as a function of angle of incidence Θ and the corresponding fit based on Eq. 4.3. a) Peak at 283.5 eV, which can be assigned to PEN, b) peak at 286 eV, which can be assigned to PFP.

of the average tilt angle in the different films. Compared with the samples prepared at higher substrate temperatures the average tilt angle is 10° larger in the sample prepared at 180 K. This confirms that in films prepared at low substrate temperatures there is a higher amount of molecules in the λ-orientation, as it was indicated by X-ray diffractions experiments [127]. An upper limit for the fraction x_λ of molecules in the λ-orientation can even be estimated assuming that the σ-orientation dominates in the samples prepared at 300 K and 330 K. In that case the tilt angle of molecules in the σ-orientation is $\alpha_\sigma \approx 15°$. Assuming further that the tilt angle α_λ for molecules in the λ-orientation is 90°, the fraction x_λ can be estimated according to $\alpha = \alpha_\sigma(1 - x_\lambda) + \alpha_\lambda x_\lambda$, with α being the average molecular tilt angle. This rough estimate yields $x_\lambda \approx 14\%$. Since the actual tilt angle α_λ in the sample will presumably be smaller than 90°, 14% is only an upper limit for x_λ.

In addition, the dependence of the peak intensity in the NEXAFS data measured at the fluorine K-edge was fitted (not shown). The fit yielded for all of the samples an average tilt angle, which is 20° larger than the values compiled in Table 4.6. As it was pointed out in Ref. [224] it can be misleading to determine the molecular tilt angle from a fit of the intensity at the fluorine K-edge due to the high density of states of electrons of the σ-orbitals. Therefore, the absolute values of the tilt angles determined using the fluorine K-edge will not be discussed further. It is noted though that the tendency of the tilt angle with decreasing substrate temperature is the same for both edges.

4.2.5.2 $\epsilon_{2,xy}(E)$ and $\epsilon_{2,z}(E)$

The effects of changing substrate temperature and accordingly, of changes in the molecular tilt angle on the optical properties of equimolar PFP:PEN blends were studied on samples

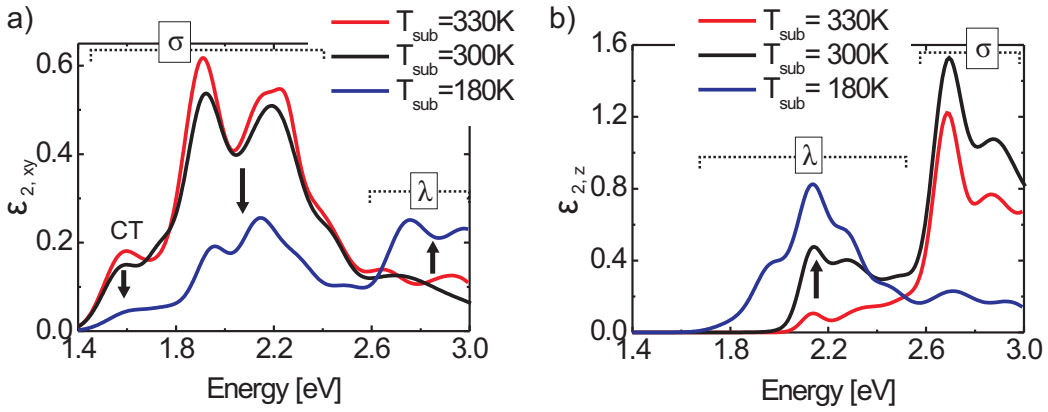

Figure 4.24: a) $\epsilon_{2,xy}(E)$ and b) $\epsilon_{2,z}(E)$ of equimolar PFP:PEN blends prepared at three different substrate temperatures (T_{sub}). The arrows indicate changes with decreasing T_{sub}.

prepared at three different substrate temperatures (T_{sub}=180 K, 300 K and 330 K), see Fig. 4.24. The increased average molecular tilt angle for the sample prepared at T_{sub} = 180 K affects clearly their optical properties which are significantly different compared with the samples prepared at higher substrate temperatures. The arrows in Fig 4.24a and b indicate changes in the shape of the spectra with decreasing substrate temperature. For $\epsilon_{2,xy}(E)$ we observe with decreasing substrate temperature a decreasing intensity of the peaks in the spectral range $E = 1.4 - 2.4$ eV and an increase in intensity of the peaks at 2.7 eV and 2.9 eV. For $\epsilon_{2,z}(E)$ (Fig 4.24b) the behavior is reversed.

In combination with the results of NEXAFS and X-ray diffraction [127] experiments these results allow to assign peaks in specific spectral regions to the spectral response of molecules in lying down (λ) and standing up (σ) orientation in the film (Fig. 4.24), if the peaks in the range $E = 1.4 - 2.4$ eV are tentatively assigned to a charge transfer (CT) transition between PEN and PFP [74, 75] and to the HOMO-LUMO transitions of PFP and PEN, respectively [59,74,113]. For PFP and PEN the transition dipole moment of the HOMO-LUMO transition is oriented along the short molecular axis [59, 113]. Therefore, the intensity of the corresponding peaks is expected to be maximal in $\epsilon_{2,xy}(E)$ ($\epsilon_{2,z}(E)$) for molecules in σ-orientation (λ-orientation). The peaks at 2.7 and 2.9 eV are tentatively assigned to PFP and have a transition dipole moment which is oriented rather along the long axis of the molecule [59]. Accordingly, for molecules in σ-orientation (λ-orientation) the intensity of this peak is expected to be high in $\epsilon_{2,z}(E)$ ($\epsilon_{2,xy}(E)$).

Note also the dependence of the intensity of the CT peak on the preparation temperature, which may be due to differences in the intermolecular interactions between PFP and PEN with changing tilt angle.

4.2.6 Summary

To summarize this section, the optical absorption spectra of blends of the relatively strongly interacting compounds PFP and PEN were studied, which form a new intermixed crystal structure. Using optical spectroscopy evidence for pronounced intermolecular coupling between PFP and PEN was observed. The effects of intermolecular interactions on the absorption spectra include the appearance of new peaks in $\epsilon_{2,xy}(E)$ and $\epsilon_{2,z}(E)$ as well as a small blue shift of the whole spectra presumably arising from a change in the polarizability of the intermolecular environment. In mixed films an increased broadening of the peaks may be caused by inhomogeneities in the film. With a decomposition into single component subbands a first step in the data analysis was performed which allowed to demonstrate the existence of pronounced *new* peaks in $\epsilon_{2,xy}(E)$ of the mixed films, including in particular a new peak at $E_c = 1.6$ eV, related to CT [74]. A related feature was observed using photoluminescence experiments at 1.4 eV [75]. Using NEXAFS experiments the averaged molecular tilt angle in equimolar blends of PFP and PEN prepared at different substrate temperatures T_{sub} was determined and found to be 10° larger in films prepared at $T_{sub} = 180$ K compared with films prepared at higher substrate temperatures. This is due to the higher fraction of domains with molecules in λ-orientation in the sample prepared at low substrate temperature [127]. These changes in the molecular tilt angle affect significantly the optical properties and allow to assign peaks in $\epsilon_{2,xy}(E)$ and $\epsilon_{2,z}(E)$ to the spectral response of molecules in the two different orientations observed in PFP:PEN blends.

4.3 Absorption spectra of PFP:DIP blends

In the previous section the absorption spectra of mixtures of PFP and PEN were studied. They are characterized by strong intermolecular interactions and almost identical sterical properties, leading to the formation of a new intermixed crystal structure and the obser-

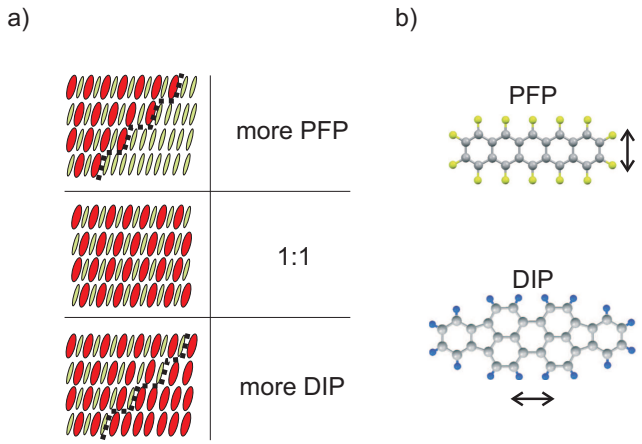

Figure 4.25: a) Schematic mixing scenarios for PFP:DIP depending on the mixing ratio. b) Sketches of the molecules. The arrows indicate the orientation of the transition dipole moments μ of the respective HOMO-LUMO transitions.

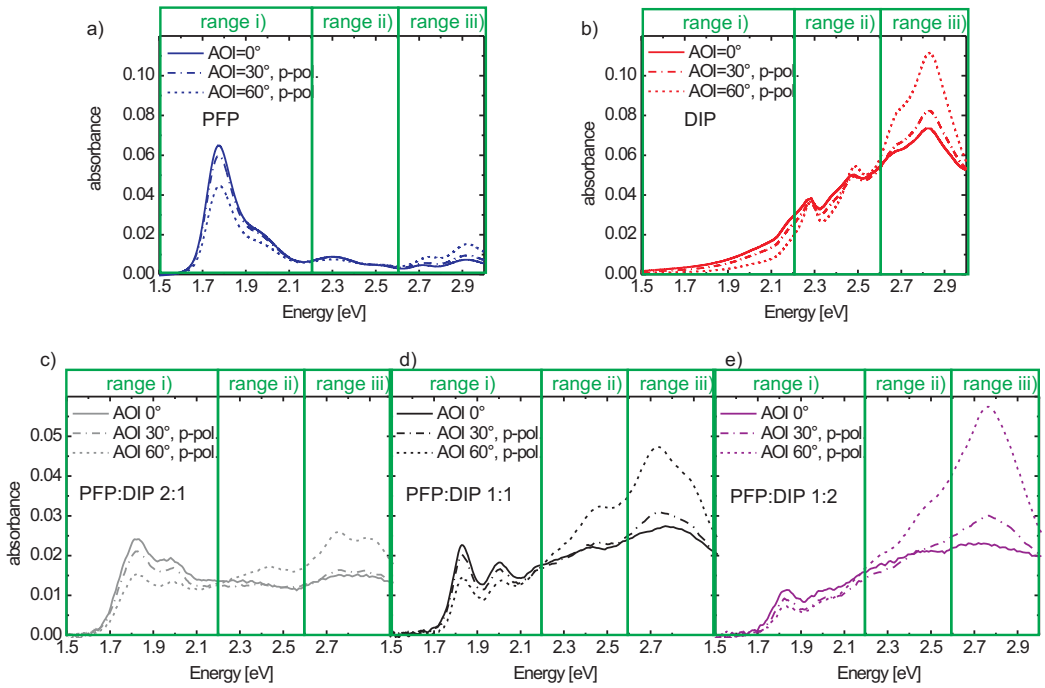

Figure 4.26: Absorbance A of a) pure PFP (simulated based on Ref. [59]), b) pure DIP (simulated based on Ref. [139]) and c)-e) PFP:DIP blends with three different mixing ratios. Picture modified from Ref. [177].

vation of a CT peak in $\epsilon_{2,xy}(E)$. In this section, blends of PFP and DIP will be studied, which form also a new intermixed crystal phase and are expected to exhibit a comparably strong intermolecular interaction but differ significantly in their steric properties. In this system, the influence of steric incompatibility in a mixed film on the optical properties of strongly interacting compounds can be investigated.

It is noted that the structural and optical properties of equimolar PFP:DIP blends were studied in Refs. [176, 231] using VASE and DRS. In order to complete the study of PFP:DIP blends, transmission spectroscopy experiments were performed and mixing ratios deviating from the 1:1 mixture were investigated using VASE and DRS. The data for the equimolar mixture were reproduced and are in agreement with the results in Refs. [176, 231].

4.3.1 Absorbance at different angles of incidence

The following section is based on Ref. [177]. The absorbance of PFP and DIP blends was measured (Fig. 4.26) to provide an overview of the optical

properties. Three characteristic spectral ranges can be identified in Fig. 4.26:
i) below 2.2 eV with peaks at 1.9 eV and 2.0 eV;
ii) between 2.2 eV and 2.6 eV with one peak at 2.44 eV;
iii) above 2.6 eV with the most representative and intense peaks at 2.7 eV and 2.8 eV.

The spectral range i) is clearly related to the spectral response of pure PFP, although the peaks are blue shifted of about max. 50 meV with respect to the pure PFP. Note that PFP:DIP blends on SiO_2 exhibit a crystalline phase with lying-down PFP molecules [176]. This phase can make a contribution to the optical response mainly in spectral range iii) with peaks at about 2.75 eV and 2.9 eV, overlapping with the optical response of DIP. Thus, the assignment of the peaks in the spectral ranges ii) and iii) of spectra collected at oblique AOI is ambiguous.

All mixing ratios exhibit a strong dependence of the spectral shape on the AOI, with no observable peak shifts, but changes in the relative intensities of peaks. Remarkably, the relative intensities of the two peaks in range i) are notably different in the blends compared with the pure film. In addition, the peak at 2.0 eV increases in intensity relative to the peak at 1.82 eV with increasing AOI, which can be observed in the pure film spectrum only to a much lower degree. This observation will be discussed in more detail in the next section.

The spectrum of the PFP:DIP 2:1 blend (Fig. 4.26c) resembles the pure PFP spectrum except for the change in relative intensities of the two peaks in spectral range i) and the peak in range ii). The intensity of the peak at 2.44 eV increases notably with increasing AOI, indicating that the corresponding transition dipole moment is oriented rather perpendicular than parallel to the substrate surface. Since this peak becomes more pronounced with increasing amount of DIP (compare Fig. 4.26c-e), it can tentatively be assigned to DIP. This is reasonable because the transition dipole moment of the HOMO-LUMO transition of DIP is oriented along the long axis of the molecule (Fig. 4.25b) and the DIP molecules are upright standing in the blends [176]. The peak at 2.4 eV cannot be attributed to lying-down molecules because the peak intensity increases with the AOI. In the spectral range iii) the peaks at 2.76 eV and 2.88 eV can tentatively be assigned to PFP, as their relative intensities and energy positions are similar to the corresponding peaks in pure PFP, although a contribution from DIP (arising from the peak at 2.83 eV) cannot be excluded.

For the equimolar PFP:DIP mixture two broad peaks are observed at 2.73 eV and around 2.86 eV in the spectral range iii) where PFP and DIP contribute to the absorbance. As there is a very strong peak related to DIP at 2.83 eV, it is likely that the absorbance in this spectral region is composed of at least three contributions, two stemming from PFP and one from DIP.

Finally, the spectral shape of the PFP:DIP 1:2 blend (Fig. 4.26e) resembles pure DIP with some differences. The peaks in the spectral range i) are still observed. In the spectral ranges ii) and iii) all peaks are significantly broadened compared with pure DIP or the other blends and their intensities exhibit a strong dependence on the AOI. There is only one peak at 2.76 eV clearly discernable in the spectral range iii), which is 30 meV blue shifted from the corresponding peak in the equimolar mixture and may also stem from a

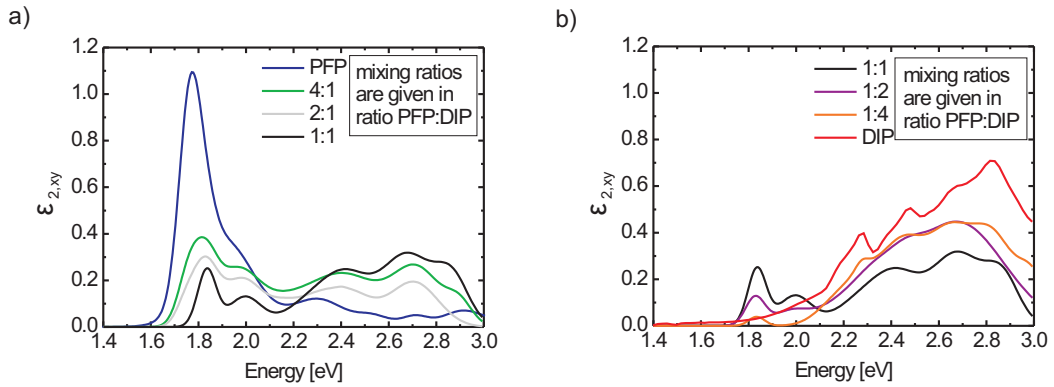

Figure 4.27: $\epsilon_{2,xy}(E)$ of PFP:DIP mixed films. For comparison the pure film spectra from Refs. [59] (PFP) and [139] (DIP) are shown. a) Mixing ratios PFP:DIP 4:1, 2:1, 1:1. b) Mixing ratios PFP:DIP 1:1, 1:2, 1:4. Picture modified from Ref. [177].

superposition of contributions by PFP and DIP.

4.3.2 $\epsilon_{2,xy}(E)$

The significant changes observable in the mixed film spectra with increasing AOI are evidence for anisotropic optical properties, as it was already reported for the equimolar PFP:DIP mixture [176]. $\epsilon_{2,xy}(E)$ and $\epsilon_{2,z}(E)$ were determined separately by a multi-sample analysis [139, 238]. The following section is based on Ref. [177].

Fig. 4.27 shows $\epsilon_{2,xy}(E)$ for PFP:DIP blends with five different mixing ratios. The shape of $\epsilon_{2,xy}(E)$ changes continuously with the mixing ratio and the contributions of the pure films can still be discerned. Compared with the corresponding peaks in the pure film spectra most of the peaks in the spectra of the blends are broadened, probably due to inhomogeneities in the local molecular environment [176]. The first two peaks, which are assigned to PFP, can be observed for all mixing ratios. In pure PFP these two peaks are either related to the two Davydov-components of the HOMO-LUMO transition or to the HOMO-LUMO transition and a corresponding vibronic progression [59, 128]. In the blends, their relative intensity is significantly different compared with the corresponding peaks in pure PFP, but only slightly changing with the mixing ratio. This results possibly from the differences in the crystal structure in the blend compared with the pure film [176], and the corresponding differences in molecular arrangement and local environment. In addition for blends containing more PFP the first peak in $\epsilon_{2,xy}$ seems to be composed of two contributions (see gray oscillator at $E = 1.75$ eV in Fig. 4.28, which matches the energy position of the HOMO-LUMO transition of pure PFP). The peak at $E = 1.75$ eV could tentatively be attributed to molecules, which are in the phase separated pure PFP

Mixing ratio	E_1 [eV]	E_2 [eV]	E_3 [eV]	E_4 [eV]	E_5 [eV]	E_6 [eV]
Pure PFP	1.75	1.94	2.28	2.48	-	-
PFP:DIP 4:1	1.82	1.99	2.19	2.35	2.50	2.72
PFP:DIP 2:1	1.82	1.99	2.16	2.28	2.42	2.71
PFP:DIP 1:1	1.84	2.00	2.14	2.34	2.57	2.70
PFP:DIP 1:2	1.82	2.01	2.23	2.39	2.54	2.73
PFP:DIP 1:4	1.83	2.19	2.28	2.43	2.62	2.83
Pure DIP	2.23	2.29	2.37	2.46	2.65	2.78

Table 4.7: Energy positions of the most pronounced peaks in $\epsilon_{2,xy}(E)$ for mixed films of PFP:DIP. The energy positions of PFP and DIP are taken from Refs. [59] (PFP) and [139] (DIP). E_1 describes the energy position of the HOMO-LUMO transition of the pure component film spectra and the energy position of the first strong peak in the mixed film spectra, respectively. The peaks are numbered with increasing energy position. Note that for mixtures with mixing ratio PFP:DIP 4:1 and 2:1 there is an additional shoulder at $E = 1.75$ eV, which is not noted here for comparison and consistency, but will be discussed later. The error in the energy position is below ± 0.005 eV for the first peak (E_1).

phase, while the other peak arises from PFP in the equimolar mixed phase and at the phase boundary. This interpretation would be in agreement with the reported film structure (Ref. [176] and Sec. 4.1.2), although it cannot be excluded that other effects influence the absorption in this spectral range.

The shape of the spectra of blends containing more DIP show clear similarities to pure DIP, although the peaks are significantly broadened (Fig. 4.27b). For $\epsilon_{2,xy}(E)$ of the PFP:DIP 1:2-mixture almost no distinct peaks can be observed, but only very broad absorption features indicating a comparably high degree of disorder in the blends with a higher volume fraction of DIP, which is consistent with the results of X-ray scattering experiments [176].

Compared with pure PFP in thin films there is a strong blue shift of the first pronounced peak in $\epsilon_{2,xy}(E)$ observable (Tab. 4.7 and Fig. 4.29), which is at maximum $\Delta E = 90$ meV for the equimolar PFP:DIP blend. A probable reason for this blue shift are changes in the polarizability of the intermolecular environment in the blend compared with the pure film. As a result of the mixing and ordering behavior (Sec. 4.1.2), the observed peak shift can be seen as a superposition of two effects:

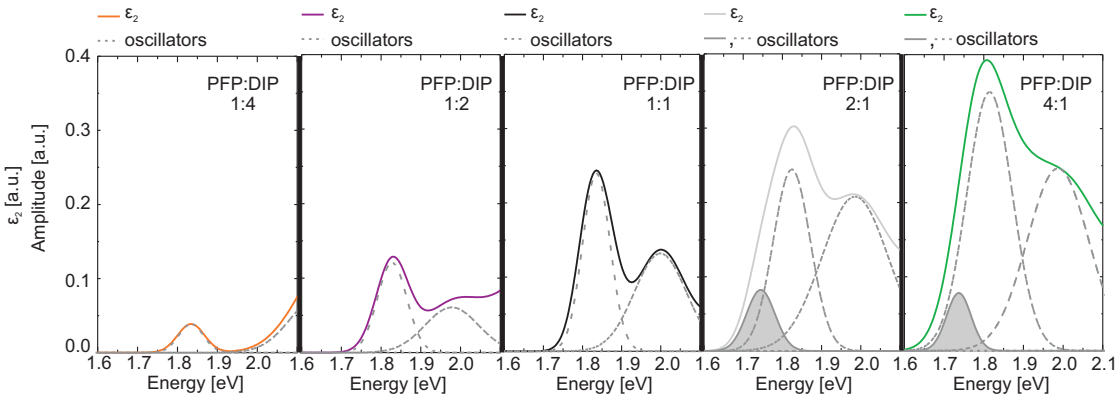

Figure 4.28: Oscillators describing the first two pronounced peaks in $\epsilon_{2,xy}(E)$ of PFP:DIP blends with different mixing ratios. Note the gray oscillator at $E = 1.75$ eV, which matches the energy position of the HOMO-LUMO transition of pure PFP.

i) A shift of the peak position to which molecules in the mixed film phase contribute due to the different polarizability of the intermolecular environment in the blend compared with the pure films. This shift is the same for all mixing ratios.

ii) A shift, which results from the changing fraction of molecules at the boundary between mixed and pure film phase with the mixing ratio. These molecules at the boundaries encounter a different polarizability of the intermolecular environment depending on the excess compound in the blend, resulting in different shifts depending on the mixing ratio.

The combination of these two effects results in a peak shift which is not monotonic, as for equimolar blends the second effect will not influence the peak position.

4.3.3 Non-linear mixing effects

In contrast to PFP:PEN blends there is no clear CT peak observable in PFP:DIP blends. This could be due to the significantly different spectral range in which PFP and DIP are absorbing or due to the orientation of the transition dipole moments of the two compounds, preventing an efficient coupling of excitations in case of upright standing molecules. However, even if there was a CT between PFP and DIP, the corresponding CT peak could be expected around 2.0 eV, based on the HOMO and LUMO position of PFP and DIP [108]. In this spectral range PFP and DIP have a non-zero $\epsilon_{2,xy}$ and $\epsilon_{2,z}$ and it could be that the weak CT peak contributes to $\epsilon_{2,xy}$ or $\epsilon_{2,z}$, but cannot be distinguished from the contributions of the pure compounds.

In order to test, if the strong intermolecular interactions which can be expected in the system PFP:DIP influence the shape of $\epsilon_{2,xy}$, $\epsilon_{2,xy}^{eff}$ was calculated similar to PFP:PEN mixtures using two effective medium approximation models (see Sec. 2.4.2.1). The results

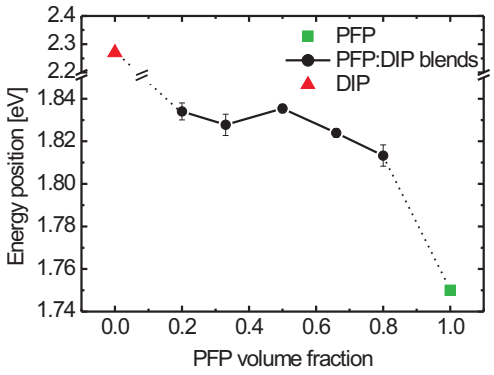

Figure 4.29: Energy position E_1 of the first pronounced peak in $\epsilon_{2,xy}(E)$ as a function of PFP volume fraction. The value for the equimolar mixture is consistent with the data published in Ref. [176].

are shown in Fig. 4.30. In the upper row of Fig. 4.30, $\epsilon_{2,xy}^{eff}$ are shown calculated based on $\epsilon_{2,xy}$ of the pure compounds using the Bruggeman model [182] (left column) and the Maxwell-Garnett model [183] (right column). For comparison the experimentally determined $\epsilon_{2,xy}$ are shown in the box. The general changes of $\epsilon_{2,xy}$ are reproduced by the calculated $\epsilon_{2,xy}^{eff}$. However, the shift of the first peak is obviously different in $\epsilon_{2,xy}^{eff}$ compared with the experimentally determined $\epsilon_{2,xy}$.

For non-equimolar mixing ratios, blends of PFP and DIP exhibit phase separation between an intermixed crystal phase and the pure phase of the excess compound. Therefore, in a next step it was tested whether $\epsilon_{2,xy}(E)$ of the different non-equimolar blends can be described as a combination of $\epsilon_{2,xy}(E)$ of the equimolar mixture and $\epsilon_{2,xy}(E)$ of the respective excess compound using the same effective medium approximations. For the mixtures containing more PFP, $\epsilon_{2,xy}(E)$ of the 1:1 mixture and $\epsilon_{2,xy}(E)$ of PFP was used for the calculations, while $\epsilon_{2,xy}(E)$ of the 1:1 mixture and $\epsilon_{2,xy}(E)$ of DIP was used to calculate $\epsilon_{2,xy}^{eff}(E)$ for mixtures containing more DIP.

The lower row in Fig. 4.30 shows $\epsilon_{2,xy}^{eff}$ calculated using the same effective medium approximation models, but based on $\epsilon_{2,xy}$ of the pure compounds and $\epsilon_{2,xy}$ of the equimolar PFP:DIP mixture. For the blends containing more DIP the absolute intensities of $\epsilon_{2,xy}^{eff}$ are in good agreement with those of $\epsilon_{2,xy}$ and the changes in the relative intensities with the mixing ratio are reproduced. However, the shift of the first peak is still different for the spectra of $\epsilon_{2,xy}^{eff}$ and $\epsilon_{2,xy}$. This indicates that this peak is influenced by effects which are not included in the models and which are probably interactions between molecules of either different or same species. In addition, the width of the peaks in the experimentally determined $\epsilon_{2,xy}$ is larger than in the calculated $\epsilon_{2,xy}^{eff}$. This may be due to structural inhomogeneities in the blends, which is induced by the different steric properties of the compounds and which cannot be taken into account in the models used here.

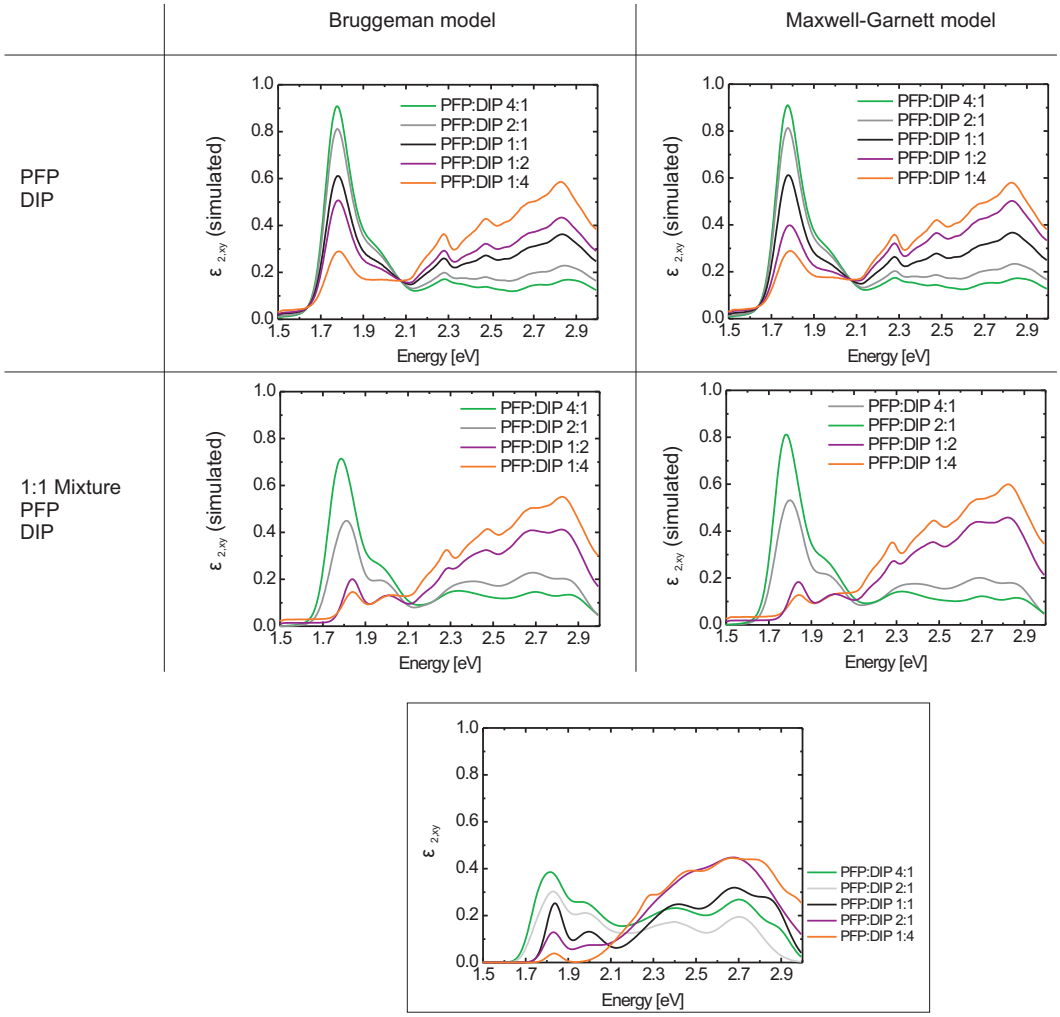

Figure 4.30: Calculated $\epsilon_{2,xy}^{eff}(E)$ based on the pure compound spectra (upper row) and based on the pure compound spectra *and* the $\epsilon_{2,xy}(E)$ of the equimolar mixture (lower row). For a detailed explanation see text. The experimentally determined $\epsilon_{2,xy}(E)$ are shown in the bottom diagram for comparison.

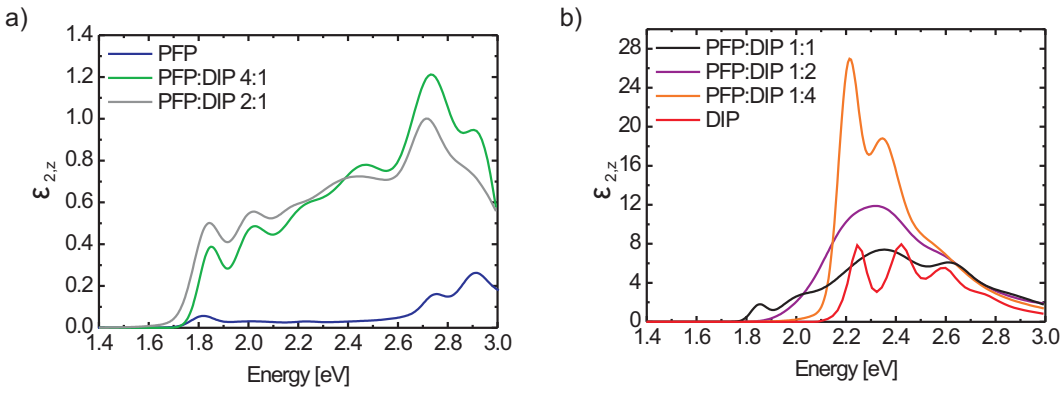

Figure 4.31: $\epsilon_{2,z}(E)$ of PFP:DIP mixed films. For comparison the pure film spectra from Refs. [59] (PFP) and [139] (DIP) are shown. a) Mixing ratios PFP:DIP 4:1, 2:1. b) Mixing ratios PFP:DIP 1:1, 1:2, 1:4.

4.3.4 $\epsilon_{2,z}(E)$

Finally, $\epsilon_{2,z}(E)$ is shown in Fig. 4.31 for the different mixing ratios of PFP:DIP. The absolute intensity of $\epsilon_{2,z}(E)$ is strongly affected by uncertainties of the film thickness, resulting in a maximum error of 50%. Therefore, this component will only be discussed qualitatively regarding the dependence of the line shape on the mixing ratio. Surprisingly, the spectral shape does not change continuously with the mixing ratio. The absorption spectra of the mixtures with mixing ratios PFP:DIP 1:1, 1:2 and 1:4 (Fig. 4.31b) have similar shapes, but are notably different from the mixtures containing more PFP. $\epsilon_{2,z}(E)$ of mixtures containing more PFP exhibit several distinctive peaks, none of which can clearly be assigned to DIP. The relative intensities and energy positions of most of the peaks resemble those found in $\epsilon_{2,xy}(E)$ and $\epsilon_{2,z}(E)$ of pure PFP films. This observation is surprising, as $\epsilon_{2,z}(E)$ of PFP is much weaker than the one of DIP. $\epsilon_{2,z}(E)$ of the PFP:DIP 1:4 blend (Fig. 4.31a) exhibits two clear peaks, which could arise from red shifted DIP-peaks. If these peaks are tentatively assigned to DIP, the first peak corresponds to the HOMO-LUMO transition and the second to a vibronic progression [139]. For pure DIP there is a second subband of the vibronic progression observable [139], which is very weak in the mixed film spectrum. Since the intensity of the vibronic progression depends on the coupling between electronic transitions and phonons, it is reasonable that the intensity of the vibronic progression is reduced in films exhibiting structural inhomogeneities. The absolute intensity of the PFP:DIP 1:4 blend is unrealistically high. Currently there is no explanation for this observation.

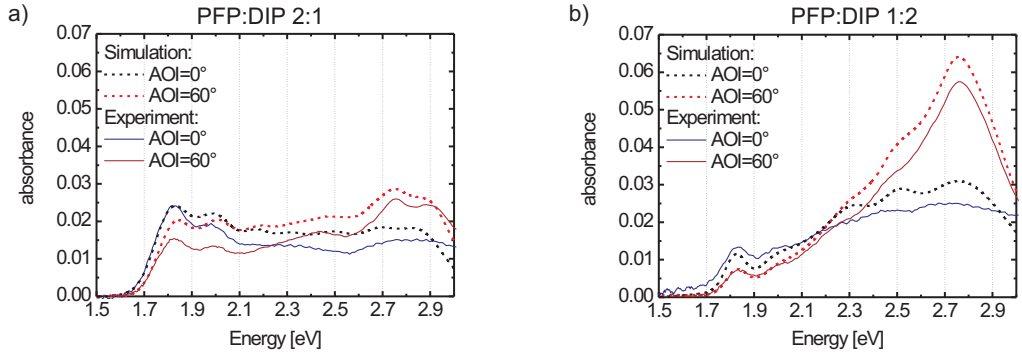

Figure 4.32: Comparison of simulated and experimentally determined absorbance for a) a PEN:DIP 2:1 and b) a PEN:DIP 1:2 blend. See text for details.

4.3.5 Comparison of transmission spectroscopy and VASE

Transmission spectroscopy is a suitable method to test the reliability of the results obtained using VASE and DRS. Based on $\epsilon_{2,xy}(E)$ determined using DRS (see Sec. 3.2) on glass and on $\epsilon_{2,z}(E)$ determined using VASE the absorbance at two different AOI (0° and 60°) was simulated and compared with the experimentally determined absorbance exemplarily for two mixing ratios (Fig. 4.32). For both mixing ratios the agreement between simulation and experiment is excellent. The small deviations are due to differences in film thickness and mixing ratio of the sample series measured with transmission spectroscopy and VASE.

4.3.6 Varying the substrate temperature

PFP:DIP blends exhibit two orientations which differ in their molecular tilt angles. There is no indication that the nucleation of one of the two orientations is strongly influenced by the substrate temperature (see Sec. 4.1.2). Therefore, no pronounced effects of changes in T_{sub} on $\epsilon_{2,xy}$ or $\epsilon_{2,z}$ are expected. Figure 4.33 shows $\epsilon_{2,xy}(E)$ and $\epsilon_{2,z}(E)$ for equimolar PFP:DIP blends prepared at different substrate temperatures T_{sub}. In contrast to the expected behavior, there are changes observable with decreasing substrate temperature (see arrows in Fig. 4.33), however, not as continuous as for PFP:PEN blends. From X-ray experiments (see Sec. 4.1.2) it can be concluded that the structural order is decreasing with descreasing T_{sub}. This may result in differences in the arrangement of the molecules within the film, changing the intermolecular environment and accordingly the intermolecular interactions which affect $\epsilon_2(E)$.

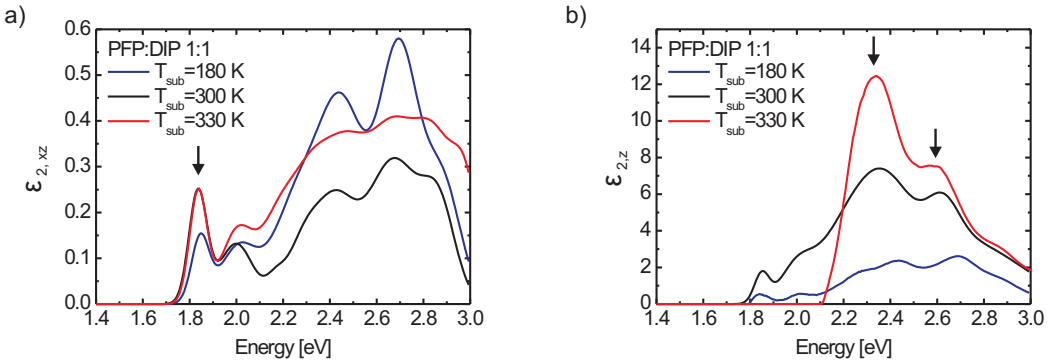

Figure 4.33: a) $\epsilon_{2,xy}(E)$ and b) $\epsilon_{2,z}(E)$ of equimolar PFP:DIP blends prepared at different substrate temperatures T_{sub}. The arrows indicate changes with decreasing T_{sub}.

4.3.7 Summary

In this section the optical properties of blends of the strongly interacting but sterically different compounds PFP and DIP were studied. Compared with blends of PFP:PEN the lower steric compatibility of PFP and DIP affected the optical properties, resulting in increasing peak widths. The mixing behavior for non-equimolar blens led to a non-monotonic shift of the energy position of the first peak. Finally, in contrast to blends of PFP:PEN, no clear CT peak was observed in the absorption spectra of PFP:DIP blends and the absorption spectra resembled a superposition of the pure film spectra. This may be due to two reasons: i) The expected energy position of the peak corresponding to the CT transition is 2.0 eV, which makes it difficult to distinguish the CT peak from peaks attributed to the pure compounds. ii) The orientation of the transition dipole moments of the HOMO-LUMO transition of PFP and DIP, respectively, as well as the relative position of the HOMO and LUMO of both compounds may prevent an efficient coupling between excitations of PFP and DIP.

4.4 Absorption spectra of PEN:DIP blends

In order to complete the study of the three combinations of blends of PFP, PEN and DIP, mixed films of PEN and DIP will be studied in this section. PEN and DIP do not interact strongly and differ in their steric properties. As discussed in Sec. 4.1.3, blends of these two compounds exhibit a reduced structural order in the substrate plane which vanishes completely for the equimolar mixture, but are well ordered perpendicular to the substrate surface. Therefore, the optical properties are not expected to be influenced by intermolecular interactions, but may be affected significantly by the reduced long-range

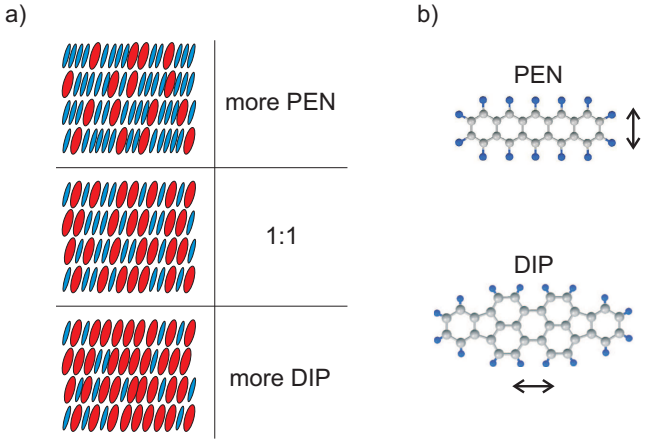

Figure 4.34: a) Schematic mixing scenarios for PEN:DIP depending on the mixing ratio. b) Sketches of the molecules. The arrows indicate the orientation of the transition dipole moments μ of the respective HOMO-LUMO transitions.

order in the films.

4.4.1 Absorbance at different angles of incidence

The following section is based on Ref. [177]. In order to provide an overview of the optical properties of PEN:DIP mixed films grown on glass, including possible anisotropies, the absorbance A of some of the samples is shown in Fig. 4.35, including the simulated absorbance of the pure compounds based on Refs. [59, 139]. The absorbance of the two blends which are not shown, follows a monotonic trend with changing mixing ratio. Together with the normal incidence spectra (AOI=0°), also the oblique incidence (AOI=30° and 60°) spectra are reported as collected under p-polarization. As expected, the spectra collected under s-polarization exhibit perfect similarity with those collected at normal incidence (not shown). Similar to PFP:DIP, three main characteristic spectral ranges can be identified in Fig. 4.35:

i) below 2.2 eV with peaks at 1.9 eV and 2.0 eV;
ii) between 2.2 eV and 2.6 eV with the most representative and intense peaks at 2.3 eV and 2.5 eV;
iii) above 2.6 eV with peaks at 2.7 eV and 2.8 eV.

In all the spectra of the PEN:DIP blends strong effects of the AOI on the measured spectral shape can be observed. The most pronounced effect is a decrease (*increase*) in intensity of peaks in range i) (*range iii)*) with increasing AOI, which can be found independently of the mixing ratio. This leads to the conclusion that the corresponding transition dipole moments are oriented nearly parallel (*perpendicular*) to the substrate surface. The transition dipole moment of the HOMO-LUMO transition of PEN (*DIP*) is indeed polarized along the short (*long*) molecular axis [59,113,139] (see Fig. 4.34b). Since the molecules in the blends are arranged upright standing on the substrate surface [36], the peaks in range i) and range iii) can be related clearly to PEN and DIP, respectively.

The mixed and the pure film spectra exhibit clear similarities, but also significant differences in particular in the relative intensities. Compared with the pure film spectrum

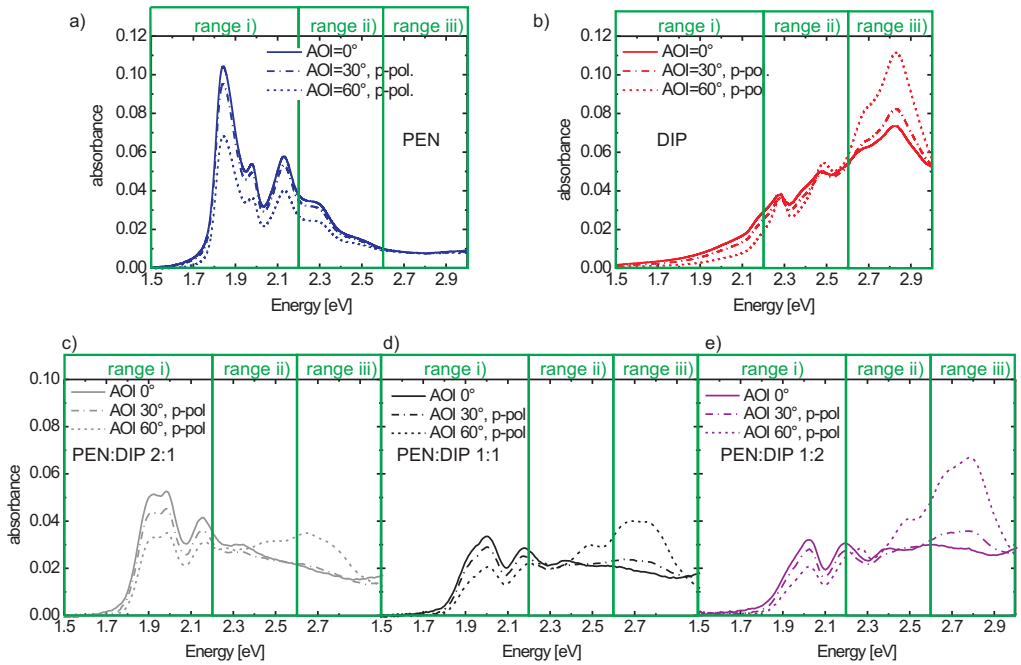

Figure 4.35: Absorbance A of a) pure PEN (simulated based on Ref. [59]), b) pure DIP (simulated based on Ref. [139]) and c)-e) PEN:DIP blends with three different mixing ratios. Picture modified from Ref. [177].

of PEN the relative intensity of the peaks in spectral range i) is significantly different and strongly changing with the mixing ratio (see Fig. 4.35a and Fig. 4.35c-e). Also the two peaks in spectral range iii) change with the mixing ratio not only in absolute but also in relative intensity. Remarkably, the intensity of the peak at 2.8 eV depends much stronger on the AOI in the blend than in the pure film (compare Fig. 4.35b and Fig. 4.35e), which may indicate a change in the molecular arrangement. Finally, in the intermediate spectral range ii), where the spectral response of PEN and DIP is overlapping, the peak at 2.3 eV shifts slightly in energy position with changing AOI, indicating that it is composed of two transitions differing in the orientation of the transition dipole moments.

4.4.2 $\epsilon_{2,xy}(E)$

Similar to blends of PFP:PEN and PFP:DIP, blends of PEN:DIP exhibit uniaxial anisotropic optical properties. In order to determine $\epsilon_{2,xy}(E)$ and $\epsilon_{2,z}(E)$ independently, a multi-sample analysis using VASE data was performed as described in Ref. [139,238]. The following section is based on Ref. [177]. In Fig. 4.36 $\epsilon_{2,xy}(E)$ for the different mixing ratios is shown. Similar to the absorbance also the shape of $\epsilon_{2,xy}(E)$ changes continuously with

	E_1 [eV]	E_2 [eV]	E_3 [eV]	E_4 [eV]	E_5 [eV]	E_6 [eV]
Pure PEN	1.85	1.97	2.11	2.28	-	-
PEN:DIP 4:1	1.90	1.99	2.14	2.31	2.40	-
PEN:DIP 2:1	1.91	2.00	2.15	2.36	2.70	-
PEN:DIP 1:1	1.93	2.02	2.17	2.32	2.58	2.82
PEN:DIP 1:2	1.94	2.03	2.20	2.39	2.67	2.78
PEN:DIP 1:4	1.95	2.06	2.23	2.42	2.60	2.78
Pure DIP	2.23	2.29	2.37	2.46	2.65	2.78

Table 4.8: Energy positions of the most pronounced peaks in $\epsilon_{2,xy}(E)$ for mixed films of PEN:DIP. The energy positions of PEN and DIP are taken from Refs. [59] and [139]. E_1 describes the energy position of the HOMO-LUMO transition of the pure component film spectra and the energy position of the first strong peaks in the mixed film spectra, respectively. The transitions are numbered with increasing energy position. The error in the energy position is below ± 0.01 eV for the first peak (E_1).

the mixing ratio. The contributions of the pure film spectra of PEN and DIP can clearly be distinguished and for non-equimolar mixing ratios the spectral shape is dominated by the more abundant molecular species.

In Table 4.8 the energy position of the peaks observable in $\epsilon_{2,xy}(E)$ (Fig. 4.36) for the different blends are compiled. Obviously the peaks around 1.9 eV and 2.0 eV can be assigned to PEN, since DIP is not absorbing in this energy range. Interestingly, there is a strong blue shift of these peaks in the blends compared with the pure films (Fig. 4.37), which increases with increasing volume fraction of DIP from $\Delta E = 50 \pm 3$ meV (PEN:DIP 4:1) to $\Delta E = 100 \pm 10$ meV (PEN:DIP 1:4). This blue shift is probably caused by changes in the polarizability of the intermolecular environment due to the presence of DIP in the blends compared with the pure films. The shift is monotonic due to the mixing and ordering behavior of PEN:DIP blends. With changing volume fraction of DIP the film structure changes from (i) Excess of DIP molecues: PEN molecules which statistically occupy sites in a lattice of DIP molecules, (ii) Equimolar blend: PEN and DIP molecules are randomly distributed in the film, (iii) Excess of PEN molecules: DIP molecules occupy sites in a lattice formed by PEN molecules. In contrast to PFP:PEN blends and PFP:DIP blends, there is a continuous transition between the scenarios (i) - (iii) in PEN:DIP blends and accordingly, the intermolecular environment changes continuously with the mixing ratio resulting in a monotonic shift of the peak. Since the peaks at higher energy positions, which can be attributed to DIP are comparatively broad, their energy position has a higher uncertainty. However, the smaller energy shift of the peak E_6 in Table 4.8 compared with the peak E_1 in Table 4.8 is in nice agreement with the smaller solvent shift observed for DIP [139] in comparison with PEN [59].

As pointed out above the contributions of the pure film spectra of PEN and DIP can still be found in $\epsilon_{2,xy}(E)$ of the mixed films, although some differences are observed.

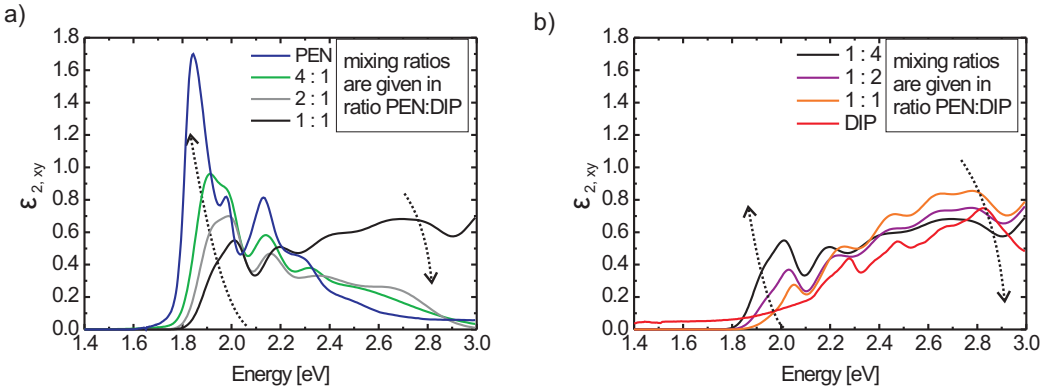

Figure 4.36: $\epsilon_{2,xy}(E)$ of PEN:DIP thin films with different mixing ratios determined by VASE. The arrows indicate changes with increasing amount of PEN. Reference spectra of the pure films are taken from Refs. [59] (PEN) and [139] (DIP). a) Mixing ratios PEN:DIP 4:1, 2:1, 1:1. b) Mixing ratios PEN:DIP 1:1, 1:2, 1:4. Data measured in collaboration with A. Aufderheide [217].

Apart from changes in the energy positions of the peaks, also the relative intensities of the peaks differ significantly. These differences are possibly caused by different intermolecular interactions due to differences in intermolecular environment resulting from the presence of two compounds (PEN and DIP), different molecular orientations and the influence of structural disorder in the blends and will be discussed in the following. In pure DIP the peak at 2.7 eV is part of the vibronic progression of the HOMO-LUMO transition, in contrast to the peak at 2.8 eV, which arises from intermolecular coupling between the DIP molecules [67, 139]. In $\epsilon_{2,xy}(E)$ of the blends, the relative intensity of these two peaks is different compared with their relative intensity in pure DIP films and changes with the mixing ratio. The differences can be rationalized by the presence of PEN in the blend and a comparably high degree of disorder present in the mixed films [36]. For blends containing more PEN, where the DIP interaction is hindered by surrounding PEN molecules, the peak at 2.8 eV can not be observed, while the strongest corresponding peak occurs for the PEN:DIP 1:4 mixture, where also the interaction between DIP molecules is facilitated. The higher degree of disorder present in the blends affects the interactions between DIP molecules, resulting in an intensity of the peak at 2.8 eV, which is less pronounced compared with the pure films.

The most remarkable influence of structural disorder on the spectral shape is found for the peaks at 1.9 eV and 2.0 eV which can be assigned to PEN, although they are blue shifted by 50 meV. In pure films the peak at 1.9 eV is very intense and the transition at 2.0 eV can be observed as giving a less intense shoulder. This is completely changed in the mixed films, where the intensities of the two peaks depend strongly on the mixing ratio

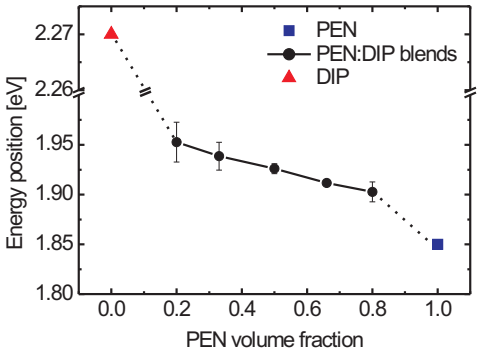

Figure 4.37: Energy position of the first peak as a function of PEN volume fraction. The energy positions of the HOMO-LUMO transition of the pure compounds are taken from Refs. [59] (PEN) and [139] (DIP).

(Fig. 4.36), as found also in the absorbance spectra discussed in the previous section.

With increasing amount of DIP the overall intensity of the two peaks decreases and a change in the relative intensities is observed, as the peak at 1.9 eV becomes less intense compared with the peak at 2.0 eV and vanishes almost completely in the spectrum of the PEN:DIP 1:4 film.

While the change in overall intensity of the two peaks with the mixing ratio can be understood in terms of a changing amount of PEN in the mixed films, the reason for the differences in the relative intensities is less obvious. In the pure films, the two peaks are related to two Davydov-components of the HOMO-LUMO transition [242]. A change of the intensities of these peaks may therefore point towards a change in the intermolecular interactions due to a change in the molecular arrangement in the mixed films compared with the pure films. From the comparison of $\epsilon_{2,xy}$(E) of PEN:DIP 4:1 and 2:1 blends with disordered PEN, reported in Ref. [185], one can even deduce that the crystalline order is significantly decreased in the blends. Although the present films do not exhibit the same thickness as those in Ref. [185] is it worth to point out that this interpretation of the shape of $\epsilon_{2,xy}(E)$ is in remarkable agreement with the results of structural investigations of PEN:DIP mixed films, which were discussed in Ref. [36]. There, independent of the mixing ratio a lower crystallinity of the films was found with a complete vanishing of in-plane order for the equimolar mixture.

The observation of two Davydov-components in the highly disordered blends can be explained by short-range order [185], since $\epsilon_{2,xy}(E)$ is mainly influenced by nearest-neighbour interactions [243]. The change of the relative intensities of the two Davydov-components with the mixing ratio is possibly caused by changes in the short-range order and in interactions between neighbouring PEN molecules, but also by a probable change in the tilt angle of the molecules with the mixing ratio as reported in Ref. [36].

Interestingly, the differences in the optical properties of the blends compared with the pure films can almost completely be rationalized by the film structure, in particular the decrease in crystalline order which results in changes in the intermolecular environ-

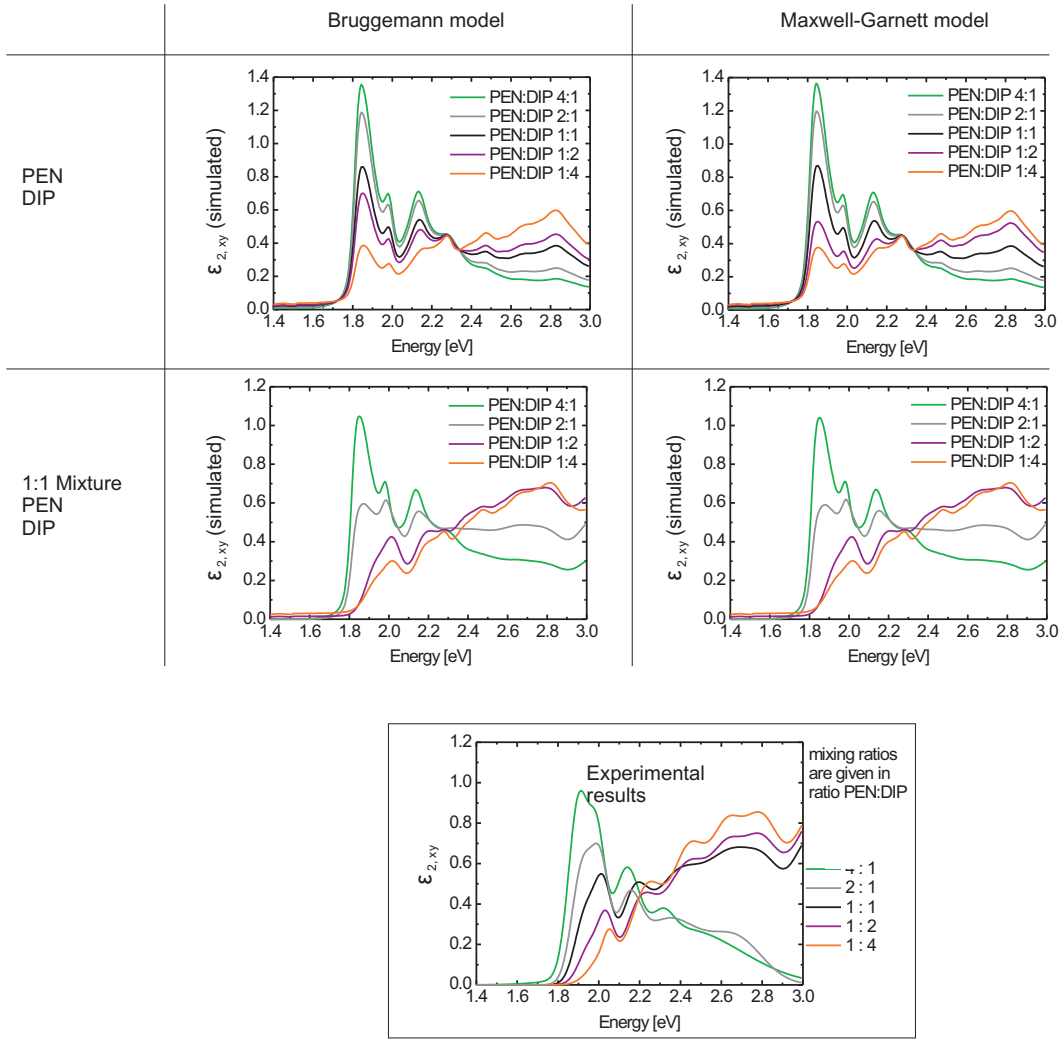

Figure 4.38: Calculated $\epsilon_{2,xy}^{eff}(E)$ based on the pure compound spectra (upper row) and based on the pure compound spectra *and* the $\epsilon_{2,xy}(E)$ of the equimolar mixture (lower row). For a detailed explanation see text. The experimentally determined $\epsilon_{2,xy}(E)$ is shown in the bottom diagram for comparison.

ment and consequently, the intermolecular interactions. This of course does not rule out that other mechanisms may also be at work which can only be elucidated by theoretical calculations.

4.4.3 Non-linear mixing effects

Based on the UPS data compiled in Ref. [108] a peak related to a possible CT transition between PEN and DIP would be expected at 1.5 eV, but there is clearly no indication for a transition at 1.5 eV in $\epsilon_{2,xy}(E)$ or $\epsilon_{2,z}(E)$ (Figs. 4.36 and 4.39). Nevertheless, the differences in the film structure may significantly influence the shape of $\epsilon_{2,xy}(E)$. Therefore, it was tested, if $\epsilon_{2,xy}(E)$ of the blends can be described by an effective medium approximation based on the pure compound spectra. The results are shown in Fig. 4.38. For those in the upper row $\epsilon_{2,xy}^{eff}(E)$ was calculated based on the $\epsilon_{2,xy}(E)$ of the pure compounds [59, 139] using the Bruggeman model [182] (left column) and the Maxwell-Garnett model [183] (right column). The general trend of the experimental data (see box in Fig. 4.38) with changing mixing ratio is reproduced, in particular regarding the decreasing intensity of the first two peaks and the increase in intensity of the peak at 2.8 eV with increasing volume fraction of DIP. This indicates that there is only weak interaction between PEN and DIP. However, the relative intensities of the first two peaks is significantly different between the calculated results and the experimental data and in addition, the shift of the first two peaks is not reproduced by the calculations.

In a next step it was tested whether $\epsilon_{2,xy}(E)$ of the different blends can be described as a combination of $\epsilon_{2,xy}(E)$ of the equimolar mixture and $\epsilon_{2,xy}(E)$ of the respective excess compound using the same effective medium approximations. For the mixtures containing more PEN, $\epsilon_{2,xy}(E)$ of the 1:1 mixture and $\epsilon_{2,xy}(E)$ of PEN was used for the calculations, while $\epsilon_{2,xy}(E)$ of the 1:1 mixture and $\epsilon_{2,xy}(E)$ of DIP was used to calculate $\epsilon_{2,xy}^{eff}(E)$ for mixtures containing more DIP. The results are shown in the lower row of Fig. 4.38 and are found to be in remarkable qualitative agreement with the experimental data. The shift of the first peak as well as changes in the relative intensities of the first two transitions are nicely reproduced. Differences in peak width of the calculated $\epsilon_{2,xy}^{eff}(E)$ compared with the experimentally determined $\epsilon_{2,xy}(E)$ are due to the increased disorder in the blends, which cannot be taken into account in the models used here. The agreement between experimental and calculated $\epsilon_{2,xy}(E)$ supports the assumption of low intermolecular interactions between PEN and DIP, while the differences reflect the influence of the film structure on $\epsilon_{2,xy}(E)$.

4.4.4 $\epsilon_{2,z}(E)$

For completeness $\epsilon_{2,z}(E)$ of different PEN:DIP mixing ratios determined with VASE are shown in Fig. 4.39. Due to the small intensity of $\epsilon_{2,z}(E)$ for pure PEN, the shape of $\epsilon_{2,z}(E)$ of the blends is dominated by contributions from DIP and exhibits only small changes with a changing mixing ratio, in particular regarding the line width, which increases with decreasing amount of DIP due to the decreasing structural order.

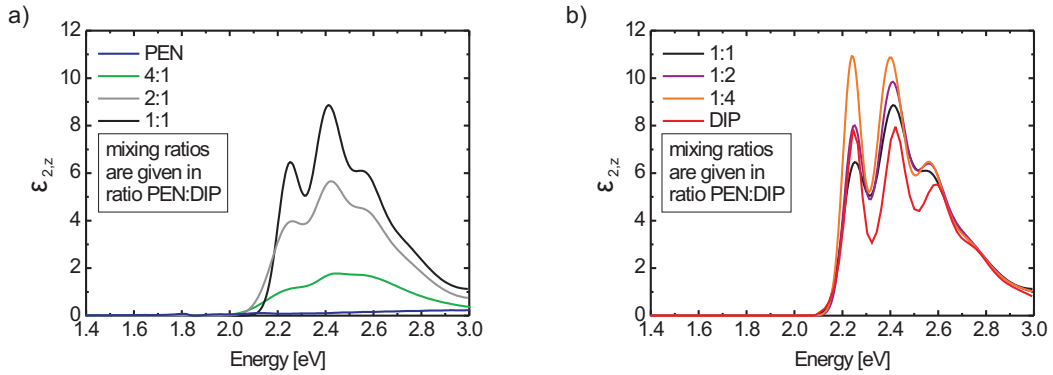

Figure 4.39: $\epsilon_{2,z}(E)$ of PEN:DIP thin films with different mixing ratios determined by VASE. Reference spectra of the pure films are taken from Refs. [59] (PEN) and [139] (DIP). Mixing ratios PEN:DIP a) 4:1, 2:1 and 1:1, b) 1:1, 1:2 and 1:4.

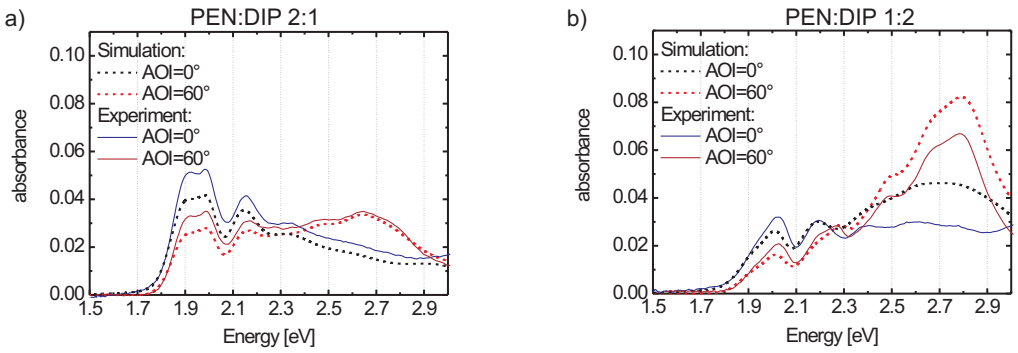

Figure 4.40: Comparison of simulated and experimentally determined absorbance for a) a PEN:DIP 2:1 and b) a PEN:DIP 1:2 blend. See text for details.

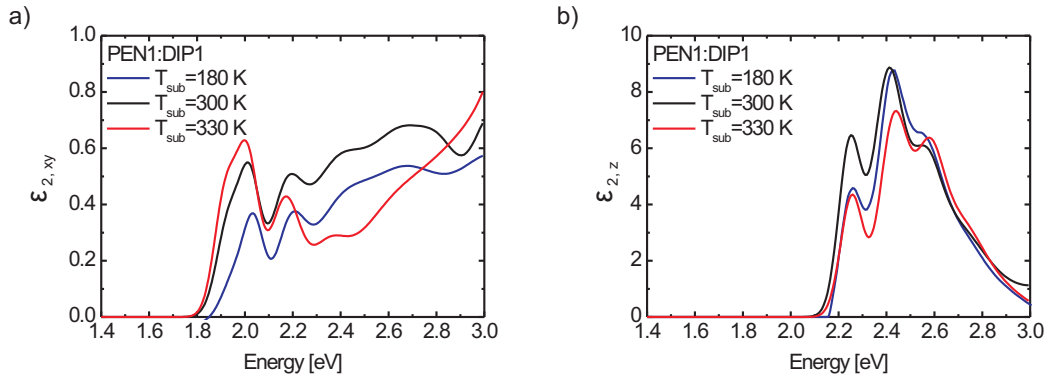

Figure 4.41: a) $\epsilon_{2,xy}(E)$ and b) $\epsilon_{2,z}(E)$ of equimolar PEN:DIP blends prepared at different substrate temperatures T_{sub}.

4.4.5 Comparison of transmission spectroscopy and VASE

Similar to PFP:DIP blends the reliability of the results obtained with VASE and DRS was tested by comparing the results with those obtained with transmission spectroscopy exemplarily for two mixing ratios (Fig. 4.40). For both mixing ratios the agreement between simulation and experiment is excellent. The small deviations are due to differences in film thickness and mixing ratio of the sample series measured with transmission spectroscopy and VASE.

4.4.6 Varying the substrate temperature

In Fig. 4.41 $\epsilon_{2,xy}(E)$ and $\epsilon_{2,z}(E)$ of equimolar PEN:DIP blends prepared at different substrate temperatures T_{sub} are shown. As there is no indication for changes in the film structure of PEN:DIP blends with changing substrate temperature, the absorption spectra are not expected to depend strongly on the substrate temperature during film growth. In agreement with this expectations, there are only very small changes observable, most pronounced for $\epsilon_{2,xy}(E)$ which are probably caused by increased disorder and accordingly, decreased short-range order within the film with decreasing substrate temperature. This is a possible explanation for the decreased intensity of the first Davydov-component in $\epsilon_{2,xy}(E)$ for the film grown at $T = 180$ K.

4.4.7 Summary

In conclusion, blends of the weakly interacting compounds PEN and DIP exhibit absorption spectra which resemble a superposition of the spectra of the pure compounds, but are significantly influenced by the decreased long-range order within the mixed films. The

first pronounced peak in $\epsilon_{2,xy}(E)$ is significantly blue shifted compared with PEN in pure films and its energy position changes continuously with the mixing ratio. This can be rationalized by the continuously changing local molecular environment, which stands in contrast to the mixing behavior of the other two mixed systems for non-equimolar mixing ratios.

4.5 Comparison

In the previous sections the absorption spectra of PFP:PEN, PFP:DIP and PEN:DIP blends were investigated. The three systems differ in mixing and ordering behavior as well as in the strength of intermolecular interactions. These differences have been found to affect the optical properties to a large extent.

For blends of PFP and PEN the shape of the absorption spectrum of the equimolar mixture is significantly different from the pure film spectra regarding the relative intensities of the peaks, including the observation of a CT peak at $E = 1.6$ eV. This is also true for mixing ratios of PFP:PEN 2:1 and 1:2, indicating strong intermolecular interactions. The shape of $\epsilon_{2,xy}(E)$ and $\epsilon_{2,z}(E)$ for mixing ratios of PFP:PEN 4:1 and 1:4 resembles the shape of the pure film spectra with some minor differences caused by inhomogeneities in the films due to the phase separation between the intermixed crystal phase and the pure phase of the respective excess compound.

For PFP:DIP blends, which were expected to exhibit a comparable intermolecular interaction, no clear CT transition was observed. This might be due to the fact that the corresponding peak can be expected at $E = 2.0$ eV, which makes it difficult to distinguish the possible CT peak from peaks arising from the pristine compounds. Another reason may be the significantly different spectral range in which PFP and DIP are absorbing or the orientation of the transition dipole moments of the two compounds, preventing an efficient coupling of excitations in case of upright standing molecules. In general, the shape of the absorption spectra of the PFP:DIP blends resembles the shape of the pure film spectra, although some differences are observable. For example, the first two peaks which could be attributed to PFP are significantly different in their relative intensities compared with the pure film spectrum, indicating changes in the intermolecular environment or the structural order. Also the "fourth mode" of DIP at 2.8 eV is weaker in the blends than in pure films due to the reduced interaction between DIP molecules.

Finally, in the absorption spectra of mixed films of PEN and DIP no indications for a CT are found. Apart from the chemical similarity of PEN and DIP, this may be due to the differences in the spectral range in which PEN and DIP are absorbing as well as in the orientation of the transition dipole moment of the HOMO-LUMO transition as discussed already for blends of PFP:DIP. The shape of $\epsilon_{2,xy}(E)$ of PEN:DIP blends changes continuously with the mixing ratio. From the changes in relative intensities of the first two peaks attributed to PEN a significantly reduced long-range order could be deduced which is in nice agreement with the reported film structure [36].

Comparing the three systems regarding the line shape of the absorption spectra, as

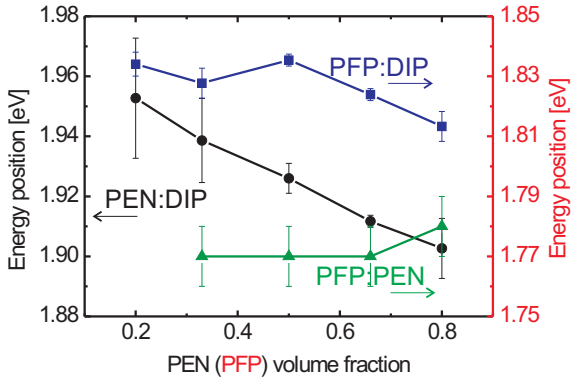

Figure 4.42: Comparison of the energy position of the first pronounced peak (except the CT transition) as a function of the volume fraction of PEN for blends of PEN:DIP (black dots) and as a function of the volume fraction of PFP for blends of PFP:PEN (green triangles) and PFP:DIP (blue squares). The energy position of the first peak for the PFP:PEN 1:4 blend is not shown as this peak is attributed to PEN instead to PFP.

well as regarding observable peak shifts, it is worth pointing out that (except for the CT transition in PFP:PEN blends) the first peak in $\epsilon_{2,xy}(E)$ is significantly blue shifted for all blends and mixing ratios. It would be interesting to study whether this blue shift is a general effect in blends of organic semiconductors. The origin of the shift could be changes in the intermolecular environment and accordingly, in the intermolecular interactions in the mixed films compared with films of the pure compounds, similar to a solvent shift observed in the absorption spectra of molecules in solution and in thin films [166].

The dependence of this blue shift on the mixing ratio is remarkably different for the three mixed systems (Fig. 4.42). While the energy position of the first pronounced peak shifts continuously to lower photon energies in the case of PEN:DIP blends, a discontinuous peak shift is observed for PFP:PEN and PFP:DIP blends. A possible explanation for this observation are the differences in the mixing and ordering behavior of the three systems.

Non-equimolar blends of PFP:PEN and PFP:DIP exhibit a phase separation between the intermixed crystal phase and the pure phase of the respective excess compound. Accordingly, the observed peak shift can be seen as a superposition of two effects:

i) A shift of the peak position to which molecules in the mixed film phase contribute due to the different polarizability of the intermolecular environment in the blend compared with the pure films. This shift is the same for all mixing ratios.

ii) A shift, which results from the changing fraction of molecules at the boundary between mixed and pure film phase with the mixing ratio. These molecules at the boundaries encounter a different polarizability of the intermolecular environment depending on the excess compound in the blend, resulting in different shifts depending on the mixing ratio.

The combination of these two effects results in a peak shift which is not monotonic.

Interestingly, for PFP:PEN blends the blue shift is strongest (30 meV) for the mixing ratio PFP:PEN 4:1 and is, within the error bar, identical for the mixing ratios PFP:PEN 2:1, 1:1 and 1:2. The shift of the first peak in $\epsilon_{2,xy}(E)$ for the PFP:PEN 1:4 mixture relative to the HOMO-LUMO transition of pure PEN is comparable to the shift of the PFP:PEN 4:1 mixture relative to the HOMO-LUMO transition of pure PFP. This is in contrast to blends of PFP:DIP, where a clear maximum in peak shift is observed for the equimolar mixture and is possibly related to the strong influences of intermolecular interactions on the optical properties of PFP:PEN blends, which makes it difficult to relate peaks to the respective pure compounds. Furthermore, the difference in energy position of the HOMO-LUMO transitions of PFP and PEN is much smaller compared with the difference of the HOMO-LUMO transitions of PFP and DIP, which makes is more difficult to distinguish peaks related to PFP from peaks related to PEN.

In contrast to the other two systems for PEN:DIP blends a continuous shift of the energy position of the first pronounced peak in $\epsilon_{2,xy}(E)$ is found, which can be rationalized by the continuous change of the film structure and accordingly, the intermolecular environment with the mixing ratio, as discussed before (Sec. 4.4.2).

Additionally, also differences in the strength of intermolecular interactions were found to affect the optical properties, with the most pronounced effect being the CT peak observable in blends of PFP:PEN. Other influences can be found when comparing $\epsilon_{2,xy}^{eff}(E)$ resulting from effective medium approximations with the experimentally determined $\epsilon_{2,xy}(E)$. For blends of PEN:DIP the evolution of relative intensities and energy positions is reasonably well reproduced by EMA models, although the shape $\epsilon_{2,xy}^{eff}(E)$ and $\epsilon_{2,xy}(E)$ exhibits slight differences since the effects of decreased long-range order cannot be taken into account in the EMA models. For the two strongly interacting systems, EMA models are not able to reproduce the line shape of $\epsilon_{2,xy}(E)$ of PFP:PEN blends or the energy shift in blends of PFP:DIP, supporting that there are indeed strong intermolecular interactions present in these systems.

In summary, in this chapter the absorption spectra of PFP:PEN, PFP:DIP and PEN:DIP blends with various mixing ratios and prepared at different substrate temperatures have been investigated post growth. For the strongly interacting and sterically highly compatible compounds PFP and PEN strong influences of intermolecular interactions have been observed, including charge transfer. Although PFP and DIP are expected to exhibit comparably strong and favorable interaction, there is no clear evidence for a charge transfer peak in the absorption spectra and contributions of the pure compunds can still be distinguished in the absorption spectra. For blends of PEN and DIP the contributions of the pure compounds can clearly be discerned. However, due to the reduced long-range order in the mixed films, there are significant differences between the absorption spectra of the mixed films and the pure films.

Apart from the influence on the line shape the differences in local molecular environment, resulting from the differences in mixing and ordering behavior were found to influence the energy position of the first observable peak (with the exception of the CT peak in PFP:PEN blends) in the absorption spectra and its dependence on the mixing ratio.

Chapter 5

Results and discussion II

Growth is a non-equilibrium process and in complex systems such as mixed films the intermolecular interactions between the two compounds as well as a possible size mismatch may lead to pronounced changes in the film structure with time. Due to the tight connection of structural and optical properties, the latter may strongly be affected by these changes. Furthermore, differences in the intermolecular interactions and the intermolecular environment as well as changes in the surface-to-bulk ratio may result in shifts of energy positions of peaks or an increase in intensity of specific peaks during growth.

As discussed in Sec. 4.1 the mixing and ordering behavior of the three mixed systems which are in the focus of this study exhibits some differences not only for equimolar blends but also for non-equimolar mixing ratios. While for non-equimolar blends of PFP:PEN and PFP:DIP a phase separation between the intermixed crystal phase and a pure phase of the excess compound is found [127,176], in blends of PEN:DIP molecules of the minority compound occupy randomly sites in a lattice formed by the excess compound [36]. Apart from the effects mentioned before, the differences in mixing and ordering behavior can influence the real-time evolution of $\epsilon_2(E)$ for the different blends and investigations of these influences may contribute to a further understanding of the connection of film structure and optical properties in mixed systems.

In the following chapter, real-time investigations of the three mixed systems will be discussed, starting with studies of possible changes in film structure of PFP:DIP and PEN:DIP blends using grazing incidence X-ray diffraction. For results of detailed real-time studies of PFP:PEN blends the reader is referred to Ref. [232].

The focus of this chapter will be on the evolution of the shape of the absorption spectra, concentrating on $\epsilon_{2,xy}(E)$, which can be investigated using DRS. The results will be presented for the five different mixing ratios and three substrate temperatures of PFP:PEN, PFP:DIP and PEN:DIP, respectively, complementing the results of absorption spectra measured post growth. Finally, possible changes observed for the three systems will be compared and discussed relating to the differences in mixing and ordering behavior and to possible structural changes during growth.

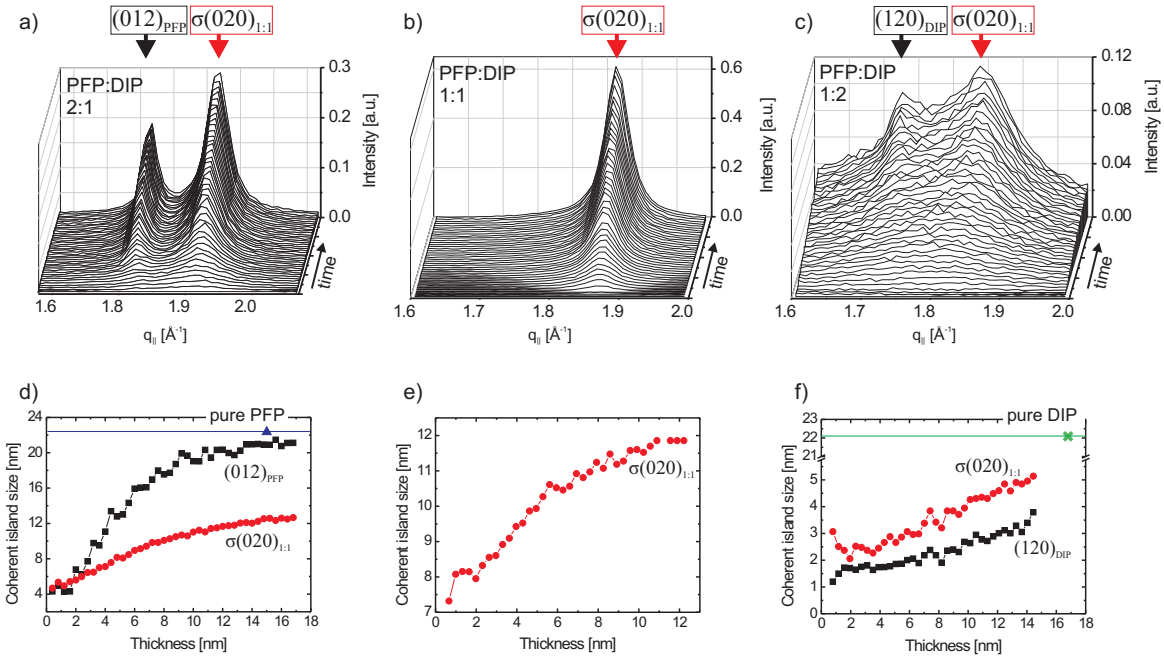

Figure 5.1: Upper row: real-time GIXD data of PFP:DIP-mixtures prepared at a substrate temperature of T_{sub} = 300 K. Lower row: coherently scattering island size as a function of film thickness d. Mixing ratios PFP:DIP: 2:1 (a, d), 1:1 (b, e) and 1:2 (c, f). For comparison the size of the coherently scattering islands of pure PFP (blue triangle and solid line Ref. [127]) and pure DIP (green cross and solid, line film measured at beam line ID10B, ESRF, France) is also shown in (d) and (f), respectively.

5.1 Real-time grazing incidence X-ray diffraction experiments

5.1.1 Blends of PFP and DIP

The following section is based on Ref. [233]. Possible changes in crystalline order and unit cell parameters during growth of PFP:DIP blends were investigated in real-time using grazing incidence X-ray diffraction (GIXD) at the SLS in Villigen, Switzerland. The range from $q_{||} = 1.61$ Å^{-1} to $q_{||} = 1.99$ Å^{-1} was probed, where the $\sigma(020)$-reflection of the mixed crystal phase is found. For non-equimolar blends the (012)-reflection of pure PFP or the (120)-reflection of pure DIP are also observed in this q-range depending on the mixing ratio and the corresponding excess compound.

Figure 5.1a-c shows the real-time GIXD data. Each line corresponds to a different film thickness d, with d increasing linearly with time. The peaks were fitted with Lorentzians using the program Fityk [229] and the size, i.e. the average diameter, l_s of the coherently

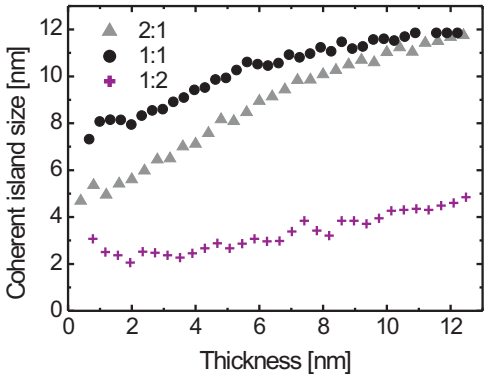

Figure 5.2: Comparison of the evolution of l_s of the mixed film phase (see data in Fig. 5.1) in the different blends. Circles: Equimolar mixture, triangles: PFP:DIP 2:1, crosses: PFP:DIP 1:2.

scattering islands was determined using the Scherrer-formula. The evolution of l_s with the film thickness d is shown in Fig. 5.1d-f.

For comparison also values for pure films are shown in Fig. 5.1d and Fig. 5.1f. Note the difference by more than a factor of 4 between the crystallite size in the pure DIP film compared to the DIP-phase in the mixture (Fig. 5.1f). In contrast to this, the crystallite size in the pure PFP film and the PFP-phase in the mixture is in remarkable agreement (Fig. 5.1d). Apart from this finding also differences in the nucleation of the crystallites are observed. In the blend containing more DIP, only small crystallites of the DIP excess phase form which do not grow significantly with film thickness (l_s = 1.7 nm for d=1.5 nm and l_s = 3.8 nm for d=14.4 nm). For the mixture containing more PFP the crystallite size of the PFP phase is l_s = 4.3 nm in the beginning of growth (d=1.5 nm) and increases by almost a factor of 5 as the growth proceeds (l_s = 20.9 nm at d=16 nm).

Remarkably, also l_s of the mixed film phase is influenced by the mixing ratio (Fig. 5.2). For the PFP:DIP 1:2 blend a maximum l_s of 5 nm is observed, which is a factor of 2 smaller compared with the l_s for the PFP:DIP 1:1 and PFP:DIP 2:1 blend. Furthermore, l_s of the mixed film phase at the beginning of film growth is largest in the equimolar mixture, indicating that the nucleation of new crystallites is hindered by the formation of crystallites of the excess compound in non-equimolar blends. It appears that the stable 1:1 mixed crystal can more easily be disturbed by a DIP excess than by a PFP excess. This means that from the point of view of the free energy potential surface an excess DIP molecule is more probable to produce a stacking error than an excess PFP molecule. Such an asymmetric mixing behavior was also observed for a 2D mixture of pentacene and perfluorinated Cu-Phtalocyanine [244].

	PEN:DIP 2:1	PEN:DIP 1:1	PEN:DIP 1:2
$T_{sub} = 330$ K	-	#4	-
$T_{sub} = 300$ K	#2	#1	#3
$T_{sub} = 280$ K	-	#5	-

Table 5.1: Samples investigated using GIXD in real-time during growth.

5.1.2 Blends of PEN and DIP

Similar to blends of PFP:DIP the growth of PEN:DIP blends was studied in real-time using GIXD. The main purpose was to investigate whether the long-range order is low from the beginning of the film growth or vanishes *during* the growth process. The GIXD experiments were performed at beamline ID10B at the European Synchrotron Radiation Facility (ESRF) in Grenoble, France with a wavelength of $\lambda = 0.9298$ Å using a Mar-CCD to probe a large range in q-space. Five different samples were investigated, which differed either in the mixing ratio or in the substrate temperature during growth, see Table 5.1

In these experiments for most preparation conditions (#1, #2, #4, #5) no indications for changes in the long-range order during growth were observed. The long-range order parallel to the substrate surface was very low for all film thicknesses, mixing ratios and substrate temperatures, with complete vanishing of in-plane order for the equimolar mixtures.

The sample #3 (PEN:DIP 1:2 prepared at 300 K) was the only sample were changes in the peak intensity were observed during film growth, see Fig. 5.3. However, the increase in intensity of the three in-plane Bragg-peaks and Bragg-peaks with a non-zero q_z-component is probably related to an increasing number of molecules in the given crystal structure. Since the width or q_{xy}-position of the peaks is not changing, there are also for this sample no apparent changes in structural order or unit cell parameters observable during film growth. Due to their q_{xy}-positions, these Bragg-peaks can be assigned to DIP [87], which is in agreement with the observed mixing and ordering behavior (Sec. 4.1.3). For non-equimolar mixing ratios minority molecules randomly occupy sites in a lattice formed by the excess compound. Accordingly, in sample #3 the lattice is formed by DIP molecules and PEN molecules occupy sites in this lattice, resulting in a behavior similar to pure DIP films. Compared with pure DIP, the long-range order is slightly reduced in the PEN:DIP blend, since the minority molecules occupy sites and lead to lattice distortion. However, as it is already observed post growth (Sec. 4.1.3), the lattice distortion is lower in blends with DIP as excess compound compared with blends with PEN as excess compound, probably due to the differences in the steric properties of PEN and DIP.

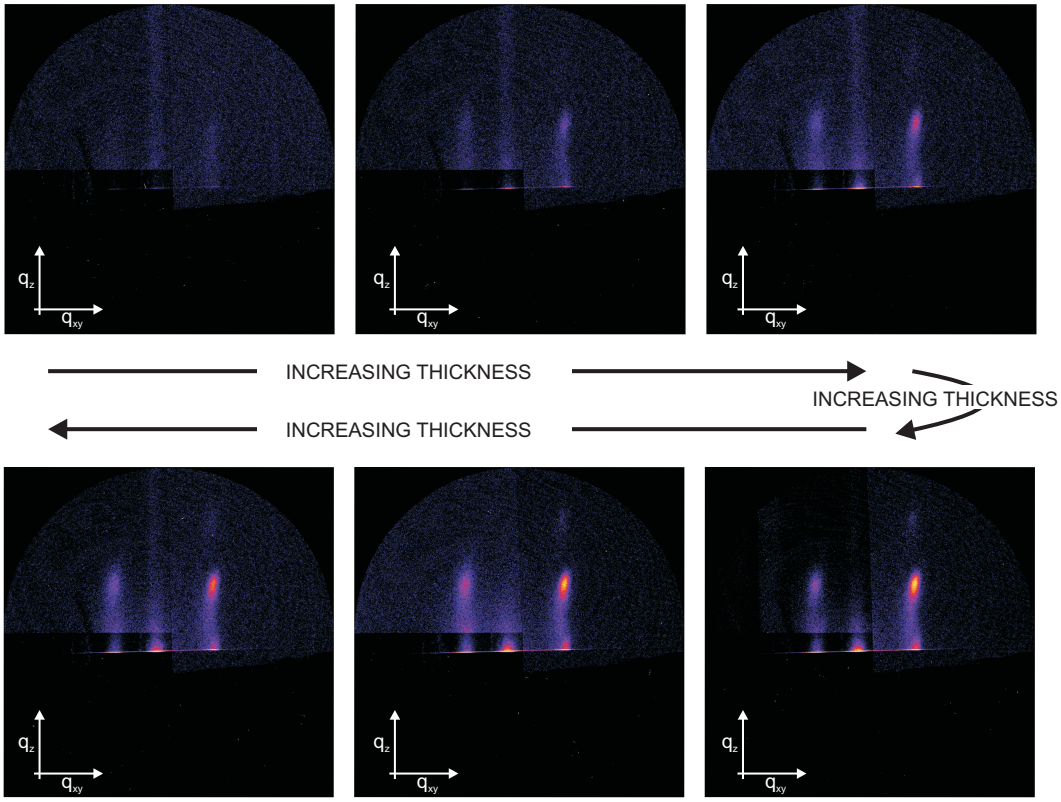

Figure 5.3: Background corrected CCD-images of a PEN:DIP 1:2 blend taken at different film thicknesses.

5.2 Real-time investigations of $\epsilon_{2,xy}(E)$: Blends of PFP and PEN

In order to complement the post growth studies of the optical properties of PFP:PEN blends discussed in Sec. 4.2, the absorption spectra were investigated in real-time during film growth using DRS. The results are compiled in Fig. 5.4 and are in reasonable agreement with the result obtained post growth using SE (Sec. 4.2). The small differences observed are due to deviations in the mixing ratio and the different morphology of the films prepared on natively oxidized silicon and glass.

There are remarkable changes observable in the shape of $\epsilon_{2,xy}(E)$ during growth of the PFP:PEN-blends with mixing ratios PFP:PEN 4:1, 2:1 and 1:2 (Fig. 5.4a, b and d). For a possible interpretation of these changes it is important to note that the spectrum of non-equimolar PFP:PEN blends is expected to resemble a superposition of the spectral response of the PFP pure film phase and the equimolar PFP:PEN mixed crystal phase due to the mixing and ordering behavior of PFP:PEN blends [127]. For blends with PFP as excess compound the intensity of a peak at 1.75 eV is clearly increasing relative to other peaks in $\epsilon_{2,xy}(E)$ with increasing film thickness (Fig. 5.5). Due to its energy position this peak can be assigned to the HOMO-LUMO transition of pure PFP [59]. A similar effect is also observed for the PFP:PEN 1:2 blend (Fig. 5.4d), where the intensity of a peak at 1.89 eV, which can be assigned to PEN, is increasing with film thickness. Since this peak is possibly overlapping with contributions from PFP, the increase in intensity is not as clear as for the blends with more PFP. For the PFP:PEN 1:4 blend there is even no pronounced change in the line shape observable.

The comparison of the relative intensities of the first two pronounced peaks in $\epsilon_2(E)$ of PFP measured in solution and in thin films provides a possible explanation for the changes in line shape of $\epsilon_{2,xy}(E)$ during growth of the PFP:PEN 4:1 and 2:1 blend (Fig. 5.6). The first two peaks in the solution spectrum of PFP (red arrows in Fig. 5.6a) are assigned to the HOMO-LUMO transition and a corresponding vibronic progression [59]. For the first two peaks in $\epsilon_{2,xy}(E)$ of PFP thin films (red arrows in Fig. 5.6b) it is not yet clear whether they can be assigned to the HOMO-LUMO transition and a vibronic progression or to two Davydov-components of the HOMO-LUMO transition [128]. The results of the real-time investigations presented here and in the following section point towards the former assignment, although this issue cannot concludingly be settled without further experiments. Assuming in the following, that the first two peaks in Fig. 5.6b are assigned to the HOMO-LUMO transition and a corresponding vibronic progression, it can be clearly seen that their relative intensities change when going from solution (i.e. the monomer spectrum) to a thin film. The intensity of the first peak is increasing compared with that of the second peak. This may be due to the increased disorder in the solution and the differences in the local molecular environment and associated intermolecular interactions in solution compared with the thin film. Based on this result the change in relative intensity of the first peak during growth of the PFP:PEN 2:1 blend (red arrow in Fig. 5.6c) can tentatively be assigned to an increasing structural order in the PFP excess phase during

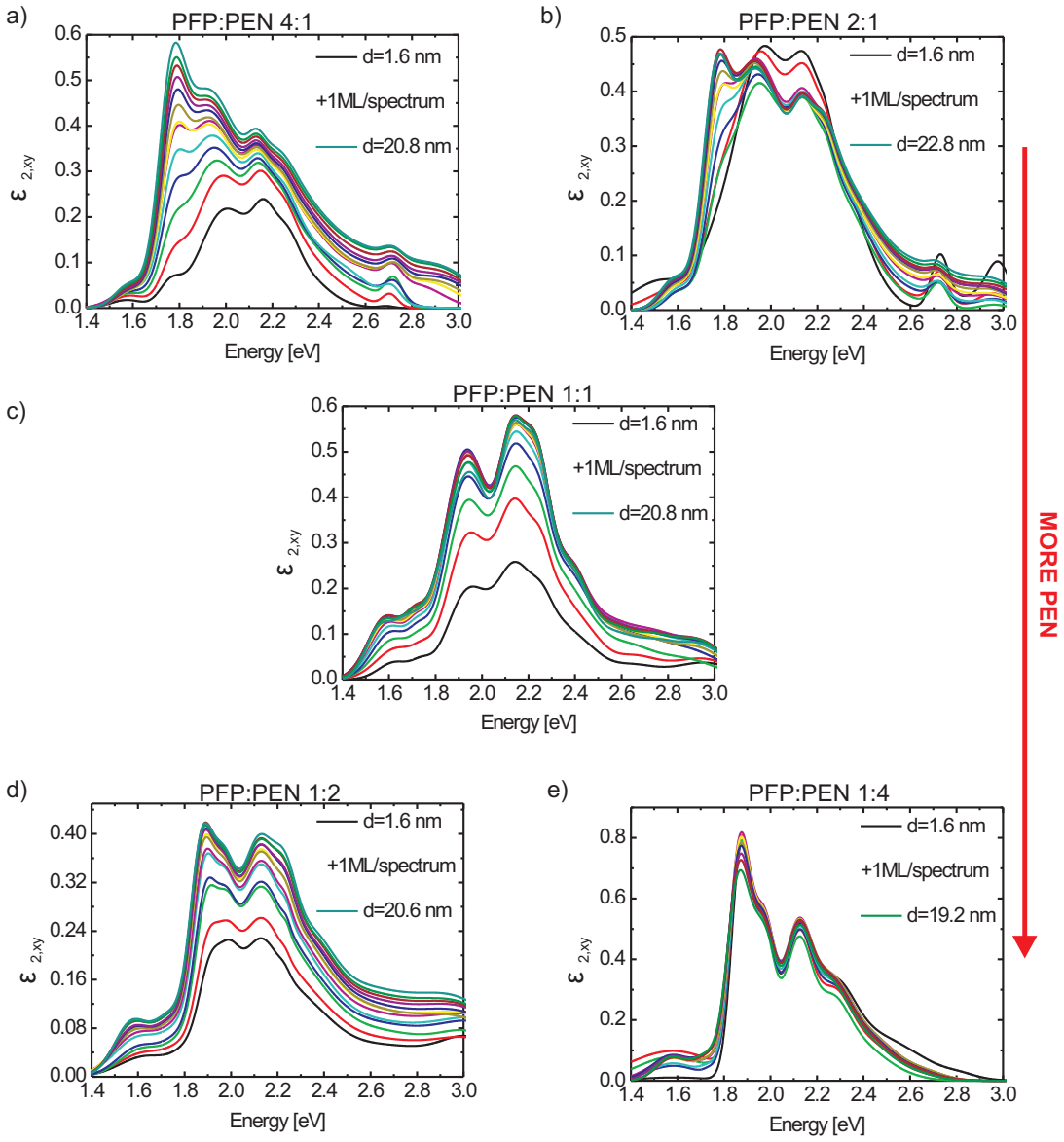

Figure 5.4: Real-time evolution of $\epsilon_{2,xy}(E)$ for blends of PFP:PEN with different mixing ratios measured using DRS. Each spectrum corresponds to a different film thickness with 1 ML $\approx$ 1.6 nm. Mixing ratios: a) PFP:PEN 4:1, b) PFP:PEN 2:1, c) PFP:PEN 1:1, d) PFP:PEN 1:2, e) PFP:PEN 1:4.

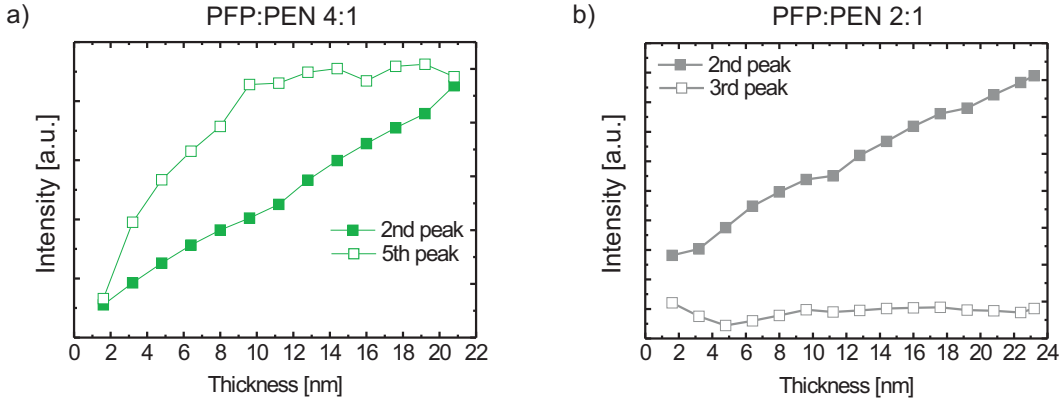

Figure 5.5: Intensity as a function of film thickness of a) the second and fifth peak in the PFP:PEN 4:1 blend and b) the second and third peak in the PFP:DIP 2:1 blend.

film growth. At the beginning of the growth, the molecules are rather disordered, leading to $\epsilon_{2,xy}(E)$ resembling $\epsilon_2(E)$ of PFP in solution. As the growth proceeds the order in the PFP excess phase is increasing and the shape of $\epsilon_{2,xy}(E)$ approaches $\epsilon_{2,xy}(E)$ of PFP in thin films.

While it is possible to rationalize the observed changes in line shape of $\epsilon_{2,xy}(E)$ with this argumentation, GIXD experiments in real-time during growth of a PFP:PEN 4:1 or 2:1 blend would be necessary to support these speculations. Although there are unfortunately no real-time investigations of the structural order in non-equimolar PFP:PEN blends reported yet, it can be expected that the structural order evolves similar to that in PFP:DIP-blends, which exhibit a similar mixing and ordering behavior [176]. As discussed in Sec. 5.1.1 there is indeed an increasing size of coherently scattering islands (which is related to the structural order) of the pure PFP phase during growth of a PFP:DIP 2:1 blend.

The changes in line shape of $\epsilon_{2,xy}(E)$ of the PFP:PEN 1:2 blend can be rationalized by a similar mechanism (increasing long-range order in the PEN excess phase during film growth), although in this case the assignment of the peaks in solution and thin film spectrum is less clear [59, 113]. In this context it is interesting to note that the shape of $\epsilon_{2,xy}(E)$ of the PFP:PEN 1:4 blend is not changing during film growth. This may indicate that the long-range order in the PEN phase is not improving but is high from the beginning of film growth.

Finally, the influence of the substrate temperature on the real-time evolution of $\epsilon_{2,xy}(E)$ of equimolar PFP:PEN blends was studied using DRS. The following is based on Ref. [178]. As discussed in Sec. 4.2.5 molecules in PFP:PEN-blends exhibit two different orientations: The σ-orientation in which the molecules are almost standing upright on the substrate

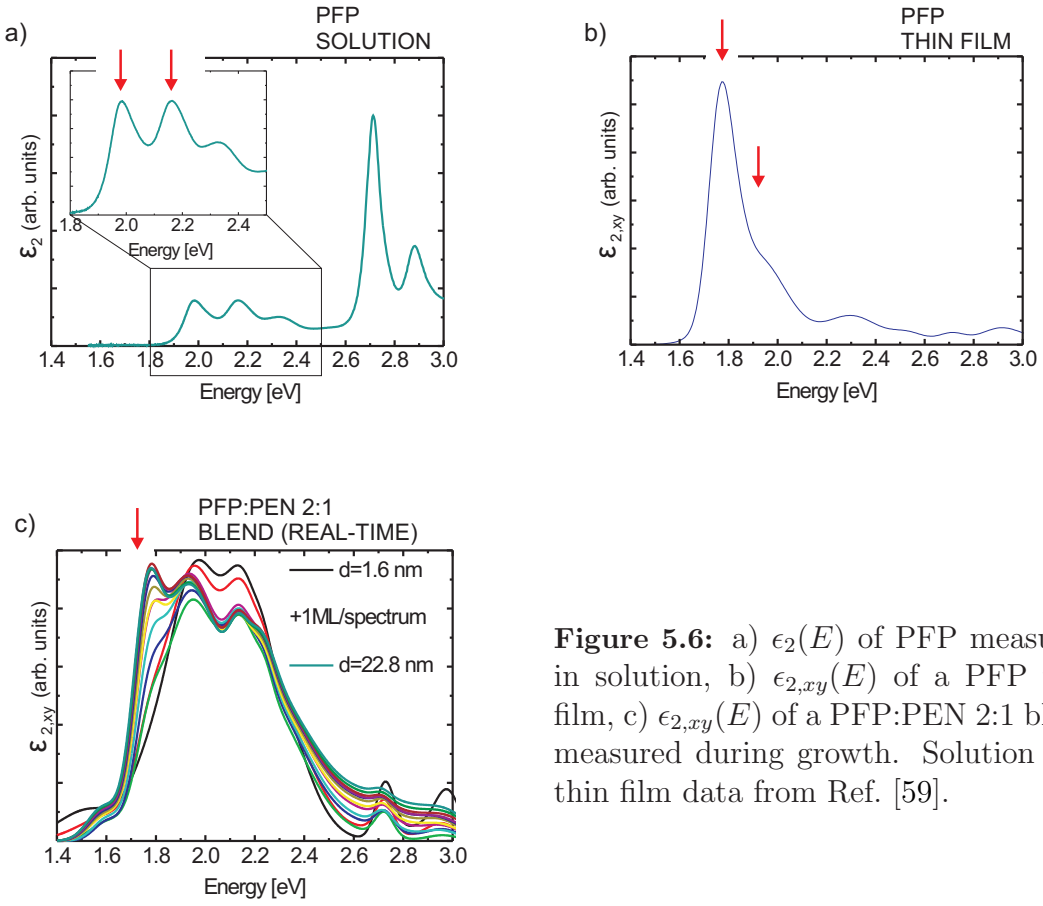

Figure 5.6: a) $\epsilon_2(E)$ of PFP measured in solution, b) $\epsilon_{2,xy}(E)$ of a PFP thin film, c) $\epsilon_{2,xy}(E)$ of a PFP:PEN 2:1 blend measured during growth. Solution and thin film data from Ref. [59].

surface and the λ-orientation in which the molecules are nearly lying down [127]. The amount of molecules in the two orientations changes with changing substrate temperature [127], which influences the shape of $\epsilon_{2,xy}(E)$ of PFP:PEN blends prepared at different substrate temperatures (Sec. 4.2.5).

The results of the real-time investigations of $\epsilon_{2,xy}(E)$ during growth are shown in Fig. 5.7. The arrows indicate changes in the line shape of $\epsilon_{2,xy}(E)$ with increasing film thickness d. Apart from a slight increase in overall intensity, the spectra of the blends prepared at substrate temperatures $T = 300$ K and $T = 330$ K are not changing for the different film thicknesses. In contrast to this, the line shape of $\epsilon_{2,xy}(E)$ of the blend prepared at $T = 180$ K changes significantly during growth, see Fig. 5.7c. Clearly, the intensity of the peak at 2.7 eV, which is assigned to the λ-orientation, is increasing in intensity relative to the other peaks in the spectrum (Fig. 5.8). This may indicate differences in the nucleation of the domains in σ- and λ-orientation. For small film thicknesses d the σ-orientation dominates and the line shape of $\epsilon_{2,xy}(E)$ resembles that of the blends prepared at higher substrate temperatures (compare Fig. 5.7a, b and

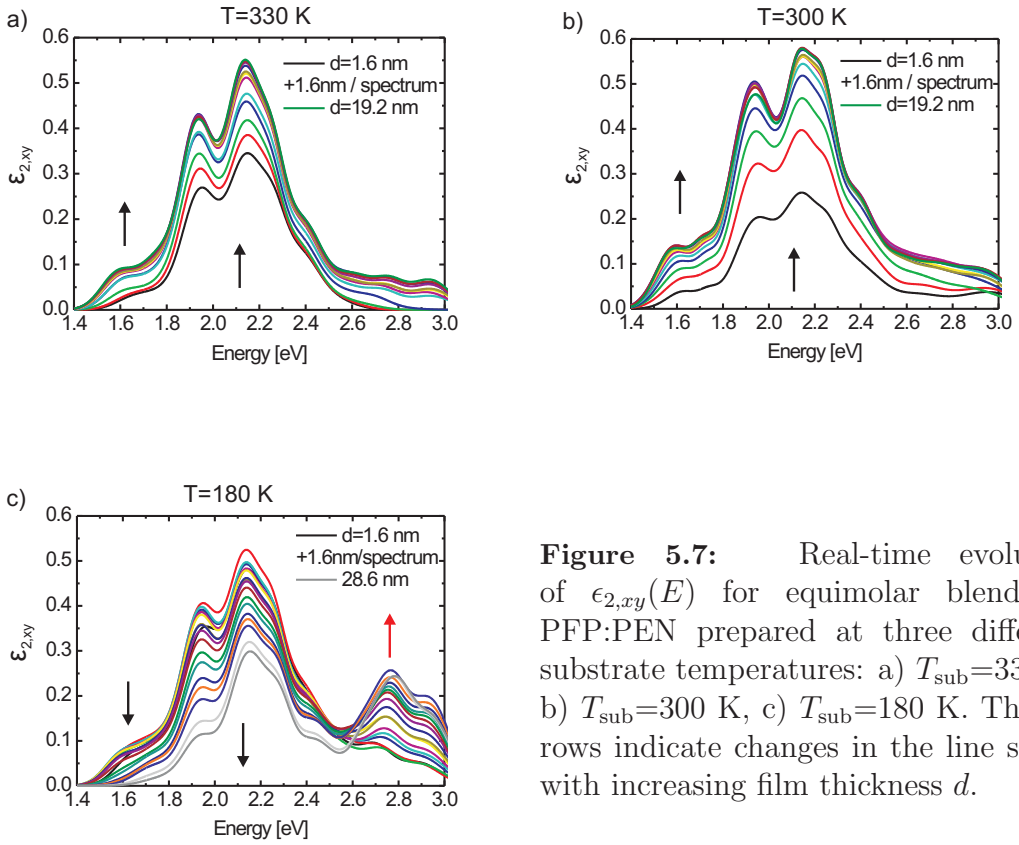

Figure 5.7: Real-time evolution of $\epsilon_{2,xy}(E)$ for equimolar blends of PFP:PEN prepared at three different substrate temperatures: a) T_{sub}=330 K, b) T_{sub}=300 K, c) T_{sub}=180 K. The arrows indicate changes in the line shape with increasing film thickness d.

Fig. 5.8a). With increasing film thickness the intensity of the peak at 2.7 eV is increasing (Fig. 5.8c), as domains with molecules in λ-orientation begin to grow. Note that there is no indication for a saturation in the investigated thickness range ($d = 1.6 - 23$ nm).

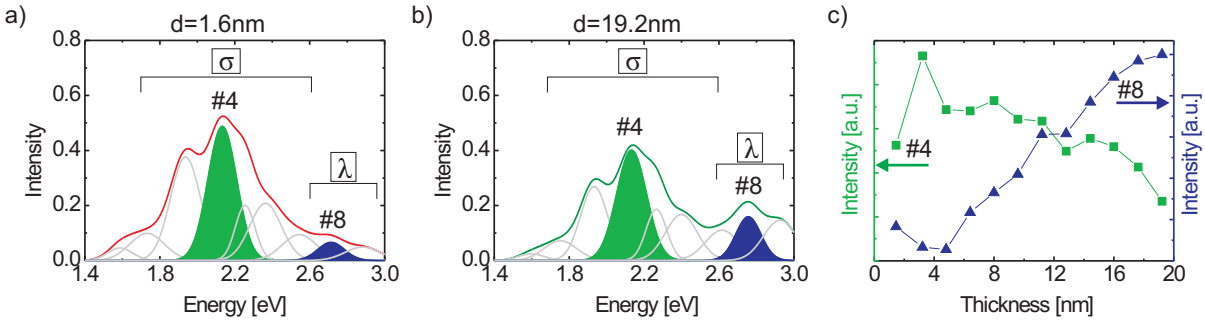

Figure 5.8: a) and b) Oscillators describing $\epsilon_{2,xy}(E)$ of an equimolar PFP:PEN blend prepared at T_{sub}=180 K for two different film thicknesses d. c) Evolution of the intensity of the peaks at $E = 2.1$ eV (#4) and $E = 2.7$ eV (#8) with increasing film thickness.

It is noted that neither the energy position nor the intensity of the CT peak at 1.6 eV is changing significantly during growth of most of the samples investigated. This indicates that the CT is only weakly influenced by changes in the film thickness, in the surface-to-bulk ratio or the volume fraction of the two molecules. The decreasing intensity of the CT peak with increasing film thickness during growth of the equimolar PFP:PEN prepared at $T = 180$ K may result from the increasing fraction of molecules in λ-orientation, for which the CT between PEN and PFP may be less efficient.

In summary, in this section the real-time evolution of $\epsilon_{2,xy}(E)$ during growth of PFP:PEN blends with different mixing ratios and prepared at different substrate temperatures was studied using DRS. Indications for a significant impact of changes in structural order on the shape of $\epsilon_{2,xy}(E)$ were found in particular during growth of non-equimolar blends containing more PFP. Furthermore, an increase in intensity of a peak at 2.7 eV in $\epsilon_{2,xy}(E)$ during growth of an equimolar blend prepared at a substrate temperature of 180 K possibly points towards a delayed nucleation of domains with molecules in λ-orientation.

5.3 Real-time investigations of $\epsilon_{2,xy}(E)$: Blends of PFP and DIP

The following section is based on Ref. [233]. Figure 5.9 shows the real-time evolution of $\epsilon_{2,xy}(E)$ for blends of PFP:DIP with different mixing ratios measured by DRS. Each spectrum corresponds to a different film thickness. The intensities and energy positions of the peaks in $\epsilon_{2,xy}$ at the final film thickness are in reasonable agreement with the results of VASE (compare Sec. 4.3.2). The small differences are probably due to deviations in the mixing ratio (which is determined with an uncertainty of 10% due to the error of the QCM) and differences in the morphology of the films on glass and silicon. It is noted that the additional shoulder at 1.75 eV which is observed for blends containing more PFP using VASE cannot be observed using DRS. This may be due to the fact that the films grown on glass are rougher and possibly exhibit a higher disorder, leading to an increase in peak width which may make it difficult to resolve the weak shoulder at 1.75 eV.

Remarkably, there are strong changes observable in the line shape of $\epsilon_{2,xy}(E)$ with increasing film thickness, in particular for the blends containing more PFP (Fig. 5.9a, b), for which the relative intensity of the first two peaks at 1.8 eV and 2.0 eV changes strongly with the film thickness d (Fig. 5.10). While the first peak is weaker than the second peak for low film thicknesses, it becomes more intense with film thickness, until the shape of $\epsilon_{2,xy}(E)$ resembles that of pure PFP [59]. These two peaks can be assigned to pure PFP and are interpreted either as the two Davydov-components of the HOMO-LUMO transition or as the HOMO-LUMO transition and a corresponding vibronic progression [59,128]. Hence, similar to PFP:PEN blends, a change in the relative intensities of the two transitions could point towards differences in the intermolecular environment and accordingly, in the intermolecular interactions during film growth. A possible origin of these changes is the increase in the size of coherently scattering islands of the PFP excess phase, which are observed in the real-time GIXD experiments (see Fig. 5.1a). Due to the small crystallite size at the beginning of the growth, the shape of $\epsilon_{2,xy}(E)$ resembles $\epsilon_2(E)$ of PFP in solution [59], in particular regarding the relative intensity of the first two peaks. With l_s increasing, and accordingly, improving structural order, the shape of $\epsilon_{2,xy}(E)$ approaches that of $\epsilon_{2,xy}(E)$ of pure PFP films. Small differences in the shape of $\epsilon_{2,xy}(E)$ between the mixed and the pure film could be due to the contributions from DIP and the different intermolecular interactions within the intermixed phase.

In the equimolar mixture (Fig. 5.9c) the most pronounced changes are observed in the spectral region from 2.2 eV to 2.6 eV. Here, clear indications for a reorientation of the molecules are found, as two strong peaks decrease significantly in intensity with increasing film thickness. From the comparison with $\epsilon_{2,z}$ of DIP, which has strong absorption features in this spectral region [139], these two peaks can tentatively be assigned to this compound. A possible explanation for the observed change in intensities could be a reorientation of the DIP molecules, as it is reported for pure DIP films [94]. In the peak position of the $\sigma(020)$-reflection of the mixed film phase a small shift of $\Delta q_{||} = 0.0015$ Å^{-1} to lower values of $q_{||}$ during film growth can be observed which supports this interpretation. Due to the

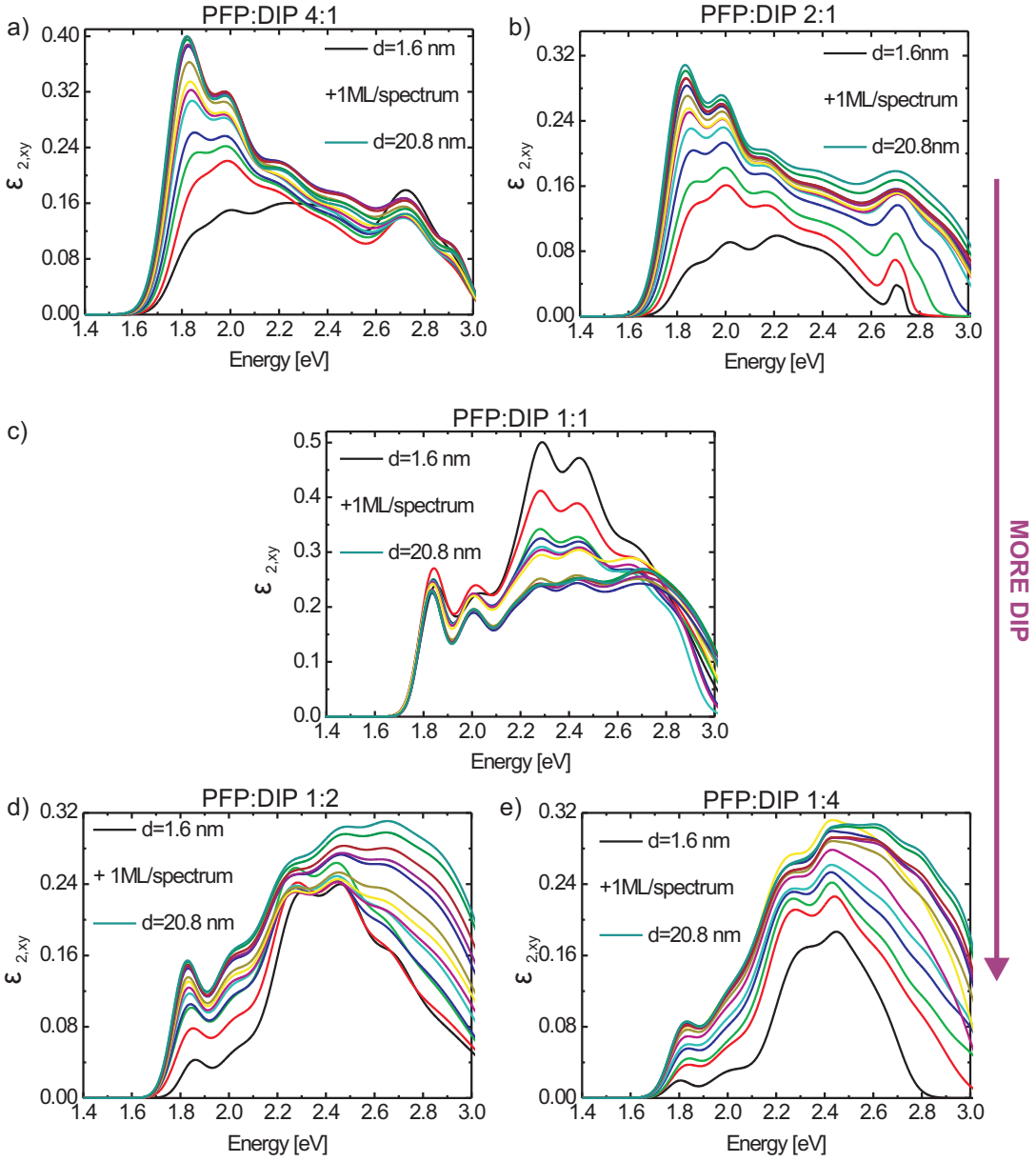

Figure 5.9: Real-time evolution of $\epsilon_{2,xy}(E)$ for blends of PFP:DIP with different mixing ratios measured using DRS. Each spectrum corresponds to a different film thickness with 1 ML $\approx$ 1.6 nm. Mixing ratios: a) PFP:DIP 4:1, b) PFP:DIP 2:1, c) PFP:DIP 1:1, d) PFP:DIP 1:2, e) PFP:DIP 1:4.

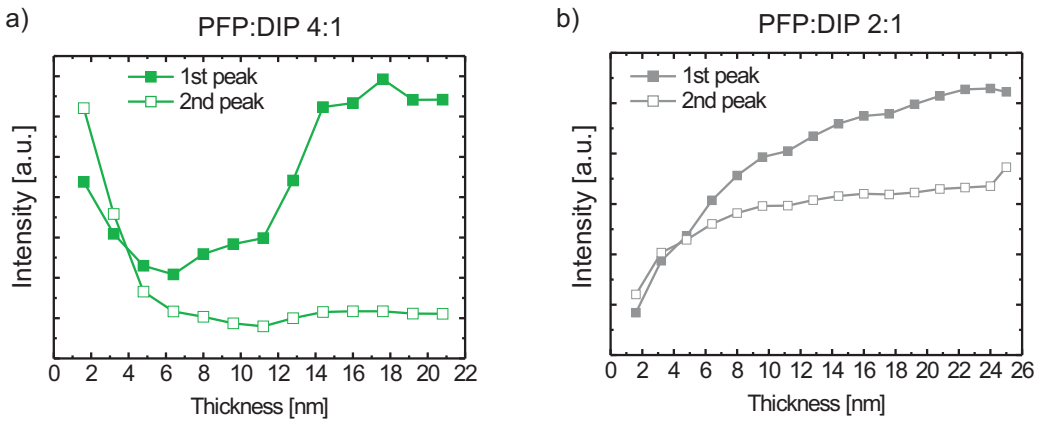

Figure 5.10: Intensity as a function of film thickness of the first two peaks in the a) PFP:DIP 4:1 blend, b) PFP:DIP 2:1 blend.

PFP:DIP	1:0	4:1	2:1	1:1	1:2	1:4	0:1 (HT) / 0:1 (LT)
ΔE_1 [meV]	-65	-24 ± 5	-35 ± 5	-13 ± 5	-34 ± 5	-11 ± 5	0 / -110

Table 5.2: Energy shift ΔE of the first peak during growth for the different mixing ratios of PFP:DIP. For comparison the energy shift of the pure films, taken from Ref. [67] is also shown. HT (LT) referrs to a pure DIP film grown at a substrate temperature of $T = 430$ K ($T = 180$ K).

high intensity of $\epsilon_{2,z}(E)$, which is for DIP much stronger than $\epsilon_{2,xy}(E)$ [139], already a small change in the molecular tilt angle can cause significant changes in the line shape.

Finally, for the blend containing more DIP (Fig. 5.9d, e) changes are observed for photon energies of 2.2 eV and above. This is especially interesting, as the "fourth mode" of DIP, which results from the interaction between DIP molecules [139] is observed at 2.8 eV. With increasing film thickness the relative intensity of the peaks between 2.2 eV to 2.6 eV remains constant, while peaks at 2.7 eV and 2.8 eV are clearly increasing in intensity. This can be rationalized by an increasing interaction between DIP molecules with increasing film thickness and crystallite size l_s. Compared with the pure film spectrum of DIP [67] the peaks are significantly broadened, indicating a lower crystalline order in the film, as it is confirmed by the low l_s determined using GIXD.

Apart from the changes in the line shape of $\epsilon_{2,xy}(E)$ there are also shifts in the energy position of the first peak observable. In Fig. 5.11 and in Table 5.2 the energy shifts ΔE_1 of the first peak for the different mixing ratios of PFP:DIP are compiled. For the definition of the first peak, the insets show the oscillators describing $\epsilon_{2,xy}(E)$ for the final

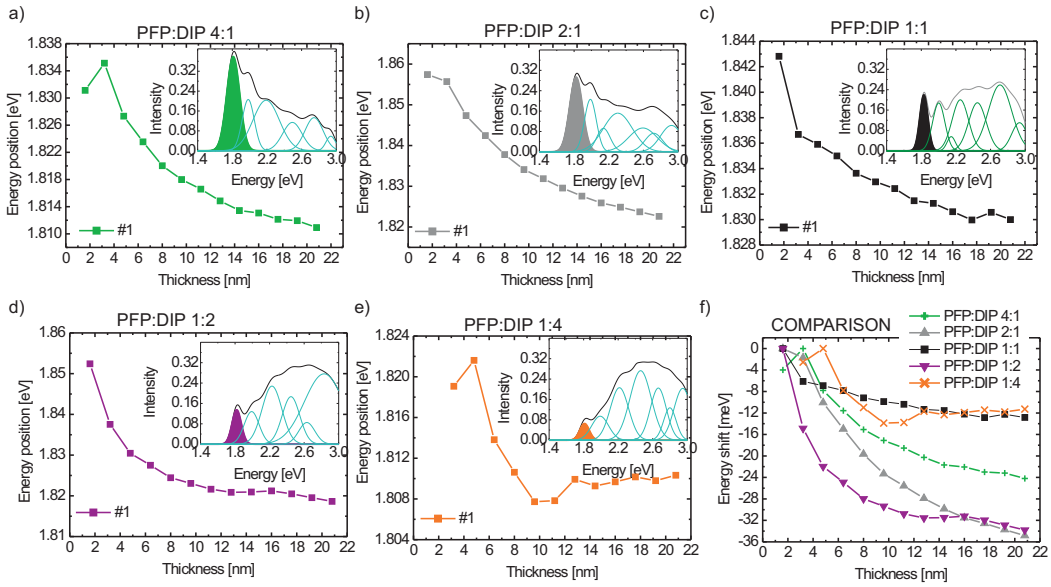

Figure 5.11: Energy position of the first peak as a function of film thickness. Mixing ratio PFP:DIP: a) 4:1, b) 2:1, c) 1:1, d) 1:2 and e) 1:4. The insets show the oscillators describing the $\epsilon_{2,xy}(E)$ for the final film thickness.

film thickness. It is noted that the error bar of ΔE_1 is comparably large due to the overlap of different peaks (see insets in Fig. 5.11).

During growth of the equimolar PFP:DIP blend, a small energy shift is reported [176], which was reproduced in this work. In contrast to this, for almost all other mixing ratios with the exception of the PFP:DIP 1:4 blend, a much larger ΔE_1 is observed during film growth. However, ΔE_1 is for all blends smaller compared with pure PFP or DIP in the LT-phase [67]. This may be due to the change in structural order during film growth, which also leads to the change in line shape of $\epsilon_{2,xy}(E)$ and the differences in the local molecular environment in the blend compared with the pure films.

One possible explanation for the differences in the absolute value of the energy shift ΔE_1 during growth observed for the different mixing ratios may be the phase separation between the intermixed crystal phase and a pure phase of the excess compound and the associated interfaces. Therefore, in non-equimolar blends different effects contribute to ΔE_1: *i)* the red shift due to the changing surface to bulk ratio with increasing film thickness, which is reported for some pure organic semiconductors [67, 245], *ii)* changes in the polarizability of the intermolecular environment during the formation and growth of the crystallites of the two phases, i.e. the mixed film phase and the pure film phase of the excess compound. Furthermore, intermolecular interactions between the molecules in the intermixed phase and at the interfaces of the different phases may contribute to ΔE_1. These may change differently during growth for the different mixing ratio, possibly

leading, in combination with the above mentioned effects, in a non-trivial dependence of the ΔE_1 on the mixing ratio.

Finally, the evolution of $\epsilon_{2,xy}(E)$ during growth of equimolar blends of PFP:DIP prepared at different substrate temperatures was studied. It is noted that in Ref. [231] real-time measurements during growth of PFP:DIP blends at $T = 300$ K and $T = 330$ K are already reported. These experiments have been reproduced and extended to samples prepared at $T = 180$ K. In Fig. 5.12 differences for the different samples are observable, regarding the shape of the spectra as well as its evolution with film thickness. The most obvious effect of the changing substrate temperature is the change in relative intensities for the two peaks between 2.2 eV and 2.6 eV. While the intensity of these two peaks is very pronounced for small film thicknesses and decreases as the film growth proceeds for the two samples prepared at 300 K and 330 K, this cannot be observed for the third sample, prepared at 180 K. Here, the intensity of the two peaks between 2.2 eV and 2.6 eV is not changing significantly with film thickness, but there is a peak at 2.75 eV which increases in intensity relative to the two former peaks.

As discussed before, the change in the intensity of the two peaks between 2.2 eV and 2.6 eV with film thickness could be caused by reorientation of DIP molecules at the beginning of film growth. Therefore, the difference in the evolution of the line shape of $\epsilon_{2,xy}(E)$ may be due to differences in the behavior of the molecules during the first two monolayers. This is reasonable, since the thermal energy of the molecules, allowing a reorientation, is much lower in films prepared at low substrate temperatures and accordingly, the line shape is not changing significantly during the film growth. The small differences in the shape of the spectra for the samples prepared at substrate temperatures of 300 K and 330 K may be due to the fact that DIP is known to grow in better crystalline order for higher substrate temperatures [133].

In conclusion, in this section the real-time evolution of the line shape of $\epsilon_{2,xy}(E)$ for PFP:DIP blends with different mixing ratios and different substrate temperatues was investigated. Pronounced influences of changes in the structural order during film growth on the shape of $\epsilon_{2,xy}(E)$ were observed. These changes include a clear increase of intensity of a peak around 1.8 eV in PFP:DIP 4:1 and 2:1 blends and a slight increase in intensity of a peak at 2.8 eV in blends containing more DIP. Based on the results of real-time GIXD experiments, both observations can be rationalized by an increase in the size of coherently scattering crystallites l_s, related to the structural order, during film growth.

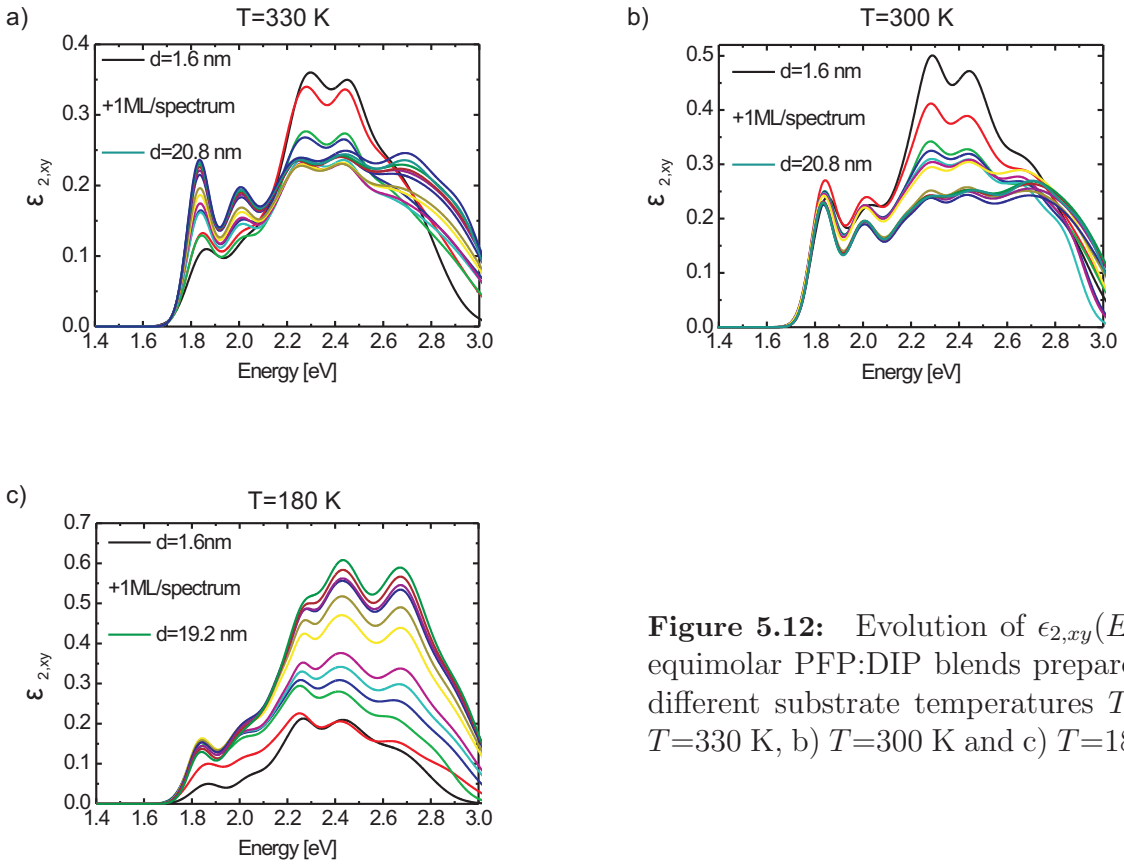

Figure 5.12: Evolution of $\epsilon_{2,xy}(E)$ for equimolar PFP:DIP blends prepared at different substrate temperatures T. a) T=330 K, b) T=300 K and c) T=180 K.

5.4 Real-time investigations of $\epsilon_{2,xy}(E)$: Blends of PEN and DIP

Finally, the evolution of $\epsilon_{2,xy}(E)$ during growth of PEN:DIP blends with different mixing ratios is shown in Fig. 5.13. Similar to the other two mixed systems, the results of DRS are in resonable agreement with the results obtained using SE (Sec. 4.4).

Apart from changes in the absolute intensity of the spectra depending on the film thickness d, the shape of $\epsilon_{2,xy}(E)$ of blends with mixing ratio PEN:DIP 4:1, 2:1 and 1:1 is not changing significantly during growth. In contrast to this, for $\epsilon_{2,xy}(E)$ of PEN:DIP blends with DIP as excess compound there are changes observable during growth, regarding the intensity of the peak at 2.8 eV, which is referred to as the "fourth mode" and which arises from interactions between DIP molecules [139] (Fig. 5.13d and e). A similar behavior, but much more pronounced, was found for pure films of DIP [67]. This is in agreement with the observed mixing and ordering behavior for non-equimolar PEN:DIP blends, since in blends with DIP as excess compound PEN molecules randomly occupy

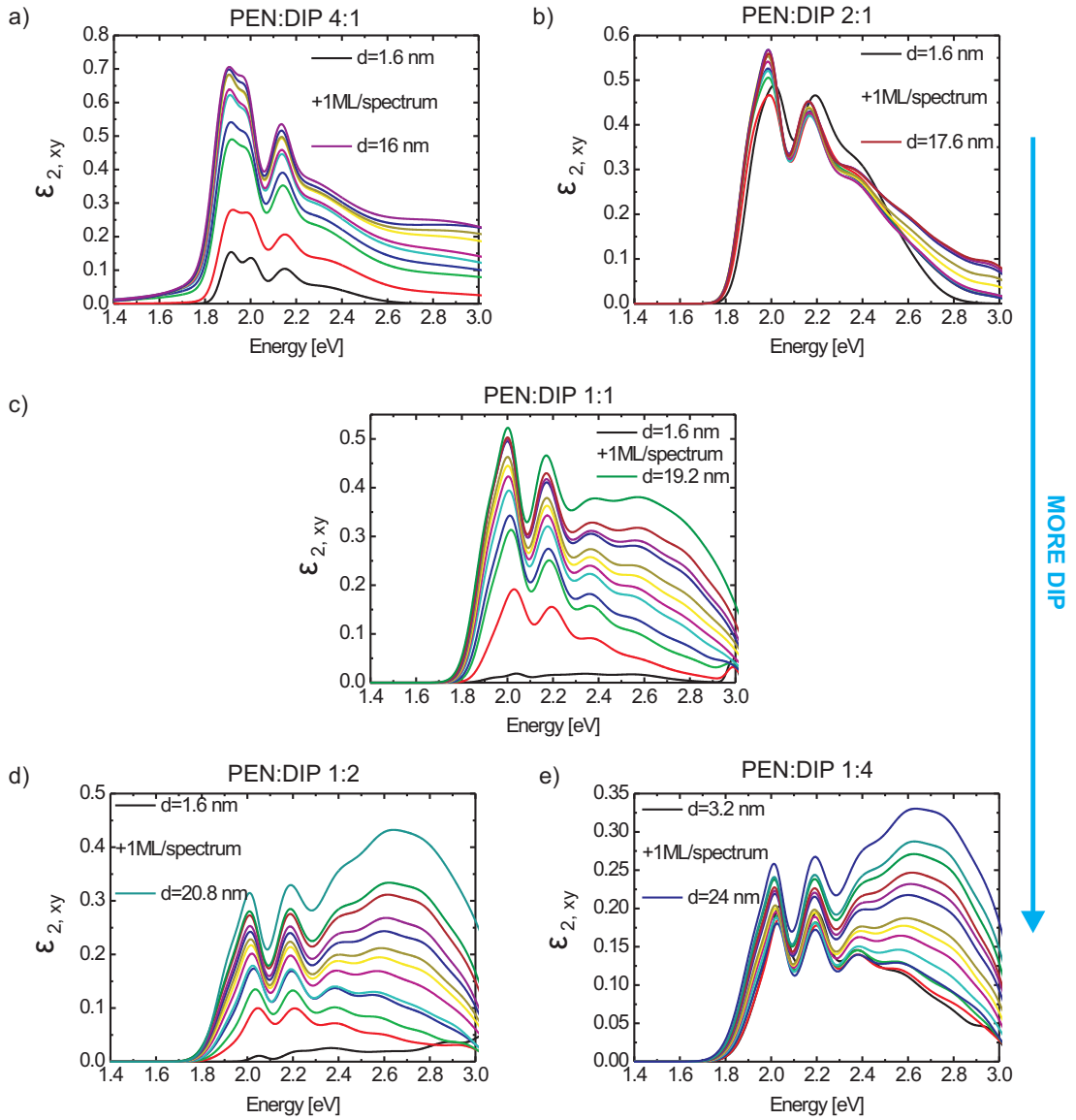

Figure 5.13: Real-time evolution of $\epsilon_{2,xy}(E)$ for blends of PEN:DIP with different mixing ratios measured using DRS. Each spectrum corresponds to a different film thickness with 1 ML $\approx$ 1.6 nm. Mixing ratios PEN:DIP: a) 4:1, b) 2:1, c) 1:1, d) 1:2, e) 1:4.

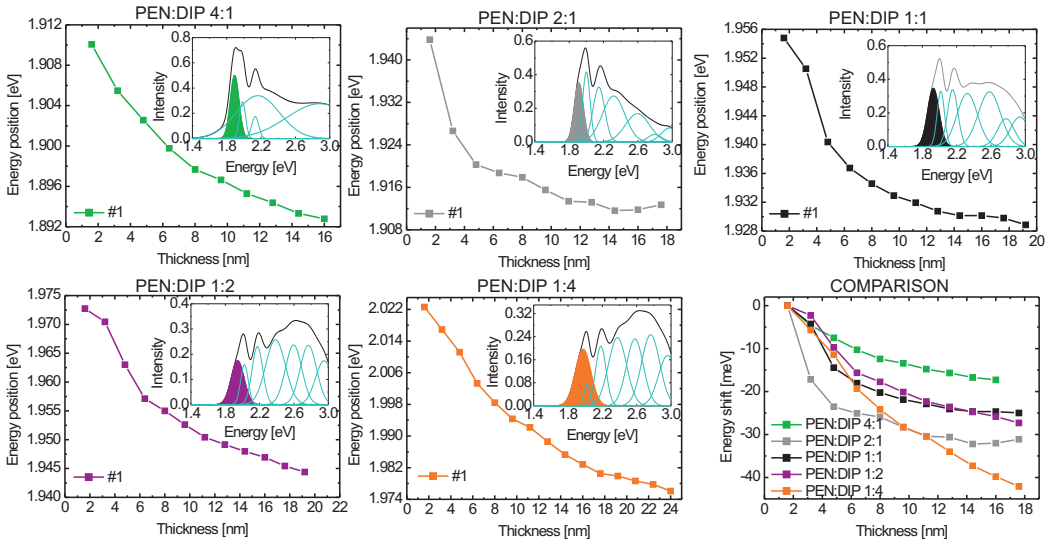

Figure 5.14: Energy shift of the first pronounced peak in PEN:DIP blends with increasing film thickness. Mixing ratio PEN:DIP a) 4:1, b) 2:1, c) 1:1, d) 1:2 and e) 1:4.

PEN:DIP	1:0	4:1	2:1	1:1	1:2	1:4	0:1 (HT) / 0:1 (LT)
ΔE_1 [meV]	-55	-22 ± 5	-28 ± 5	-26 ± 5	-31 ± 5	-47 ± 5	0 / -110

Table 5.3: Energy shift ΔE_1 of the first peak for the different mixing ratios of PEN:DIP. For comparison the energy shift of the pure films, taken from Ref. [67] is also shown.

sites in a lattice formed by the DIP molecules. Therefore, a behavior similar to pure DIP films is expected. Obviously, the presence of PEN molecules hinders interactions between the DIP molecules, resulting in an evolution of the "fourth mode" which is less pronounced compared with pure DIP films.

Although the shape of $\epsilon_{2,xy}(E)$ is not changing significantly during growth for all of the mixing ratios, a shift of the energy position ΔE_1 of the first pronounced peak can be found for all samples investigated (Fig. 5.14 and Table 5.3). It is noted that, similar to blends of PFP:DIP, the error bars of the absolute value of ΔE_1 are comparably large, due to the overlap of different peaks (insets in Fig. 5.14).

Similar to blends of PFP:DIP, ΔE_1 during growth of PEN:DIP blends is lower compared with ΔE_1 during growth of the respective pure films (Table 5.3). This may result from the differing local molecular environment due to the presence of two compounds in the mixed systems and the significantly lower long-range order in the blends compared with the pure films.

The almost monotonic change in ΔE_1 with the mixing ratio, which is in contrast to

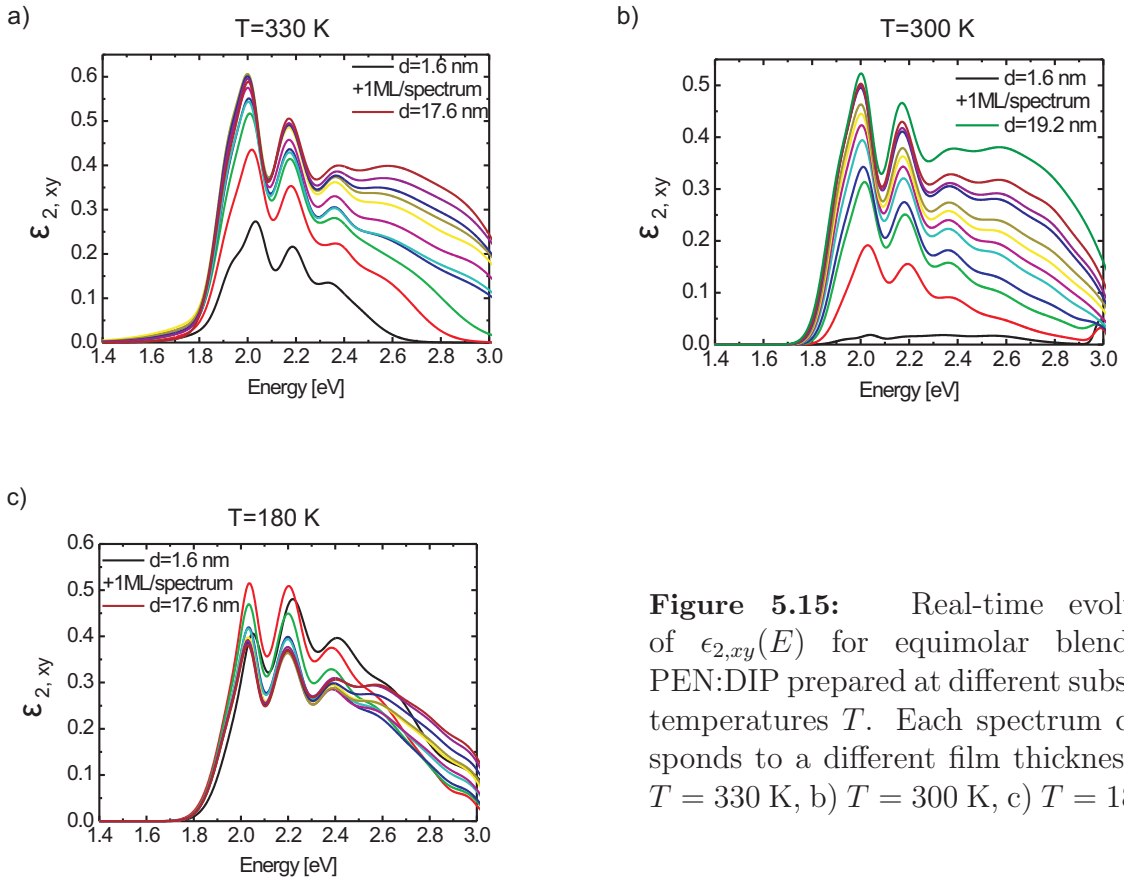

Figure 5.15: Real-time evolution of $\epsilon_{2,xy}(E)$ for equimolar blends of PEN:DIP prepared at different substrate temperatures T. Each spectrum corresponds to a different film thickness. a) $T = 330$ K, b) $T = 300$ K, c) $T = 180$ K.

PFP:DIP blends, can possibly be rationalized by the mixing and ordering behavior. For non-equimolar mixing ratios the minority molecules occupy randomly sites in a lattice formed by the excess compound. This results in less different types of interfaces present in the PEN:DIP blends compared with PFP:DIP and accordingly, in a dependence of ΔE_1 on the mixing ratio which is less complex. Furthermore, the intermolecular interactions between PEN and DIP are expected to the weaker that between PFP and DIP, which possibly also influences ΔE_1.

The real-time investigations of PEN:DIP blends were completed by *in situ* studies of the growth of equimolar PEN:DIP blends prepared at three different substrate temperatures. As it can be seen from Fig. 5.15, there are only very small differences in the evolution of $\epsilon_{2,xy}(E)$ with film thickness for the different samples. The intensity of the "fourth mode" at 2.8 eV is slightly increasing in intensity in $\epsilon_{2,xy}(E)$ for the two blends prepared at $T = 300$ K and $T = 330$ K, which cannot be observed for the sample prepared at $T = 180$ K. This may be due to changes in the molecular arrangement in the low

temperature sample, for which the long-range order perpendicular to the substrate surface is reduced compared with the other two samples.

To conclude, the real-time evolution of $\epsilon_{2,xy}(E)$ was investigated for PEN:DIP blends with five different mixing ratios, prepared at three different substrate temperatures. In contrast to the other two mixed systems studied in this work, only small changes in the shape of $\epsilon_{2,xy}(E)$ could be observed, which are probably related to properties of the pure compounds [67].

5.5 Comparison

In summary, in this chapter the results of real-time investigations of PFP:PEN, PFP:DIP and PEN:DIP blends were presented. GIXD experiments during growth of PFP:DIP revealed pronounced changes in size l_s of coherent scattering islands during film growth for all observable structural phases (i.e. depending on the mixing ratio for the PFP and DIP excess phases as well as for the intermixed crystal phase). Furthermore, the steric incompatibility as well as the coexistence of different phases influences l_s. This results in a significantly reduced l_s in PFP:DIP blends with DIP as excess compound compared with pure DIP films, while l_s of the PFP excess phase in PFP:DIP blends is comparable to l_s in pure PFP films. For PEN:DIP blends for most of the preparation conditions no significant change in the long-range order was observed during film growth.

The focus of this second part of the results was on the real-time investigation of $\epsilon_{2,xy}(E)$ during film growth, in particular to study how it may be affected by differences in the mixing and ordering behavior of the three systems. The most dramatic difference observed is the strong change in the shape of $\epsilon_{2,xy}(E)$ for blends containing more PFP and which can be observed in PFP:PEN as well as in PFP:DIP. A comprehensible explanation for this effect is a change in local molecular environment due to the increasing size of coherent scattering islands in the PFP excess phase, which is supported by real-time GIXD experiments. It cannot be excluded, though, that other mechanisms contribute to the change in line shape.

For blends containing more DIP an increase of the intensity of the "fourth mode" was observed, which could, based on the results of real-time GIXD experiments, be explained by the faciliated intermolecular interactions between DIP molecules during film growth for PFP:DIP as well as for PEN:DIP and which is also observed during growth of pure DIP films [67].

Interestingly, no significant change in the line shape of blends containing more PEN is observed. Depending on the system investigated, there are several possible explanations for this finding. For blends of PFP:PEN the peaks related to the HOMO-LUMO transition and the corresponding vibronic progression are not clearly distinguishable in $\epsilon_{2,xy}(E)$. This makes it difficult to resolve changes in their relative intensities. Furthermore, it may be possible that the local molecular environment in the PEN excess phase is not changing significantly during film growth. Real-time GIXD or XRR experiments would be necessary to support this speculation.

For blends of PEN:DIP the results of real-time GIXD experiments show that the long-range order in blends containing more PEN is not improving during film growth and no indications for structural changes have been found. Therefore, it is reasonable that the shape of $\epsilon_{2,xy}(E)$ is not changing during growth.

For blends of PFP:DIP and PEN:DIP a red shift of the energy position of the first peak ΔE_1 is observed during film growth, which is for all mixing ratios significantly smaller compared with ΔE_1 during growth of the pure films. For both mixed systems this can be rationalized by changes in the local molecular environment in the blend compared with the pure films. Comparing the dependence of ΔE_1 on the mixing ratio for blends of PFP:DIP and PEN:DIP, differences are observed. While ΔE_1 is found to be almost monotonic for PEN:DIP blends, for PFP:DIP blends ΔE_1 exhibits a local minimum at the equimolar mixing ratio, which may be due to the differences in mixing and ordering behavior of the two systems.

Due to the strong influences of intermolecular interactions and the close overlap of peaks assigned to PFP and PEN in $\epsilon_{2,xy}(E)$ of PFP:PEN blends, it is difficult to determine the energy position of the first pronounced peak as a function of film thickness precisely. Therefore, a possible shift of E_1 was not discussed in the respective section.

Finally, the dependence of the shape of $\epsilon_{2,xy}(E)$ on the substrate temperature was investigated. For blends of PFP:DIP and PEN:DIP $\epsilon_{2,xy}(E)$ measured post-growth as well as its evolution with film thickness is only weakly affected by the preparation temperature. This is in contrast to blends of PFP:PEN, where the molecular orientation significantly influences the shape of $\epsilon_{2,xy}(E)$. Furthermore, the real-time DRS experiments point towards changes in the molecular orientation with increasing film thickness, as a peak, which is assigned to the λ-orientation, is increasing in intensity during film growth.

Chapter 6

Summary

In this work a systematic, comparative study of the influence of film structure and intermolecular interactions on the optical properties of blends of small-molecule OSCs was presented. Since a detailed summary of the results was given at the end of each of the respective chapters, more general conclusions will be summarized in this final chapter. For more details on the results the interested reader is referred to Sec. 4.1.4, Sec. 4.5 and Sec. 5.5. In this work, three mixed systems with different properties were investigated:

1. PFP:PEN

   (a) Strong and favorable intermolecular interactions ($\chi < 0.5$)

   (b) High steric compatibility of the two compounds

   (c) Transition dipole moments of the HOMO-LUMO transition for both compounds oriented along the short molecular axis

   (d) Film structure: Mixing on a molecular level and formation of a new crystal phase for equimolar blends;
   phase separation between the intermixed crystal phase and the pure film phase of the respective excess compound for non-equimolar blends [127]

2 PFP:DIP

   (a) Strong and favorable intermolecular interactions ($\chi < 0.5$)

   (b) Low steric compatibility of the two compounds

   (c) Transition dipole moment of the HOMO-LUMO transition oriented along the short molecular axis (PFP) and long molecular axis (DIP)

   (d) Film structure: Mixing on a molecular level for equimolar blends and formation of a new crystal phase;
   for non-equimolar blends phase separation between the intermixed crystal phase and the pure film phase of the respective excess compound [176]

3 PEN:DIP

(a) Weak intermolecular interactions ($\chi \approx 0$)

(b) Low steric compatibility of the two compounds

(c) Transition dipole moment of the HOMO-LUMO transition oriented along the short molecular axis (PEN) and long molecular axis (DIP)

(d) Film structure: "Frozen" smectic C-phase for equimolar blends;
in non-equimolar blends random occupation of sites by minority molecules in a lattice formed by the excess compound [36]

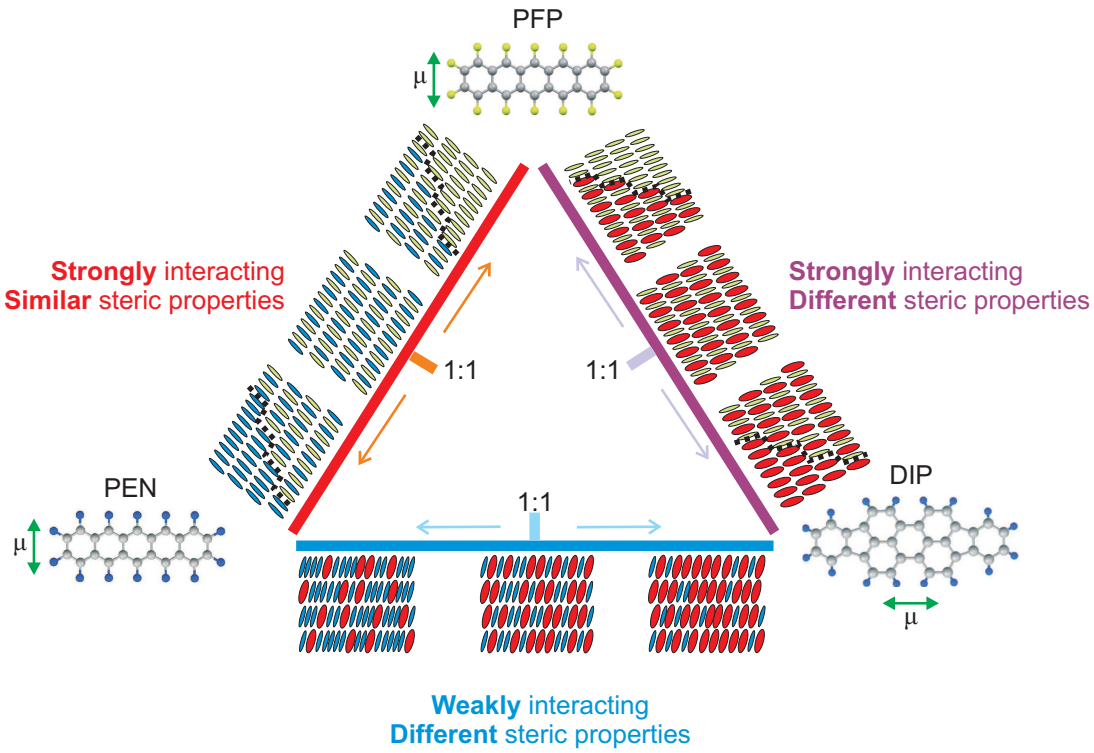

Figure 6.1: The triangle of steric compatibility and intermolecular interactions formed by PFP, PEN and DIP with schemes of the mixing scenarios for equimolar and non-equimolar blends.

For each of the three systems, blends with five different mixing ratios prepared at three different substrate temperatures were studied. The differences in the intermolecular interactions and steric compatibility of the compounds resulted in differences in the mixing and ordering behavior. The observed differences in the film structure of the three different mixed system were rationalized by extending a well-established mean-field theory, taking anisotropic interactions as well as anisotropic steric properties into account [36].

One general phenomenon, which was observed independent of the mixed system, is a lower roughness of the blends compared with the pure films, which is a surprising effect and worth to be investigated in more detail. However, this was beyond the scope of this work.

The focus of the present work was on the optical properties of the three systems, in particular on $\epsilon_2(E)$, which is related to the absorption spectrum of the thin film. Compared with the pure film spectra, two general effects can be observed remarkably independent of the system:

1. A broadening of peaks.

2. A shift of the first peak (except the CT-peak in PFP:PEN blends) to higher energies.

Both effects can be rationalized by differences in the local molecular environment in the blends compared with the pure films. The broadening is caused by inhomogeneities in the local environment, while the blue shift of the peak is probably due to the change in the polarizability of the environment. Furthermore, the dependence of this shift on the mixing ratio is found to be clearly affected by the mixing and ordering behavior of the system. For blends of PFP:PEN and PFP:DIP a non-monotonic dependence is observed, consistent with the phase separation between two phases for non-equimolar blends. In contrast to this for blends of PEN:DIP the continuous change in the film structure with the mixing ratio leads to a continuous change in the local molecular environment and consequently to a continuous peak shift.

Apart from these general effects, the influence of intermolecular interactions and steric compatibility on the shape of $\epsilon_{2,xy}(E)$ was investigated in detail for the different mixed systems. The strong intermolecular interactions between PFP and PEN result in a spectral shape clearly deviating from the pure film spectra for blends with mixing ratios close to the equimolar mixture. In particular a clear indication for a CT between PFP and PEN in the excited state is observed [74, 75]. Furthermore, for equimolar blends of PFP:PEN prepared at different substrate temperatures the changing molecular orientation result in changes in the shape of the spectra. By determining the average molecular tilt angle quantitatively for the different samples, it is possible to assign peaks in $\epsilon_{2,xy}(E)$ and $\epsilon_{2,z}(E)$ to the spectral response of molecules in two different orientations.

For the other two systems, $\epsilon_{2,xy}(E)$ resembles a superposition of $\epsilon_{2,xy}(E)$ of the pure film spectra for all mixing ratios and substrate temperatures. This may be due to the significantly different spectral ranges in which PEN (PFP) and DIP are absorbing or due to the orientation of the transition dipole moments of the HOMO-LUMO transition of the two compounds, preventing an efficient coupling of excitations in case of upright standing molecules. Neither for PFP:DIP blends nor for PEN:DIP blends a clear CT peak is found in $\epsilon_{2,xy}(E)$ or $\epsilon_{2,z}(E)$, which may be due to the orientation of the transition dipole moments of the two compounds. In addition, for blends of PFP:DIP a CT peak would be expected around 2.0 eV, making it difficult to distinguish the CT peak from the contributions of pure PFP.

For blends of PEN:DIP, $\epsilon_{2,xy}(E)$ was found to be strongly affected by the reduced long-range order parallel to the substrate surface, influencing in particular the relative intensities of the first two transitions, which are related to the two Davydov-components of the HOMO-LUMO transition. Due to the weak intermolecular interactions, the shape of the absorption spectra can almost completely be rationalized by the film structure.

Finally, the influence of mixing and ordering behavior on the real-time evolution of $\epsilon_{2,xy}(E)$ was investigated during growth. The separation of two structural phases observed in non-equimolar blends of PFP:PEN and PFP:DIP result in significant changes in the shape of the absorption spectra, in particular for blends containing more PFP. The results of real-time GIXD experiments on PFP:DIP blends are pointing towards changes in the local molecular environment due to an increasing crystallite size as origin of the observed changes in $\epsilon_{2,xy}(E)$. In agreement with this interpretation for blends of PEN:DIP a change in the line shape during growth is found only for blends containing more DIP where GIXD experiments show that the long-range order is improving.

Interestingly, there are different effects observed for the three compounds, which are independent of the specific system. For blends containing more PFP the spectral response of PFP exhibits significant changes during film growth, indicating differences in the local molecular enviroment in the excess phase. The same is observed for DIP, where the intensity of the "fourth mode" is increasing in intensity due to the facilitated interaction between DIP molecules. In contrast to this, the spectral response of PEN shows only slight changes in blends of PFP:PEN and remains unchanged during growth of PEN:DIP blends. This may be due to the spectral range, where PEN is absorbing but possibly also due to the structural properties of the PEN excess phase.

In summary, the presented work sheds light on the impact of film structure (in particular of mixing and ordering behavior) and intermolecular interactions on absorption spectra of mixed films measured post growth as well as in real-time. The changes in the local molecular environment in the blend compared with the pure films affect the peak widths as well as the energy position of the first pronounced peak and its dependence on the mixing ratio. They also may play a crucial role in the real-time evolution of the shape of the absorption spectra, which depends significantly on the development of the film structure (such as the long-range order or the molecular orientation) during growth. Finally, it can be speculated that the orientation of the transition dipole moments and the relative position of the HOMO and LUMO levels of the pure compounds affect the observation of CT peaks in the optical absorption spectra of the mixed system.

Chapter 7

Outlook

Based on the results of this thesis, the following experiments, which were beyond the scope of this work, could be of interest for a general understanding of mixed films:

- The evolution of the size of coherently scattering islands during film growth could be studied for blends of PFP:PEN to support the interpretation of the structural order as origin of the change in the line shape of $\epsilon_{2,xy}(E)$ during growth of a PFP:PEN 2:1 blend.

- The question whether CT can be observed in PFP:DIP could be addressed by photoluminescence (PL) measurements at low temperatures. In this context, the present work and the study in Ref. [75] could be complemented by measuring PL for all of the samples investigated.

- For PEN:DIP, temperature dependent powder diffraction experiments could be employed to investigate whether there are conditions, under which an ordered mixed phase exists or whether phase separation occurs.

- Differential scanning calorimetry or thermal desorption spectroscopy could be used to further investigate the interaction energies in the systems and to study the impact of differences in intermolecular interactions in the three systems on the formation of a stable phase.

- For a better understanding of the intermolecular interactions and the absorption spectra of PFP:PEN it would be very helpful to determine the full crystal structure of the intermixed phase. The same applies for PFP:DIP.

- One interesting result is the observation that the most pronounced changes in the relative intensities are found for peaks related to PFP and DIP, while only small changes can be observed for peaks assigned to PEN. It would be interesting to investigate this further by testing blends of PEN with other OSCs, which exhibit the same mixing behavior as blends of PFP:PEN. Possible candidates could be pentacenequinone, picene, perfluoropicene or perfluorinated diindenoperylene.

- The present study could be extended using another material with very different sterical and optical properties, such as e.g. rubrene, which is non-planar and may, therefore, lead to a more complex mixing and ordering behavior.
- Furthermore, compounds with similar orientations of the transition dipole moments, but different intermolecular interactions could be choosen to perform a comparable study. This would allow to exclude the influence of the orientation of the transition dipole moments on coupling between different compounds.
- It would be interesting to investigate whether it is a general phenomenon that the roughness of the blends is lower compared with the pure films by studying further mixed systems.
- Similarly, it could be investigated, whether the blue shift of the first pronounced peak in mixed film spectra compared with the HOMO-LUMO transition of the pure compound with the smallest optical gap is a general effect.
- Finally, theoretical calculations of the absorption spectra of the blends would be helpful to shed light on the origin of specific peaks. Furthermore, theoretical investigations are necessary to further elucidate how the observation of CT transitions in blends is affected by specific properties of the pure compounds. However, these calculations are very demanding for such complex systems and require the knowledge of the full crystal structures.

Chapter 8

Appendix: Substrate characterization and fitting of DRS data

8.1 AFM images of bare substrates

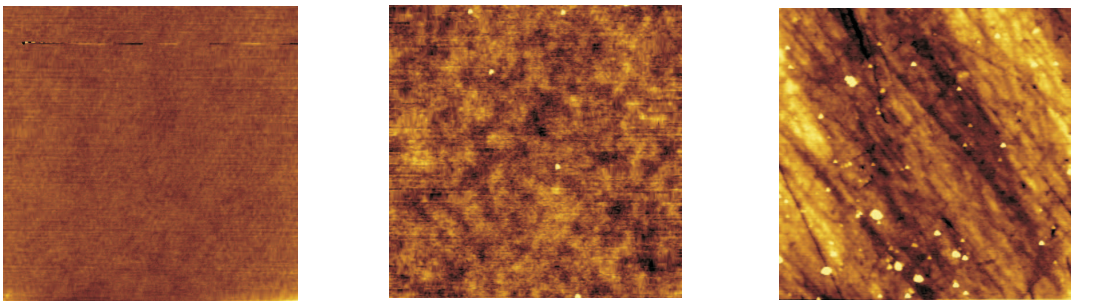

Figure 8.1: AFM images of the bare substrates used in this thesis (area 5 μm×5 μm) and corresponding roughness σ.

8.2 DRS: Comparison of experimental data and fit results

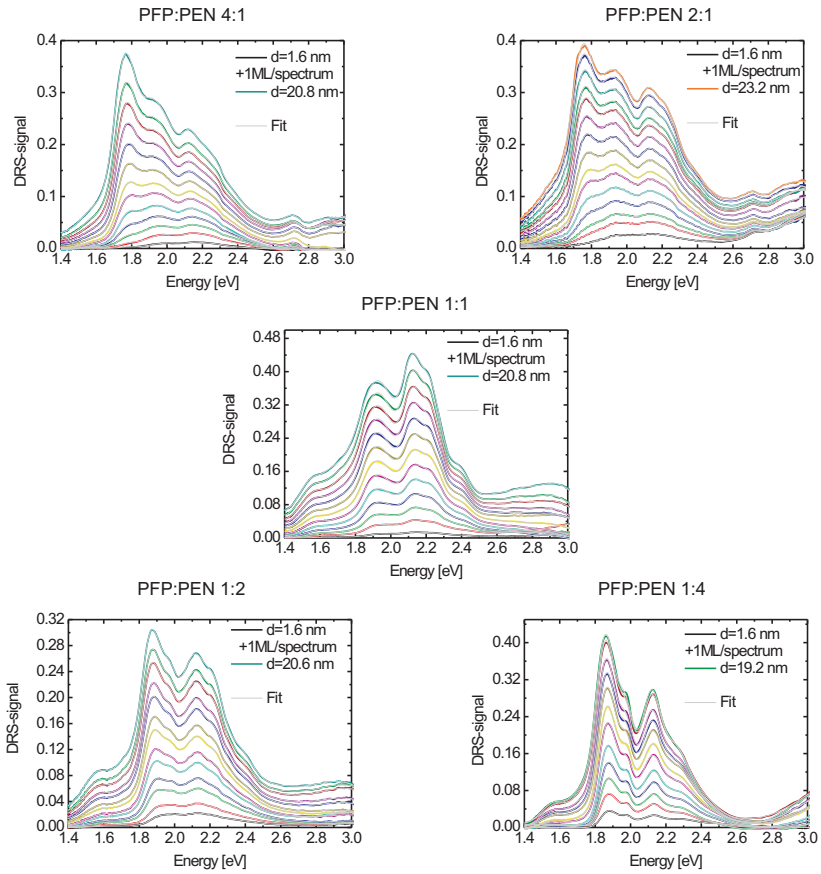

Figure 8.2: DRS data (thick lines) and fit result (thin lines) for PFP:PEN blends with different mixing ratios.

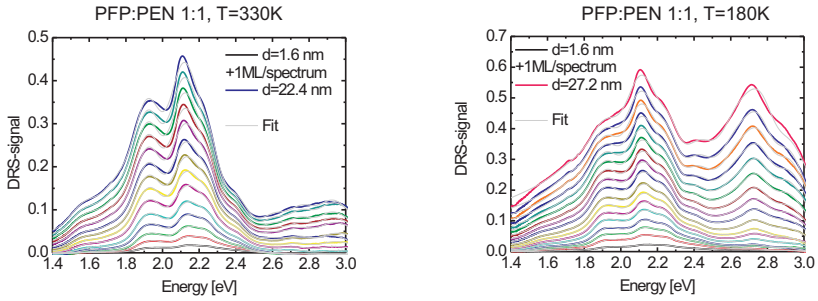

Figure 8.3: DRS data (thick lines) and fit result (thin lines) for equimolar PFP:PEN blends prepared at different substrate temperatures.

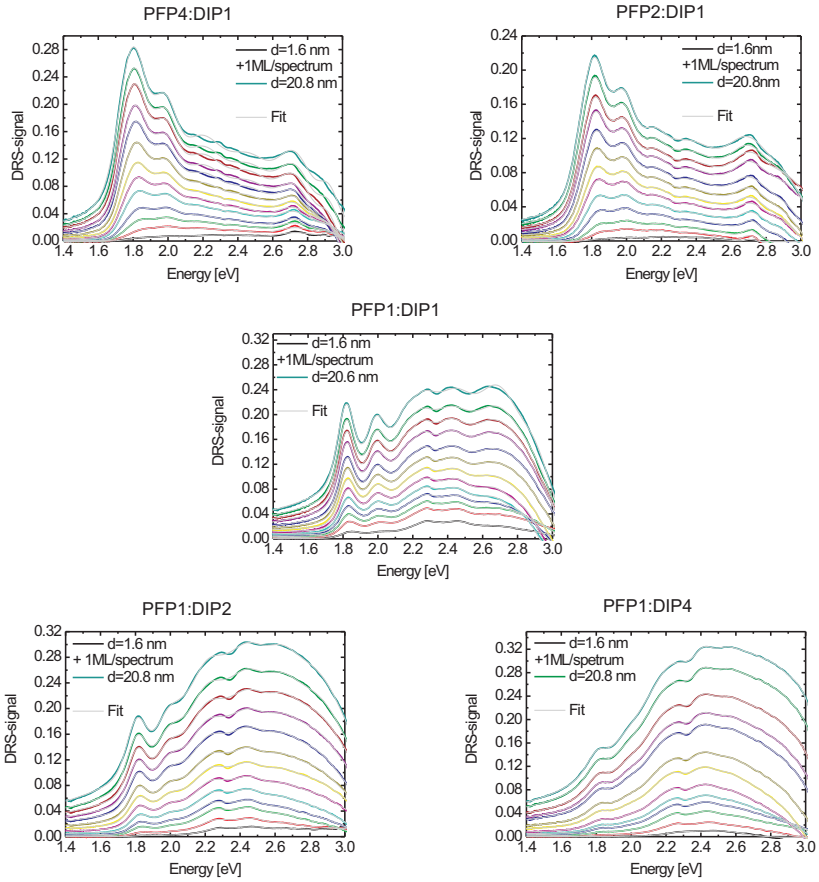

Figure 8.4: DRS data (thick lines) and fit result (thin lines) for PFP:DIP blends with different mixing ratios.

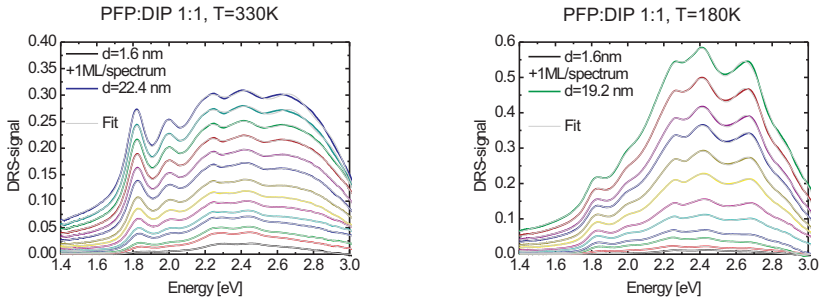

Figure 8.5: DRS data (thick lines) and fit result (thin lines) for equimolar PFP:DIP blends prepared at different substrate temperatures.

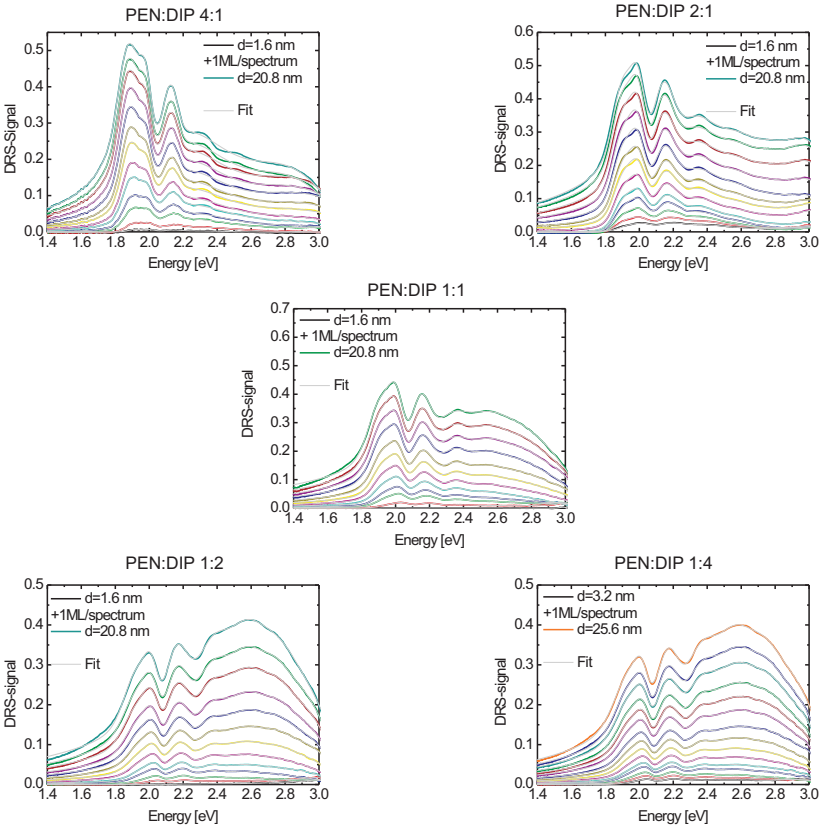

Figure 8.6: DRS data (thick lines) and fit result (thin lines) for PEN:DIP blends with different mixing ratios.

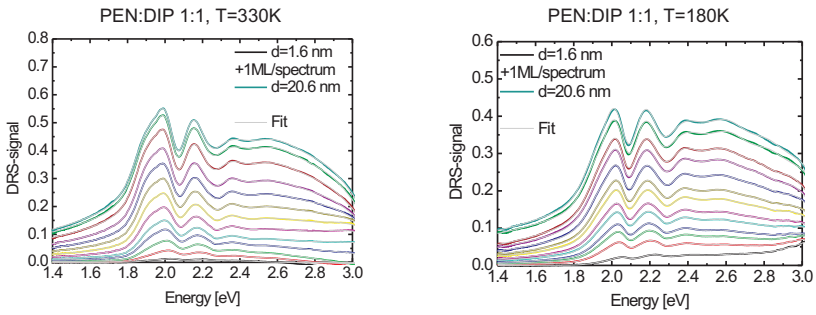

Figure 8.7: DRS data (thick lines) and fit result (thin lines) for equimolar PEN:DIP blends prepared at different substrate temperatures.

List of abbreviations

A-E

A	Absorbance
AFM	Atomic force microscopy
AOI	Angle of incidence
CCD	Charge-coupled device
CT	Charge transfer
d	Film thickness
DIP	Diindenoperylene ($C_{32}H_{16}$)
DRS	Differential reflectance spectroscopy
DSC	Differential scanning caliometry
EMA	Effective medium approximation

F-N

FWHM	Full width half maximum
FT	Fourier transformation
GIXD	Grazing incidence X-ray diffraction
HOMO	Highest occupied molecular orbital
HT	High temperature
HV	High vaccum
KK	Kramers-Kronig
LUMO	Lowest unoccupied molecular orbital
l_s	Size of coherently scattering crystallites
ML	Monolayer
NEXAFS	Near-edge X-ray absorption fine structure spectroscopy
NtveSi	Silicon wafer covered with a native $Si0_2$-layer

O-R

OMBD	Organic molecular beam deposition
OSC	Organic semiconductor
PDTS	Polarization dependent transmission spectroscopy
PEN	Pentacene ($C_{22}H_{14}$)
PFP	Perfluoropentacene ($C_{22}F_{14}$)
p-polarized light	Light polarized parallel to the plane of incidence
QCM	Quartz-crystal microbalance
RC	Rotating compensator
RT	Room temperature

S-Z

s-polarized light	Light polarized perpendicular to the plane of incidence
SE	Spectroscopic ellipsometry
ThermSi	Thermally oxidized silicon wafer
TMP	Turbo molecular pump
TSP	Titan sublimation pump
UHV	Ultra-high vaccum
VASE	Variable angle spectroscopic ellipsometry
XRR	X-ray reflectivity

Bibliography

[1] A. Pochettino, Atti Acad. Lincei Rend. **15(1)**, 355 (1906).

[2] A. Pochettino, Atti Acad. Lincei Rend. **15(2)**, 171 (1906).

[3] J. Shinar, *Organic light-emitting devices: A survey*, Springer, New York (2004).

[4] O. D. Jurchescu, *Molecular organic semiconductors for electronic devices*, Ph.D. thesis, Rijksuniversiteit Groningen, 2006.

[5] W. Brütting, *Charge carrier injection and transport in organic light-emitting devices* Ph.D. thesis, Universität Bayreuth, 2000.

[6] N. R. Armstrong, W. Wang, D. M. Alloway, D. Placencia, E. Ratcliff, and M. Brumbach, Macromol. Rapid Commun. **30**, 717 (2009): *Organic/organic heterojunctions: Organic light emitting diodes and organic photovoltaic devices.*

[7] M. Pope and C. E. Swenberg, *Electronic processes in organic crystals and polymers*, Oxford University Press, New York (1999).

[8] M. Schwoerer and H. C. Wolf, *Organische molekulare Festkörper*, Wiley VCH-Verlag GmbH & Co., Weinheim (2005).

[9] W. Brütting, S. Berleb, and A. G. Mückl, Org. Electron. **2**, 1 (2001): *Device physics of organic light-emitting diodes based on molecular materials.*

[10] T. W. Kelley, P. F. Baude, C. Gerlach, D. E. Ender, D. Muyres, M. A. Haase, D. E. Vogel, and S. D. Theiss, Chem. Mater. **16**, 4413 (2004): *Recent progress in organic electronics: Materials, devices, and processes.*

[11] J. Lewis, Mater. Today **9**, 38 (2006): *Material challenge for flexible organic devices.*

[12] W. Brütting, H. Riel, T. Beierlein, and W. Riess, J. Appl. Phys. **89**, 1704 (2001): *Influence of trapped and interfacial charges in organic multilayer light-emitting devices.*

[13] S. R. Forrest, Nature **428**, 911 (2004): *The path to ubiquitous and low-cost organic electronic appliances on plastic.*

[14] M. Grobosch, R. Schuster, T. Pichler, M. Knupfer, and H. Berger, Phys. Rev. B **74**, 155202 (2006): *Analysis of the anisotropy of excitons in pentacene single crystals using reflectivity measurements and electron energy-loss spectroscopy.*

[15] J. E. Anthony, Chem. Rev. **106**, 5028 (2006): *Functionalized acenes and heteroacenes for organic electronics.*

[16] E. Cantatore, Proceedings of the SAFE/IEEE workshop 27 (2000): *Organic materials: A new chance for electronics?*

[17] J. E. Anthony, A. Facchetti, M. Heeney, S. R. Marder, and X. Zhan, Adv. Mater. **22**, 3876 (2010): *n-Type organic semiconductors in organic electronics.*

[18] W. Brütting and C. Adachi, *Physics of organic semiconductors*, Wiley VCH-Verlag GmbH & Co., Weinheim (2012).

[19] W.-B. Chen, H.-F. Xiang, Z.-X. Xu, B.-P. Yan, V. A. L. Roy, C.-M. Che, and P.-T. Lai, Appl. Phys. Lett. **91**, 191109 (2007): *Improving efficiency of organic photovoltaic cells with pentacene-doped CuPc layer.*

[20] J. Bisquert and G. Garcia-Belmonte, J. Phys. Chem. Lett. **2**, 1950 (2011): *On voltage, photovoltage, and photocurrent in bulk heterojunction organic solar cells.*

[21] M. Y. Chan, C. S. Lee, S. L. Lai, M. K. Fung, F. L. Wong, H. Y. Sun, K. M. Lau, and S. T. Lee, J. Appl. Phys. **100**, 094506 (2006): *Efficient organic photovoltaic devices using a combination of exciton blocking layer and anodic buffer layer.*

[22] J.-L. Brédas, J. E. Norton, J. Cornil, and V. Coropceanu, Acc. Chem. Res. **42**, 1691 (2009): *Molecular understanding of organic solar cells: The challenges.*

[23] C. Brabec, V. Dyakonov, J. Parisi, and N. Sariciftci, *Organic photovoltaics: Concepts and applications*, Springer, Heidelberg (2003).

[24] C. J. Brabec, Sol. Energ. Mat. Sol. C. **83**, 273 (2004): *Organic photovoltaics: Technology and market.*

[25] B. Brousse, B. Ratier, and A. Moliton, Thin Solid Films **451**, 81 (2004): *Vapor deposited solar cells based on heterojunction or interpenetrating networks of zinc phthalocyanine and C_{60}.*

[26] T. Aernouts, P. Vanlaeke, W. Geens, J. Poortmans, P. Heremans, S. Borghs, R. Mertens, R. Andriessen, and L. Leenders, Thin Solid Films **451**, 22 (2004): *Printable anodes for flexible organic solar cell modules.*

[27] A. Afzali, C. D. Dimitrakopoulos, and T. L. Breen, J. Am. Chem. Soc. **124**, 8812 (2002): *High-performance, solution-processed organic thin film transistors from a novel pentacene precursor.*

[28] C. J. Brabec, N. S. Sariciftci, and J. C. Hummelen, Adv. Funct. Mater. **11**, 15 (2001): *Plastic solar cells.*

[29] A. Hinderhofer and F. Schreiber, ChemPhysChem **13**, 628 (2012): *Organic-organic heterostructures: Concepts and applications.*

[30] K. Akaike, K. Kanai, Y. Ouchi, and K. Seki, Adv. Funct. Mater. **20**, 715 (2010): *Impact of ground-state charge transfer and polarization energy change on energy band offsets at donor/acceptor interface in organic photovoltaics.*

[31] M. R. Brown, P. Rees, R. J. Cobley, K. S. Teng, S. Wilks, and A. Hughes, J. Appl. Phys. **102**, 113711 (2007): *The effect of interface roughness on multilayer heterostructures.*

[32] A. Al-Mahboob, J. Sadowski, Y. Fujikawa, and T. Sakurai, Surf. Sci. **603**, L53 (2009): *The growth mechanism of pentacene-fullerene heteroepitaxial films.*

[33] L. M. Andersson and O. Inganäs, Chem. Phys. **357**, 120 (2009): *From short to long: Optical and electrical transients in photovoltaic bulk heterojunctions of polyfluorene/fullerenes.*

[34] K. Ariga, J. P. Hill, Y. Wakayama, M. Akada, E. Barrena, and D. G. de Oteyza, J. Porphyrins Phthalocyanines **13**, 22 (2009): *New aspects of porphyrins and related compounds: selfassembled structures in two-dimensional molecular arrays.*

[35] W. Chen, D.-C. Qi, H. Huang, X. Gao, and A. T. S. Wee, Adv. Funct. Mater. **21**, 410 (2011): *Organic-organic heterojunction interfaces: Effect of molecular orientation.*

[36] A. Aufderheide, K. Broch, J. Novák, A. Hinderhofer, R. Nervo, A. Gerlach, R. Banerjee, and F. Schreiber, Phys. Rev. Lett. **109**, 156102 (2012): *Mixing-induced anisotropic correlations in molecular crystalline systems.*

[37] M. Brumbach, D. Placencia, and N. R. Armstrong, J. Phys. Chem. C **112**, 3142 (2008): *Titanyl phthalocyanine/$C_6$0 heterojunctions: Band-edge offsets and photovoltaic device performance.*

[38] F. A. Castro, H. Benmansour, J.-E. Moser, C. F. O. Graeff, F. Nüesch, and R. Hany, Phys. Chem. Chem. Phys. **11**, 8886 (2009): *Photoinduced hole-transfer in semiconducting polymer/low-bandgap cyanine dye blends: evidence for unit charge separation quantum yield.*

[39] W. Chen, H. Zhang, H. Huang, L. Chen, and A. T. S. Wee, ACS Nano **2**, 693 (2008): *Orientationally ordered C_{60} on p-sexiphenyl nanostripes on Ag(111).*

[40] W. Chen, S. Chen, H. Huang, D. C. Qi, X. Y. Gao, and A. T. S. Wee, Appl. Phys. Lett. **92**, 063308 (2008): *Molecular orientation dependent interfacial dipole at the F_{16}CuPc/CuPc organic heterojunction interface.*

[41] D. Cheyns, H. Gommans, M. Odijk, J. Poortmans, and P. Heremans, Sol. En. Mater. Sol. Cells **91**, 399 (2007): *Stacked organic solar cells based on pentacene and C_{60}.*

[42] D. Cheyns, B. P. Rand, and P. Heremans, Appl. Phys. Lett. **97**, 033301 (2010): *Organic tandem solar cells with complementary absorbing layers and a high open-circuit voltage.*

[43] K.-C. Chiu, L.-T. Juey, C.-F. Su, S.-J. Tang, M.-N. Jong, S.-S. Wang, J.-S. Wang, C.-S. Yang, and W.-C. Chou, J. Cryst. Growth **310**, 1734 (2008): *Effects of source and substrate temperatures on the properties of ITO/CuPc/C_{60} heterostructure prepared by physical vapor deposition.*

[44] B. R. Conrad, J. Tosado, G. Dutton, D. B. Dougherty, W. Jin, T. Bonnen, A. Schuldenfrei, W. G. Cullen, E. D. Williams, J. E. Reutt-Robey, and S. W. Robey, Appl. Phys. Lett. **95**, 213302 (2009): *C_{60} cluster formation at interfaces with pentacene thin-film phases.*

[45] S. Duhm, I. Salzmann, G. Heimel, M. Oehzelt, A. Haase, R. L. Johnson, J. P. Rabe, and N. Koch, Appl. Phys. Lett. **94**, 033304 (2009): *Controlling energy level offsets in organic/organic heterostructures using intramolecular polar bonds.*

[46] W. Gao and A. Kahn, Appl. Phys. Lett. **82**, 4815 (2003): *Effect of electrical doping on molecular level alignment at organic-organic heterojunctions.*

[47] Y. Gao and J. K. Grey, J. Am. Chem. Soc. **131**, 9654 (2009): *Resonance chemical imaging of polythiophene/fullerene photovoltaic thin films: Mapping morphology-dependent aggregated and unaggregated CdC species.*

[48] B. Kessler, Appl. Phys. A Mater. **67**, 125 (1998): *Phthalocyanine-C_{60} composites as improved photoreceptormaterials?*

[49] U. H. F. Bunz, Chem. Eur. J. **15**, 6780 (2009): *N-heteroacenes.*

[50] J. E. Anthony, Angew. Chem. Int. Ed. **47**, 452 (2008): *The larger acenes: Versatile organic semiconductors.*

[51] J. Aragó, P. M. Viruela, E. Ortí, R. M. Osuna, V. Hernández, J. T. L. Navarrete, C. R. Swartz, and J. E. Anthony, Theor. Chem. Acc. **128**, 521 (2011): *Functionalized pentacenes: a combined theoretical, Raman and UV-Vis spectroscopic study.*

[52] M. Böhringer, W.-D. Schneider, K. Glöckler, E. Umbach, and R. Berndt, Surf. Sci. **419**, L95 (1998): *Adsorption site determination of PTCDA on Ag(110) by manipulation of adatoms.*

[53] M. Bendikov, F. Wudl, and D. F. Perepichka, Chem. Rev. **104**, 4891 (2004): *Tetrathiafulvalenes, oligoacenenes, and their buckminsterfullerene derivatives: The brick and mortar of organic electronics.*

[54] B. W. Boudouris, F. Molins, D. A. Blank, C. D. Frisbie, and M. A. Hillmyer, Macromolecules **42**, 4118 (2009): *Synthesis, optical properties, and microstructure of a fullerene-terminated poly(3-hexylthiophene).*

[55] G. R. Desiraju and A. Gavezzotti, Acta Crystallogr., Sect. B: Struct. Sci **45**, 473 (1989): *Crystal structures of polynuelear aromatic hydrocarbons. Classification, rationalization and prediction from molecular structure.*

[56] F. Babudri, G. M. Farinola, F. Naso, and R. Ragni, Chem. Commun. **10**, 1003 (2007): *Fluorinated organic materials for electronic and optoelectronic applications: the role of the fluorine atom.*

[57] K. Reichenbächer, H. I. Süss, and J. Hulliger, Chem. Soc. Rev. **34**, 22 (2005): *Fluorine in crystal engineering - the little atom that could.*

[58] Y. Sakamoto, T. Suzuki, M. Kobayashi, Y. Gao, Y. Inoue, and S. Tokito, Mol. Cryst. Liq. Cryst. **444**, 225 (2006): *Perfluoropentacene and perfluorotetracene: Syntheses, crystal structures, and FET characteristics.*

[59] A. Hinderhofer, U. Heinemeyer, A. Gerlach, S. Kowarik, R. M. J. Jacobs, Y. Sakamoto, T. Suzuki, and F. Schreiber, J. Chem. Phys. **127**, 194705 (2007): *Optical properties of pentacene and perfluoropentacene thin films.*

[60] I. Salzmann, S. Duhm, G. Heimel, J. P. Rabe, N. Koch, M. Oehzelt, Y. Sakamoto, and T. Suzuki, Langmuir **24**, 7294 (2008): *Structural order in perfluoropentacene thin films and heterostructures with pentacene.*

[61] H.-Y. Chen and I. Chao, Chem. Phys. Lett. **401**, 539 (2005): *Effect of perfluorination on the charge-transport properties of organic semiconductors: density functional theory study of perfluorinated pentacene and sexithiophene.*

[62] J. Chen, S. Subramanian, S. R. Parkin, M. Siegler, K. Gallup, C. Haughn, D. C. Martin, and J. E. Anthony, J. Mater. Chem. **18**, 1961 (2008): *The influence of side chains on the structures and properties of functionalized pentacenes.*

[63] J.-O. Vogel, I. Salzmann, R. Opitz, S. Duhm, B. Nickel, J. P. Rabe, and N. Koch, J. Phys. Chem. B **111**, 1409 (2007): *Sub-nanometer control of the interlayer spacing in thin films of intercalated rodlike conjugated molecules.*

[64] C. Bobisch, T. Wagner, A. Bannani, and R. Möller, J. Chem. Phys. **119**, 9804 (2003): *Ordered binary monolayer composed of two organic molecules: Copperphthalocyanine and 3,4,9,10-perylene-tetra-carboxylic-dianhydride on Cu(111).*

[65] J. Bernstein, J. Phys. D Appl. Phys. **26**, 666 (1993): *Crystal growth, polymorphism and structure-property relationships in organic crystals.*

[66] M. Brinkmann, G. Gadret, M. Muccini, C. Taliani, N. Masciocchi, and A. Sironi—, J. Am. Chem. Soc. **122**, 5147 (2000): *Correlation between molecular packing and optical properties in different crystalline polymorphs and amorphous thin films of mer-Tris(8-hydroxyquinoline)aluminum(III).*

[67] U. Heinemeyer, K. Broch, A. Hinderhofer, M. Kytka, R. Scholz, A. Gerlach, and F. Schreiber, Phys. Rev. Lett. **104**, 257401 (2010): *Real-time changes in the optical spectrum of organic semiconducting films and their thickness regimes during growth.*

[68] L. M. Blinov, S. P. Palto, G. Ruani, C. Taliani, A. A. Tevosov, S. G. Yudin, and R. Zamboni, Chem. Phys. Lett. **232**, 401 (1995): *Location of charge transfer states in alpha-sexithienyl determined by the electroabsorption technique.*

[69] J. B. Birks, J. Phys. B. **3**, 1704 (1970): *Energy transfer in organic systems X. Pure and mixed crystals.*

[70] P. J. Bounds, P. Petelenz, and W. Siebrand, Chem. Phys. **63**, 303 (1981): *Charge-transfer excitons in anthracene crystals. A theoretical investigation of their optical absorption and thermal dissociation.*

[71] J.-L. Brédas, D. Beljonne, V. Coropceanu, and J. Cornil, Chem. Rev. **104**, 4971 (2004): *Charge-transfer and energy-transfer processes in π-conjugated oligomers and polymers: A molecular picture.*

[72] I. Salzmann, S. Duhm, G. Heimel, M. Oehzelt, R. Kniprath, R. L. Johnson, J. P. Rabe, and N. Koch, J. Am. Chem. Soc. **130**, 12870 (2008): *Tuning the ionization energy of organic semiconductor films: The role of intramolecular polar bonds.*

[73] J. L. Cabellos, D. J. Mowbray, E. Goiri, A. El-Sayed, L. Floreano, D. G. de Oteyza, C. Rogero, J. E. Ortega, and A. Rubio, J. Phys. Chem. C **116**, 17991 (2012): *Understanding charge transfer in donor-acceptor/metal systems: A combined theoretical and experimental study.*

[74] K. Broch, U. Heinemeyer, A. Hinderhofer, F. Anger, R. Scholz, A. Gerlach, and F. Schreiber, Phys. Rev. B **83**, 245307 (2011): *Optical evidence for intermolecular coupling in mixed films of pentacene and perfluoropentacene.*

[75] F. Anger, J. O. Ossó, U. Heinemeyer, K. Broch, R. Scholz, A. Gerlach, and F. Schreiber, J. Chem. Phys. **136**, 054701 (2012): *Photoluminescence spectroscopy of pure pentacene, perfluoropentacene, and mixed thin films.*

[76] T. Drori, J. Holt, and Z. V. Vardeny, Phys. Rev. B **82**, 075207 (2010): *Optical studies of the charge transfer complex in polythiophene/fullerene blends for organic photovoltaic applications.*

[77] L. Goris, A. Poruba, L. Hodakova, M. Vanecek, K. Haenen, M. Nesladek, P. Wagner, D. Vanderzande, L. D. Schepper, and J. V. Mancab, Appl. Phys. Lett. **88**, 052113 (2006): *Observation of the subgap optical absorption in polymer-fullerene blend solar cells.*

[78] M. Hallermann, S. Haneder, and E. D. Como, Appl. Phys. Lett. **93**, 053307 (2008): *Charge-transfer states in conjugated polymer/fullerene blends: Below-gap weakly bound excitons for polymer photovoltaics.*

[79] J. Clark, R. Archer, T. Redding, C. Foden, J. Tant, Y. Geerts, R. H. Friend, and C. Silva, J. Appl. Phys. **103**, 124510 (2008): *Charge recombination in distributed heterostructures of semiconductor discotic and polymeric materials.*

[80] L. Sebastian, G. Weiser, and H. Bässler, Chem. Phys. **61**, 125 (1981): *Charge transfer transitions in solid tetracene and pentacene studied by electroabsorption.*

[81] R. Forker and T. Fritz, Phys. Chem. Chem. Phys. **11**, 2142 (2009): *Optical differential reflectance spectroscopy of ultrathin epitaxial organic films.*

[82] O. Auciello and A. R. Krauss, *In situ real time characterization of thin films*, Wiley and Sons Inc., New York (2001).

[83] G. Back, T. Hanada, Y. Yoshida, H. Takiguchi, K. Abe, N. Tanigaki, and K. Yase, Mol. Cryst. Liq. Cryst. Sci. Tech., Sec. A Mol. Cryst. Liq. Cryst. **327**, 147 (1999): *Growth mechanism of highly ordered oriented films of copper(II) phthalocyanine on solid substrates.*

[84] S. Kowarik, A. Gerlach, M. W. A. Skoda, S. Sellner, and F. Schreiber, Europ. Phys. J. - Special Topics **167**, 11 (2009): *Real-time studies of thin film growth: Measurement and analysis of X-ray growth oscillations beyond the anti-Bragg point.*

[85] S. Kowarik, A. Gerlach, A. Hinderhofer, S. Milita, F. Borgatti, F. Zontone, T. Suzuki, F. Biscarini, and F. Schreiber, Phys. Stat. Sol. RRL **2**, 120 (2008): *Structure, morphology, and growth dynamics of perfluoro-pentacene thin films.*

[86] A. S. Bader, W. Faschinger, C. Schumacher, J. Geurts, L. W. Molenkamp, R. B. Neder, and G. Karczewski, Appl. Phys. Lett. **82**, 4684 (2003): *Real-time in situ x-ray diffraction as a method to control epitaxial growth.*

[87] S. Kowarik, A. Gerlach, S. Sellner, L. Cavalcanti, O. Konovalov, and F. Schreiber, Appl. Phys. A Mater. **95**, 233 (2009): *Real-time x-ray diffraction measurements of structural dynamics and polymorphism in diindenoperylene growth.*

[88] C. Weber, C. Frank, S. Bommel, T. Rukat, W. Leitenberger, P. Schäfer, F. Schreiber, and S. Kowarik, J. Chem. Phys. **136**, 204709 (2012): *Chain-length dependent growth dynamics of n-alkanes on silica investigated by energy-dispersive x-ray reflectivity in situ and in real-time.*

[89] S. Kowarik, A. Gerlach, S. Sellner, F. Schreiber, J. Pflaum, L. Cavalcanti, and O. Konovalov, Phys. Chem. Chem. Phys. **8**, 1834 (2006): *Anomalous roughness evolution during growth of rubrene thin films.*

[90] D. A. Evans, A. R. Vearey-Roberts, O. R. Roberts, A. C. Brieva, A. Bushell, G. T. Williams, D. P. Langstaff, G. Cabailh, and I. T. McGovern, J. Vac. Sci. & Techn. B **28**, C5F5 (2010): *Real-time monitoring of the evolving morphology and molecular structure at an organic-inorganic semiconductor interface: SnPc on GaAs(001).*

[91] R. Ruiz, D. Choudhary, B. Nickel, T. Toccoli, K. Chang, A. C. Mayer, P. Clancy, J. M. Blakely, R. L. Headrick, S. Iannotta, and G. G. Malliaras, Chem. Mater. **16**, 4497 (2004): *Pentacene thin film growth.*

[92] C. C. Mattheus, A. B. Dros, J. Baas, G. T. Oostergetel, A. Meetsma, J. L. de Boer, and T. T. Palstra, Synth. Met. **138**, 475 (2003): *Identification of polymorphs of pentacene.*

[93] T. Watanabe, T. Hosokai, T. Koganezawa, and N. Yoshimoto, Mol. Cryst. Liq. Cryst. **566**, 18 (2012): *In situ real-time x-ray diffraction during thin film growth of pentacene.*

[94] S. Kowarik, A. Gerlach, S. Sellner, F. Schreiber, L. Cavalcanti, and O. Konovalov, Phys. Rev. Lett. **96**, 125504 (2006): *Real-time observation of structural and orientational transitions during growth of organic thin films.*

[95] S. Kowarik, A. Gerlach, and F. Schreiber, J. Phys.: Condens. Matter **20**, 184005 (2008): *Organic molecular beam deposition: Fundamentals, growth dynamics, and in-situ studies.*

[96] S. Kowarik, A. Gerlach, W. Leitenberger, J. Hu, G. Witte, C. Wöll, U. Pietsch, and F. Schreiber, Thin Solid Films **515**, 5606 (2007): *Energy-dispersive x-ray reflectivity and for real-time growth studies of pentacene thin films.*

[97] B. Wedl, R. Resel, G. Leising, B. Kunert, I. Salzmann, M. Oehzelt, N. Koch, A. Vollmer, S. Duhm, O. Werzer, G. Gbabode, M. Sferrazzag, and Y. Geerts, RSC Advances **2**, 4404 (2012): *Crystallisation kinetics in thin films of dihexyl-terthiophene: the appearance of polymorphic phases.*

[98] T. Wagner, D. R. Fritz, and P. Zeppenfeld, Org. Electron. **12**, 442 (2011): *Standing and flat lying alpha-6T molecules probed by imaging photoelectron spectroscopy.*

[99] S. Milita, C. Dionigi, F. Borgatti, W. Porzio, and F. Biscarini, Nucl. Instr. Meth. Phys. Res. Sec. B **268**, 411 (2010): *Monitoring the crystallization process of nano-confined organic molecules by synchrotron X-ray diffraction.*

[100] S. Milita, C. Dionigi, F. Borgatti, A. N. Lazar, W. Porzio, S. Destri, D. Wermeille, R. Felici, J. W. Andreasen, M. M. Nielsen, and F. Biscarini, J. Phys. Chem. C **112**, 12177 (2008): *Crystallization of organic semiconductor molecules in nanosized cavities: Mechanism of polymorphs formation studied by in situ XRD.*

[101] D. Cahen and A. Kahn, Adv. Mater. **15**, 271 (2003): *Electron energetics at surfaces and interfaces: Concepts and experiments.*

[102] D. Beljonne, J. Cornil, L. Muccioli, C. Zannoni, J.-L. Brédas, and F. Castet, Chem. Mater. **23**, 591 (2011): *Electronic processes at organic-organic interfaces: Insight from modeling and implications for opto-electronic devices.*

[103] V. I. Arkhipov, P. Heremans, and H. Bässler, Appl. Phys. Lett. **82**, 4605 (2003): *Why is exciton dissociation so efficient at the interface between a conjugated polymer and an electron acceptor?*

[104] J. Blochwitz, T. Fritz, M. . Pfeiffer, K. Leo, D. M. Alloway, P. A. Lee, and N. R. Armstrong, Org. Electron. **2**, 97 (2001): *Interface electronic structure of organic semiconductors with controlled doping levels.*

[105] S. Blumstengel, N. Koch, S. Sadofev, P. Schäfer, H. Glowatzki, R. L. Johnson, J. P. Rabe, and F. Henneberger, Appl. Phys. Lett. **92**, 193303 (2008): *Interface formation and electronic structure of alpha-sexithiophene on ZnO.*

[106] M. Bronner, A. Opitz, and W. Brütting, Phys. Stat. Sol. a **205**, 549 (2008): *Ambipolar charge carrier transport in organic semiconductor blends of phthalocyanine and fullerene.*

[107] S. Duhm, I. Salzmann, R. L. Johnson, and N. Koch, J. Electron Spectrosc. Relat. Phenom. **174**, 40 (2009): *Electronic non-equilibrium conditions at C_{60}-pentacene heterostructures.*

[108] A. Opitz, J. Wagner, W. Brütting, I. Salzmann, N. Koch, J. Manara, J. Pflaum, A. Hinderhofer, and F. Schreiber, IEEE J. Sel. Top. Quant. Electr. **16**, 1707 (2010): *Charge separation at molecular donor-acceptor interfaces: Correlation between morphology and solar cell performance.*

[109] A. Hinderhofer, T. Hosokai, C. Frank, J. Novák, A. Gerlach, and F. Schreiber, J. Phys. Chem. C **115**, 16155 (2011): *Templating effect for organic heterostructure film growth: Perfluoropentacene on diindenoperylene.*

[110] S. P. Park, S. S. Kim, J. H. Kim, C. N. Whang, and S. Ima, Appl. Phys. Lett. **80, No. 16**, 2872 (2002): *Optical and luminescence characteristics of thermally evaporated pentacene films on Si.*

[111] R. Schuster and M. Knupfer, Phys. Rev. Lett. **98**, 037402 (2007): *Exciton band structure of pentacene molecular solids: Breakdown of the Frenkel exciton model.*

[112] I. Bouchoms, W. Schoonveld, J. Vrijmoeth, and T. Klapwijk, Synth. Met. **104**, 175 (1999): *Morphology identification of the thin film phases of vacuum evaporated pentacene on SiO_2 substrates.*

[113] M. Dressel, B. Gompf, D. Faltermeier, A. Tripathi, J. Pflaum, and M. Schubert, Opt. Express **16 No. 24**, 19770 (2008): *Kramers-Kronig-consistent optical functions of anisotropic crystals: generalized spectroscopic ellipsometry on pentacene.*

[114] C. C. Mattheus, G. A. de Wijs, R. A. de Groot, and T. T. M. Palstra, J. Am. Chem. Soc. **125**, 6323 (2003): *Modeling the polymorphism of pentacene.*

[115] H.-L. Cheng, Y.-S. Mai, W.-Y. Chou, and L.-R. Chang, Appl. Phys. Lett. **90**, 171926 (2007): *Influence of molecular structure and microstructure on device performance of polycrystalline pentacene thin-film transistors.*

[116] M. L. Tiago, J. E. Northrup, and S. G. Louie, Phys. Rev. B **67**, 115212 (2003): *Ab initio calculation of the electronic and optical properties of solid pentacene.*

[117] J. E. Northrup, M. L. Tiago, and S. G. Louie, Phys. Rev. B **66**, 121404 R! (2002): *Surface energetics and growth of pentacene.*

[118] K. O. Lee and T. Gan, Chem. Phys. Lett. **51**, 120 (1977): *Influence of substrate temperature on the optical properties of evaporated films of pentacene.*

[119] A. C. Mayer, R. Ruiz, H. Zhou, R. Headrick, A. Kazimirov, and G. G. Malliaras, Phys. Rev. B **73**, 205307 (2006): *Growth dynamics of pentacene thin films: Real-time synchrotron x-ray scattering study.*

[120] M. Schubert, C. Bundesmann, G. Jacopic, H. Maresch, and H. Arwin, Appl. Phys. Lett. **84**, 200 (2004): *Infrared dielectric function and vibrational modes of pentacene thin films.*

[121] R. B. Campbell, J. M. Robertson, and J. Trotter, Acta Cryst. **14**, 705 (1961): *The crystal and molecular structure of pentacene.*

[122] S. Kowarik, K. Broch, A. Hinderhofer, A. Schwartzberg, J. O. Ossó, D. Kilcoyne, F. Schreiber, and S. R. Leone, J. Phys. Chem. C **114**, 13061 (2010): *Crystal grain orientation in organic homo- and heteroepitaxy of pentacene and perfluoropentacene studied with X-ray spectromicroscopy.*

[123] Y. Sakamoto, T. Suzuki, M. Kobayashi, Y. Gao, Y. Fukai, Y. Inoue, F. Sato, and S. Tokito, J. Am. Chem. Soc. **126**, 8138 (2004): *Perfluoropentacene: High-performance p-n junctions and complementary circuits with pentacene.*

[124] Y. Inoue, Y. Sakamoto, T. Suzuki, M. Kobayashi, Y. Gao, and S. Tokito, Jpn. J. Appl. Phys. **44**, 3663 (2005): *Organic thin-film transistors with high electron mobility based on perfluoropentacene.*

[125] K. Fujii, C. Himcinschi, M. Toader, S. Kera, D. Zahn, and N. Ueno, J. El. Spec. Rel. Phen. **174**, 65 (2009): *Vibrational properties of perfluoropentacene thin film.*

[126] N. G. Martinelli, Y. Olivier, S. Athanasopoulos, M.-C. R. Delgado, K. R. Pigg, D. A. da Silva Filho, R. S. Sanchez-Carrera, E. Venuti, R. G. D. Valle, J.-L. Bredas, D. Beljonne, and J. Cornil, ChemPhysChem **10**, 2265 (2009): *Influence of intermolecular vibrations on the electronic coupling in organic semiconductors: The case of anthracene and perfluoropentacene.*

[127] A. Hinderhofer, C. Frank, T. Hosokai, A. Resta, A. Gerlach, and F. Schreiber, J. Chem. Phys **134**, 104702 (2011): *Structure and morphology of coevaporated pentacene-perfluoropentacene thin films.*

[128] T. Breuer and G. Witte, Phys. Rev. B **83**, 155428 (2011): *Epitaxial growth of perfluoropentacene films with predefined molecular orientation: A route for single-crystal optical studies.*

[129] J. Götzen, C. H. Schwalb, C. Schmidt, G. Mette, M. Marks, U. Höfer, and G. Witte, Langmuir **27**, 993 (2011): *Structural evolution of perfluoro-pentacene films on Ag(111): Transition from 2D to 3D growth.*

[130] H. Glowatzki, G. Heimel, A. Vollmer, S. L. Wong, H. Huang, W. Chen, A. T. S. Wee, J. P. Rabe, and N. Koch, J. Phys. Chem. C **116**, 7726 (2012): *Impact of fluorination on initial growth and stability of pentacene on Cu(111).*

[131] C. Schmidt, T. Breuer, S. Wippermann, W. G. Schmidt, and G. Witte, J. Phys. Chem. C **116**, 24098 (2012): *Substrate induced thermal decomposition of perfluoropentacene thin films on the coinage metals.*

[132] T. Yokoyama, C. B. Park, T. Nishimura, K. Kita, and A. Toriumi, Japanese Journal of Applied Physics **47, No.5**, 3643 (2008): *Oxygen-related degradation mechanisms for on- and off-states of perfluoropentacene thin-film transistors.*

[133] A. C. Dürr, F. Schreiber, M. Münch, N. Karl, B. Krause, V. Kruppa, and H. Dosch, Appl. Phys. Lett. **81**, 2276 (2002): *High structural order in thin films of the organic semiconductor diindenoperylene.*

[134] A. C. Dürr, F. Schreiber, K. A. Ritley, V. Kruppa, J. Krug, H. Dosch, and B. Struth, Phys. Rev. Lett. **90**, 016104 (2003): *Rapid roughening in thin film growth of an organic semiconductor (Diindenoperylene).*

[135] A. Dürr, B. Nickel, V. Sharma, U. Täffner, and H. Dosch, Thin Soid Films 21393 (2005): *Observation of competing modes in the growth of diindenoperylene on SiO_2.*

[136] A. K. Tripathi and J. Pflaum, Appl. Phys. Lett. **89**, 082103 (2006): *Correlation between ambipolar transport and structural phase transition in diindenoperylene single crystals.*

[137] M. A. Heinrich, J. Pflaum, A. K. Tripathi, W. Frey, M. L. Steigerwald, and T. Siegrist, J. Phys. Chem. C **111**, 18878 (2007): *Enantiotropic polymorphism in diindenoperylene.*

[138] M. B. Casu, I. Biswas, B. E. Schuster, M. Nagel, P. Nagel, S. Schuppler, and T. Chassé, Appl. Phys. Lett. **93**, 024103 (2008): *Molecular orientation in diindenoperylene thin films deposited on polycrystalline gold.*

[139] U. Heinemeyer, R. Scholz, L. Gisslén, M. I. Alonso, J. O. Ossó, M. Garriga, A. Hinderhofer, M. Kytka, S. Kowarik, A. Gerlach, and F. Schreiber, Phys. Rev. B **78**, 085210 (2008): *Exciton-phonon coupling in diindenoperylene thin films.*

[140] S. Kowarik, A. Gerlach, S. Sellner, L. Cavalcanti, and F. Schreiber, Adv. Eng. Mater. **11**, 291 (2009): *De-wetting in an organic semiconductor thin film observed in real-time.*

[141] M. Heilig, M. Domhan, and H. Port, J. Lumin. **110**, 290 (2004): *Optical properties and morphology of thin diindenoperylene films.*

[142] A. Hinderhofer, A. Gerlach, S. Kowarik, F. Zontone, J. Krug, and F. Schreiber, Europhys. Lett. **91**, 56002 (2010): *Smoothing and coherent structure formation in organic-organic heterostructure growth.*

[143] J. Wagner, M. Gruber, A. Hinderhofer, A. Wilke, B. Bröker, J. Frisch, P. Amsalem, A. Vollmer, A. Opitz, N. Koch, F. Schreiber, and W. Brütting, Adv. Funct. Mater. **20**, 4295 (2010): *High fill factor and open circuit voltage in organic photovoltaic cells with diindenoperylene as donor material.*

[144] R. Scholz, L. Gisslen, B.-E. Schuster, M. B. Casu, T. Chassé, U. Heinemeyer, and F. Schreiber, J. Chem. Phys. **134**, 014504 (2011): *Resonant Raman spectra of diindenoperylene thin films.*

[145] L. M. Ramaniah and M. Boero, Phys. Rev. A **74**, 042505 (2006): *Structural, electronic, and optical properties of the diindenoperylene molecule from first-principles density-functional theory.*

[146] X. Zhang, E. Barrena, D. de Oteyza, and H. Dosch, Surf. Sci. **601**, 2420 (2007): *Transition from layer-by-layer to rapid roughening in the growth of DIP on SiO_2.*

[147] A. C. Dürr, N. Koch, M. Kelsch, A. Rühm, J. Ghijsen, R. L. Johnson, J.-J. Pireaux, J. Schwartz, F. Schreiber, H. Dosch, and A. Kahn, Phys. Rev. B **68**, 115428 (2003): *Interplay between morphology, structure, and electronic properties at diindenoperylene-gold interfaces.*

[148] A. Hinderhofer, T. Hosokai, K. Yonezawa, A. Gerlach, K. Kato, K. Broch, C. Frank, J. Novák, S. Kera, N. Ueno, and F. Schreiber, Appl. Phys. Lett. **101**, 033307 (2012): *Post-growth surface smoothing of thin films of diindenoperylene.*

[149] M. Born and E. Wolf, *Principles of optics*, Pergamon Press, Oxford (1959).

[150] W. Demtröder, *Experimentalphysik 2: Elektrizität und Optik*, Springer Verlag, Heidelberg (2004).

[151] J. D. Ingle and S. R. Crouch, *Spectrochemical analysis*, Prentice-Hall Interantional Editions, Old Tappan (1988).

[152] H. Kuzmany, *Festkörperspektroskopie*, Springer Verlag, Berlin (1990).

[153] M. Dressel and G. Grüner, *Electrodynamics of Solids: Optical properties of electrons in matter*, Cambridge University Press, Cambridge (2002).

[154] U. Heinemeyer: *Optical properties of organic semiconductor thin films: Static spectra and real-time growth studies*, Ph.D. thesis, Eberhard Karls Universität Tübingen, 2009.

[155] J. Lekner *Theory of reflection of electromagnetic and particle waves* Kluwer Academic Publishers Group, Dordrecht (1987).

[156] J. B. Birks, *Photophysics of aromatic molecules*, Wiley-Interscience, New York (1970).

[157] H. Haken and H. C. Wolf, *Molekülphysik und Quantenchemie*, Springer Verlag, Heidelberg (1998).

[158] R. G. Mortimer, *Physical chemistry*, Elsevier Academic Press, Heidelberg (2008).

[159] E. A. Meyer, R. K. Castellano, and F. Diederich, Angew. Chem. Int. Ed. **42**, 1210 (2003): *Interactions with aromatic rings in chemical and biological recognition.*

[160] J. H. Williams, Acc. Chem. Res. **26**, 593 (1993): *The molecular electric quadrupole moment and solid-state architecture.*

[161] A. Hinderhofer: *Growth studies of organic heterostructures for photovoltaic applications*, Ph.D. thesis, Eberhard Karls Universität Tübingen, 2011.

[162] R. Scholz, in *Encyclopedia of Condensed Matter Physics* edited by G. Bassani, G. Liedl, and P. Wyder Elsevier, New York (2005): *Organic semiconductors.*

[163] R. Scholz, A. Kobitski, T. Kampen, M. Schreiber, D. Zahn, G. Jungnickel, M. Elstner, M. Sternberg, and T. Frauenheim, Phys. Rev. B **61**, 13659 (2000): *Resonant Raman spectroscopy of 3,4,9,10-perylene-tetracarboxylic-dianhydride epitaxial films.*

[164] M. Kasha, in *Spectroscopy of the excited state* edited by B. DiBartole Plenum Press, New York (1976).

[165] A. S. Davydov, Usp. Fiz. Nauk **82**, 393 (1964): *The theory of molecular excitons.*

[166] N. S. Bayliss, J. Chem. Phys. **18**, 292 (1950): *The effect of the electrostatic polarization of the solvent on electronic absorption spectra in solution.*

[167] N. S. Bayliss and E. G. McRae, J. Phys. Chem. **58**, 1002 (1954): *Solvent effects in organic spectra: dipole forces and the Franck-Condon principle.*

[168] J. A. Venables, *Introduction to surface and thin film processes*, Cambridge University Press, Cambridge (2000).

[169] A.-L. Barabasi and H. E. Stanley, *Fractal concepts in surface growth*, Cambridge University Press, Cambridge (1995).

[170] J. H. Hildebrand, J. Am. Chem. Soc. **51**, 66 (1929): *Solubility. XII. Regular solutions.*

[171] A. Kitaigorodsky, in *Molecular crystals and molecules* edited by E. M. Loebl, Academic Press, London, New York (1973).

[172] A. Kitaigorodsky, in *Mixed crystals* edited by M. Cordona, Springer Verlag, Heidelberg (1984).

[173] B. P. Rand, J. Xue, S. Uchida, and S. R. Forrest, J. Appl. Phys. **98**, 124902 (2005): *Mixed donor-acceptor molecular heterojunctions for photovoltaic applications. I. Material properties.*

[174] G. Ruani, C. Fontanini, M. Murgia, and C. Taliani, J. Chem. Phys. **116**, 1713 (2002): *Weak intrinsic charge transfer complexes: A new route for developing wide spectrum organic photovoltaic cells.*

[175] T. M. Clarke, F. C. Jamieson and J. R. Durrant, J. Phys. Chem. C **113**, 20934 (2009): *Transient absorption studies of bimolecular recombination dynamics in polythiophene/fullerene blend films.*

[176] J. P. Reinhardt, A. Hinderhofer, K. Broch, U. Heinemeyer, S. Kowarik, A. Vorobiev, A. Gerlach, and F. Schreiber, J. Phys. Chem. C **116**, 10917 (2012): *Structural and optical properties of mixed diindenoperylene:perfluoropentacene thin films.*

[177] K. Broch, A. Aufderheide, L. Raimondo, A. Sassella, A. Gerlach, and F. Schreiber, J. Phys. Chem. C **117**, 13952 (2013): *Optical properties of blends: Influence of mixing-induced disorder in pentacene:diindenoperylene vs. perfluoropentacene:diindenoperylene.*

[178] K. Broch, C. Bürker, J. Dieterle, S. Krause, A. Gerlach, and F. Schreiber, Phys. Stat. Sol. (RRL) **submitted**: *Impact of molecular tilt angle on the absorption spectra of pentacene:perfluoropentacene blends.*

[179] D. Datta, V. Tripathi, P. Gogoi, S. Banerjee, and S. Kumar, Thin Solid Films **516**, 7237 (2008): *Ellipsometric studies on thin film CuPc:C_{60} blends for solar cell applications.*

[180] G. Ruani, V. Dediu, M. Liess, E. Lunedei, R. Michel, M. Muccini, M. Murgia, C. Taliani, and R. Zarnboni, Synth. Met. **103**, 2392 (1999): *Photoinduced charge transfer in complex architectured films of C_{60} and donor-like molecules.*

[181] J. A. Woollam Co., *WVASE32 Manual.*

[182] D. A. G. Bruggeman, Ann. Phys. **416**, 636 (1935): *Berechnung verschiedener physikalischer Konstanten von heterogenen Substanzen. I. Dielektrizitätskonstanten und Leitfähigkeiten der Mischkörper aus isotropen Substanzen.*

[183] J. C. M. Garnett, Phil. Trans. R. Soc. Lond. A **203**, 385 (1904): *Colours in metal glasses and in metallic films.*

[184] D. Käfer and G. Witte, Phys. Chem. Chem. Phys. **7**, 2850 (2005): *Growth of crystalline rubrene films with enhanced stability.*

[185] R. Hesse, W. Hofberger, and H. Bässler, Chem. Phys. **49**, 201 (1980): *Absorption spectra of disordered solid tetracene and pentacene.*

[186] S. Schiefer, M. Huth, A. Dobrinevski, and B. Nickel, J. Am. Chem. Soc. **129**, 10316 (2007): *Determination of the crystal structure of substrate-induced pentacene polymorphs in fiber structured thin films.*

[187] H. Yoshida, K. Inaba, and N. Sato, Appl. Phys. Lett. **90**, 181930 (2007): *X-ray diffraction reciprocal space mapping study of the thin film phase of pentacene.*

[188] H.-L. Cheng, Y.-S. Mai, W.-Y. Chou, L.-R. Chang, and X.-W. Liang, Adv. Funct. Mater. **17**, 3639 (2007): *Thickness-dependent structural evolutions and growth models in relation to carrier transport properties in polycrystalline pentacene thin films.*

[189] G. Yoshikawa, T. Miyadera, R. Onoki, K. Ueno, I. Nakai, S. Entani, S. Ikeda, D. Guo, M. Kiguchi, and H. Kondoh, Surf. Sci. **600**, 2518 (2006): *In-situ measurement of molecular orientation of the pentacene ultrathin films grown on SiO_2 substrates.*

[190] S. Verlaak and P. Heremans, Phys. Rev. B **75**, 115127 (2007): *Molecular microelectrostatic view on electronic states near pentacene grain boundaries.*

[191] O. Ostroverkhova, D. G. Cooke, S. Shcherbyna, R. F. Egerton, and F. A. Hegmann, Phys. Rev. B **71**, 035204 (2005): *Bandlike transport in pentacene and functionalized pentacene thin films revealed by subpicosecond transient photoconductivity measurements.*

[192] V. I. Arkhipov, V. A. Kolesnikov, and A. Rudenko, J. Phys. D **17**, 1241 (1984): *Dispersive transport of charge carriers in polycrystalline pentacene layers.*

[193] N. E. Gruhn, D. A. da Silva Filho, T. G. Bill, M. Malagoli, V. Coropceanu, A. Kahn, and J.-L. Brédas, J. Am. Chem. Soc. **124**, 7918 (2002): *The vibrational reorganization energy in pentacene: Molecular influences on charge transport.*

[194] H.-Y. Chen and I. Chao, Chem. Phys. Lett. **401**, 539 (2005): *Effect of perfluorination on the charge-transport properties of organic semiconductors: density functional theory study of perfluorinated pentacene and sexithiophene.*

[195] M. C. R. Delgado, K. R. Pigg, D. A. da Silva Filho, N. E. Gruhn, Y. Sakamoto, T. Suzuki, R. M. Osuna, J. Casado, V. Hernandez, J. Teodomiro, L. Navarrete, N. G. Martinelli, J. Cornil, R. S. Sanchez-Carrera, V. Coropceanu, and J.-L. Brédas, J. Am. Chem. Soc. **131**, 1502 (2009): *Impact of perfluorination on the charge-transport parameters of oligoacene crystals.*

[196] S. B. Heidenhain, Y. Sakamoto, T. Suzuki, A. Miura, H. Fujikawa, T. Mori, S. Tokito, and Y. Taga, J. Am. Chem. Soc. **122**, 10240 (2000): *Perfluorinated oligo(p-phenylene)s: Efficient n-type semiconductors for organic light-emitting diodes.*

[197] B. M. Medina, D. Beljonne, H.-J. Egelhaaf, and J. Gierschner, J. Chem. Phys. **126**, 111101 (2007): *Effect of fluorination on the electronic structure and optical excitations of pi-conjugated molecules.*

[198] F. Schreiber, Phys. Stat. Sol. a **201**, 1037 (2004): *Organic molecular beam deposition: Growth studies beyond the first monolayer.*

[199] G. Witte and C. Wöll, J. Mater. Res. **19**, 1889 (2004): *Growth of aromatic molecules on solid substrates for applications in organic electronics.*

[200] M. Kytka: *Characterization of rubrene thin films by optical techniques*, Ph.D. thesis, Slovak University of Technology in Bratislava, 2008.

[201] H. Proehl, R. Nitsche, T. Dienel, K. Leo, and T. Fritz, Phys. Rev. B **71**, 165207 (2005): *In situ differential reflectance spectroscopy of thin crystalline films of PTCDA on different substrates.*

[202] J. McIntyre and D. Aspnes, Surf. Sci. **24**, 417 (1971): *Differential reflection spectroscopy of very thin surface films.*

[203] R. Forker, M. Gruenewald, and T. Fritz, Annu. Rep. Prog. Chem., Sect. C: Phys. Chem. **108**, 34 (2012): *Optical differential reflectance spectroscopy on thin molecular films.*

[204] R. Forker, T. Dienel, and T. Fritz, Phys. Rev. B **74**, 165410 (2006): *Optical evidence for substrate-induced growth of ultrathin hexa-peri-hexabenzocoronene films on highly oriented pyrolytic graphite.*

[205] R. Nitsche and T. Fritz, Phys. Rev. B **70**, 195432 (2004): *Determination of model-free Kramers-Kronig consistent optical constants of thin absorbing films from just one spectral measurement: Application to organic semiconductors.*

[206] R. M. A. Azzam and N. M. Bashara, *Ellipsometry and polarized light*, North Holland Publishing Company, Amsterdam and New York (1977).

[207] B. Johs, Thin Solid Films **234**, 395 (1993): *Regression calibration method for rotating element ellipsometers.*

[208] E. Bortchagovsky, Thin Solid Films **307**, 192 (1997): *Ellipsometric method for investigation of the optical anisotropy of thin films: theory and calculations.*

[209] U. Heinemeyer, A. Hinderhofer, M. I. Alonso, J. O. Ossó, M. Garriga, M. Kytka, A. Gerlach, and F. Schreiber, Phys. Stat. Sol. (a) **205**, 927 (2008): *Uniaxial anisotropy of organic thin films determined by ellipsometry.*

[210] J. Als-Nielsen and D. McMorrow, *Elements of modern X-ray physics*, Wiley, Chichester (2000).

[211] M. Birkholz, *Thin Film Analysis by X-Ray Scattering*, Wiley-VCH, Weinheim (2006).

[212] S. Kowarik: *Real-time studies of thin film growth of organic semiconductors*, Ph.D. thesis, Wadham College, Oxford, 2006.

[213] K. Ritley, B. Krause, F. Schreiber, and H. Dosch, Rev. Sci. Instrum. **72**, 1453 (2001): *A portable UHV organic molecular beam deposition system for in situ x-ray diffraction measurements.*

[214] L. G. Parratt, Phys. Rev. **95**, 359 (1954): *Surface studies of solids by total reflection of x-rays.*

[215] Christian Braun, HMI Berlin, Parratt 32 software, 1997-2002.

[216] M. Björck and G. Andersson, J. Appl. Crystallogr. **40**, 1174 (2007): *GenX: an extensible x-ray reflectivity refinement program utilizing differential evolution.*

[217] A. Aufderheide: *Optical and structural properties of molecular mixtures of pentacene and diindenoperylene in thin films*, Diploma thesis, Eberhard Karls Universität Tübingen, 2011.

[218] S. Morita, R. Wiesendanger, and E. Meyer (Editors) *Noncontact atomic force microscopy*, Springer-Verlag Heidelberg (2002).

[219] J. Stöhr, *NEXAFS spectroscopy*, Springer-Verlag Heidelberg (2003).

[220] F. Stöhr and D. A. Outka, Phys. Rev. B **36**, 7891 (1987): *Determination of molecular orientations on surfaces from the angular dependence of near-edge x-ray-absorption fine-structure spectra.*

[221] G. Hähner, Chem. Soc. Rev. **35**, 1244 (2006): *Near edge X-ray absorption fine structure spectroscopy as a tool to probe electronic and structural properties of thin organic films and liquids.*

[222] E. W. Thulstrup and J. Michl, *Elementary Polarization Spectroscopy*, Wiley VCH and Sons Inc. New York (1989).

[223] G. Gauglitz and T. Vo-Dinh (Editors) *Handbook of Spectroscopy*, Wiley-VCH Verlag GmbH & Co. Weinheim (2003).

[224] D. de Oteyza, A. Sakko, A. El-Sayed, E. Goiri, L. Floreano, A. Cossaro, J. Garcia-Lastra, A. Rubio, and J. Ortega, Phys. Rev. B **86**, (2012): *Inversed linear dichroism in F K-edge NEXAFS spectra of fluorinated planar aromatic molecules.*

[225] M. Cerruti, C. Rhodes, M. Losego, A. Efremenko, J.-P. Maria, D. Fischer, S. Franzen, and J. Genzer, J. Phys. D: Appl. Phys. **40**, 4212 (2007): *Influence of indium tin oxide surface structure on the ordering and coverage of carboxylic acid and thiol monolayers.*

[226] L. Raimondo, M. Campione, M. Laicini, M. Moret, A. Sassella, P. Spearman, and S. Tavazzi, Appl. Surf. Sci. **253**, 271 (2006): *Absorbance spectra of polycrystalline samples and twinned crystals of oligothiophenes.*

[227] A. Sassella, D. Braga, M. Campione, T. Ciabattoni, M. Moret, J. Parravicini, and G. B. Parravicini, J. Appl. Phys. **109**, 013529 (2011): *Probing phase transitions and stability of organic semiconductor single crystals by dielectric investigation.*

[228] Perkin Elmer Inc. LLC, *Lambda 800/900 Users Guide*, 2001.

[229] M. Wojdyr, J. Appl. Cryst. **43**, 1126 (2012): *Fityk: a general-purpose peak fitting program.*

[230] C. Frank: *Röntgen-Untersuchungen an funktionalisierten organischen Halbleiter-strukturen* Diploma thesis, Eberhard Karls Universität Tübingen, 2010.

[231] J. Reinhardt: *Structural, Optical, and Photovoltaic Properties of Blended Perfluo-rinated Pentacene and Diindenoperylene in Thin Films* Diploma thesis, Eberhard-Karls Universität Tübingen, 2011.

[232] C. Frank, Ph.D. thesis, Eberhard Karls Universität Tübingen, **in preparation**.

[233] K. Broch, A. Gerlach, C. Lorch, J. Dieterle, J. Novák, A. Hinderhofer, and F. Schreiber, J. Chem. Phys. **submitted**: *Structure formation in perfluoropentacene:diindenoperylene blends and its impact on transient effects in the optical properties studied in real-time during growth.*

[234] P. Müller-Buschbaum, Lecture Notes in Phys. **776**, 61 (2009): *A basic introduction to grazing incidence small-angle x-ray scattering.*

[235] R. Lazzari, J. Appl. Crystallogr. **35**, 406 (2002): *IsGISAXS: a program for grazing-incidence small-angle x-ray scattering analysis of supported islands.*

[236] P. de Gennes and J. Prost, *The physics of liquid crystals*, Oxford Univ. Press Oxford (1993).

[237] K. Broch: *Optische Spektroskopie an Pentacen-Perfluoropentacen Einzel- und Mischsystemen* Diploma thesis, Eberhard-Karls Universität, Tübingen, 2010.

[238] U. Heinemeyer, A. Hinderhofer, M. I. Alonso, J. O. Ossó, M. Garriga, M. Kytka, A. Gerlach, and F. Schreiber, Phys. Stat. Sol. a **205**, 927 (2008): *Uniaxial anisotropy of organic thin films determined by ellipsometry.*

[239] M. Kytka, A. Gerlach, J. Kováč, and F. Schreiber, Appl. Phys. Lett. **90**, 131911 (2007): *Real-time observation of oxidation and photo-oxidation of rubrene thin films by spectroscopic ellipsometry.*

[240] M. P. Marder, *Condensed matter physics*, Wiley-Interscience New York (2000).

[241] K.-S. Lee, T.-J. Smith, K.-C. Dickey, J.-E. Yoo, K.-J. Stevenson, and Y.-L. Loo, Adv. Funct. Mater. **16**, 2409 (2006): *High-resolution characterization of pentacene/polyaniline interfaces in thin-film transistors.*

[242] J. Helzel, S. Jankowski, M. El Helou, G. Witte, and W. Heimbrodt, Appl. Phys. Lett. **99**, 211102 (2011): *Temperature dependent optical properties of pentacene films on zinc oxide.*

[243] S.-H. Lim, T. G. Bjorklund, F. C. Spano, and C. J. Bardeen, Phys. Rev. Lett. **92**, 107402 (2004): *Exciton delocalization and superradiance in tetracene thin films and nanoaggregates.*

[244] Y. Wakayama, D. G. de Oteyza, J. M. Garcia-Lastra, and D. J. Mowbray, ACS Nano **5**, 581 (2011): *Solid-state reactions in binary molecular assemblies of F_{16}CuPc and pentacene.*

[245] H. Proehl, T. Dienel, R. Nitsche, and T. Fritz, Phys. Rev. Lett. **93**, 097403 (2007): *Formation of solid-state excitons in ultrathin crystalline films of PTCDA: From single molecules to molecular stacks.*

List of publications

1. U. Heinemeyer, K. Broch, A. Hinderhofer, M. Kytka, R. Scholz, A. Gerlach, and F. Schreiber, Phys. Rev. Lett. **104**, 257401 (2010), *Real-time changes in the optical spectrum of organic semiconducting films and their thickness regimes during growth.*

2. R. Srnanek, J. Jakabovic, E. Dobrocka, G. Irmer, U. Heinemeyer, K. Broch, F. Schreiber, A. Vincze, V. Machovic, J. Kovac, and D. Donoval, Chem. Phys. Lett. **484**, 299 (2010), *Evidence of pentacene bulk and thin film phase transformation into an orthorhombic phase by iodine diffusion.*

3. S. Kowarik, K. Broch, A. Hinderhofer, A. Schwartzberg, J. O. Ossó, D. Kilcoyne, F. Schreiber, and S. R. Leone, J. Phys. Chem. C **114**, 13061 (2010), *Crystal grain orientation in organic homo- and heteroepitaxy of pentacene and perfluoropentacene studied with X-ray spectromicroscopy.*

4. K. Broch, U. Heinemeyer, A. Hinderhofer, F. Anger, R. Scholz, A. Gerlach, and F. Schreiber, Phys. Rev. B **83**, 245307 (2011), *Optical evidence for intermolecular coupling in mixed films of pentacene and perfluoropentacene.*

5. F. Anger, J. O. Ossó, U. Heinemeyer, K. Broch, R. Scholz, A. Gerlach, and F. Schreiber, J. Chem. Phys. **136**, 054701 (2012), *Photoluminescence spectroscopy of pure pentacene, perfluoropentacene and mixed thin films.*

6. J. Reinhardt, A. Hinderhofer, K. Broch, U. Heinemeyer, S. Kowarik, A. Vorobiev, A. Gerlach, and F. Schreiber, J. Phys. Chem. C **116**, 10917 (2012), *Structural and optical properties of mixed diindenoperylene-perfluoropentacene thin films.*

7. A. Hinderhofer, T. Hosokai, K. Yonezawa, A. Gerlach, K. Kato, K. Broch, C. Frank, J. Novák, S. Kera, N. Ueno, and F. Schreiber, Appl. Phys. Lett. **101**, 033307 (2012), *Post-growth surface smoothing of thin films of diindenoperylene.*

8. A. Aufderheide, K. Broch, J. Novák, A. Hinderhofer, R. Nervo, A. Gerlach, R. Banerjee and F. Schreiber, Phys. Rev. Lett. **109**, 156102 (2012), *Mixing-induced anisotropic correlations in molecular crystalline systems.*

9. A. Hinderhofer, A. Gerlach, K. Broch, T. Hosokai, K. Yonezawa, K. Kato, S. Kera, N. Ueno, and F. Schreiber, J. Phys. Chem. C **117**, 1053 (2013), *Geometric and electronic structure of templated C_{60} on diindenoperylene thin films.*

10. F. Anger, R. Scholz, E. Adamski, K. Broch, A. Gerlach, Y. Sakamoto, T. Suzuki, and F. Schreiber, Appl. Phys. Lett. **102**, 13308 (2013), *Optical properties of fully and partially fluorinated rubrene in films and solution.*

11. F. Liscio, C. Albonetti, K. Broch, A. Shehu, S. D. Quiroga, L. Ferlauto, C. Frank, S. Kowarik, R. Nervo, A. Gerlach, S. Milita, F. Schreiber, and F. Biscarini, ACS Nano **7**, 1257 (2013), *Molecular reorganization in organic field-effect transistors and its effect on two-dimensional charge transport pathways.*

12. C. Frank, J. Novák, A. Gerlach, G. Ligorio, K. Broch, A. Hinderhofer, A. Aufderheide, R. Banerjee, R. Nervo and F. Schreiber, J. Appl. Phys. **114**, 043515 (2013), *Real-time X-ray scattering studies on temperature dependence of perfluoropentacene thin film growth.*

13. K. Broch, A. Aufderheide, L. Raimondo, A. Sassella, A. Gerlach and F. Schreiber, J. Phys. Chem. C **117**, 13952 (2013), *Optical properties of blends: Influence of mixing-induced disorder in pentacene:diindenoperylene vs. perfluoropentacene:diindenoperylene.*

14. A. Horrer, C. Schäfer, D. Gollmer, K. Broch, J. Rogalski, Y. Fulmes, D. Zhang, A.J. Meixner, F. Schreiber, D.P. Kern, M. Fleischer, SMALL, *Parallel fabrication of plasmonic nanocone sensing arrays*, in print.

15. K. Vasseur, K. Broch, A. L. Ayzner, B. P. Rand, D. Cheyns, C. Frank, F. Schreiber, M. F. Toney, L. Froyen, P. Heremans, ACS Applied Materials & Interfaces, *Controlling the texture and crystallinity of evaporated lead phthalocyanine thin films for near-infrared sensitive solar cells*, in print.

16. K. Broch, C. Bürker, J. Dieterle, S. Krause, A. Gerlach and F. Schreiber, Phys. stat. sol. RRL, *Impact of molecular tilt angle on the absorption spectra of pentacene:perfluoropentacene blends*, in print.

17. X. Wang, K. Broch, F. Schreiber, A. J. Meixner, D. Zhang, *Probing the local structural order in pentacene thin films*, submitted.

18. K. Broch, A. Gerlach, C. Lorch, J. Dieterle, J. Novák, A. Hinderhofer and F. Schreiber, J. Chem. Phys., *Structure formation in perfluoropentacene:diindenoperylene blends and its impact on transient effects in the optical properties studied in real-time during growth*, accepted.

Danksagung

An dieser Stelle möchte ich mich bei allen bedanken, die durch ihre Unterstützung zum Gelingen dieser Arbeit beigetragen haben.

Prof. Dr. Frank Schreiber danke ich für das Ermöglichen dieser Arbeit und für die gute Betreuung.

Prof. Dr. Monika Fleischer danke ich dafür, dass sie sich bereit erklärt hat, diese Arbeit als Zweitkorrekteurin zu begutachten.

Mein Dank gilt auch Dr. Alexander Gerlach für seine Hilfe bei Fragen zur Vakuumkammer und zur Röntgenstreuung, hilfreiche Diskussionen und seine Unterstützung während Strahlzeiten.

Antje Aufderheide danke ich besonders für die gute Zusammenarbeit während ihrer Diplomarbeit und ihre Messungen an PEN:DIP-Mischungen, die eine wichtige Grundlage für die Ergebnisse dieser Doktorarbeit waren. Darüber hinaus danke ich ihr für viele interessante Diskussionen und ihre Unterstützung während Strahlzeiten und arbeitsreicher Wochenenden.

Prof. Dr. Adele Sassella und Dr. Luisa Raimondo danke ich für die Möglichkeit, Transmissionsspektroskopie an PFP:DIP und PEN:DIP Mischungen zu messen, ihre Unterstützung und Gastfreundlichkeit während dieser Messungen an der Università di Milano-Bicocca in Mailand, die geduldige Beantwortung aller Fragen und die Hilfe bei der Interpretation der Daten. Desweiteren danke ich Dr. Reinhard Scholz, der mit der Beantwortung einiger theoretischer Fragen und der Diskussion der Daten viel zum Gelingen dieser Arbeit beigetragen hat.

Der "Studienstiftung des Deutschen Volkes" danke ich für finanzielle Unterstützung meiner Doktorarbeit.

Bei Dr. Jiří Novák möchte ich mich für seine Hilfe während Stahlzeiten und bei der Auswertung von Röntgendaten bedanken. Ausserdem danke ich Dr. Rupak Banerjee, Johannes Dieterle, Christopher Lorch, Dr. Roberto Nervo, Prof. Dr. Phil Willmott, Christoph Bürker, Max Bauer, Dr. Antje Vollmer und Dr. Stefan Krause für ihre Unterstützung während Strahlzeiten an der ESRF (Grenoble), der SLS (Villigen) oder BESSY II (Berlin). Dr. Robert Jacobs, Marco Gruenewald und Johannes Dieterle danke ich für hilfreiche Diskussionen zur Auswertung der DRS-Daten und Dr. Markus Ströbele für DSC-Messungen. Desweiteren danke ich Dr. Dai Zhang, Dr. Xiao Wang und Prof. Dr. Alfred Meixner für die gute Zusammenarbeit. Für das Korrekturlesen meiner Arbeit danke ich Antje Aufderheide, Dr. Alexander Hinderhofer, Dr. Jiří Novák, Johannes Dieterle, Dr. Alexander Gerlach, und Christoph Bürker. Bei der gesamten Arbeitsgruppe Schreiber, sowie dem Sekretariat möchte ich mich für die fachliche und außerfachliche Unterstützung bedanken. Der Feinmechanik-Werkstatt der Universität Tübingen und insbesondere Antje Treftz danke ich für die Zusammenarbeit.

Schliesslich möchte ich mich bei meiner Schwester für Gesellschaft während arbeitsreicher Wochenenden und viele gemütliche Abendessen bedanken. Ihr und meinen Eltern danke ich für inspirierende Gespräche und ihre Unterstützung während der letzten Jahre.